CYCLIC DEFORMATION OF MONOCRYSTALLINE NICKEL ALUMINIDE AND HIGH TEMPERATURE COATINGS

by

ESTEBAN PEDRO BUSSO

ING. ELECTRO - MECH., National University of Cordoba, Argentina (1980)

M.S., Mechanical Engineering, Massachusetts Institute of Technology, U.S.A. (1987)

SUBMITTED IN PARTIAL FULFILLMENT

OF THE REQUIREMENTS FOR THE

DEGREE OF

DOCTOR OF PHILOSOPHY

IN MECHANICAL ENGINEERING

at the

MASSACHUSETTS INSTITUTE OF TECHNOLOGY

May, 1990

Signature of Author_____

Department of Mechanical Engineering
May, 1990

Certified by_____

Professor Frank A. McClintock
Thesis Supervisor

Accepted by_____

Professor Ain A. Sonin, Chairman
Departmental Committee on Graduate Studies

CYCLIC DEFORMATION OF MONOCRYSTALLINE NICKEL ALUMINIDE AND HIGH TEMPERATURE COATINGS

by

Esteban P. Busso

Submitted to the Department of Mechanical Engineering
in partial fulfillment of the
requirements for the Degree of Doctor of Philosophy in
Mechanical Engineering

Abstract

The thermal fatigue life of a gas-turbine airfoil protective coating is predicted from an understanding of the mechanisms responsible for its degradation. Thermal fatigue tests under realistic service conditions revealed that cyclic degradation consisted primarily of coating cracking. Inelastic structural analysis of both coating and single crystal substrate showed the cracking to critically depend on the coating strain ranges and tensile cooling stresses. At high cooling rates, there was early cracking of the protective oxide scale with surface initiation. At normal cooling rates, cracks originated from internal diffusion-induced (Kirkendall) voids, and grew from the original coating-substrate interface towards the coating surface for $\Delta\epsilon > 0.51\%$.

The study of the deformation of monocrystalline Ni-aluminide under [001] loadings within the 750-850°C range revealed two different modes of deformation, namely kinematic hardening in the small strain range regime, and isotropic hardening during large monotonic deformation. A detailed analysis of the observed dislocation structure showed that the total flow stress is due to lattice resistance to dislocation motion and to discrete obstacle resistance due to forest dislocations, all of which were found to be impenetrable within the temperature and flow stress ranges studied here. A mechanistic interpretation of the macroscopic stress-strain response indicated that appreciable plastic flow is not observed until forest dislocations can be bypassed, which can occur without a noticeable increase in dislocation density. For strains of up to 35%, dislocations travel larger distances and develop sessile segments or are held by dislocation forests forcing them to act as multiplication sources, causing the dislocation density to increase over the level needed to balance dynamic recovery processes.

Based on the above understanding, a slip-system micromechanics model has been proposed which successfully corrolates the flow stress dependence on temperature, strain rate, and structure. For stresses above the flow stress, the kinematic and isotropic hardening modes associated with bowing and storage respectively of gliding dislocations are properly represented. This model has been applied to study the development of surface roughening in NiAl coatings.

Thesis Supervisor: Dr. Frank A. McClintock
Title: Prof. of Mechanical Engineering

ACKNOWLEDGEMENTS

There are many people who, in different dimensions, have made the five years of my MIT graduate education a memorable and rewarding experience.

My greatest appreciation goes to my beautiful wife and son, Hilary and Daniel Sebastian, who have so patiently supported and stood by me during the last five years. I would have been lost without them.

I would like to express my deep gratitude to my thesis advisor, Prof. Frank A. McClintock, for his invaluable guidance, continuous support and encouragement, and for offering me the opportunity to pursue my doctoral research.

I would also like to express my very special gratitude to Prof. Ali S. Argon for the numerous challenging discussions and his pointed remarks that so much benefitted my research. I would also like to thank Profs. Samuel M. Allen and Rohan Abeyaratne for participating in my Thesis Committee and for some helpful discussions and comments in the last part of my thesis.

Special thanks to my friends Gustavo Weber, Curt Bronkhorst, Sarah Wineman, and Vijay Gupta whose support and frienship made it all worthwhile.

To my officemates Jim Easter, Yun Yae Kim, and Zi Ming, and to all my colleague graduate students with whom I have shared innumerable hours in the computer room, my gratitude for their friendship and cheerful ways. I have enjoyed their company very much.

I greatly appreciate the support of General Motors - Allison Turbine Division and General Electric - Evendale through the donation of the single crystal materials for this study. My special appreciation also to Ya Pin Liu for his excellent TEM work, and to John Holmes and Glenn Romanousky for their help on my experiments.

It is a pleasure to acknowledge the financial support of the Center for Materials Science and Engineering of MIT through a National Science Foundation grant DMR 87-19217.

Contents

General Introduction

The pre-stated goals set in high temperature materials research, which were originally characterized mainly on the basis of simple properties such as melting temperature, density, and elastic modulus, are now also shaped by the very sophisticated strengthening mechanisms present in some alloys. The tendency has been to design components with lower densities that can operate at higher service temperatures. The potential payoffs of developing new materials that can operate at higher temperatures and with lower densities include reduced weight for the component or unit (e.g. turbine engine), reduced cooling requirements, and higher operating temperatures with a resulting increase in thermodynamic efficiency. These improvements will then lead to a reduction in fuel consumption.

Before a new material can be fully integrated into the final design process, analytical models are usually needed to predict the component durability and reliability (e.g. distortions, fracture, microstructural changes). By developing more realistic constitutive models for both high temperature inelastic deformation and fracture, improved accuracy in predicting lifetimes and producing economic designs can be expected. These models are usually characterized by appropriate flow and evolutionary equations, that is a mathematical representation of the deformation response of the material to externally applied loading, in terms of internal parameters which themselves evolve with time, temperature, stress, and strain. The models are usually contained in finite element and other analyses in order to predict stresses, inelastic strains, crack growth rates, etc. The problems simulated are nonlinear and time-dependent in nature.

This research deals with the study of two aspects of the high temperature behavior of a gas turbine airfoil, namely the thermal fatigue degradation of its protective

coating, and the thermo-mechanical behavior of its monocrystalline substrate. This work strives towards the achievement of a microstructure-based theory of mechanical behavior of an engineering alloy. In general terms, the scope of this work is not only relevant in the design of components in hot-sections of modern jet engines, but also in aerospace propulsion systems, supersonic airframes, and in other power-generation and energy-related applications.

This thesis is structured in two parts. Part I (Chapters 1 to 3) discusses the thermal fatigue degradation of a NiCoCrAlY overlay protective coating. Chapter 1 studies the thermally induced stress and strain histories in both coating and substrate. Chapter 2 deals with the effects of strain histories on coating durability, and describes the type of coating degradation observed. Chapter 3, discusses the mechanisms of nucleation and growth of the diffusion-induced interface voids, from which cracks initiate under typical loading conditions.

Part II (Chapters 4 to 8) deals with high temperature cyclic behavior of cubic NiAl single crystals. This alloy is of particular interest as a substrate phase material, as a protective coating, and also as the matrix material in metal-matrix composites. Chapter 4 investigates the dislocation structure of undeformed NiAl. The mechanisms responsible for the cyclic behavior of NiAl are examined in Chapter 5, and a slip-system micromechanics model to predict its behavior is proposed in Chapter 6. This model is then used as a guide to derive functional forms to study the development of surface roughening in Chapter 7. Finally, a different approach is presented in Chapter 8 to model the visco-plastic material behavior in materials with a well-developed subgrain structure and a more pronounced Bauschinger effect.

List of Figures

Part I
Thermal Fatigue of High Temperature Protective Coatings

Chapter 1

Stress-Strain Histories in Coatings on Single Crystal Specimens of a Turbine Blade Alloy

Abstract

The stress-strain response of an electron beam physical vapor deposited (EB-PVD) NiCoCrAlY overlay coating applied to a single crystal nickel base superalloy (CMSX-3) was investigated by subjecting stepped-disk fatigue specimens to thermal cycles with different rates of heating (from 520 to 1090°C in 4.5, 6, and 20s) and cooling (to 520°C in 7s and 15s).

Rate-dependent material anisotropy was modeled using a creep (or flow) potential for a cubic crystal and the associated flow rule. An anisotropic creep finite element analysis of the substrate revealed that continued cycling does not affect the strain ranges, which play a role in coating degradation. However, continued cycling does produce an increase of the peak tensile stresses (from 13 MPa for the first cycle to

about 250 Mpa at the 6000th cycle for 4.5s heating history). Most of this transition occurs before the 500th cycle. As a consequence of these tensile stresses, crack propagation rates into the substrate are expected to be more severe than the predictions from a thermo-elastic analysis. However, the conventional thermo-elastic analysis was very accurate at estimating the strain ranges.

For the coating, an isotropic creep finite element analysis showed that the mechanical strain range ($\Delta\epsilon^e + \Delta\epsilon^c$) and tensile peak stresses responsible for crack initiation and crack growth, with 0.52% strain range in the substrate, are 0.83% and 460 MPa for the 4.5s heating cycle, due in large part to the thermal expansion mismatch between the coating and substrate.

1.1 Introduction

The drive toward better performance and fuel economy for aircraft gas turbine engines has resulted in ever-higher turbine inlet temperatures. The resulting heating and cooling rates are higher along the airfoil edges than in the bulk of the blade, generating cyclic thermal strain gradients. During take-off the leading and trailing edges of a first stage blade can rise from 520 to 1090 °C in under 8 sec (Thulin et al., 1982; Kaufman and Halford, 1984). During turbine shut-down immediately after landing and thrust reverse, the edge temperatures can decrease from 1090 to 520 °C in 5 to 17 seconds.

The choice of the substrate material is usually based on its creep and fatigue strengths for given operating conditions. Material chemistry may enhance these mechanical properties but does little to improve resistance against oxidation, hot corrosion, and surface erosion experienced by materials at high temperatures. This deficiency is overcome by applying a 50-100 μm thick protective coating. However,

the ever-increasing operating conditions make coating degradation a life-limiting phenomenon.

Knowledge of the stress-strain histories of both the substrate (e.g. blades by Kaufman and Halford, 1984) and the coating is necessary to predict how these histories cause coating cracking or spalling, reducing its ability to protect the substrate. Unfortunately, direct measurements of stresses and strains during service are not possible. Therefore, simulation of service conditions with feasible experiments is necessary. Furthermore, due to interaction between material properties and the inhomogeneous temperatures, these experiments are usually coupled with highly complex analysis.

Considerable work has been done in the past on thermal fatigue of uncoated (Howes, 1976) and coated specimens (Leverant et al., 1976; Nesbitt et al., 1984; Rickerby and Wood, 1986). However, many limitations arise from the gas burner and fluidized bed techniques used to simulate service conditions. During this investigation, induction heating of the periphery of coated stepped-disk specimens was used to reproduce heating rates and ranges of cyclic thermal strains typical of those developed in trailing edges of blades and vanes during normal operating conditions. This technique, developed by Holmes and McClintock (1987), and adapted to 14mm diameter specimens by Busso (1987), offers substantial improvements over the more traditional gas burner and fluidized beds techniques (Howes, 1976). The main advantages of induction heating are reduced costs and the increased flexibility in selecting the desired temperature cycle and the environment to which the specimens will be subjected. As in gas burner rigs and fluidized bed tests, the temperatures can be measured with appropriately placed thermocouples. This eliminates the need for expensive heat transfer analysis to determine the temperature distributions in the specimen during the thermal cycle.

Here we address the problem of finding the coating strain histories due to imposed

loading from the substrate under various heating and cooling rates in the convenient disk-shaped specimens used with induction heating. Accompanying thermal fatigue experiments have been reported elsewhere (Busso, 1987; chapter 2).

As an example, CMSX-3 was chosen as a typical precipitation hardened Ni-based superalloy. An electron beam - physical vapor deposited (EB-PVD) NiCoCrAlY overlay coating was selected as the protective coating (see Table 1.1 for chemical compositions).

1.2 Experimental Procedure

1.2.1 Specimen geometry

Stepped-disk specimens of 14mm-diameter (Fig. 1.1) were machined from a single crystal rod of CMSX-3 with their faces were normal to the $< 001 >$ crystal growth direction and with external radii typical of those of blade trailing edges. Specimens were subsequently given a 95μm thick coating and a combined aging and diffusion treatment.

Due to the anisotropic elastic and creep material properties interacting with the radially inhomogeneous temperatures, the strain range along the specimen periphery is a function of its local crystallographic orientation, changing from a maximum at the $< 100 >$ to a minimum at the $< 110 >$ periphery orientation. This allows the use of a single specimen to simultaneously obtain coating durability and crack initiation data from various strain levels, all subject to the same temperature histories.

1.2.2 Control of coating strain history

Since the thin coating gives negligible constraints to the substrate, the total in-plane strain history of the coating is determined by the total in-plane strain history of the substrate.

Programming of the power input to the concentrator coil allows control of the heating and cooling rates. These rates in turn determine the transient strains in the periphery from the temperature distributions throughout the specimen. Enough steady state compression in the periphery to simulate cruise conditions is achieved by passing compressed air through the center of the specimen and its supporting rods.

For higher tensile strains during cooling, high pressure air was blown on the specimen periphery from an upper and a lower cooling manifold.

1.2.3 Selection of thermal cycles

To determine the effect of different strain histories on coating degradation, three different heating rates were used on the periphery, all with minimum temperatures of 520°C, a holding time of 60s at 1090°C, and cooling back to 520°C in 15s. The rapid 4.5s heating of Fig. 1.2a, the intermediate 6s heating of Fig. 1.2b, and the slow 20s heating cycle of Fig. 1.2c were chosen to show how the strain histories obtained from these different cycles affect coating life. The intermediate heating (6s) rate was combined with a fast cooling (7s) rate to evaluate the effect of higher tensile peak stresses generated during cycle cooling (Fig. 1.2d). The temperature profiles in the specimen were established by using four chromel-alumel thermocouples (0.13 mm wire diameter) at various radii (see Fig. 1.3).

1.3 Finite Element Analysis

In the disk-shaped specimen discussed here, the stress-strain history of its periphery is found from the measured temperature history throughout the specimen. The non-linear finite-element program ABAQUS (1985) was used for this purpose.

It is common practice in industry to use elastic strain ranges as a way to describe

coating conditions. In general, a high temperature component is subjected to both static (creep) and cyclic (fatigue) loadings. A flow and evolutionary model for a general history in the Bauschinger regime ($\epsilon < 1\%$) would be needed to account for all types of inelastic strains which develop during service. However, due to the lack of such data, anisotropic power law creep was assumed as an initial approximation to determine the effects of inelasticity on the stress-strain response, compared with a thermo-elastic analysis.

1.3.1 Model of substrate

Due to symmetry, a 45^o octant of the anisotropic stepped-disk specimen was sufficient for finite element modeling (Fig. 1.3). 112 eight-node plane stress elements with full Gaussian integration were used. Symmetry boundary conditions were applied along the $< 100 >$ and $< 110 >$ radial directions.

The mean coefficients of thermal expansion for the single crystal CMSX-3 are given in Fig. 1.4 (Allison-GM, 1986).

Elastic compliance data, determined ultrasonically (Allison-GM, 1986), were given in terms of

$$S_{11} = \frac{1}{E_{<100>}}, \quad S_{12}, \quad \text{and} \quad S_{66} = \frac{1}{G_{<100>}} \ . \tag{1.1}$$

Because the bulk modulus K, determined from

$$K = \frac{1}{3\,(S_{11} + 2\,S_{12})} \ , \tag{1.2}$$

showed some irregularities (see Fig. 1.5), the data were smoothed with a second order polynomial. These smoothed values, together with $E_{<100>}$ and $G_{<100>}$, were then used to obtain the elastic compliances. For cubic symmetry, the stiffness constants, denoted E_{ijkl} in ABAQUS (1985), are related to the usual two-index stiffness

constants C_{ij} and the compliance components S_{ij} by

$$\begin{aligned} E_{1111} = E_{2222} = E_{3333} &= C_{11} = \frac{S_{11} + S_{12}}{(S_{11} - S_{12})(S_{11} + 2S_{12})} \\ E_{1122} = E_{1133} = E_{2233} &= C_{12} = \frac{-S_{12}}{(S_{11} - S_{12})(S_{11} + 2S_{12})} \\ E_{1212} = E_{1313} &= C_{66} = C_{44} = \frac{1}{S_{44}} \ . \end{aligned} \tag{1.3}$$

The final elastic stiffnesses C_{ij} are given in Fig. 1.6.

The steady state creep data from < 100 > specimens of Table 1.2 (Allison-GM, 1986), provided at 1010 and 1066°C, were expressed in terms of the relation

$$\dot{\epsilon}_{ss} = \dot{\epsilon}_R \ e^{-Q/RT} \ \left(\frac{\sigma}{\sigma_o}\right)^{m(T)} = \dot{\epsilon}_o(T) \ \left(\frac{\sigma}{\sigma_o}\right)^{m(T)} , \tag{1.4}$$

where the nominal strength σ_o(= 200 MPa) is the stress at which the creep activation energy of 397 $KJ \cdot mol^{-1}$ was found from a plot of $ln\ \dot{\epsilon}_o$ vs. 1/T. In ABAQUS (1985), the resulting $\dot{\epsilon}_o(T)$ was linearly interpolated within 10°C intervals, with a maximum relative error of 3 %.

1.3.2 Creep anisotropy

Hill's stress function

For creep anisotropy, ABAQUS (1985) employs a generalization of the Mises yield criterion proposed by Hill (1950), which for axes with cubic symmetry is given in terms of a parameter R (=1 for isotropy):

$$\begin{aligned} \bar{\sigma}^2 &= \frac{1}{2}\left[(\sigma_{22} - \sigma_{33})^2 + (\sigma_{11} - \sigma_{22})^2 + (\sigma_{33} - \sigma_{11})^2\right] \\ &+ \ 3\,R\left[\sigma_{23}^2 + \sigma_{31}^2 + \sigma_{12}^2\right] \ . \end{aligned} \tag{1.5}$$

Eq. 1.5 can also be expressed in terms of stress deviators. These are defined as the differences of normal components from the mean normal stress $s_{ij} \equiv \sigma_{ij} -$

$\delta_{ij}\,\sigma$, where $\sigma \equiv \sigma_{ii}/3$,

$$\begin{aligned}\bar{\sigma}^2 &= \frac{3}{2}\,s_{ij}\,s_{ij}\Big|_{(i=j)} + \frac{3}{2}R\,s_{ij}\,s_{ij}\Big|_{(i\neq j)} \\ &= \frac{3}{2}\left(s_{11}^2 + s_{22}^2 + s_{33}^2\right) + \frac{3}{2}R\left(s_{12}^2 + s_{21}^2 + s_{23}^2 + s_{32}^2 + s_{31}^2 + s_{13}^2\right). \qquad (1.6)\end{aligned}$$

The shear stress components σ_{12} (relative to cubic, < 100 >, axes) will be different from zero primarily near the < 110 > axes, so that R affects the creep rates in that region. To find R, a functional relation between it and the available < 100 > and < 110 > creep data must be developed.

The associated flow rule

The fact that the strain increment vector associated with a given point on the yield locus must always be normal to the locus[1] (derived by Bishop and Hill, 1951) from the resolved shear stress law for all slip systems within a crystal, a polycrystal, or a structure) implies that there is a proportionality between components of plastic strain increment and the corresponding components of the outward normal to the yield locus in the stress space. This relation is called *the associated flow rule.* For incompressible materials (with strains equal to strain deviators) it gives the strain increments in terms of the stress deviators, partial derivatives, and a proportionality constant $d\lambda$:

$$d\epsilon_{ij}^p = \frac{\partial\bar{\sigma}}{\partial s_{ij}}\;d\lambda. \qquad (1.7)$$

Differentiating the stress function $\bar{\sigma}$ in the form of (1.6) gives the anisotropic stress-strain relations:

$$d\epsilon_{11}^p = \frac{\partial\bar{\sigma}}{\partial s_{11}}\,d\lambda = \frac{1}{2\bar{\sigma}}\frac{\partial\bar{\sigma}^2}{\partial s_{11}}\,d\lambda = \frac{3}{2}\,s_{11}\,\frac{d\lambda}{\bar{\sigma}}\;, \quad d\epsilon_{22}^p = \quad \ldots$$

[1]Except at any sharp corner on the yield surface.

$$d\gamma_{12}^p = 2\,d\epsilon_{12}^p = 2\,\frac{\partial\bar{\sigma}}{\partial s_{12}}\,d\lambda = \frac{1}{\bar{\sigma}}\frac{\partial\bar{\sigma}^2}{\partial s_{12}}\,d\lambda = 3\,R\,s_{12}\,\frac{d\lambda}{\bar{\sigma}} \quad , \qquad \ldots \tag{1.8}$$

Note that the one-to-one relationship between $d\epsilon_{ij}^p$ and the corresponding component s_{ij} is only true for materials which exhibit isotropic or cubic anisotropic behavior.

Finding the proportionality constant $d\lambda$. The plastic work done as a body undergoes deformation can be thought of as the dot product of the deviatoric stress and plastic strain increment:

$$\begin{aligned} dW^p &= s_{ij}d\epsilon_{ij} \\ &= s_{11}d\epsilon_{11}^p + s_{22}d\epsilon_{22}^p + s_{33}d\epsilon_{33}^p + 2\,s_{23}d\epsilon_{23}^p + 2\,s_{31}d\epsilon_{31}^p + 2\,s_{12}d\epsilon_{12}^p \ . \end{aligned} \tag{1.9}$$

Now substituting (1.8) into (1.9)

$$dW^p = \frac{d\lambda}{\bar{\sigma}}\,[\frac{3}{2}\,(s_{11}^2 + s_{22}^2 + s_{33}^2) + 3\,R\,(s_{23}^2 + s_{31}^2 + s_{12}^2)] = \frac{d\lambda}{\bar{\sigma}}\,\bar{\sigma}^2 \ . \tag{1.10}$$

An increment in equivalent plastic strain can thus be defined as the work per unit equivalent stress:

$$d\lambda = \frac{dW^p}{\bar{\sigma}} \equiv d\bar{\epsilon}^p \ . \tag{1.11}$$

For creep, rates rather than strain increments must be described. Equation 1.8, with $d\lambda$ replaced by $d\bar{\epsilon}^p$ from (1.11) becomes,

$$\dot{\epsilon}_{11}^p = \frac{3}{2}\,s_{11}\,\frac{\dot{\bar{\epsilon}}^p}{\bar{\sigma}} \quad , \qquad \ldots \qquad \dot{\gamma}_{12}^p = 3\,R\,s_{12}\,\frac{\dot{\bar{\epsilon}}^p}{\bar{\sigma}} \quad , \qquad \ldots \tag{1.12}$$

We assume that $\dot{\bar{\epsilon}}^p$ follows power law creep:

$$\dot{\bar{\epsilon}}^p = \dot{\epsilon}_0\left(\frac{\bar{\sigma}}{\sigma_0}\right)^m \ . \tag{1.13}$$

Finding R from uniaxial < 100 > and < 110 > creep data

Loading aiong a < 100 > orientation. The applied stress $\sigma_{<100>}$ gives a longitudinal creep rate $\dot{\epsilon}_{11}^p$ (in cubic axes). From the power law relation of (1.13),

with $\bar{\sigma} = \sigma_{<100>}$ and $\dot{\epsilon}^p_{11} = \dot{W}^p/\sigma_{<100>} = \dot{\bar{\epsilon}}^p$,

$$\dot{\epsilon}^p_{11} = \dot{\epsilon}_0 \left(\frac{\sigma_{<100>}}{\sigma_0} \right)^m \quad . \tag{1.14}$$

Loading along a < 110 > orientation. Here there is no cubic symmetry, so the yield locus is no longer represented by the cubic form of Hill's yield function (1.5). To avoid having to find a new yield function for this orientation, we rotate the reference frame back to cubic axes. The stress field in a < 110 > specimen (system 1'-2' of Fig. 1.7a) is

$$\sigma_{1'1'} = \sigma_{<110>} \neq 0 \quad , \quad \sigma_{2'2'} = \sigma_{3'3'} = 0 \quad .$$

Now find the stress components for the cubic axes (system 1-2 of Fig. 1.7a) through the Mohr's circle of Fig. 1.7b:

$$\sigma_{11} \;=\; \sigma_{22} \;=\; \sigma_{12} \;=\; \frac{\sigma_{<110>}}{2} \quad . \tag{1.15}$$

The mean normal stress is

$$\sigma = \frac{\sigma_{11} + \sigma_{22}}{3} = \frac{\sigma_{<110>}}{3} \quad ,$$

and the deviatoric components of (1.15) are

$$s_{11} = s_{22} = \frac{\sigma_{<110>}}{6} \quad , \quad s_{33} = -\frac{\sigma_{<110>}}{3} \quad . \quad s_{12} = s_{21} = \frac{\sigma_{<110>}}{2} \quad . \tag{1.16}$$

Substituting (1.16) into (1.6) gives the equivalent stress in cubic axes in terms of the applied stress $\sigma_{<110>}$ and R:

$$\bar{\sigma}^2 = \frac{\sigma^2_{<110>}}{4} (1 + 3\,R) \quad . \tag{1.17}$$

To find the strain rates in cubic axes, substitute (1.16) and (1.17) into (1.12):

$$\begin{aligned}
\dot{\epsilon}^p_{11} \;&=\; \dot{\epsilon}^p_{22} \;=\; \frac{3}{2} \frac{\sigma_{<110>}}{6} \frac{2}{\sigma_{<110>}(1 + 3\,R)^{1/2}} \dot{\bar{\epsilon}}^p = \frac{1}{2} \frac{1}{(1 + 3\,R)^{1/2}} \dot{\bar{\epsilon}}^p \\
\dot{\epsilon}^p_{33} \;&=\; -\,\dot{\epsilon}^p_{11} \,-\, \dot{\epsilon}^p_{22} \;=\; -\,\frac{1}{(1 + 3\,R)^{1/2}} \dot{\bar{\epsilon}}^p \\
\dot{\gamma}^p_{12} \;&=\; 3\,R\,\frac{\sigma_{<110>}}{2} \frac{2}{\sigma_{<110>}(1 + 3\,R)^{1/2}} \dot{\bar{\epsilon}}^p \;=\; 3\,R\,\frac{1}{(1 + 3\,R)^{1/2}} \dot{\bar{\epsilon}}^p \quad .
\end{aligned} \tag{1.18}$$

Using Mohr's circle once again (Fig. 1.7c), gives the $< 110 >$ creep rates from the $< 100 >$ rates of (1.18) in terms of the $< 100 >$ equivalent strain rate $\dot{\bar{\epsilon}}^p(\bar{\sigma})$:

$$\dot{\epsilon}^p_{1'1'} = \left(\frac{1}{2} + \frac{3}{2}\,R\right) \frac{1}{(1+3\,R)^{1/2}}\,\dot{\bar{\epsilon}}^p(\bar{\sigma}) \ . \tag{1.19}$$

Express $\dot{\bar{\epsilon}}^p(\bar{\sigma})$ in terms of $\bar{\sigma}$ from power law creep (1.13) and $\bar{\sigma}$ in terms of $\sigma_{<110>}$ from (1.17):

$$\dot{\epsilon}^p_{1'1'} = \left(\frac{\sqrt{1+3R}}{2}\right)^{m+1} \dot{\epsilon}_0 \left(\frac{\sigma_{<110>}}{\sigma_0}\right)^m . \tag{1.20}$$

Substituting $\dot{\epsilon}_0$ and σ_0 from (1.14) into (1.20) and replacing $\dot{\epsilon}^p_{11}$ of (1.14) by the identical $\dot{\epsilon}^p_{<100>}$ gives R from $< 100 >$ and $< 110 >$ creep data:

$$\dot{\epsilon}^p_{1'1'} = \dot{\epsilon}^p_{<110>} = \left(\frac{\sqrt{1+3R}}{2}\right)^{m+1} \left(\frac{\sigma_{<110>}}{\sigma_{<100>}}\right)^m \dot{\epsilon}^p_{<100>} \ . \tag{1.21}$$

$< 110 >$ and $< 100 >$ creep data (Allison-GM, 1986) taken at at 1090°C, gave $R = 1.13$.

1.3.3 Model of the coating

Since in a thin coating the stress and strain rate are homogeneous, the coating was modeled with a single four-node plane stress element. The plane of the model was the (traction-free surface) r plane of the substrate coordinates (Fig. 1.8). Since the in-plane components of displacements are the same in both the coating and substrate, they determine the in-plane components of total strain (the tangential $\epsilon^{applied}_{\theta\theta}(t)$ and the through-specimen-thickness $\epsilon^{applied}_{zz}(t)$ strain components of Fig. 1.8) in the coating, which constitute its imposed loads. The $\epsilon^{applied}_{zz}(t)$ component can be conveniently found by modeling the external row of elements of Fig. 1.3 with generalized plane strain elements with $\sigma_{zz} = 0$. The temperature history for the coating was that of the outer radius of the specimen for the most severe heating time, 4.5s (Fig. 1.2a at R= 6.5mm).

The NiCoCrAlY coating was assumed isotropic. Its elastic dynamic modulus was obtained from Hillery et al. (1986) and fitted with a second-order polynomial as shown in Fig. 1.9a. Due to the lack of accurate data, the Poisson's ratio at high temperatures for the NiCoCrAlY had to be approximated from the ratios for materials which exhibit similar homologous temperature dependence in the Young's modulus. Comparison of available modulus data for several materials (Simmons and Wang, 1971) showed the NiCoCrAlY to have similar temperature dependence to *Al* and *W* (Fig. 1.9a). The elastic modulus and Poisson's ratio were normalized by dividing their values at zero absolute temperature, and the temperature by the melting point temperature, T_m. Fig. 1.9b shows *Al* and *W* Poisson's ratio as well as the interpolated values for the NiCoCrAlY. The mean coefficient of thermal expansion for the isotropic NiCoCrAlY coating is given in Fig. 1.4 (Allison-GM, 1986).

The creep behavior was modeled from data at 661, 850 and 1050°C obtained by Hebsur and Miner (1986) on a plasma sprayed NiCoCrAlY coating. In order to interpolate creep data at intermediate temperatures logarithmically and to avoid occasional narrow-band temperature interpolation inaccuracies, a user's material subroutine containing the power law creep model and a forward gradient time-integration procedure was implemented.

1.4 Results and Discussion

Substrate

Anisotropic thermo-elastic analysis. A feeling for the stress-strain histories can be obtained by following the cycle of Fig. 1.10a. For the $< 100 >$ rim orientation, the initial heating drives the rim into compression (A to B). From B to C, although the temperature is still increasing, the stresses become less compressive due to a

decrease in the radial temperature gradient. (The sharp corner at B is due to the discrete time-temperature input in the finite element model). From C to D, the rim temperature is kept constant at 1090°C but the core temperature is still rising and the rim stress is becoming less compressive, both approaching the steady-state D after only 10-20s.

Cooling decreases the compressive stresses, and with fast cooling (7s), they even become tensile (see last column of Table 1.3). After this peak at E, the material starts unloading elastically until the beginning of the next cycle at A. The peak cooling stress σ_{max} will be discussed further in connection with the creep analysis. A similar behavior is observed at the $< 110 >$ rim orientation (Table 1.3).

Anisotropic creep analysis. Since fatigue and fracture are unaffected by the thermal strains per se, the results of the creep analysis will be discussed in terms of the mechanical strains, $\epsilon^{mech} \equiv \epsilon^e + \epsilon^c = \epsilon^T - \epsilon^{th}$:

1. The extreme strains and the strain ranges at both $< 100 >$ and $< 110 >$ locations are hardly affected by creep, as shown by comparing the thermo-elastic cycle with the first creep cycle in Fig. 1.10b and with successive creep cycles in Figs. 1.10c and 1.11-1.12.

2. The shape of the hysteresis loops remains relatively unchanged by creep, as shown in Figs. 1.10 to 1.12 (the break in the slope during heating for cycles after the first one, at $\epsilon^{mech} = 0.3\%$, is due to having increased the tolerance for the solution of the equilibrium equations for economy in running eight thermal cycles). Furthermore, the strain range remains almost constant, showing a change of less than 2% between the 1st and 8th cycle for any given thermal history.

3. For the $< 100 >$ rim location, continued cycling produces ratchetting of the hysteresis loop (Figs. 1.10 to 1.12). The peak compressive and tensile strains and the

stress range remain nearly constant, but the peak cooling stress increases, shifting the loop upward. To see the source of the shift, compare the elastic and creep strains during the first cycle for the 4.5s history (Fig. 1.10b). Significant compressive creep begins at about 1010°C, increasing the mean stress of the cycle. The compressive stress then decreases rapidly with only slightly increasing temperatures, reducing the creep rate. For the first cycle, approximately half of the creep strains accumulate in the first few seconds after 1000°C is reached (e.g. Fig. 1.10b). The remaining half of the creep accumulates during simulated cruise conditions at constant temperature. This stress relaxation diminishes as the cycles shift to higher peak cooling stresses.

Since the tensile stresses introduced during cooling take place at temperatures below those where creep and stress relaxation occur and are insufficient to cause yield (according to data from Mackay et al., 1980), such cooling involves only elastic strains. These high tensile stresses would accelerate the crack propagation into the substrate. This may be critical if a cracked substrate could perform its functions for a limited length of time.

4. To estimate the long-time ratchetting of the $< 100 >$ cooling stress, a mechanics-inspired model is proposed. Since the mean mechanical strain remains constant, the decrease in elastic strain is the increase in creep strain. The shifting of the stresses per cycle, $d\sigma/dN$, will then be proportional to the creep strain accumulated during each cycle ϵ^c, which is in turn proportional to the creep rate divided by the cycling rate, $\dot{\epsilon}^c/\dot{N}$. $\dot{\epsilon}^c$ in turn, has an approximate power law dependence on the stresses (1.13):

$$\frac{d\sigma}{dN} \propto -E\,\epsilon^c \propto -\frac{E\,\dot{\epsilon}_o}{\dot{N}} \left|\frac{\sigma}{\sigma_0}\right|^m \mathrm{sgn}(\sigma) \ . \tag{1.22}$$

Consider the stress at that point in the cycle which will have zero stress at steady state (Point C in Fig. 1.13). Express σ in terms of the changing peak cooling stress

σ_{max}, and a fraction f of the total stress range $\Delta\sigma$ (which remains nearly constant during cycling), as shown in Fig. 1.13:

$$\sigma = \sigma_{max} - f\Delta\sigma \ . \tag{1.23}$$

Using (1.23) to integrate (1.22) leads to an expression for σ_{max} in terms of the above variables plus the maximum cooling stress at the end of the first cycle $\sigma_{max}(1)$, and two unknown constants: the creep exponent m, and a constant C, which reduces to the proportion of the creep strain to the elastic strain for the first cycle $[\dot{\epsilon}^c(1)/\dot{N}] \,/\, \epsilon^e(1)$:

$$\sigma_{max}(N) = [\sigma_{max}(1) - f\Delta\sigma(1)] \ [1 + (m-1)\,C\,(N-1)]^{-1/(m-1)} + f\,\Delta\sigma \ . \tag{1.24}$$

Equation 1.24 is based on a stress σ which shifts towards zero as cycles accumulate. At steady state ($\sigma = 0$), compressive creep (before the stress in the cycle reaches zero) generated during the heating and part of the holding period is counteracted by tensile creep (after the stress in the cycle reaches zero, toward the end of the holding period). The point in the cycle which would go to zero stress at steady state would thus be somewhere in between B and D in Fig. 1.13, since both forward and backward creep would take place within this region.

The parameter f in (1.24) allows us to estimate the possible values of σ_{max} at steady state. For example, assuming steady state to occur when σ, defined at half-way between the peak compressive stress σ_{min} and the stress at the end of the holding period σ_h (Point C in Fig. 1.13), reached zero gives the values of f shown in Table 1.4. With f chosen, and $\sigma_{max}(1)$ and $\Delta\sigma$ known, C and m from (1.24) can be evaluated from the calculated transients of each thermal cycle (Figs. 1.10c to 1.12). Fig. 1.14 shows least square curve fittings to (1.24) for the 4.5s heating and for the 6s heating histories with two different cooling rates. Table 1.4 shows the resulting constants C and m, and how σ_{max} increases with cycling from (1.24).

Most of the rise in σ_{max} for the three histories reaches 2/3 of its final value before the first 500 cycles.

Different values of f were chosen to evaluate its effect on σ_{max}. At one extreme, take the point in the cycle at which $\sigma = 0$ at steady state to be the stress at the end of the holding period (Point D in Fig. 1.13). In this case, for the 4.5s history (Fig. 1.10b), f= 0.45. The above procedure then gave a stress at steady state of $\sigma_{max} = 201$ MPa (against 321 MPa for f= 0.73 when σ is at half-way from compressive peak to hold). At the other extreme, for σ at the compressive peak, $f = 1$, giving $\sigma_{max} = 441$ MPa.

While the half-way basis for f in Table 1.4 was somewhat arbitrary, we think that a computer solution for σ_{max} at steady state (if it were feasible) would be lower than that of Table 1.4 by 10-30 %. In any event, it is clear that the tensile stresses appear early in the 6000 cycle life.

5. The < 110 > orientation exhibits ratchetting similar to the < 100 > but less pronounced. It, also, shows no changes in the strain range.

6. From all the preceding discussion, the thermo-elastic analysis was very good at estimating the strain ranges, but it badly underestimated the σ_{max} obtained from the creep analysis (for example, −20 MPa vs. 245 MPa after 6000 cycles for the 4.5s heating history at a < 100 > location).

Coating

The effect of the strain on the coating life is again reflected only in the mechanical part of the total strain, since the thermal strains will not by themselves cause damage. The mechanical strain ranges (as absolute values) for the coating were obtained by adding the thermal expansion mismatch strain range (0.31%), which only depends

on α_s, α_c, and the extreme cycle temperatures, to those of the substrate:

$$\begin{aligned} \Delta\epsilon_c^{mech} &= \Delta\epsilon_s^{mech} + (\alpha_c - \alpha_s)\,\Delta T \qquad \text{for constant } \alpha, \text{ or} \\ &= \Delta\epsilon_s^{mech} + \Delta[\alpha_c(T - T_{ref}) - \alpha_s(T - T_{ref})] \end{aligned} \tag{1.25}$$

For instance, for the most severe cycle with a mechanical strain range for the substrate of $\Delta\epsilon_{subs}^{mech} = 0.52\%$ (Table 1.3), the coating range is $\Delta\epsilon_{coat}^{mech} = 0.83\%$.

The coating crack initiation life is driven not only by the mechanical strain range but also by the stresses. A finite element analysis of the coating was carried out to evaluate these stresses. The accuracy of the finite-element analysis was set by a nodal force tolerance for equilibrium of 0.1 N (for a 0.05 mm^2 element section), and by a maximum change in the equivalent tensile plastic strain during an increment of 10^{-5}. The initial residual stress in the coating was tentatively assumed to be zero. (As shown below, initial residual stresses, due to the aging treatments and their change due to further relaxation and differential contraction on cooling, would disappear after the first cycle). An estimate of the shear stresses on the coating/substrate interface due to centrifugal forces in a turbine blade gave only 0.4 MPa, which turns out to be negligible.

With zero initial stress, heating to 520°C gives a compressive stress at the beginning of the first cycle (Point A of Fig. 1.15). Subsequently, the high creep rates make the stresses relax almost to zero during the first 3s of the heating period. Steady state is approximately reached in the second cycle (Fig. 1.15) due to the fact that the forward creep generated when $\sigma < 0$ is offset by backward creep generated mainly during beginning of cooling. The breaks in the slope during the cycles are due to the discrete creep data input into the finite element model.

The negligible effect of an initial residual stress can now be seen. Any residual stress could not have shifted the stress at the start of the first cycle (520°C) any

higher than Point B, because the tensile stress would have exceeded yield. Any initial stress starting the cycle between A and B would converge to steady state even faster than the zero initial stress corresponding to Point A.

The maximum tensile stress in the coating, σ^c_{max} = 460 MPa (compared to 245 MPa for 6000 cycles for the substrate, Table 1.4), is reached at 546°C during cooling (Fig. 1.15). At this stress and temperature, the coating will be on the verge of yielding (Strangman, 1977). This high coating stress will certainly promote substrate as well as coating cracking, since even after a coating crack propagates to the substrate/coating interface, the high coating stresses will still augment the crack tip stress intensity and hence the propagation rate (unless interface spalling were to occur).

The only crack initiation data found in the literature was that of Leverant et al. (1976). For comparative purposes, Fig. 1.16 shows crack initiation in a NiCoCrAlY coating on various superalloy substrates which were tested with a 67s heating cycle. Based on these data and on our coated CMSX-3 strain ranges, crack initiation for our simulated service should take place almost immediately. Thermal fatigue tests performed in conjunction with this work, (Busso, 1987; Chapter 2), show that coating cracks may not occur before 6000 cycles even with strain ranges of up to 0.51% (Fig. 1.16)[2], whereas Leverant et al.'s (1976) reported this limit to be around 0.22%[3]. This discrepancy may be associated with the level of the tensile cooling stresses, and also with different shapes of the hysteresis loops, causing different interactions of stress, strain, and temperature. However, since Leverant et al. (1976) did not report these details, a quantitative comparison cannot be carried out.

To minimize the level of these tensile stresses and strain ranges in the coat-

[2]Thermal fatigue tests done by Holmes et al. (1987) on an aluminide coating revealed that crack-like defects extending into the substrate required a mechanical strain range for the coating greater than 0.59 %.

[3]Other data, unpublished, appear to be closer to our results than to Leverant's.

ing, thermal expansion mismatch strains between coating and substrate should be minimized. Beyond that, further crack initiation and crack propagation data for the coating, with realistic stress-strain-temperature histories, are necessary to accurately correlate realistic strain ranges with the development of damage.

1.5 Conclusions

1. The general anisotropic formulation for creep of cubic crystals was obtained in terms of uniaxial $< 100 >$ and $< 110 >$ data.

2. For the substrate, the conventional thermo-elastic analysis is a good predictor of strains and strain ranges, even for cycles with creep. The shape of the hysteresis loops is little affected by creep. Mechanical strain ranges for the $< 100 >$ substrate orientations vary from 0.52 % for the 4.5s heating cycle to 0.31 % for the 20s heating cycle.

3. Continued cycling produces ratchetting of the stresses for both crystal orientations but does not affect the strain ranges, which play a role in coating degradation.

4. Peak tensile stresses generated in the substrate during cooling increase considerably during cycling. This increase was 6 to 8 times greater for the $< 100 >$ than for the $< 110 >$ rim location. A mechanics-inspired model of long time ratchetting revealed that the main effect of different heating rates on cooling peak stresses will be seen before the 500th cycle, when the rise in peak stress reaches 2/3 of its final value for all thermal histories. For the most severe 4.5s heating time, the peak stress rises from 13 MPa at the first cycle to 245 MPa at the 6000th cycle. These values, compared to the -20 MPa estimated from the conventional thermo-elastic analysis, indicate that the cooling stress levels calculated thermoelastically were highly underestimated, and as a result, their effects in the crack initiation process and subsequent crack propagation rates may be substantial.

A decrease in the cooling times for the 6s heating cycle from 15s to 7s (while maintaining the same heating rate) resulted in an increase in the peak cooling stresses from 203 to 251 MPa at the 6000th cycle.

5. For the coating, to minimize the level of the tensile cooling stresses and strain ranges, thermal expansion mismatch strains between coating and substrate should be minimized. In our case, with α_c typically 1.3 α_s, the most severe imposed substrate strain range (0.53 %) induced a 0.83 % strain range and 460 MPa tensile cooling stress in the coating. Future work on determining crack initiation and crack propagation data for NiCoCrAlY coatings for the 520 - 1090°C temperature range is needed to correlate these strain ranges and stresses with the development of damage.

Bibliography

[1] ABAQUS (1985). A general purpose finite element code with emphasis on nonlinear applications, version 4.5. *Hibbitt, Karlsson, and Sorensen Inc.*. Providence, R.I..

[2] Allison, General Motors Turbine Division (1986). Private communication.

[3] Bishop, J.F., and Hill, R. (1951). A theory of the plastic distortion of a polycrystalline aggregate under combined stress. *Phil. Mag.* **42**, 414-427.

[4] Busso, E.P. (1987). Thermal fatigue of an overlay coating for single crystal Nickel-base superalloys. MSc thesis, Dep. Mech. Eng., MIT, May.

[5] Hebsur, M.G., and Miner, R.V. (1986). High temperature tensile and creep behavior of low pressure plasma-sprayed NiCoCrAlY coating alloy. *Mat. Sci. Eng.* **83**, 239-245.

[6] Hill, R. (1950). *The Mathematical Theory of Plasticity.* Clarendon Press, Oxford, England, p. 320.

[7] Hillery, R.V., Pilsner, B.H., Cook, T.S., and Kim, K.S. (1986). Thermal barrier coating life prediction model. General Electric Co., NASA CR - 179504.

[8] Holmes, J.W., McClintock, F.A., O'Hara, K.S., and Conners, M.E. (1987). Thermal fatigue testing of coated monocrystalline superalloys, in *Low-Cycle Fatigue*, ASTM STP 942, H.D. Salomon et al. (eds.), pp. 672-691.

[9] Howes, M.A.H. (1976). A study of thermal fatigue mechanisms. *Thermal Fatigue of Materials and Components.* ASTM STP 612, D.A. Spera and D.F.Mowbray, Eds., 86-105.

[10] Kaufman, A., and Halford, G.R. (1984). Engine cyclic durability by analysis and material testing. NASA Technical Memorandum 83577.

[11] Leverant, G.R., Strangman, T.E, and Langer, B.S. (1976). Parameters controlling the thermal fatigue properties of conventionally cast and directionally solidified turbine alloys. *Superalloys 1976*, AIME High Temp. Alloys Committee, 285-295.

[12] Mackay, R.A., Dreshfield, R.L., and Maier, R.D. (1980). Anisotropy of Nickel-base superalloy single crystals. *Superalloys 1980*, AIME High Temp. Alloys Committee, 385-394.

[13] Nesbitt, J.A., Pilsner, B.H., Carol, L.A., and Heckel, R.W. (1984). Cyclic oxidation behavior of $\beta + \gamma$ overlay coatings on γ and $\gamma + \gamma\prime$ alloys. *Superalloys 1984*, The Met. Soc. of AIME, 699-710.

[14] Rickerby, D.S., and Wood, M.I. (1986). Evaluation of ion plated CoCrAlY and NiCrAlTi coatings for gas turbines. *J. Vac. Sci. Technol.* A **6**, 2557-2570.

[15] Simmons, G., and Wang, H. (1971). *Single Crystal Elastic Constants and Calculated Aggregate Properties.* MIT Press, Cambridge, MA..

[16] Strangman, T.E. (1977). Fatigue crack initiation and propagation in EB-PVD coatings for gas turbine superalloys. *Thin Solid Films* **45**, 499-506.

[17] Thulin, E.D., Howe, D.C., and Singer, I.D. (1982). Energy efficient engine: high performance turbine detailed design report. NASA Report No. CR-165608, Pratt & Whitney Aircraft Group, East Hartford, CT..

Table 1.1 Nominal chemical compositions of substrate and coating

		Ni	Co	Cr	Mo	W	Ti	Al	Ta	Y
CMSX-3 substrate (MAR-M-247 derivative)	*Wt.%*	66.4	4.6	7.9	0.5	8.0	1.0	5.6	6.0	–
	At.%	67.9	4.7	9.1	0.3	2.6	1.1	12.4	1.9	–
NiCoCrAlY coating	*Wt. %*	50.	20.	18.	–	–	–	12.	–	0.2
	At. %	42.4	17.6	17.8	–	–	–	22.	–	0.05

Table 1.2 Creep coefficients of Eq.1.4 for CMSX-3

T, °C	$\dot{\epsilon}_o$, s^{-1}	m
1010	1.209×10^{-7}	8.27
1066	5.734×10^{-7}	8.06

Table 1.3 Comparison of substrate thermo-elastic and creep analyses

Cycle	Rim orientation	*Anisotropic creep (8th cycle)*			*Thermo-elastic*
		Strain history, %		Peak cool. stress, MPa	
		ϵ^{cr}_{min}	Range, $\Delta\epsilon^{cr}$	σ^{cr}_{max}	σ^{el}_{max}
20s-15s	< 110 >	−0.169	0.152	−10.	−19.
20s-7s	< 110 >	−0.165	0.180	26.	22.
6s-15s	< 110 >	−0.213	0.197	−5.	−16.
4.5s-15s	< 110 >	−0.273	0.258	−1.	−1.
20s-15s	< 100 >	−0.333	0.304	45.	−21.
20s-7s	< 100 >	−0.334	0.356	98.	27.
6s-15s	< 100 >	−0.425	0.399	60.	−20.
4.5s-15s	< 100 >	−0.543	0.519	87.	−20.

Table 1.4 Changes in σ_{max} with cycles for < 100 > (Eq. 1.24)

Heat. time	*Cool. time*	$\sigma_{max}(1)$, MPa	$\Delta\sigma$, MPa	f	C	m	σ_{max}, *MPa, for cycle no.:*			
							100	500	6000	*Steady st.*
4.5s	15s	13.1	441.	0.73 0.45 1.00	0.09	6.8	168.	205.	245.	321. 201. 441.
6s	15s	−2.	323.	0.80	0.08	6.2	134.	167.	203.	258.
6s	7s	49.	374.	0.83	0.07	6.1	181.	215.	251.	309.

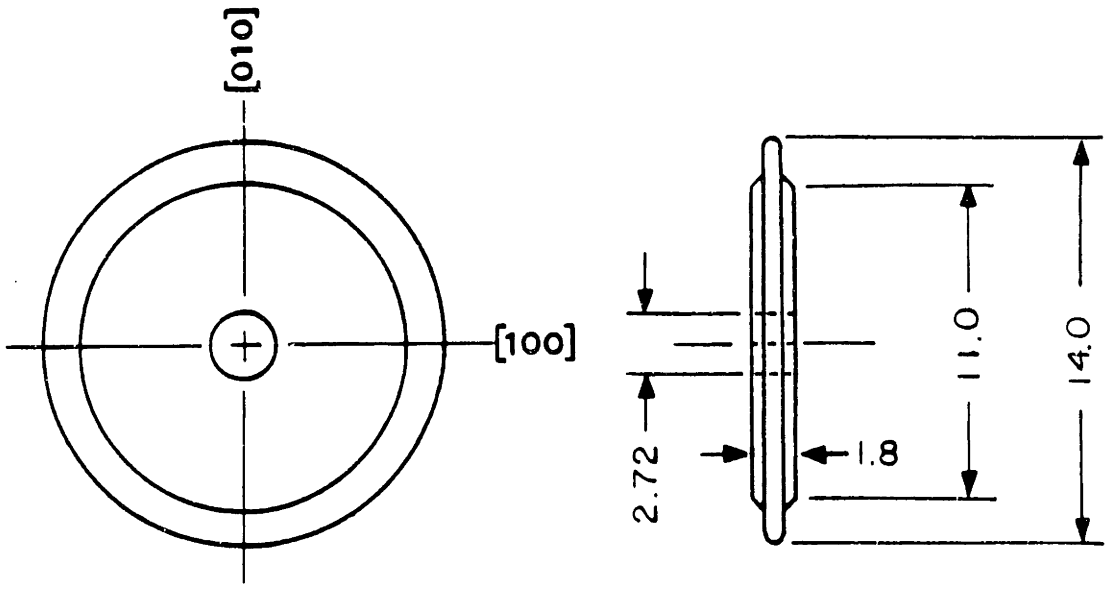

(a) specimen geometry

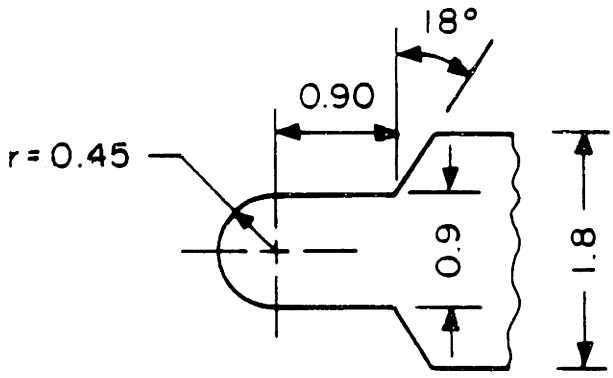

(b) detail of specimen periphery

Fig. 1.1 Detailed drawing and orientation of stepped-disk specimen (all dimensions in mm). After Holmes et al. (1987)

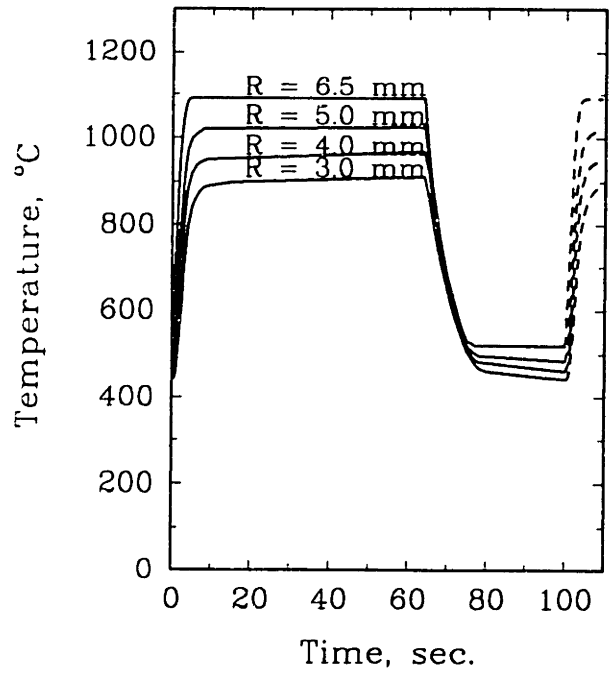

(a) 4.5s heat, 60s hold and 15s cool.

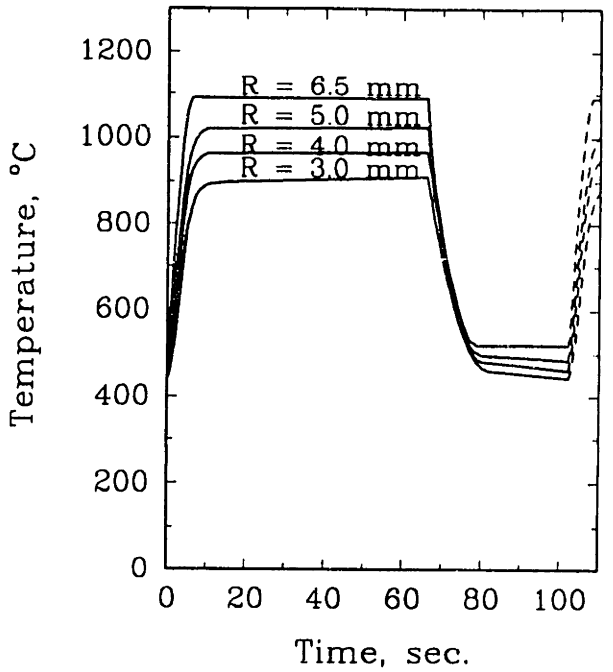

(b) 6s heat, 60s hold and 15s cool.

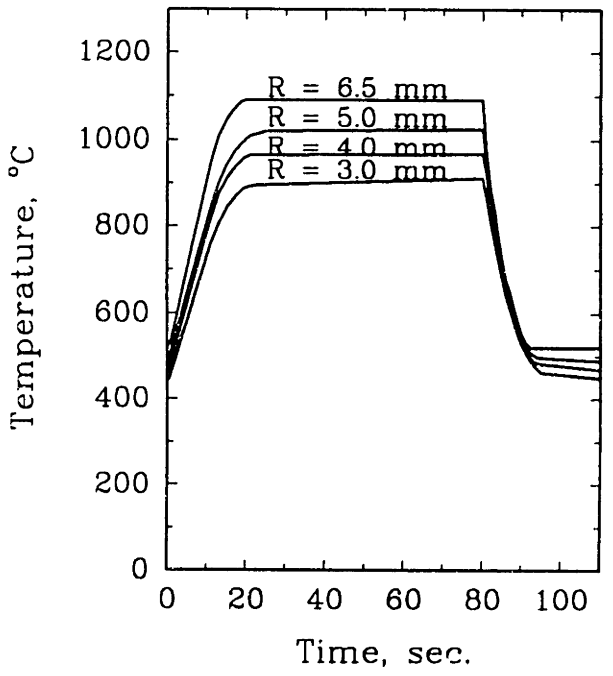

(c) 20s heat, 60s hold, and 15s cool.

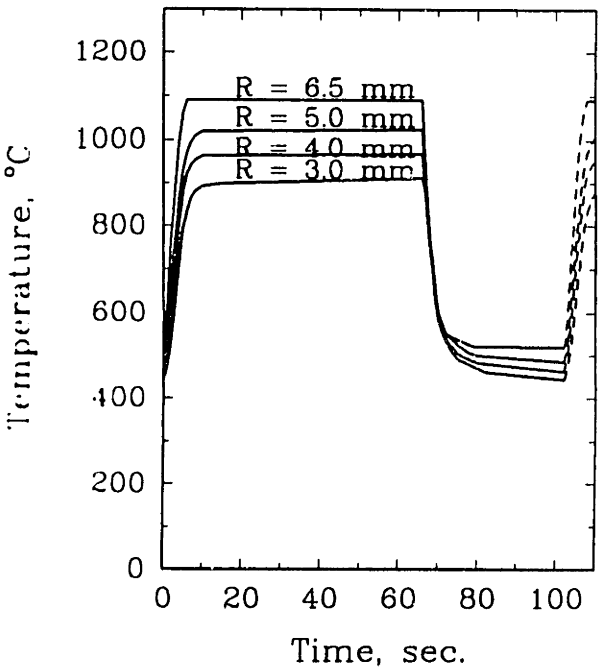

(d) 6s heat, 60 s hold and 7s cool.

Fig. 1.2 **Radial temperature distributions in specimen when its periphery temperature is cycled from 520°C to 1090°C**

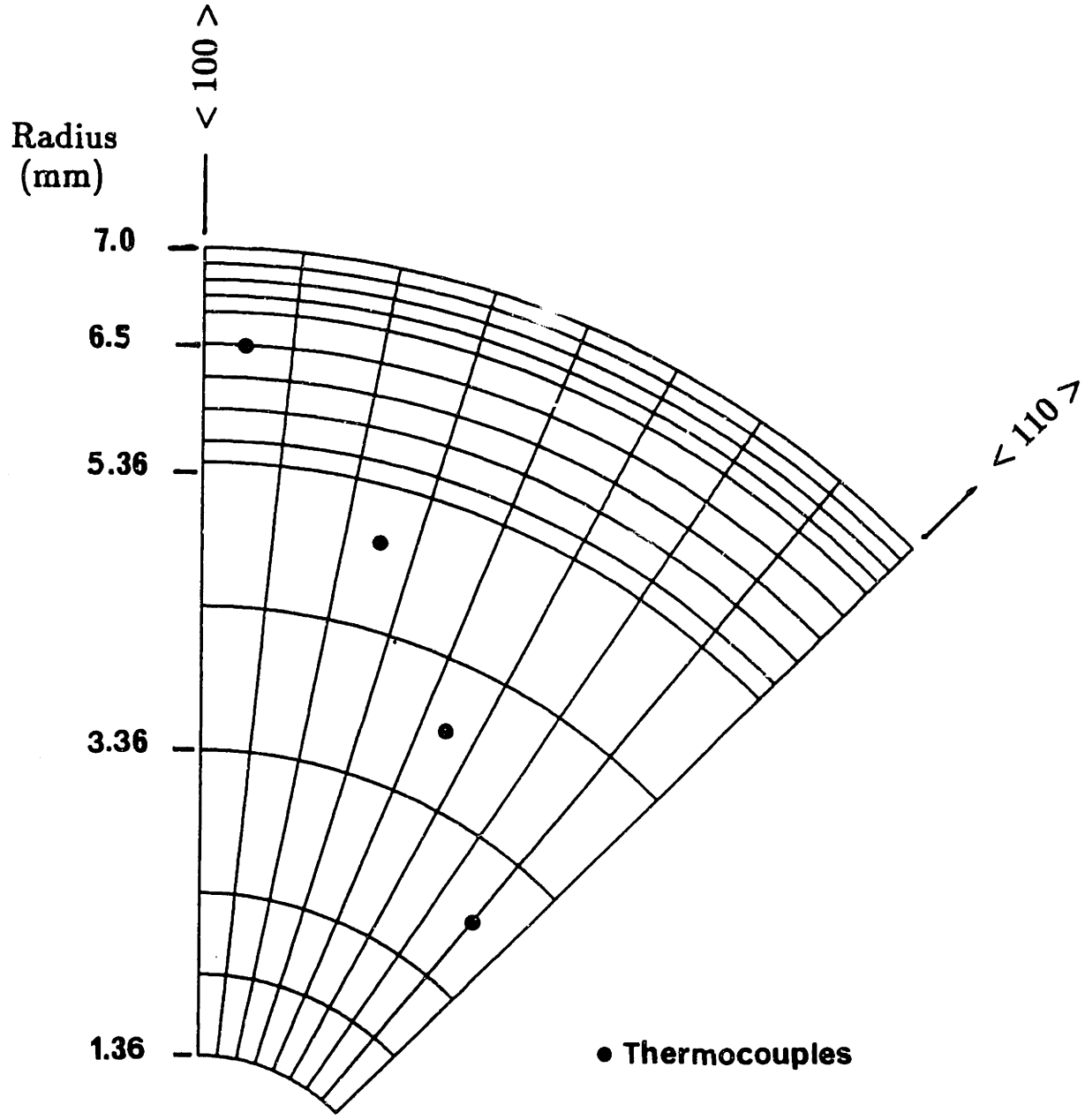

Fig. 1.3 **Finite-element mesh of stepped-disk specimen**

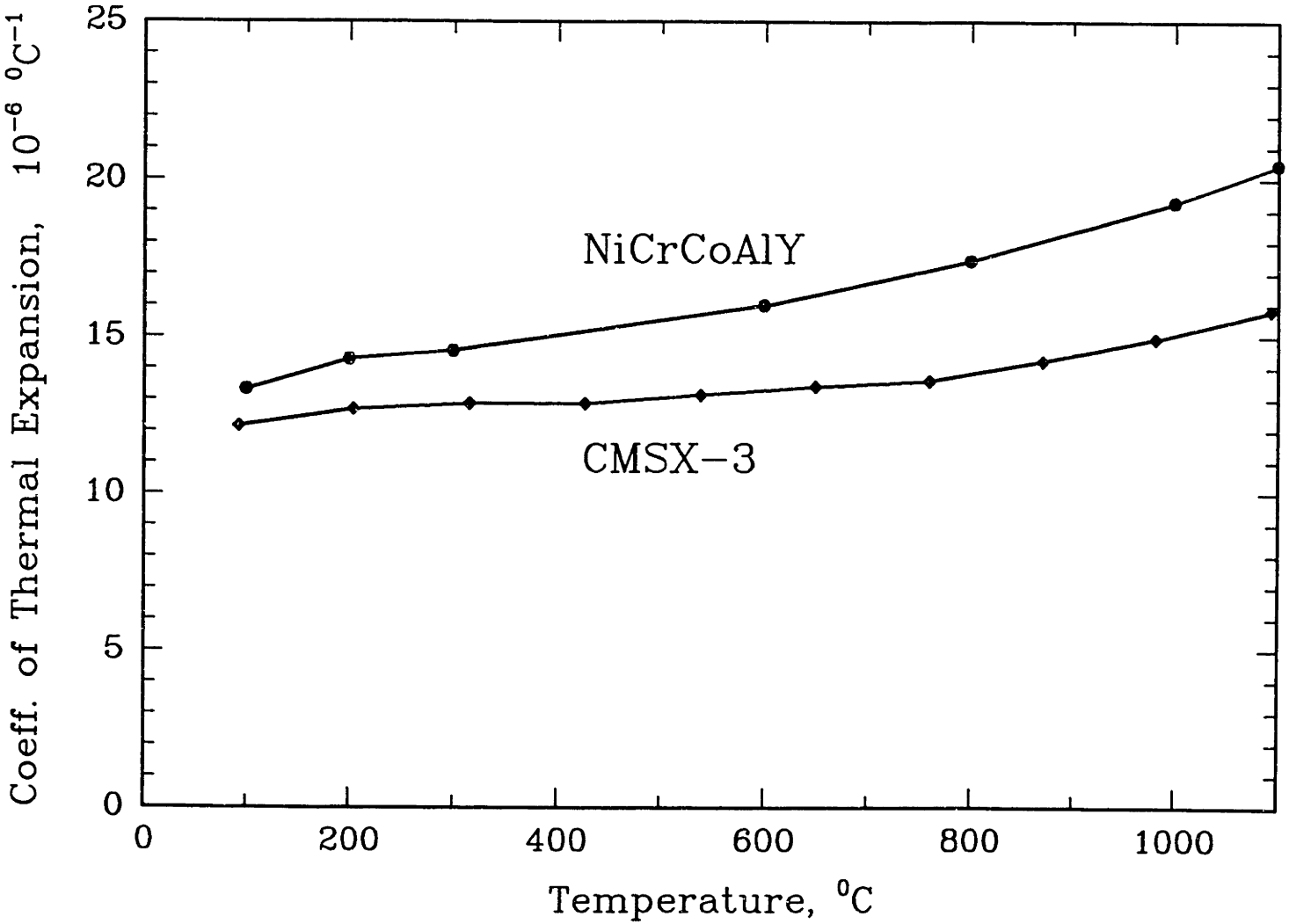

Fig. 1.4 **Coefficients of thermal expansion for the substrate (CMSX–3) and coating (NiCoCrAlY). (Reference temperature = 25°C)**

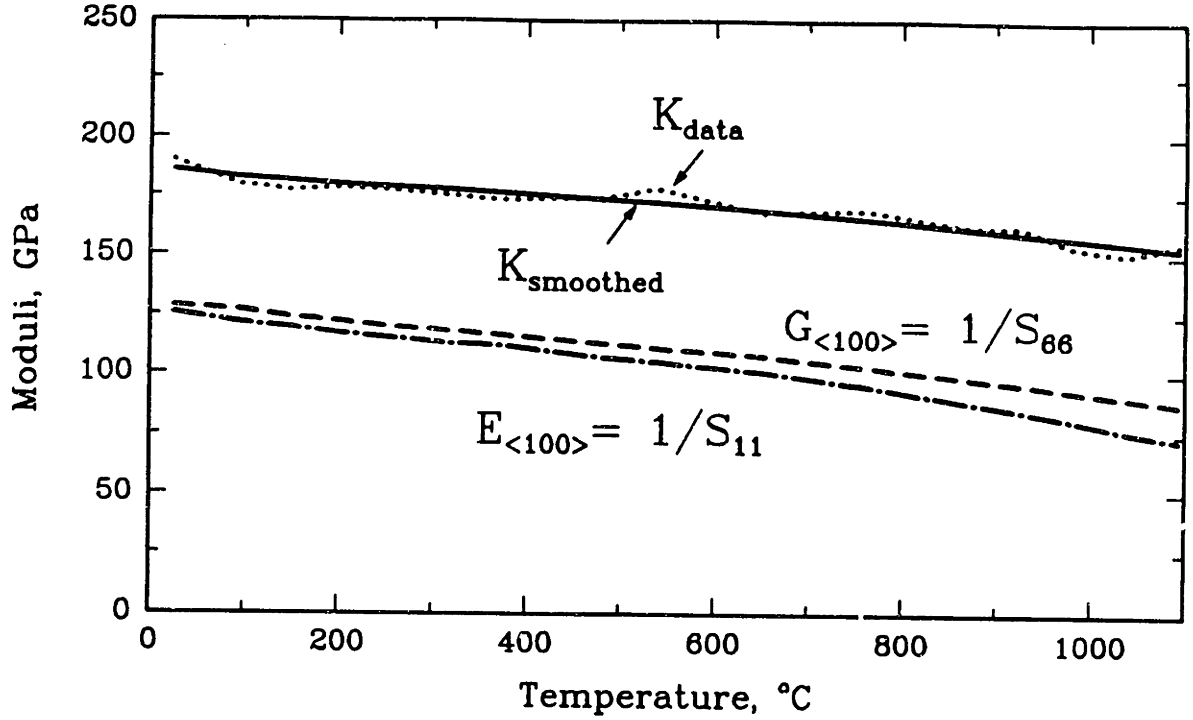

Fig. 1.5 **Original and smoothed bulk modulus K, Young's modulus, and shear modulus for <100> crystal orientation**

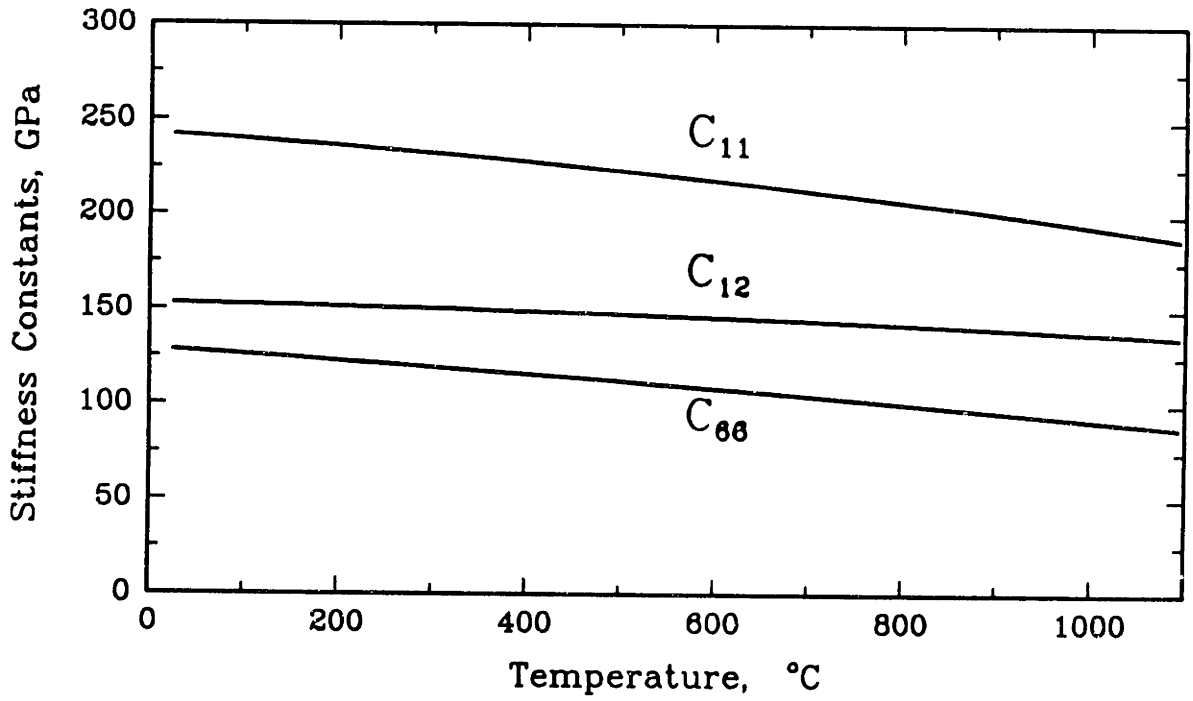

Fig. 1.6 **Stiffness constants C_{ij} versus temperature for CMSX–3**

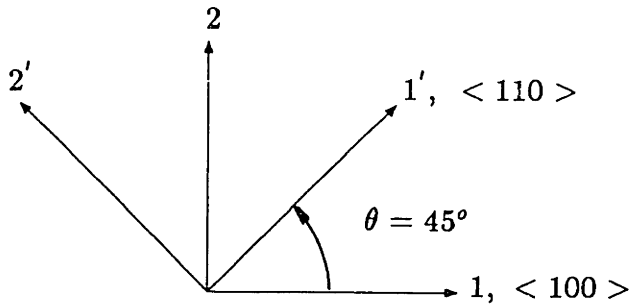

Fig. 1.7a **Physical plane**

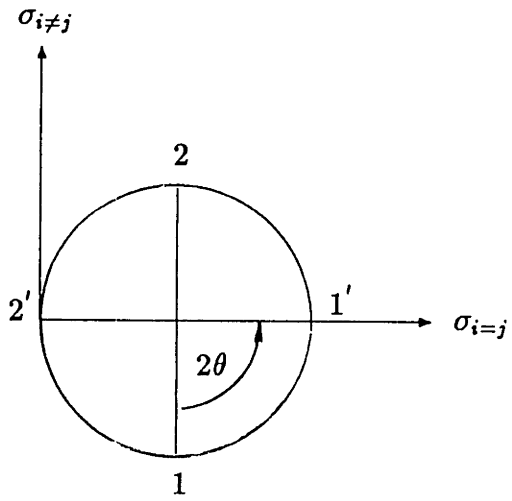

Fig. 1.7b **Stress plane**

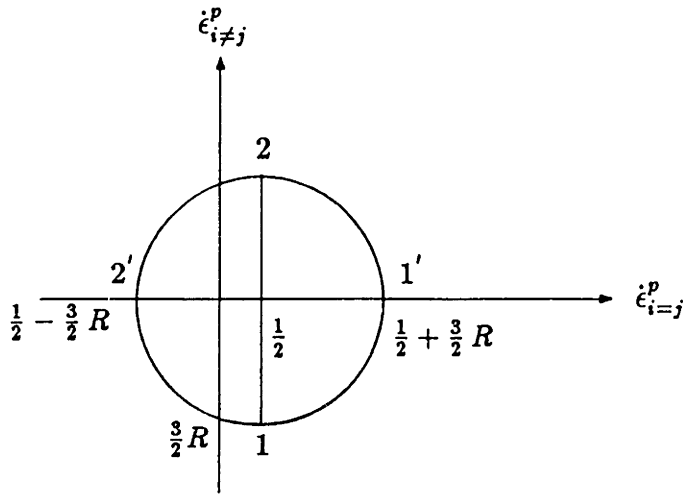

Fig. 1.7c **Strain (rate) plane,** units of $\dot{\bar{\epsilon}}^p \,/\, (1+3R)^{-1/2}$

$$\epsilon_{ij}^{applied}(t) = \epsilon_{ij}^{e}(t) + \epsilon_{ij}^{c}(t) + \epsilon_{ij}^{th}(t)$$

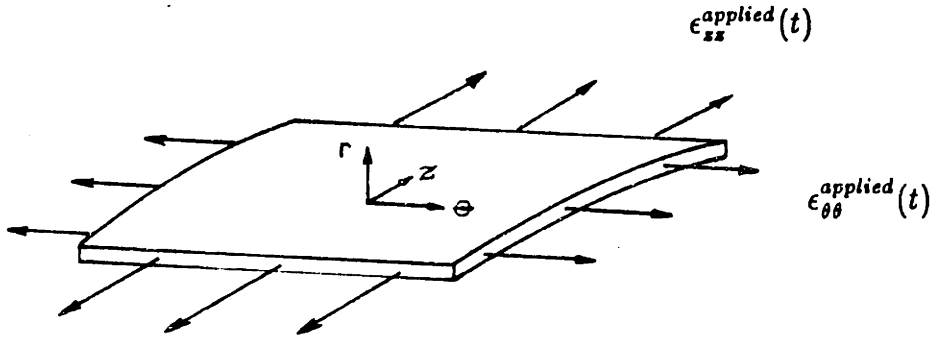

Fig. 1.8 **Model of coating**

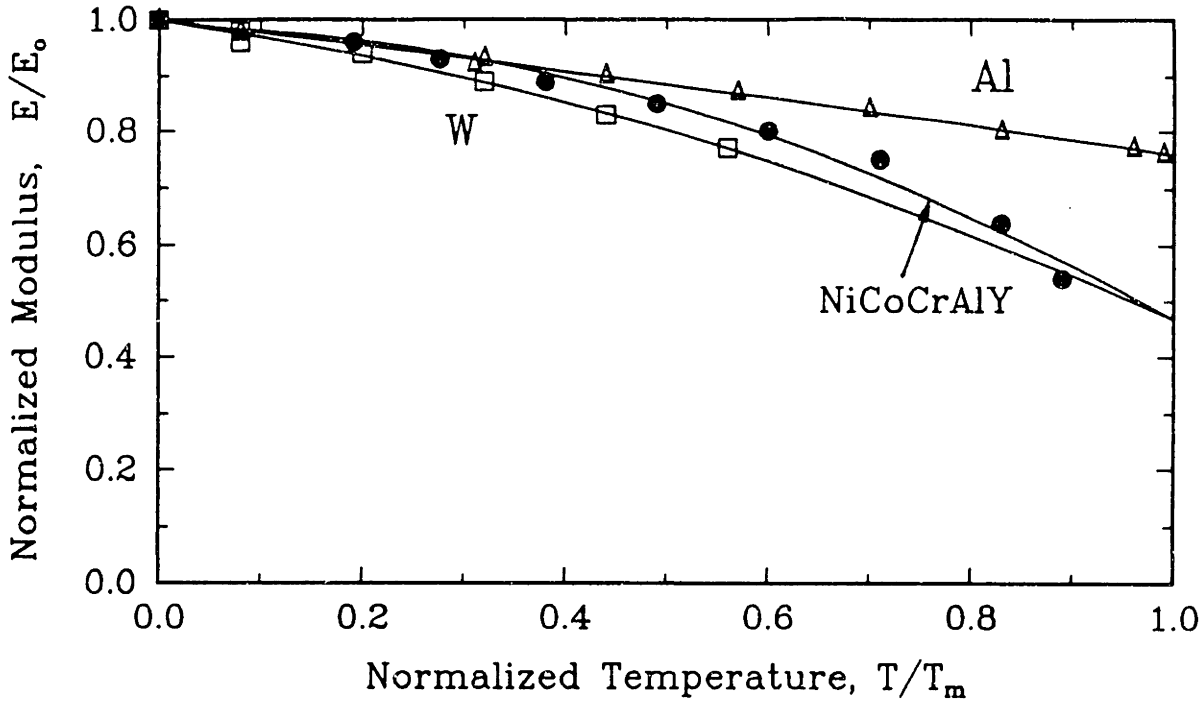

(a) Temperature dependence of Young's Modulus

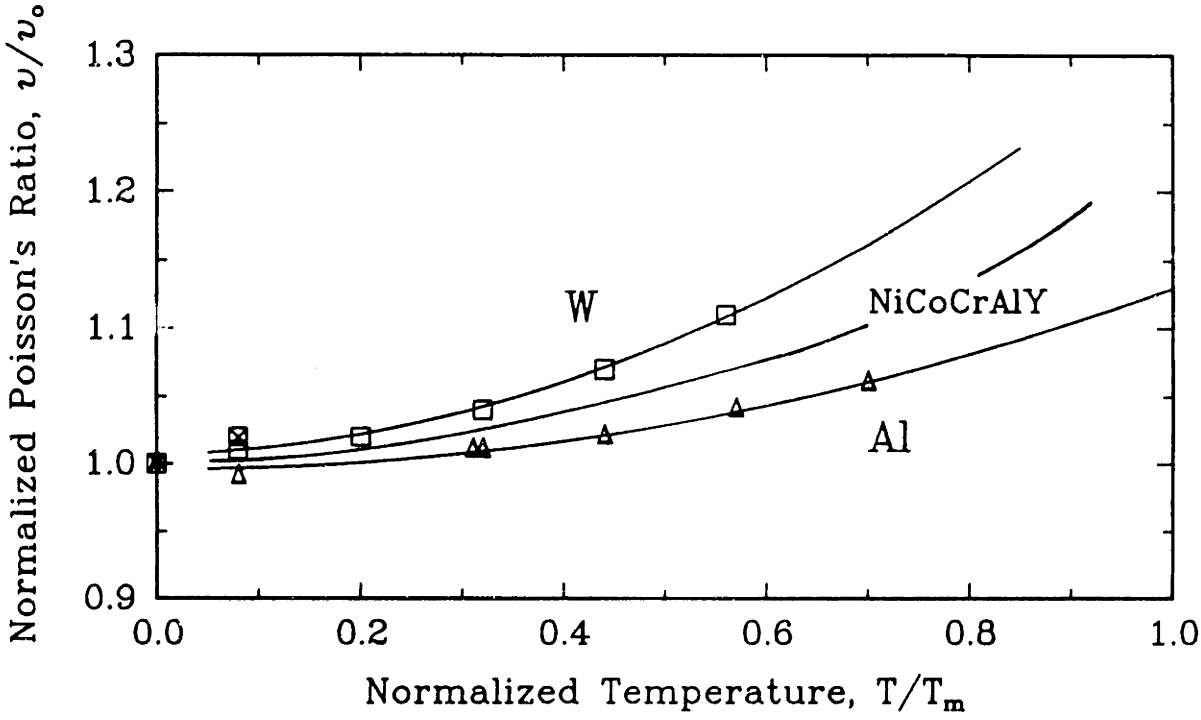

(b) Temperature dependence of Poisson's ratio

Fig. 1.9 **Interpolation of Poisson's ratio for NiCoCrAl from Al and W data (temperature normalized with the melting point, E and υ normalized with their values at 0 °K)**

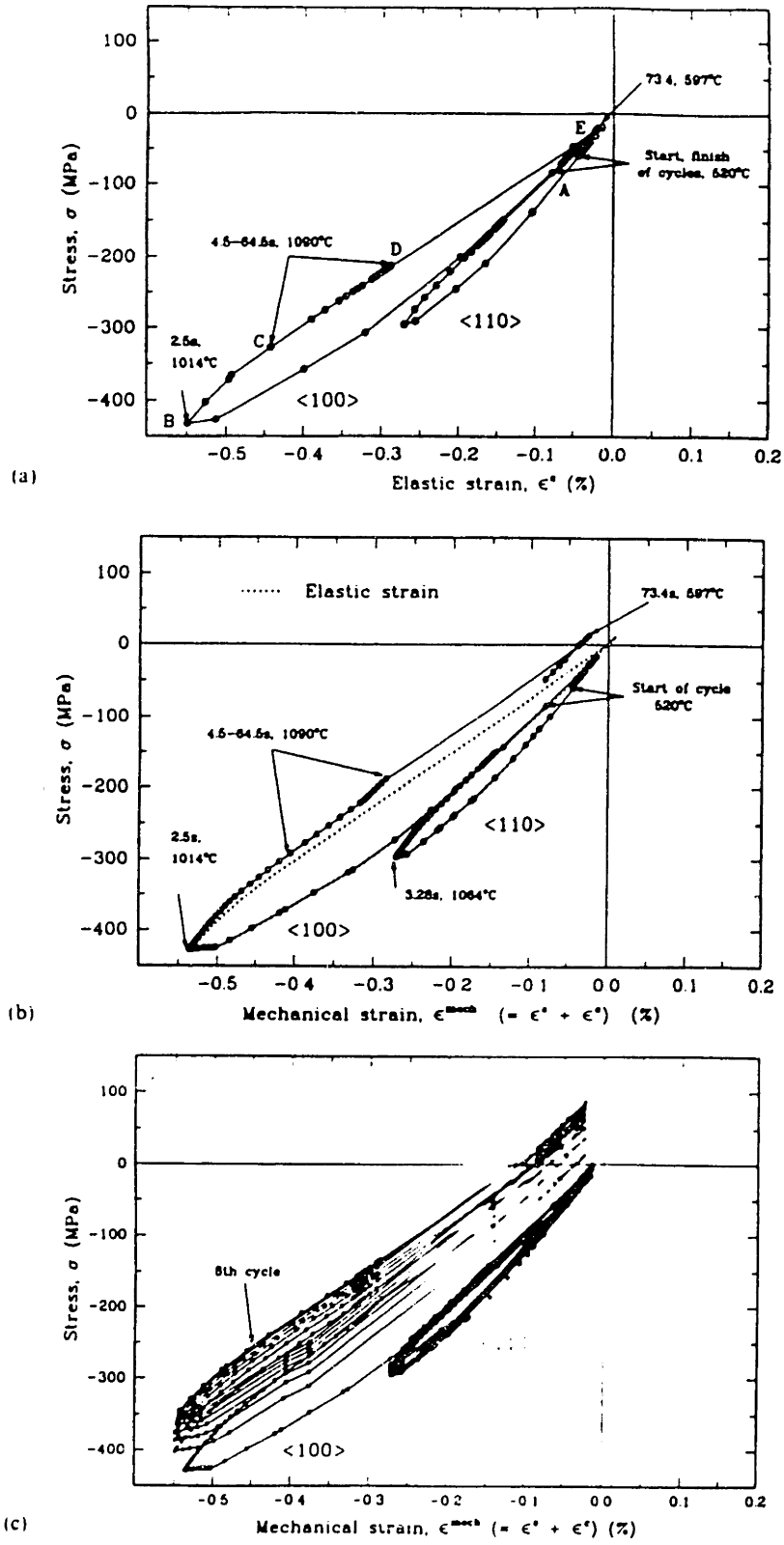

Fig. 1.10 Stress-strain hysteresis loops of the specimen rim in the < 100 > and < 110 > orientations for 4.5s heating cycle: (a) thermo-elastic analysis; (b) anisotropic creep analysis, first cycle; (c) anisotropic creep analysis, later cycles.

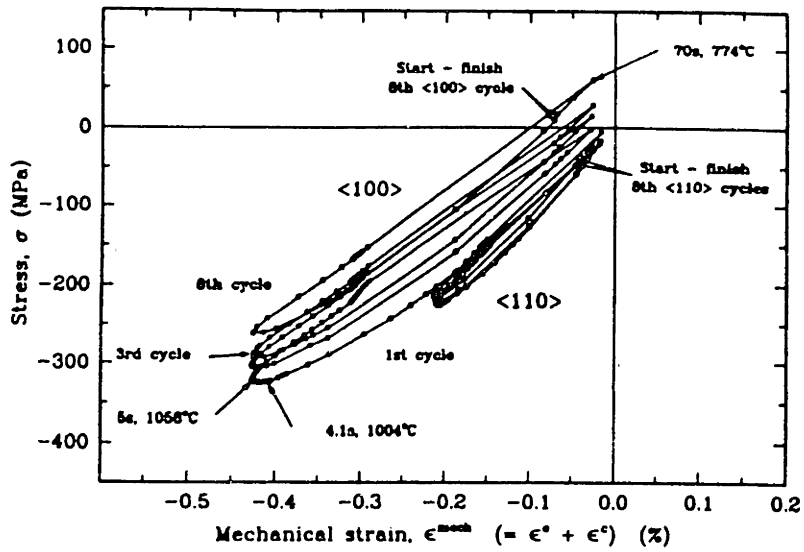

(a)

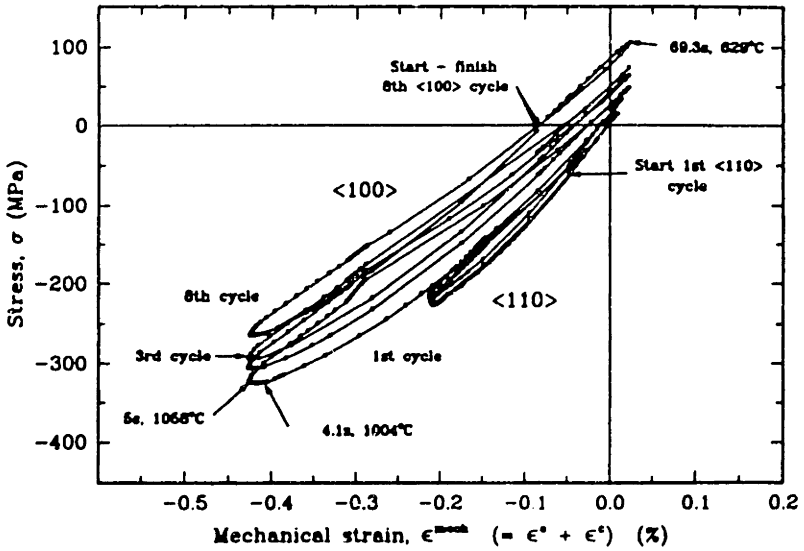

(b)

Fig. 1.11 Anisotropic creep analysis for 6 s heating, 60 s hold with (a) 15 s cooling; (b) 7 s cooling.

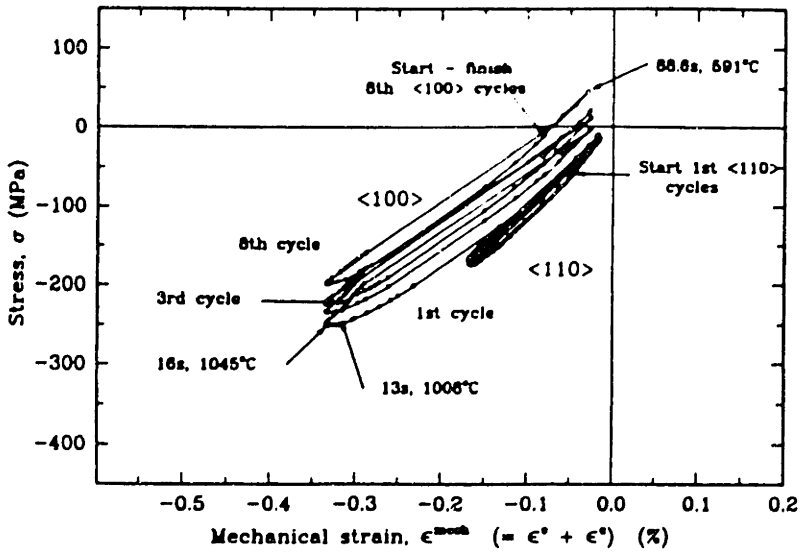

Fig. 1.12 Anisotropic creep analysis for 20 s heating, 60 s hold and 15 s cooling.

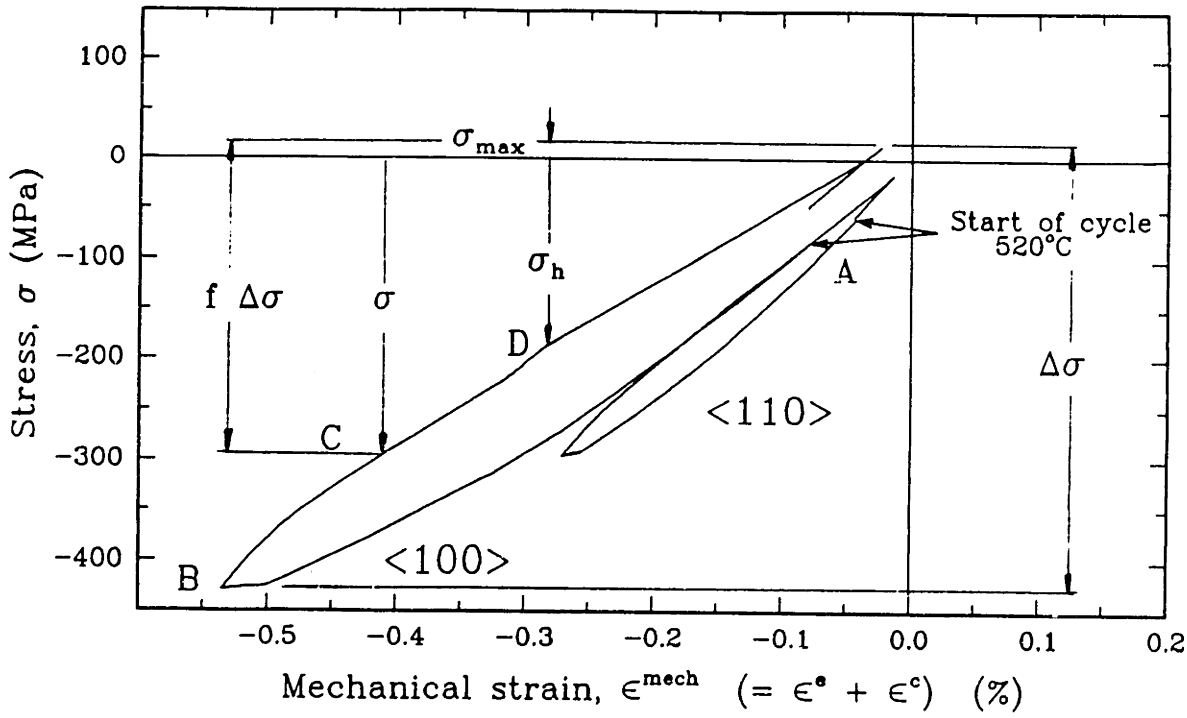

Fig. 1.13 **Parameters used from first cycle to estimate σ_{max}**

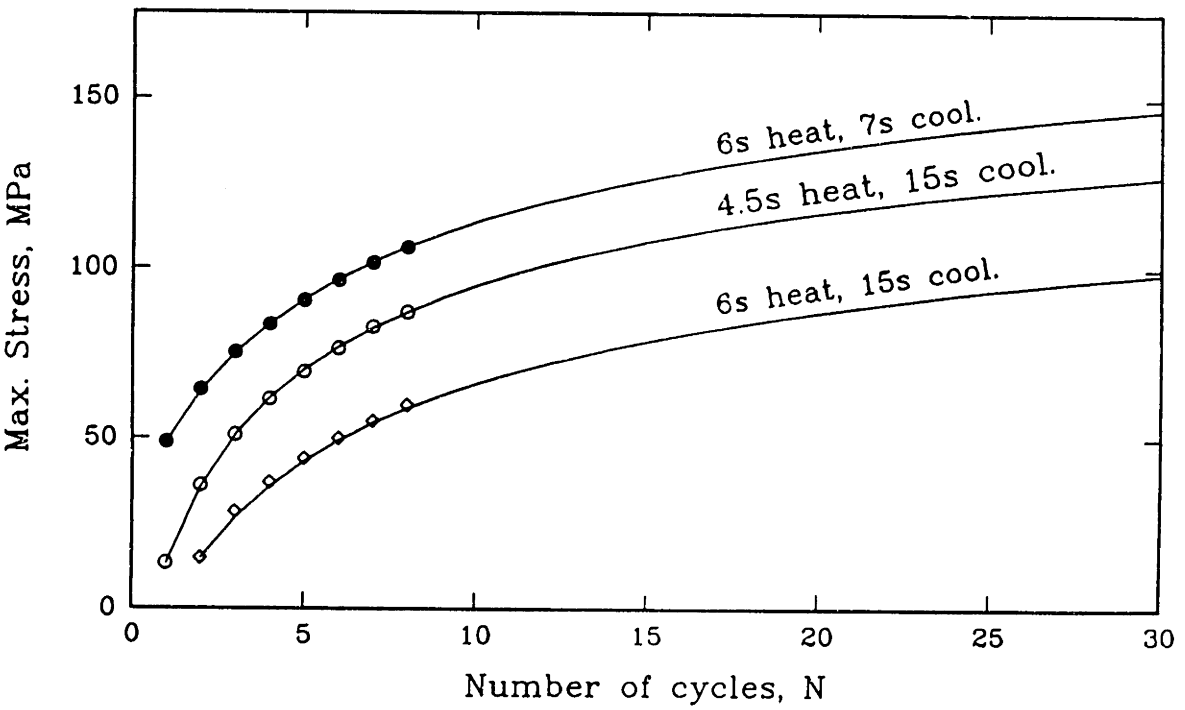

Fig. 1.14 **Changes in the peak stresses encountered during cooling according to Equation 24**

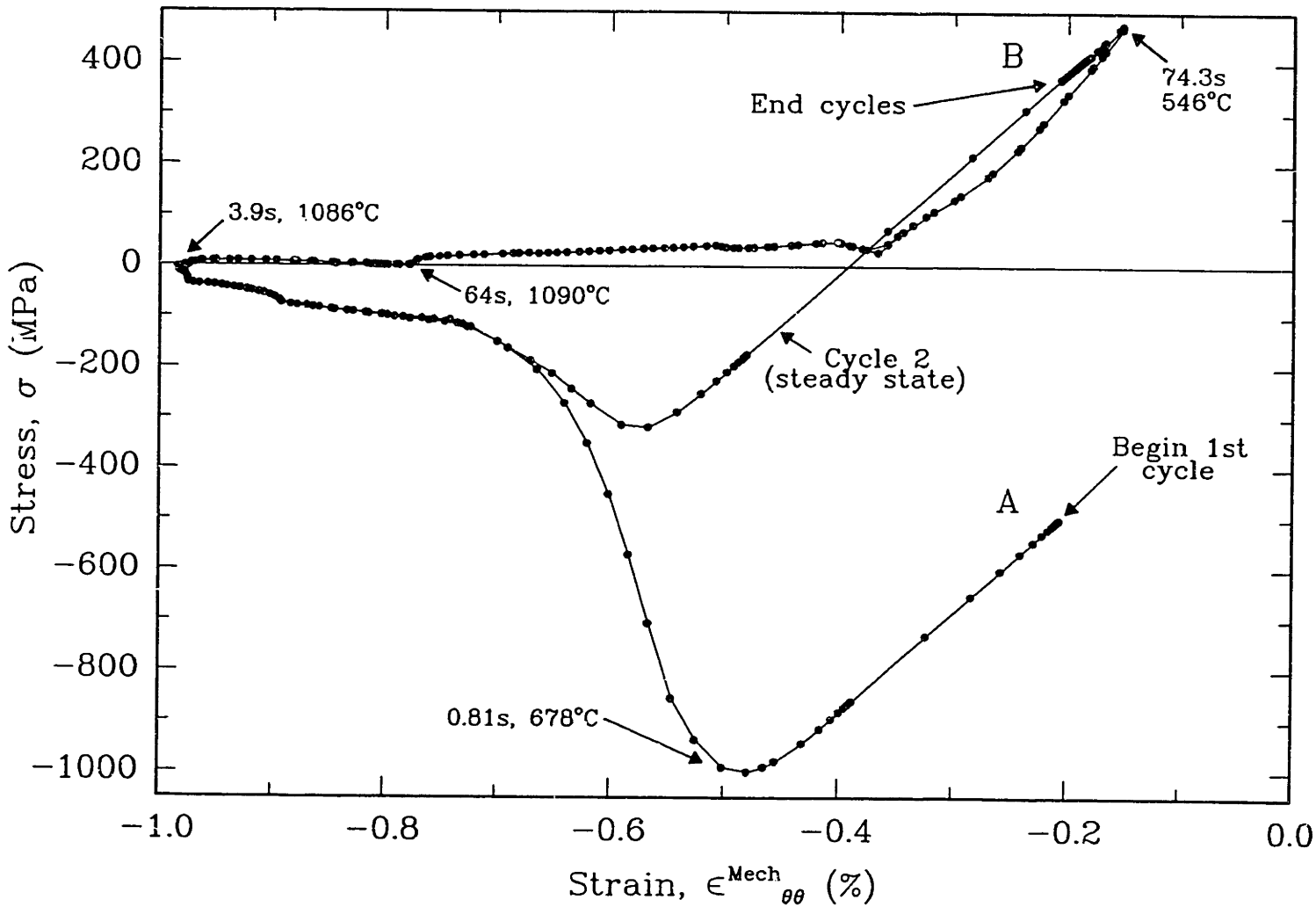

Fig. 1.15 **Hysteresis loop for NiCoCrAlY coating for the 4.5s, 60s hold, and 15s cooling cycle.(Imposed displacements from <100> substrate)**

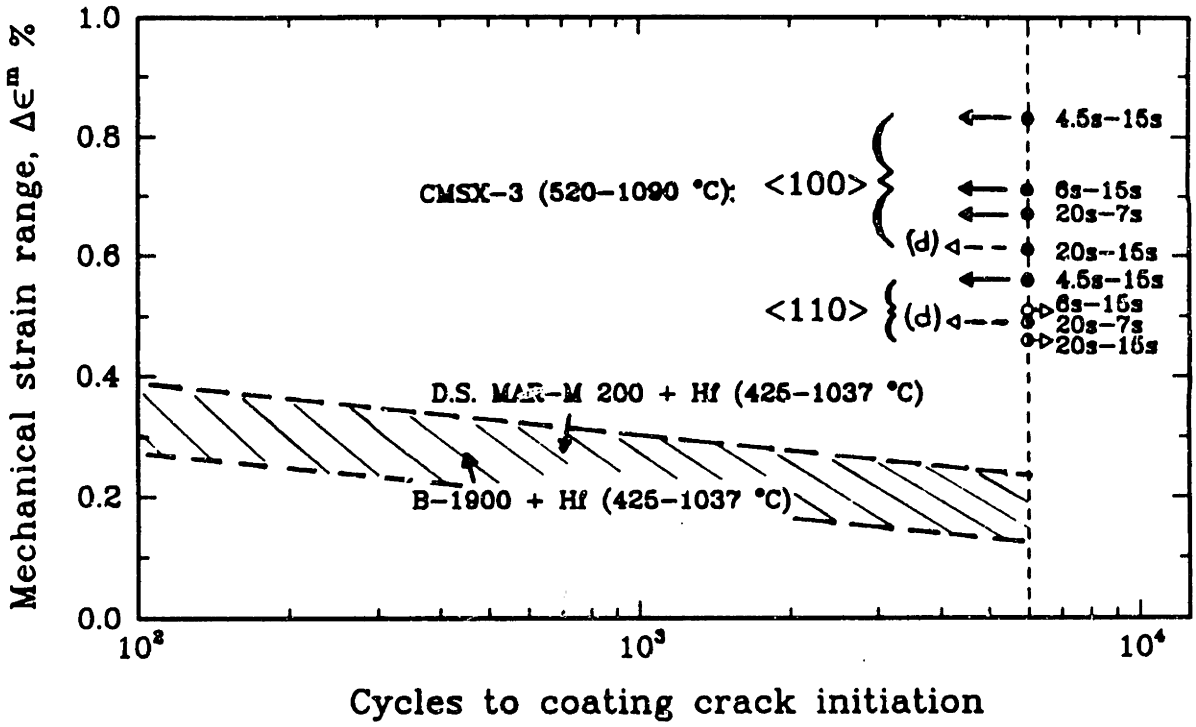

(d) indicates cracks which originated from surface porosities

Fig. 1.16 **Crack initiation in NiCoCrAlY coating on different substrates (Leverant et al. (1976))**

Chapter 2

Thermal Fatigue Degradation of a NiCoCrAlY Overlay Coating

Abstract

The degradation of a 92 μm-thick EB-PVD - NiCoCrAlY overlay coating applied to single crystals of a nickel base superalloy (CMSX-3) was studied by subjecting stepped-disk specimens to 6000 thermal cycles with different rates of heating (from 520 to 1090°C in 4.5, 6, and 20s) and cooling (to 520°C in 7s and 15s). Diffusion during coating deposition and aging gave a 10 μm $\beta-\alpha-\gamma$ transition zone between the coating and substrate, which grew to 80 μm and transformed into a single γ phase after cycling for the most severe history ($\Delta\epsilon_{coat}^{mech} = 0.83\%$). An isothermal test at 1090°C revealed little thinning, no interface voids, and no cracking.

Cyclic degradation consisted of severe cracking, which in some cases propagated well into the substrate, and critically depended on the coating strain ranges and oxide cooling stresses. Two different crack initiation processes were observed in the absence of initial surface defects (pits). At normal cooling rates (15s) cracks appeared to originate from interface voids, which grew from the original coating-substrate interface towards the coating surface. These voids were associated with coating strain ranges of 0.57% and above. At high cooling rates (7s), giving maximum oxide

stresses of 218 MPa rather than 116 MPa, there was early cracking of the protective oxide scale with surface initiation.

2.1 Introduction

In the previous chapter, the problem of determining stress and strain histories in a NiCoCrAlY overlay coating under realistic service conditions was addressed. However, the ultimate objective of this work is to be able to predict, from an understanding of the mechanisms responsible for coating degradation, how life is affected by changes in service conditions so that system improvements can be proposed. To that end, the study of the thermal fatigue degradation of a NiCoCrAlY overlay coating will be reported in this chapter. It basically involved:

1. Thermal fatigue tests with induction heating to cyclicly heat the periphery of coated stepped-disk single crystal Ni-base specimens.

2. Monitoring the specimens for oxidation, roughening, void formation, and cracking, and studying the changes in the composition and morphology of phases during service, using micro-probe analysis.

The induction heating technique used to reproduce cyclic thermal strains typical of those developed in leading and trailing edges of blades during normal operating conditions was developed by Holmes and McClintock (1983, 1986, 1987) and adapted to smaller specimens by Busso (1987). The main advantage of this technique, is the flexibility in selecting the desired temperature cycle and environments. It also eliminates the need to perform heat transfer analysis with uncertain boundary conditions to determine the temperature distributions in the specimen during the thermal cycle. Instead, the temperature gradients can be measured with appropriately placed thermocouples.

Prior work will be discussed in connection with each task.

2.2 Protective Coatings

2.2.1 General overview

Comprehensive reviews of protective coatings for turbine applications have recently been published by Goward (1979, 1986) and Bunshah (1982). In summary:

The first coatings to be widely used were *diffusion coatings*, based on surface enrichment with aluminum (Goward, 1986). These aluminide coatings are still in used even though they provide limited protection in modern applications involving very high temperatures or severe hot corrosion environments.

Overlay coatings, represented by the MCrAlY series (M = Fe, Co, Ni, or any combination of these), allow increased flexibility of design of compositions. They are deposited on the metal surface and their chemical composition is usually tailored to the operating environment. Oxidation and hot corrosion resistance as well as ductility can be varied over wide ranges to meet severe operating requirements.

Ceramic thermal barrier coatings have been used in the last decade to insulate metals from the effects of high temperature gaseous environments. These coatings, applied by plasma spraying, usually consist of two layers, a bond coat of an oxidation-resistant alloy and a top coat of a zirconia-based ceramic. The major problems involving these coatings are the mismatch in thermal expansion between the zirconia and the base material, causing serious coating spallation during service, and the oxidation of the base material due to the permeability of the ceramic. However, from the work carried out in recent years (Vogan et al., 1982; Bennett, 1986), the potential of such coatings for reducing metal temperatures or reducing cooling air requirements, with subsequent increase in turbine efficiency, is quite large.

For this study, we chose an overlay coating since diffusion coatings have already

been the subject of extensive isothermal and cyclic oxidation studies (Holmes et al., 1986, 1987, 1988; Saunders, 1986). Furthermore, Ni-base bond coatings often are an important sublayer for ceramic thermal barrier coatings.

2.2.2 Selection criteria for the composition of the overlay coating

The composition for our overlay coating was based on the following considerations:

1. *Operating conditions:* our choice of high temperature oxidizing conditions suggested a Ni-rich coating composition. Conversely, if hot corrosion conditions were prevailing, a Co based alloy would be more appropriate (Goebel, 1975).

2. *Relative stability at high temperatures and oxidation resistance:* at high temperatures, coating-substrate interdiffusion plays a significant role in coating degradation, with the NiCrAlY being more stable on Ni-based substrates than the Co-based alloy (Levine, 1978). Its oxidation resistance derives from the formation of an Al_2O_3 protective oxide. Improved resistance to spallation under thermal cycling is provided by yttrium which improves oxide adherence. Degradation proceeds mainly by Al_2O_3 spallation with the resultant depletion of Al from the coating. Afterwards, less protective oxides such as Cr_2O_3 and NiO or CoO form (Goward, 1979).

3. *Ductility and brittle-to-ductile transition temperature (BTDTT):* since coating ductility continuously *increases* as the volume fraction of CoAl or NiAl *decreases*, an increase in ductility is obtained at a sacrifice of Al content and hence of oxidation and hot corrosion resistance. In general, MCrAlY overlay coatings can provide a more desirable BTDTT than the diffusion aluminide coatings (Leverant et al., 1976). NiCoCrAlY fully complies with this argument,

since for our particular temperature histories, the maximum tensile stresses are reached at high temperatures relative to the BTDTT, where the coating exhibits ductile behavior (Gupta et al., 1984). It is then extremely important to select a coating which exhibits a brittle-to-ductile transition temperature below the minimum cycle temperatures, if tensile stresses are expected there.

4. *Thermal expansion mismatch between coating and substrate:* to minimize strain ranges and tensile stresses in the coating, the thermal expansion coefficients of the coating and substrate should be as similar as possible at the operating temperatures. When cooling from high temperatures, the worst situation in a typical gas turbine arises when $\alpha_c > \alpha_s$. Although the NiCoCrAlY has a considerably higher thermal expansion coefficient than the substrate at high temperatures (Fig. 1.4), it is widely used in industry due to the other advantages discussed in this Section.

2.3 Experimental Procedure

2.3.1 Coating preparation and characteristics

For this study, the same substrate (CMSX-3) and coating material (NiCoCrAlY) as those introduced in Chapter 1 were used (see chemical composition in Table 2.1 and specimen configuration in Fig. 2.1). After degreasing the single crystal specimens surface with acetone, they were coated to 92μm using physical vapor deposition by the electron beam process (EB-PVD). After a diffusion bonding heat treatment at 1079°C for 4 h in vacuum, specimens were cooled to 760°C at approximately 46°C/min. A subsequent aging treatment at 871°C for 20h in argon allowed further precipitate growth.

The coating microstructure consists primarily of a brittle intermetallic compound,

NiAl (β phase), and a ductile matrix of Ni solid solution (γ phase), discussed in Section 2.5.1. The Ni-Cr-Al phase diagram of Fig. 2.2 shows the coating composition relative to the $\gamma - \gamma'$ substrate[1].

The final coating had a microstructure of 1-3 μm grain size embedded in a columnar growth structure with two types of defects. Columnar voids (sometimes called *leaders*) were found on the curved surfaces of the specimen with an average spacing of 300 μm. As shown in Fig. 2.3, they were successfully closed half way through the thickness after first glass-bead pinning the coating up to an Almen intensity of 15 N before the above heat treatments. The other type of defect was *surface pits* of 40-60 μm diameter which formed during the pinning operation due to the detachment of cone-shaped grains produced by preferential nucleation and growth on a non-metallic particle (Fig. 2.4; see also (Bettridge, 1986). Six to ten surface pits were found in the curved rim of each specimen, and their penetration depths appeared to be 60 to 90% of the coating thickness.

2.3.2 Test apparatus

Fig. 2.5 shows the experimental set-up used to heat the periphery of the coated CMSX-3 stepped-disk specimens. Thermal cycling of the specimens is produced by using a concentrator coil to inductively heat the periphery of the specimen. The coil is connected to a Lepel solid state 2.5 Kw high frequency (450 kHz) induction generator. Specimens are held in the center of the load coil using stainless steel rods attached to aluminum forced-air cooling manifolds (Fig. 2.5). A microprocessor is used to give automatic control to the induction generator as well as to activate an

[1] When considering the behavior of the coating or substrate using the ternary Ni-Al-Cr diagram as a model, it is convenient to work with equivalent quantities. Thus, Ni_{eq} = Ni + Co and Al_{eq} = Al + Ti + Ta + Mo. These equivalences are based on similarities in their ternary diagrams, in their atomic dimensions, and in their relative diffusion behaviors, i.e. diffusivities of Al and Cr are approximately the same in Ni and Co (Holmes, 1986; Lindblad, 1969; Swindells, 1986).

on-off switch for the air flow through the cooling manifolds .

2.3.3 Thermal history

Due to the anisotropic elasticity and creep interacting with the radially inhomogeneous temperatures, the strain range along the specimen periphery (Fig. 2.1) ranged from a maximum along the $< 100 >$ to a minimum along the $< 110 >$ crystal direction. This allowed the use of a single specimen to obtain coating durability and cracking patterns simultaneously for different strain levels but identical temperature histories.

Since the thin coating gives negligible constraint to the substrate, the total in-plane strain history of the coating is determined by the in-plane strain history of the substrate. Control of the latter is achieved by programming the power input to the concentrator coil. The resulting heating and cooling rates in turn determine the transient strains in the periphery from the temperature distributions throughout the specimen. Enough steady state compression in the periphery to simulate cruise conditions is achieved by circulating compressed air through the axial supporting tubes (Fig. 2.5).

For higher tensile stresses during cooling, high pressure air was blown onto the specimen periphery from the upper and lower cooling manifolds.

To determine the effect of different strain histories on coating degradation, three different heating rates were used on the periphery: the rapid 4.5s heating of Fig. 2.6a, the intermediate 6s heating of Fig. 2.6b, and the slow 20s heating cycle of Fig. 2.6c, all with minimum temperatures of 520°C, holding times of 60s at 1090°C, and cooling back to 520°C in 15s. The slow heating (20s) rate was combined with a fast cooling (7s) rate to study the effect of higher tensile peak stresses (Fig. 2.6d).

2.4 Stress and Strain Histories

The stress-strain history in the periphery of the disk-shaped specimen is found from the measured axisymmetric temperature history using non-linear finite-element. (Should the reader be familiar with the main conclusions of Chapter 1, it is suggested that he/she skips this section, also see Busso and McClintock, 1988).

Substrate. The temperatures were measured using four chromel-alumel thermocouples (0.13 mm wire diameter) at various radii (see Fig. 1.3). The mean coefficients of thermal expansion and elastic data for the single crystal CMSX-3 were already given in Fig. 1.4 and 1.6 respectively.

Due to lack of material data in the Bauschinger regime ($\epsilon < 1\%$), anisotropic power law creep was assumed as an approximation to inelasticity on the stress-strain response to compare it with the thermo-elastic analysis commonly used in industry.

Anisotropy was modeled using a creep (or flow) potential for a cubic crystal and the associated flow rule using a shear stress pre-multiplier parameter R. An analysis for R (e.g. see Chapter 1) in terms of the available uniaxial $< 100 >$ and $< 110 >$ creep rates, $\dot{\epsilon}^p_{<100>}$ and $\dot{\epsilon}^p_{<110>}$, and the uniaxial applied stresses $\sigma_{<100>}$ and $\sigma_{<110>}$ for the $< 100 >$ and $< 110 >$ specimens gave:

$$\dot{\epsilon}^p_{<110>} = \left(\frac{\sqrt{1+3R}}{2}\right)^{m+1} \left(\frac{\sigma_{<110>}}{\sigma_{<100>}}\right)^m \dot{\epsilon}^p_{<100>} \cdot \tag{2.1}$$

For CMSX-3 at 1090°C, R was 1.13

The steady state $< 100 >$ creep data provided by Allison-GM (1986) at 1010 and 1066°C were expressed as a power law relation with $m \approx 8$. Fig. 2.7a shows the resulting hysteresis loops for the first eight cycles of the 4.5s heating history, and Table 2.2 the results of the thermo-elastic and creep analyses (8th cycle), all for the substrate. These strain ranges correlate well with several values reported for the trailing edges of high-pressure turbine blades, ranging from 0.7% for aircraft fighter

jets (Thulin et al., 1982) to 0.3% for commercial aircraft engines (Kaufman, 1984).

Long time ratchetting of the peak cooling stresses was estimated through a mechanism-inspired model (Busso and McClintock, 1986) where the shifting of stress with cycling, $d\sigma/dN$, depends on the amount of creep strain accumulated during each cycle, ϵ^c. This yielded an expression for the peak cooling stresses in terms of the stress range $\Delta\sigma_{max}$, the number of cycles N, the cooling stress at the first cycle $\sigma_{max}(1)$, the creep exponent m, a constant f which defines the stress at that point in the cycle which would go to zero at steady-state, and a constant C which reduces to the proportion of the creep strain to the elastic strain for the first cycle:

$$\sigma_{max}(N) = [\sigma_{max}(1) - f\,\Delta\sigma(1)]\,[1 + (m-1)C(N-1)]^{-1/(m+1)} + f\,\Delta\sigma\ . \quad (2.2)$$

Table 2.3 gives the changes in the stresses encountered during cyclic cooling due to creep according to Eq. 2.2.

Coating. The coating was modeled in plane stress with its plane normal to the radius of the specimen. Since the in-plane components of displacements are the same in both the coating and substrate, they determine the in-plane component of <u>total</u> strain (the tangential $\epsilon_{\theta\theta}^{applied}(t)$, and the through-specimen-thickness $\epsilon_{zz}^{applied}(t)$) in the coating, which constitute its imposed loads.

The polycrystalline NiCoCrAlY coating was assumed isotropic, and its elastic and thermal expansion properties have already been reported elsewhere (see Chapter 1). The creep behavior was modeled with a power law fitted to data at 661, 850 and 1050°C obtained from Hebsur and Miner (1986).

The temperature cycle for the coating was that of the outer radius of the specimen for the most severe heating time, 4.5s (Fig. 2.6a at R= 6.5mm). The initial residual stress in the coating was tentatively assumed to be zero due to its unknown magnitude at the end of the holding stage of the second aging treatment, and its change due to further relaxation and differential contraction on cooling.

The coating strain ranges were obtained by adding the thermal expansion mismatch strain range, $\Delta\epsilon^{th}$ =0.31% (which only depends on the coefficients of thermal expansion of the substrate and coating, and on the temperature range), to those of the substrate (Table 2.2). For example, the creep analysis of the coating for the 4.5s heating cycle, which gives rise to $\Delta\epsilon^{mech}_{subs} = 0.52$ % in the substrate, gave a mechanical strain range of $\Delta\epsilon^{mech}_{coat} = 0.83\%$ in the coating. Fig. 2.7b shows the coating hysteresis loops. The maximum cooling stress in the coating, σ_{coat} = 460 MPa (compared to 245 MPa for 6000 cycles for the substrate, Table 2.3), is reached at 546°C during cooling.

2.5 Results and Discussion

2.5.1 Microstructural changes

For microprobe analysis, the specimens were nickel-plated, ground parallel to their faces, and etched with a solution of 33% HNO_3, 33% HCl, 33% $C_3H_8O_3$ (glycerol) and 1% HF. A JOEL Model 7320 electron microprobe was used to determine the chemical composition of the coating: a) in the as received condition, and b) after 6000 cycles of the 4.5s, 6s, and 20s heating histories, all with slow cooling (15s). X-ray intensities and K_α lines of the alloy elements were compared to those of pure element standards. Composition was obtained using a ZAP (atomic number, absorption, and fluorescence) correction program. The incident electron beam was operated at an accelerating potential of 15 KV and a current of 20 nA. The beam diameter to analyze the separate phases or precipitates was 3/4 μm, with a positioning accuracy of better than 5 nm. Average compositions along radial paths, running from the coating surface down to the substrate, were performed with a 10 μm beam diameter.

In the backscattered electron micrographs, obtained with an accelerating voltage of 25 KV for optimum contrast, the lighter the shade of gray, the higher the average

atomic number of elements in that region.

As-received. Fig. 2.8 shows a backscattered electron micrograph of the coating cross section in the as-received condition, (after the heat treatments referred to in Section 2.3.1), along with the results of the microprobe analysis[2].

As a result of interdiffusion between the NiCoCrAlY coating and the $\gamma - \gamma'$ substrate, the alloy developed a region represented by the dashed traces 2 in Fig. 2.2 and and Region 2 in Fig. 2.8, intermediate between the bulk substrate composition of Point 1 and the main coating region, Point 3.

Region 2 or transition zone: the limited interdiffusion is dominated by a predominantly *outward* diffusion of Ni from the substrate (68 at.%) to the coating (43 at.% Ni) (Levine, 1978). Simultaneously, the higher Al content of the coating (24.2 at.%) versus the lower one for the substrate (12.4 at.%, Al_{eq}[3]= 15.7 at.%), generates an *inward* diffusion of Al (and similarly Cr). This zone extends from 75 to 100 μm beneath the coating surface and is connected to the substrate by a $\gamma - \gamma\prime$ region with varying $\gamma\prime$ volume fraction. It formed due to diffusion of enough Ni from the prior substrate to transform this region from a $\gamma - \gamma'$ to a β(NiAl) - α(Cr)$-\gamma$. Fig. 2.2 shows possible composition paths for different positions of trace lines beginning at the substrate and ending in the coating. The transition zone shows two subzones with different precipitate sizes: the thinner subzone, 90 to 100 μm below the surface, contained not only α(Cr) precipitates, identified as less intense particles (Point c) in Fig. 2.8, but also other refractory-rich precipitates of elements previously in solution in the substrate γ phase, such as Ti-Ta-W rich precipitates, shown as bright particles (Point d) in Fig. 2.8. The thicker subzone, 75 to 90 μm below the surface, contained

[2]The darker 'grains' in the outer part of the coating are holes formed from NiAl grains broken off during polishing.

[3]Al_{eq} = Al + Ti + Ta + Mo and Ni_{eq} = Ni + Co, as defined above in Section 2.2.3

0.5 to 1 μm $\alpha(Cr)$ precipitates, along with γ and β. The presence of α precipitates, seen as faint light dots, can be explained by the decreasing Al and increasing Cr at relatively constant Ni towards the substrate (see left hand dashed line 2 in Fig. 2.2). *Region 3 or $\gamma - \beta$ zone of coating:* this is a 75 μm region with 24 at.% aluminum characterized by a $\beta + \gamma$ microstructure (Point 3 in Figs. 2.2 and 2.8). The $\gamma - \beta$ zone also shows a 1-3 μm Al-rich β strip underneath a 0.5-1 μm surface layer of oxide. Fig. 2.9 shows microprobe dot-maps of Cr and Y (the lighter the color, the higher the element concentration). Both elements show a pronounced diffusion outward from the $\gamma - \beta$ zone towards both the transition zone and the coating surface. Y has a low solubility in the alloy and it appears as a finely distributed Co/Ni-Y intermetallic compound (Goward, 1979). However, since in the microprobe analysis the Y content in the coating was at the limits of detectable amounts (0.05 at.%), the margin of error in the Y content is $\pm$ 100%. Thus only a qualitative interpretation can be gained from Fig. 2.9b.

Isothermal exposure. A secondary electron micrograph of the coating cross section after 100 hr. at 1090°C is shown in Fig. 2.10. During isothermal oxidation, the coating microstructure coarsened (from 1-3 μm to 10-15 μm grain size for the β phase) and formed γ zones, 15-20 μm thick at the surface and 55 μm thick at the coating-substrate interface (Table 2.4), indicating that β depletion is not only due to diffusion of Al to the oxide-coating interface (coating oxidation) but also due to interdiffusion between coating and substrate, as discussed above. The oxide thickened to 2-4 μm and spalled off in places, with no preference of rim orientations. Furthermore, since the subsurface leader defects remaining after pinning were not seen in the coating cross section, they must have diffused shut during the isothermal oxidation.

Cyclic exposure. Micrographs of the coating and their corresponding concentration - distance profiles for the main coating elements near the < 100 > rim orientation for the 20s, 6s, and 4.5s heating with 15s cooling thermal histories ($\Delta\epsilon_{coat}^{mech}$ increasing from 0.61% to 0.83%) are shown in Figs. 2.11. Table 2.4 shows the thicknesses of the coating-substrate regions after cycling.

Results for $\Delta\epsilon_{coat}^{mech} = 0.61\%$ in Fig. 2.11a show elongated β particles (Point a), above a transition zone characterized by a Ni solid solution or γ phase with composition similar to Point b, and Mo-Ta and Cr-W precipitates (Points c and d respectively) of size ranging from 1 to 3 μm. The diffusion of Ni from the original substrate towards the coating saturated these precipitates in the Ni-solid solution. The radial trace shows an average Al depletion along the coating and the transition zone from the original 24 at.% to 19 at.%.

For $\Delta\epsilon_{coat}^{mech} = 0.71\%$, the microstructure was similar to that for $\Delta\epsilon_{coat}^{mech} = 0.61\%$ but with a lower volume fraction of β phase in the coating, and of the transition zone Mo-Ta and Cr-W precipitates (Points c and d in Fig. 2.11b respectively). The radial trace in Fig. 2.11b shows an average Al depletion in the coating from 24 to 13 at.%.

For $\Delta\epsilon_{coat}^{mech} = 0.83\%$, the coating and transition zone shows two phases: a Ni solid solution phase, γ, and isolated grains of γ' (Ni_3Al) (Points c and a in Figs. 2.2 and 2.11c). The grains, originally β (NiAl), were gradually depleted of Al down to the level of the γ' intermetallic compound, as would be expected from the ternary diagram of Fig. 2.2. This indicates that oxidation gradually depletes the β grains uniformly of Al, while maintaining their original crystallographic orientation. The radial trace shows a fairly constant average Al depletion along the coating γ matrix and transition zone (approximately from 24 to 12 at.%).

It is important to point out that cyclic oxidation, after an initial thinning of the $\beta + \gamma$ zone, does not deplete the coating of its Al content by decreasing the thickness of the $\beta + \gamma$ zone gradually, but it instead maintains a constant thickness with uniform composition, while reducing the β volume fraction in this region, as seen by comparing Figs. 2.11a-c. The radial elongation of the β grains as cycling progresses is an indication that the aluminum in the β phase is diffusing at a higher rate across the radial β/γ interfaces, normal to the coating surface.

An interesting one-dimensional diffusion model was recently implemented by Lee et al. (1987) to predict, among other things, the thickness of the $\gamma + \beta$ region as well as the β volume fraction on a Co(Ni)CrAlY coating with a $\gamma - \gamma'$ substrate. To extend models like this to two dimensions and to incorporate mechanical effects, such as realistic thermal strain rates, into the diffusion coefficients poses an interesting challenge for future work.

2.5.2 Cracking observations

Oxidation by itself, without imposed cyclic deformation, produced some oxide spalling, but no coating cracking (Fig. 2.10). Cyclic deformation gave none of the surface waviness or *scalloping* (sometimes called *rumpling*) occasionally observed in some coatings (Holmes et al., 1986; Schneider et al., 1983).

Surface cracks appeared with all the cyclic histories. They are classified in Table 2.5 according to their final lengths (l) relative to the coating thickness (t), as major ($l/t > 5$), intermediate ($5 \geq l/t > 2$), and small ($l/t \leq 2$). Inspection of the coating surface after testing revealed that some of the cracks had originated from initial surface defects (pits) like the one shown in Fig. 2.4. It is however not clear whether they would have initiated in the absence of surface pits, so they will be excluded from further discussion.

Micrographs showing coating degradation for different applied strain ranges are shown in Figs. 2.12 to 2.16. Figure 2.12 shows coating degradation for the threshold coating strain range of 0.51%. A typical crack of *intermediate* length at $\Delta\epsilon^{mech} = 0.57\%$ is shown in Fig. 2.13. *Major cracking* ($l/t > 5$, shown in Figs. 2.11b-c, 2.14, 2.15, and 2.16) was associated with large coating strain ranges, between 0.67% and 0.83%, and large coating peak tensile stresses, between 404 and 460 MPa (Table 2.5). Furthermore, the greater the strain amplitude, the greater the crack length. Damage for the 20s heating cycle with forced cooling, 7s ($\Delta\epsilon^{mech}_{coat} = 0.67\%$), is shown in Fig. 2.14.

Visual observation of the coating showed that at the higher strain ranges oxide spalling was heavier (Figs. 2.13a and 2.16a) and occurred in 1/3 to 1/4 the time of that at the lowest strain range (Fig. 2.12a).

Cracks into the substrate initiated at two different sites in the EB-PVD NiCoCrAlY coating: at the internal interface, due to voids, and at the coating surface, due to early cracking of the protective oxide scale apparently as a consequence of excessive cooling rates, as discussed above.

In some cases, inspection of the coating cross section after cyclic exposure revealed voids near to and distributed along the coating original interface (e.g. in Fig. 2.11b for the 4.5s heating cycle). No relation was found between the initial columnar defect spacing of 300μm, as the one shown in Fig. 2.3, and the mean interface void spacing which, for a $\Delta\epsilon^{subs}_{coat} = 0.83\%$, was between 60 to 100 μm. Furthermore, voids were only found for substrate strain ranges higher than 0.20% ($\Delta\epsilon^{mech}_{coat} > 0.51\%$). The isothermal test at 1090^{0}C did not reveal any voids either (Fig. 2.10). The voids show a quasi-cylindrical shape and seemed to have grown from the original coating-substrate interface towards the coating surface following the receding β phase in the coating (Fig. 2.17a). Fig. 2.17b shows how some of these voids eventually developed

into cracks. Such voids have also been reported by Swindells (1986), Lee et al. (1987), Nesbitt (1982), and Gedwill (1982), among others, but with no associated cracking. A more detailed discussion of the mechanisms associated with interface void nucleation and growth will be presented in Chapter 3.

The only cracks with no signs of interface voids were found after the 20s heating history with forced cooling (7s), which exhibited cracks near the $< 100 >$ rim orientation ($\Delta\epsilon_{subs}^{mech} = 0.36\%$, $\Delta\epsilon_{coat}^{mech} = 0.67\%$), like the one seen in Fig. 2.14. It also gave early cracking and spalling of the protective Al_2O_3 oxide scale (at 4/5 of the time of the 20s-15s history). Under these conditions, the oxide develops high tensile stresses dictated by the substrate total strains (mechanical plus thermal) and the thermal contraction strains of the oxide. Note that, if the oxide scale lies on a thin coating, as here, the oxide stresses are *independent* of the coating thermal expansion coefficient since the coating only constitutes a vehicle for the total in-plane substrate strain components.

Effect of maximum oxide stresses on oxide breakdown. To obtain the maximum oxide stress, consider a plane stress elastic model of the oxide with its plane normal to the radial direction of the specimen. Since the surface oxide (e.g. Al_2O_3) forms mainly during the holding period at 1090°C and since the growth strains during this period are negligibly small (Holmes, 1986), assume that the oxide stresses before specimen cooldown (at the end of the holding period) can be neglected. With this stress-free configuration, the tangential oxide stress at temperature T, $\sigma_{\theta\theta}(T)$, expressed in terms of its elastic modulus and Poisson's ratio, $E(T)$ and $\nu(T)$[4], the total applied oxide strains, $\epsilon_{\theta\theta}^{total}(T)$ and $\epsilon_{zz}^{total}(T)$, and the oxide thermal strain $\epsilon^{th}(T)$,

[4]Thermodynamical changes of α with stress turn out to be of the order of 3% and can therefore be neglected.

turns out to be (see Appendix 2.A),

$$\sigma_{\theta\theta}(T) = \frac{E(T)}{[1-\nu(T)^2]} \left[\epsilon_{\theta\theta}^{total}(T) + \nu(T)\, \epsilon_{zz}^{total}(T) - (1+\nu(T))\, \epsilon^{th}(T)\right] . \qquad (2.3)$$

$\epsilon_{\theta\theta}^{total}(T)$ and $\epsilon_{zz}^{total}(T)$ will be given by the total *substrate* strains at temperature T relative to those at the end of the holding period. Similarly, $\epsilon^{th}(T)$ will be the oxide contraction as a result of the temperature drop from $T_{hld} = 1090°C$ to T. $\epsilon^{th}(T)$ can be expressed in terms of the average oxide coefficient of thermal expansion to T from the reference temperature T_o (from which α_T is experimentally measured):

$$\epsilon^{th}(T) = \frac{\alpha_T\,(T-T_o) - \alpha_{T_{hld}}\,(T_{hld}-T_o)}{1+\alpha_{T_{hld}}\,(T_{hld}-T_o)} . \qquad (2.4)$$

(See Appendix 2.A for the derivation of Eq. 2.4). When the thermal and total substrate strain histories are known from thermocouple measurements and a finite element analysis respectively, Eqs. 2.3 and 2.4 give the oxide stress history.

The maximum tensile oxide stress can be found by following the cooling part of the cycle. In the early stages of cooldown, where the magnitude of the negative thermal strain ϵ^{th}(T) is greater than the magnitude of the negative contribution of the total applied oxide strains (first two terms in right hand side of Eq. 2.3), the oxide is in tension. At a later stage during cooldown, the negative ϵ^{th}(T) will be offset by negative total applied oxide strains driving the oxide scale into compression. For example, the maximum tensile tangential oxide stress for the high cooling rate cycle (20s-7s) at the $< 100 >$ orientation turns out to be 218 MPa at 997°C. Conversely, a normal cooling rate cycle (4.5s-15s) at $< 100 >$ gave a stress of 116 MPa at 968°C. Thus, oxide breakdown is a likely precursor to crack initiation, which will most likely occur with high coating inelastic strain ranges and when high tensile stresses in the coating are generated during the cooling part of the cycle (e.g. $\sigma_{coat}^{max} = 404$ MPa for the 20s-7s history, as per Table 2.5).

2.5.3 Overall coating life

The only crack initiation data found in the literature for a NiCoCrAlY coating was that of Leverant et al. (1976), who tested different superalloy substrates with a 67s heating and cooling cycle (Fig. 2.18). Their data predict that, for a life of 6000 cycles, the maximum coating strain range to avoid crack initiation will be around 0.22%. However, our data, also shown in Fig. 2.18, gave no coating cracks before 6000 cycles even with strain ranges of up to 0.51 %. Since Leverant et al. did not report the level of the tensile cooling stresses or the shapes of the hysteresis loops, which will cause different interactions of stress, strain, and temperature, this discrepancy cannot be analyzed[5]. Note also that when the coating strain range is less than 0.49% (at $< 110 >$ for the 20s-7s history), cracks initiate only from pre-existing surface defects.

2.6 Conclusions and Recommendations

1. The degradation of an EB-PVD NiCoCrAlY overlay coating in an oxidizing environment under 6000 thermal cycles ($0.57\% \leq \Delta\epsilon_{coat}^{mech} \leq 0.83\%$) consisted of severe cracking, which in some cases propagated well into the substrate, and it critically depended on the coating strain ranges and oxide cooling stresses.

2. Two different crack initiation processes were observed (in the absence of surface pits). At high (7s) cooling rates, which induced maximum oxide stresses of 218 MPa, there was early cracking of the protective oxide scale with surface initiation. At normal cooling rates (15s), with give maximum oxide stresses of 116 MPa, cracks appeared to originate from internal voids located at the coating/substrate interface which grew from the original coating-substrate in-

[5]Other data, unpublished, appear to be closer to our results than Leverant's

terface towards the coating surface. These voids were associated with coating strain ranges of 0.57% and above. Should a gas turbine have to operate with a coating with these characteristics, cracking could be reduced by accelerating to full power at a slower rate (in 30s rather than 4.5s for example), and by avoiding excessive cooling rates during engine shutdown and maneuvering.

3. As is known, thermal expansion mismatch strains should be minimized to reduce the level of the tensile stresses and strain ranges. Beyond that, further crack initiation and propagation data for the coating, with realistic stress-strain histories, are necessary to accurately correlate realistic strain ranges with the development of damage.

4. Diffusion during coating deposition and aging gave a 10 μm $\beta-\alpha-\gamma$ transition zone between the coating and substrate, which grew to 80 μm and transformed into a single γ phase after cycling for the most severe history, 4.5s heating ($\Delta\epsilon_{coat}^{mech} = 0.83\%$).

5. An isothermal test at 1090°C revealed little thinning, no interface voids, and no cracking.

Bibliography

[1] Allison-General Motors Turbine Division (1986). Private communication.

[2] Bennett, A. (1986), 'Properties of thermal barrier coatings', *Mat. Sci. Technol.* **2**, 257-261.

[3] Bettridge, D.F., and R.G. Ubank (1986), 'Quality Control of high-temperature protective coatings', *Mat. Sci. Technol.* **2**, 232-242.

[4] Bunshah, R.F. (1982), *Deposition Technologies for Films and Coatings: Development and Applications*, Park Ridge, N.J., Noyes Publications.

[5] Busso, E.P. (1987), *Thermal Fatigue of an Overlay Coating for Single Crystal Nickel-Base Superalloys*, MSc Thesis, Dept. Mech. Eng., M.I.T., May.

[6] Busso, E.P., and F.A. McClintock (1988), 'Stress-strain histories in coatings on single crystal specimens of a turbine blade alloy', *Int. J. Solids Structures* , **24**, 1113-1130.

[7] Gedwill, M.A., T.K. Glasgow, and S.R. Levine (1982), 'A new diffusion oxidation resistant coating for superalloys', *Thin Solid Films* **95**, 65-72.

[8] Goebel, J.A., and F.S. Pettit (1975), 'Hot corrosion of Co-based alloys', Report ARL TR75-0235, *Air Force Contract F33615-72-C-1757*, June.

[9] Goward, G.W. (1979), 'Protective coatings for high temperature alloys', *Source Book on Materials for Elevated Temperature Applications*, ASM Eng. Bookshelf, E.F. Bradley (ed.), pp. 369-384.

[10] Goward, G.W. (1986), 'Protective coatings - purpose, role, and design', *Mat. Sci. Technol.* **2**, 194-200.

[11] Gupta, D.K., and D.S. Duvall (1984),'A Si and Hf modified plasma sprayed MCrAlY coating for single crystal superalloys', *Superalloys 1984*, The Metal. Soc. of AIME, pp. 711-721.

[12] Hebsur, M.G., and R.V. Miner (1986), 'High temperature tensile and creep behavior of low pressure plasma-sprayed NiCoCrAlY coating alloy', *Mat. Sci. Eng.* **83**, 239-245.

[13] Holmes, J.W., and F.A. McClintock (1983), 'Induction heating of thin disk specimens as a means of studying thermal shock encountered by Nickel-base superalloys', *Scripta Met.* **17**, 1365-1370.

[14] Holmes, J.W. (1986), *Thermal Fatigue Oxidation and SO_2 Corrosion of an Aluminide-coated Superalloy*, PhD Thesis, Dept. Mat. Sci. Eng., Massachussets Institute of Technology, Sept.

[15] Holmes, J.W., and F.A. McClintock, K.S. O'Hara, and M.E. Conners (1987), 'Thermal fatigue testing of coated monocrystalline superalloys, *Low-Cycle Fatigue*, ASTM STP 942, H.D. Salomon, G.R. Halford, L.R. Kaisand, and B.N. Leis (eds.), pp. 672-691.

[16] Holmes, J.W., and F.A. McClintock (1988), 'The chemical and mechanical processes of thermal fatigue degradation of an aluminide coating, *Met. Trans.*.

[17] Howes, M.A. (1976),'A study of thermal fatigue mechanisms', *Thermal Fatigue of Materials and Components*, ASTM STP 612, D.A. Spera and D.F. Mowbray (eds.), pp. 86-105.

[18] Kaufman, A., and R.H. Halford (1984), 'Engine cyclic durability by analysis and material testing', *NASA Tech. Memo. 83577.*

[19] Lee, E.Y., D.M. Chartier, R.R. Biederman, and R.D. Sisson Jr. (1987), 'Modeling the microstructural evolution and degradation of M-Cr-Al-Y coatings during high temperature oxidation', *Surface and Coatings Technol.* **32**, 19-39.

[20] Leverant, G.R., T.E. Strangman, and B.S. Langer (1976),'Parameters controlling the thermal fatigue properties of conventionally cast and directionally solidified turbine alloys', *Superalloys 1976*, AIME High Temp. Alloys Committee, Warrendale, PA, pp. 285-295.

[21] Levine, S.R. (1978), 'Reaction diffusion in the NiCrAl and CoCrAl systems', *Met. Trans. A* **9** , 1237-1250.

[22] Lindblad, N.R. (1969), 'A review of the behavior of aluminide-coated superalloys', *Oxid. Met.* **1**, 143-150.

[23] Nesbitt, J.A. (1982),'Solute transport during the cyclic oxidation of Ni-Cr-Al alloys', *NASA Report 165544.*

[24] Saunders, S.R. (1986), 'Correlation between laboratory corrosion rig testing and service experience', *Mat. Sci. and Technol.*, **2**, 282-289.

[25] Schneider, K., and H.W. Grünling (1983), 'Mechanical aspects of high temperature coatings', *Thin Solid Films* **107**, 395-416.

[26] Swindells, N. (1986), 'Structural stability of coatings', *Mat. Sci. Technol.* **2**, 250-255.

[27] Taylor, A., and R.W. Floyd (1954), 'Ni-Al-Cr systems', *J. Inst. Met.* **81**, 451-464.

[28] Thulin, E.D., D.C. Howe, and I.D. Singer (1982), 'Energy efficient engine: high performance turbine detailed design report', *NASA Report CR-165608*, Pratt & Whitney Aircraft Group, East Hartford, CT.

[29] Vogan J.W., and A.R. Stetson (1982), 'Advanced ceramic-coating development for industrial/utility gas turbines, DOE/NASAA/0109-1, *NASA Report CR 169852.*

Table 2.1 Chemical compositions of substrate and coating

		Ni	Co	Cr	Mo	W	Ti	Al	Ta	Y
CMSX-3 substrate (MAR-M-247 derivative)	Wt.%	66.4	4.6	7.9	0.5	8.0	1.0	5.6	6.0	–
	At.%	67.9	4.7	9.1	0.3	2.6	1.1	12.4	1.9	–
CMSX-3 constituent phases	γ									
	Wt.%	61.1	7.3	18.8	0.9	9.4	0.4	2.0	0.1	–
	At.%	62.4	7.4	21.6	0.5	3.0	0.5	4.4	0.04	–
	γ'									
	Wt.%	69.	3.2	2.0	0.3	7.3	1.3	7.6	9.2	–
	At.%	70.6	3.2	2.3	0.2	2.3	1.6	16.7	3.1	–
NiCoCrAlY coating	Wt. %	49.3	19.7	15.9	–	–	–	12.7	–	< 0.2
	At. %	42.8	17.1	15.7	–	–	–	24.2	–	< 0.05

Table 2.2 Comparison of substrate thermo-elastic and creep analyses

Cycle	Rim orientation	Anisotropic creep (8th cycle)			Thermo-elastic
		Strain history, %		Peak cool. stress, MPa	
		ϵ^{cr}_{min}	Range, $\Delta\epsilon^{cr}$	σ^{cr}_{max}	σ^{el}_{max}
20s-15s	< 110 >	−0.169	0.152	−10.	−19.
20s-7s	< 110 >	−0.165	0.180	26.	22.
62-15s	< 110 >	−0.213	0.197	−5.	−16.
4.5s-15s	< 110 >	−0.273	0.258	−1.	−1.
20s-15s	< 100 >	−0.333	0.204	45.	−21.
20s-7s	< 100 >	−0.334	0.356	98.	27.
6s-15s	< 100 >	−0.425	0.399	60.	−20.
4.5s-15s	< 100 >	−0.543	0.519	87.	−20.

Table 2.3 Changes in σ_{max} with cycles for $< 100 >$ (Eq. 2.2)

Heat. time	Cool. time	$\sigma_{max}(1)$, MPa	$\Delta\sigma$, MPa	f	C	m	σ_{max}, MPa, for cycle no.:			
							100	500	6000	Steady st.
20s	15s	-3.	248.	0.89	0.08	7.2	104.	131.	161.	219.
20s	7s	42.	293.	0.90	0.07	4.1	181.	214.	241.	264.
6s	15s	−2.	323.	0.80	0.08	6.2	134.	167.	203.	258.
4.5s	15s	13.1	441.	0.73	0.09	6.8	168.	205.	245.	321.

Table 2.4 Sizes of β-depleted zones in the coating and interface

Cycle	Orientation	γ zone at coat. surface (μm)	$\beta - \gamma$ zone in coat. (μm)	γ zone at interface (μm)
Isothermal	All	15	65	55
20s - 15s	All	10	70	70
20s - 7s	All	10	70	80
6s - 15s	$< 100 >$	20	45	70
	$< 110 >$	20	65	60
4.5s - 15s	$< 100 >$	50	10	80
	$< 110 >$	20	40	60

Table 2.5 **Comparison of substrate and coating inelastic stress analyses and cracking observed after tests**

Cycle	Rim orientation	Substrate		Coating		Cracks (in units of coating thickness)[2]					
		Strain %	Stress MPa	Strain %	Stress MPa	Major ($l > 5$)		Intermediate ($5 \geq l > 2$)		Small ($l \leq 2$)	
		$\Delta\epsilon^{mech}$	$\sigma_{max}(6000)^1$	$\Delta\epsilon^{mech}$	$\sigma_{max}(6000)^1$	No.	Length	No.	Length	No.	Length
Isothermal	< 100 >	–	–	–	–	0	–	0	–	0	–
	< 110 >	–	–	–	–	0	–	0	–	0	–
20s-15s	< 110 >	0.15	n.c.	0.46	n.c.	0	–	0	–	0	–
20s-7s	< 110 >	0.18	n.c.	0.49	n.c.	1	8^d	0	–	0	–
62-15s	< 110 >	0.20	n.c.	0.51	n.c.	0	–	0	–	0	–
4.5s-15s	< 110 >	0.26	n.c.	0.57	n.c.	0	–	3	5,3,3	6	1 to 2
20s-15s	< 100 >	0.30	161.	0.61	n.c.	3	$14^d, 7^d, 6^d$	1	3^d	4	$1^d, 1^d, 1.5^d, 2^d$
20s-7s	< 100 >	0.36	241.	0.67	404.	3	$8, 9, 20^d$	1	3^d	0	–
6s-15s	< 100 >	0.40	203.	0.71	n.c.	2	6, 12	1	2.5^d	0	–
4.5s-15s	< 100 >	0.52	245.	0.83	460.	3	20^d, 18, 15	2	2.5, 3^d	18	1 to 2

1.(n.c.) not calculated except for critical cases due to extensive post-processing requirements
2. (d) indicates cracks which originated from surface defects or pits

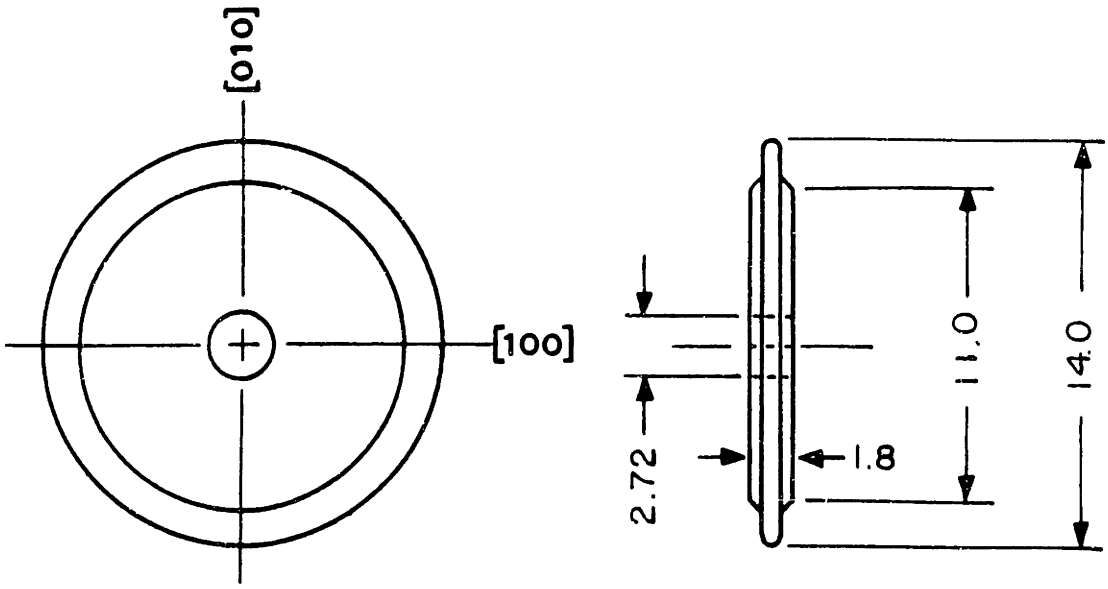

(a) specimen geometry

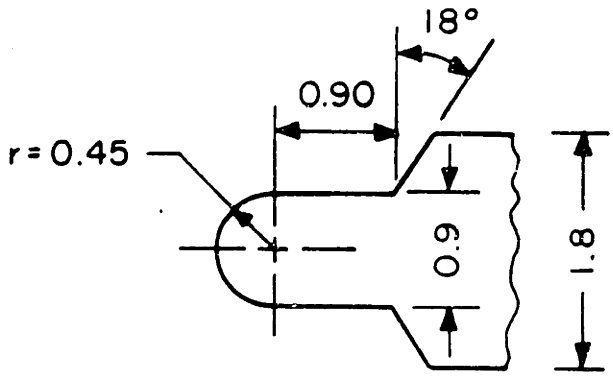

(b) detail of specimen periphery

Fig. 2.1 Detailed drawing and orientation of stepped-disk specimen (All dimensions in mm). After Holmes [1987]

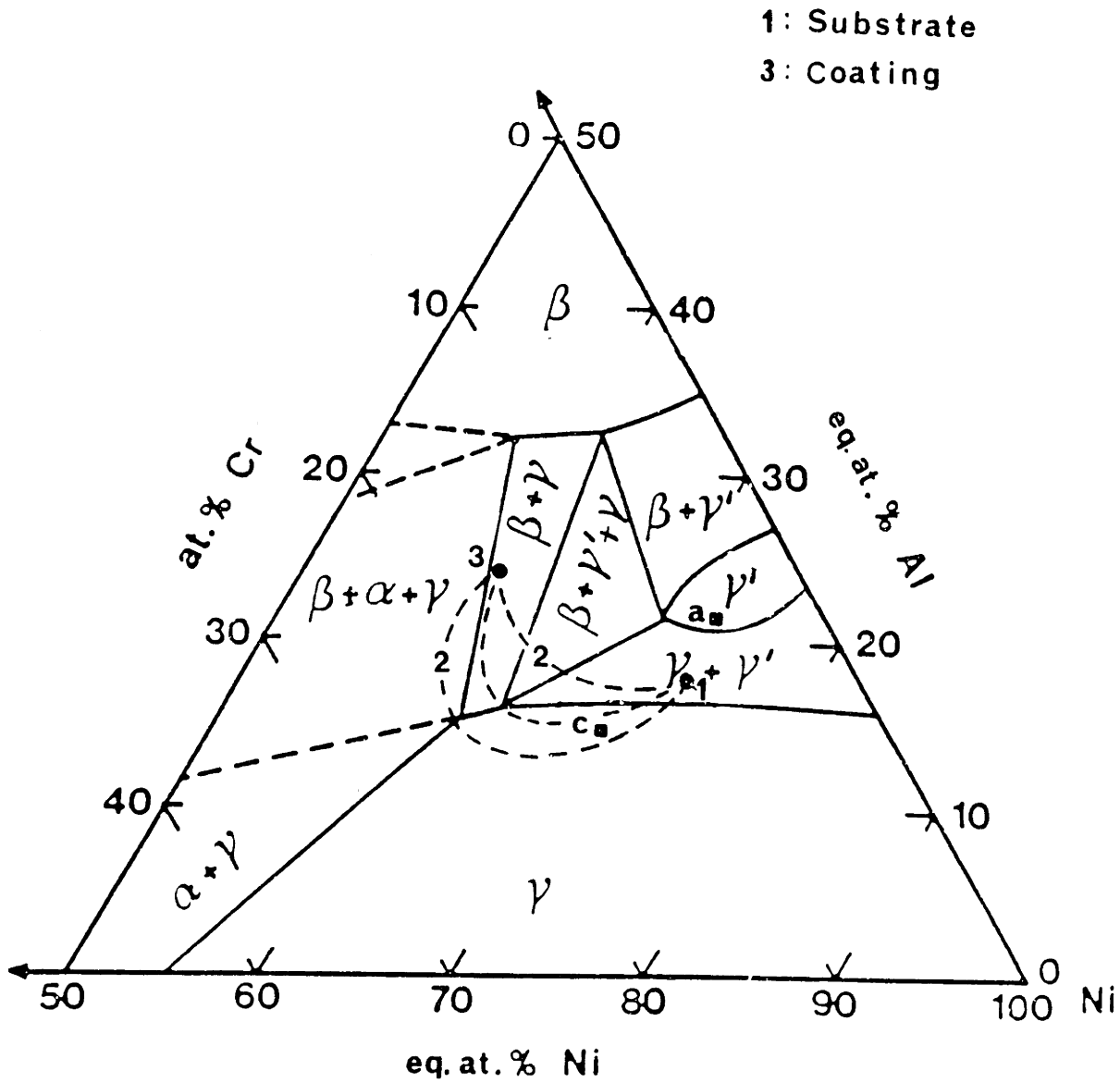

Fig. 2.2 Ni-Cr-Al phase diagram at 1090°C (from interpolation between Taylor and Floyd's data (1954) at 1000 and 1150°C) (after Holmes, 1986). *As coated* composition path: 1 to 3. *Cyclic*(4.5s-20s): Points a and c.

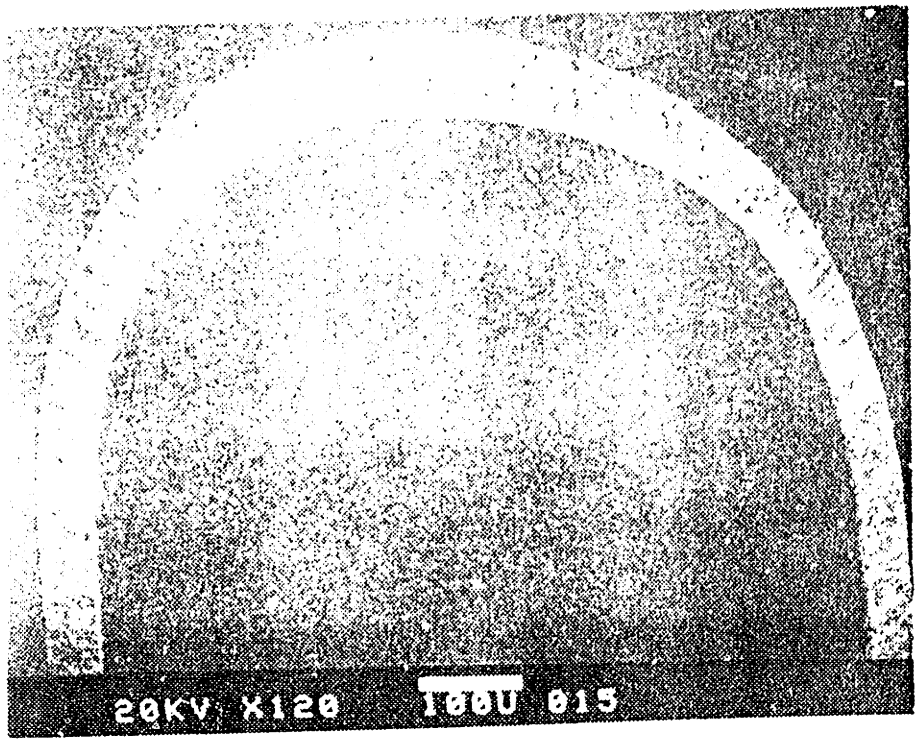

(a) Coating profile on the rim of the specimen

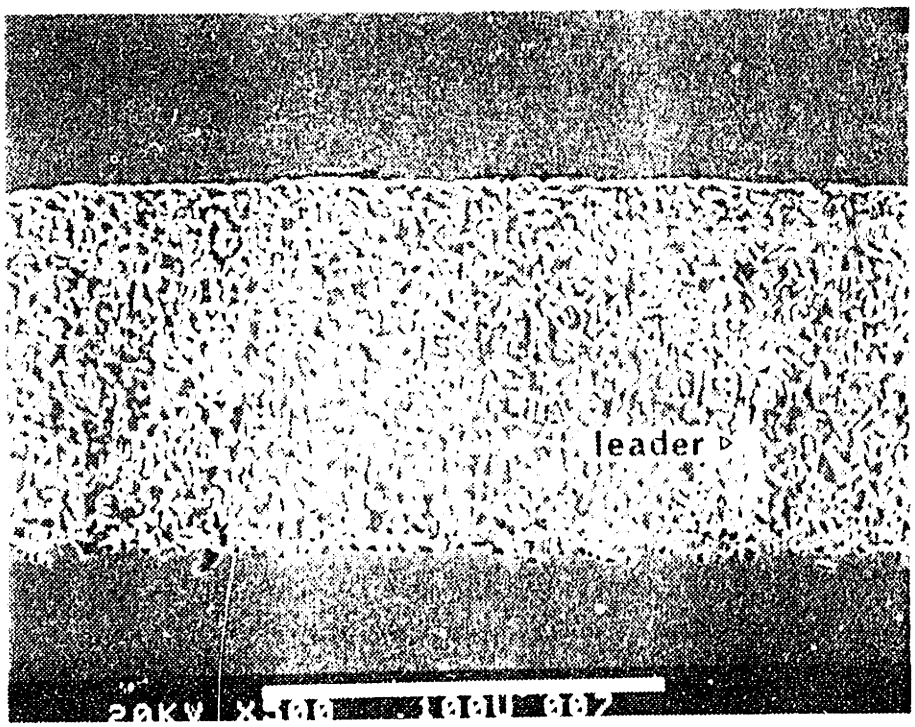

(b) Coating cross-sectional view with nickel plate at the top and substrate at the bottom

Fig. 2.3 SEM micrographs of EB-PVD NiCoCrAlY coating after peening and a diffusion bonding heat treatment of 4h in vacuum at 1079°C

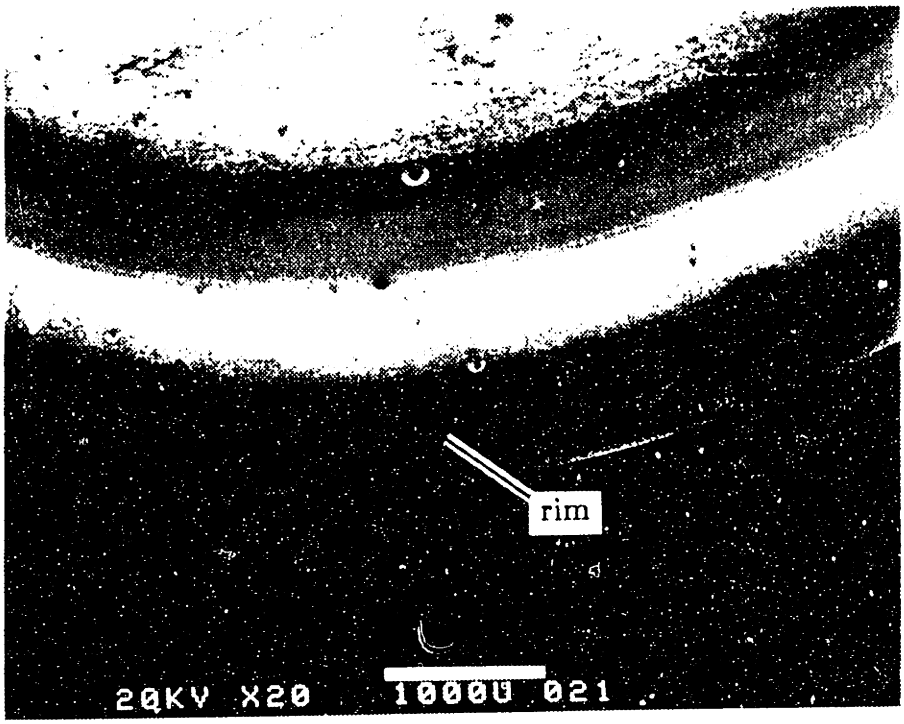

(a) Surface porosities on the rim of the specimen

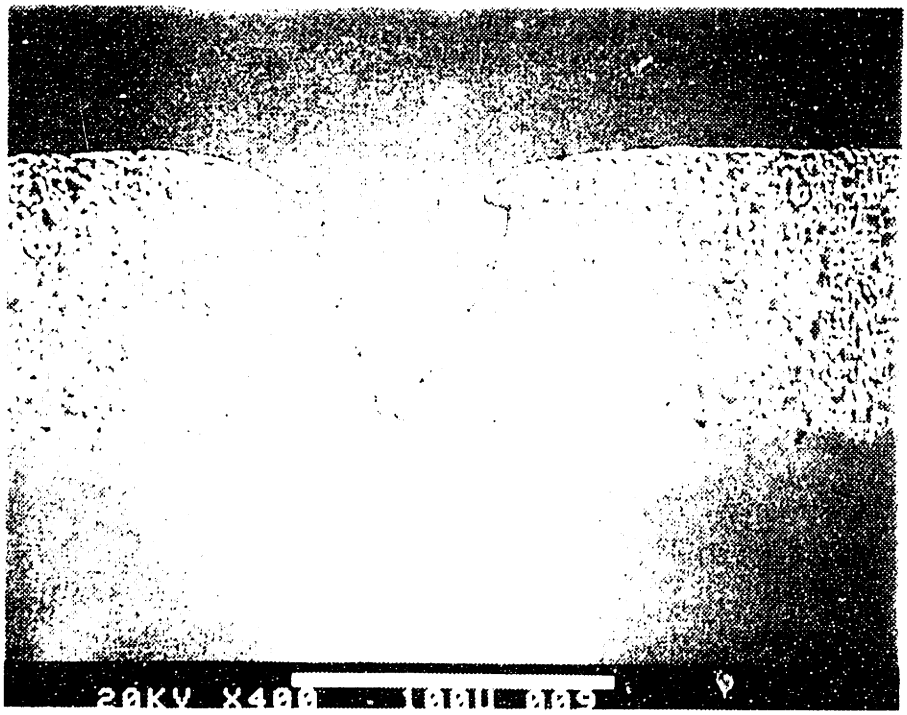

(b) Cross-sectional view of an average-size porosity

Fig. 2.4 Surface defects or pits formed during the EB-PVD process in NiCoCrAlY coating

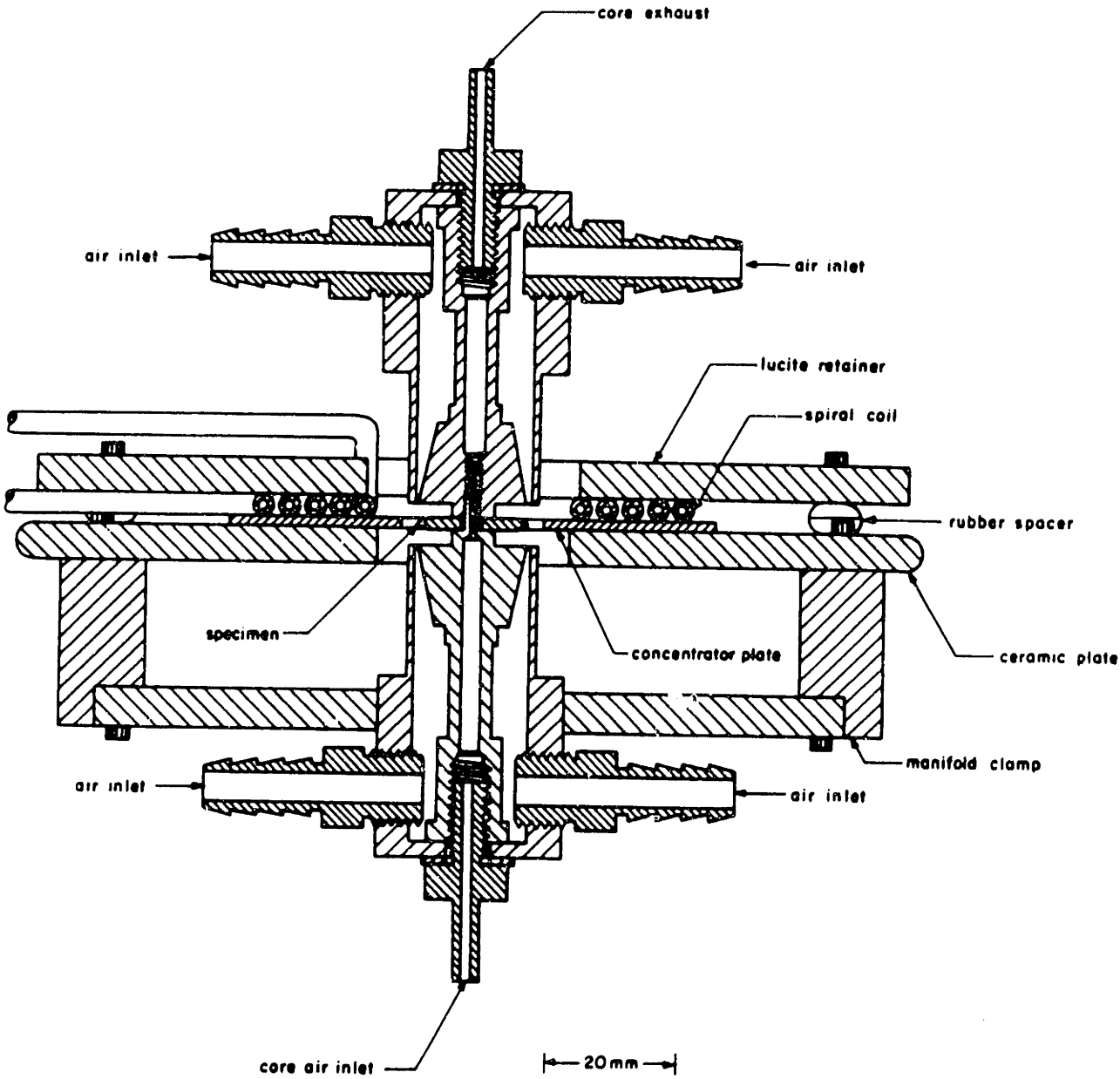

Fig. 2.5 Test apparatus to study thermal fatigue in air (from Holmes, 1986)

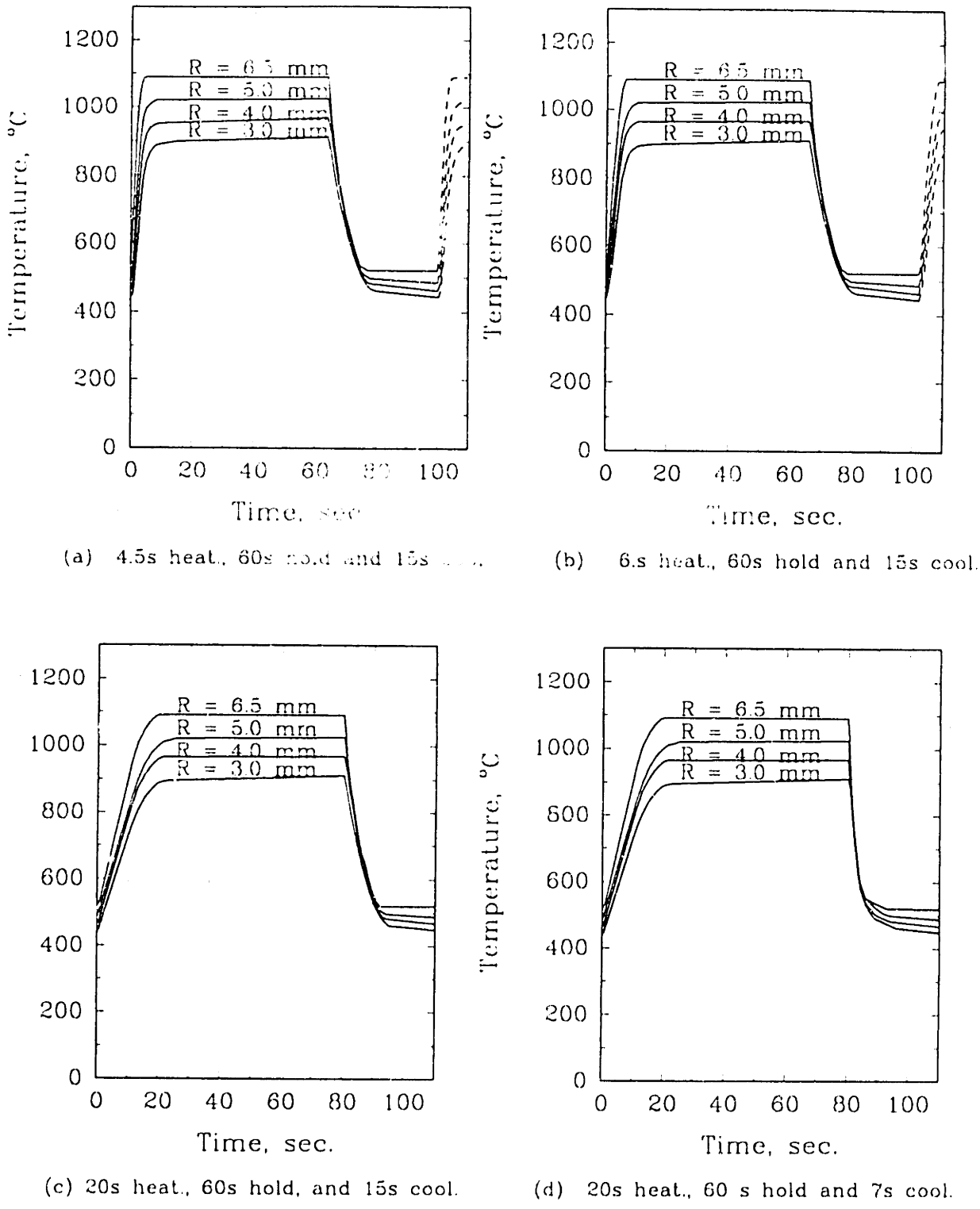

(a) 4.5s heat., 60s hold and 15s cool.

(b) 6.s heat., 60s hold and 15s cool.

(c) 20s heat., 60s hold, and 15s cool.

(d) 20s heat., 60 s hold and 7s cool.

Fig. 2.6 **Radial temperature histories in specimen when its periphery temperature is cycled from 520°C to 1090°C**

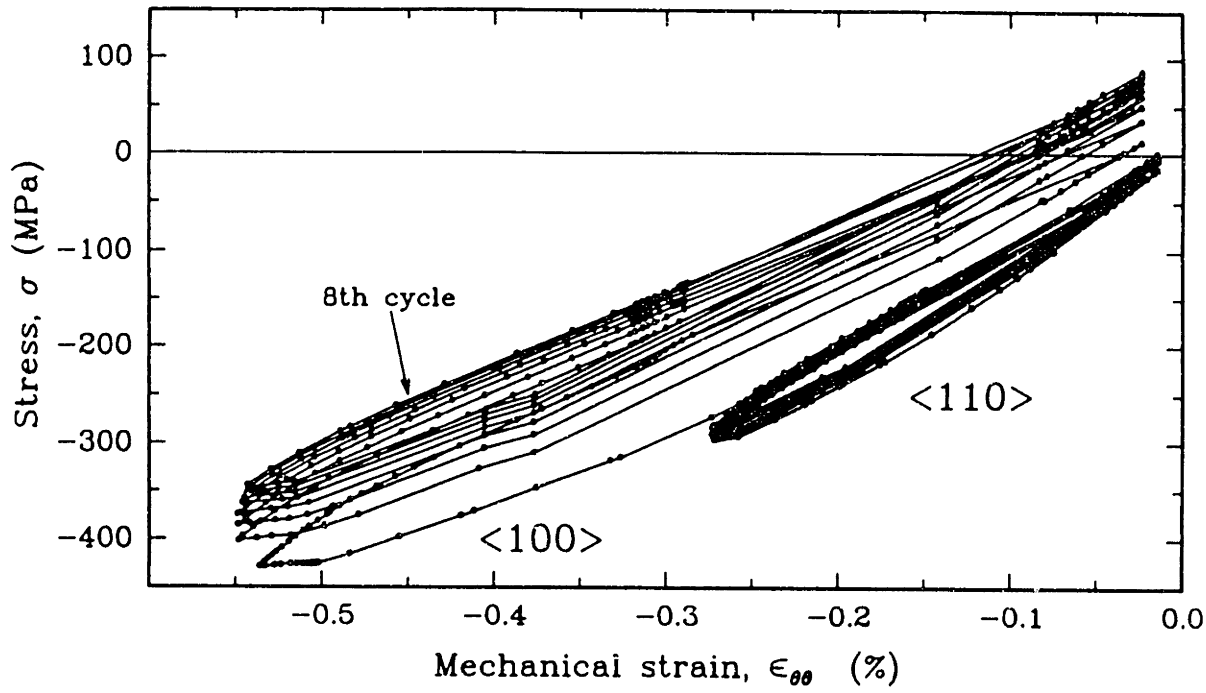

(a) Hysteresis loops for the γ–γ' anisotropic substrate

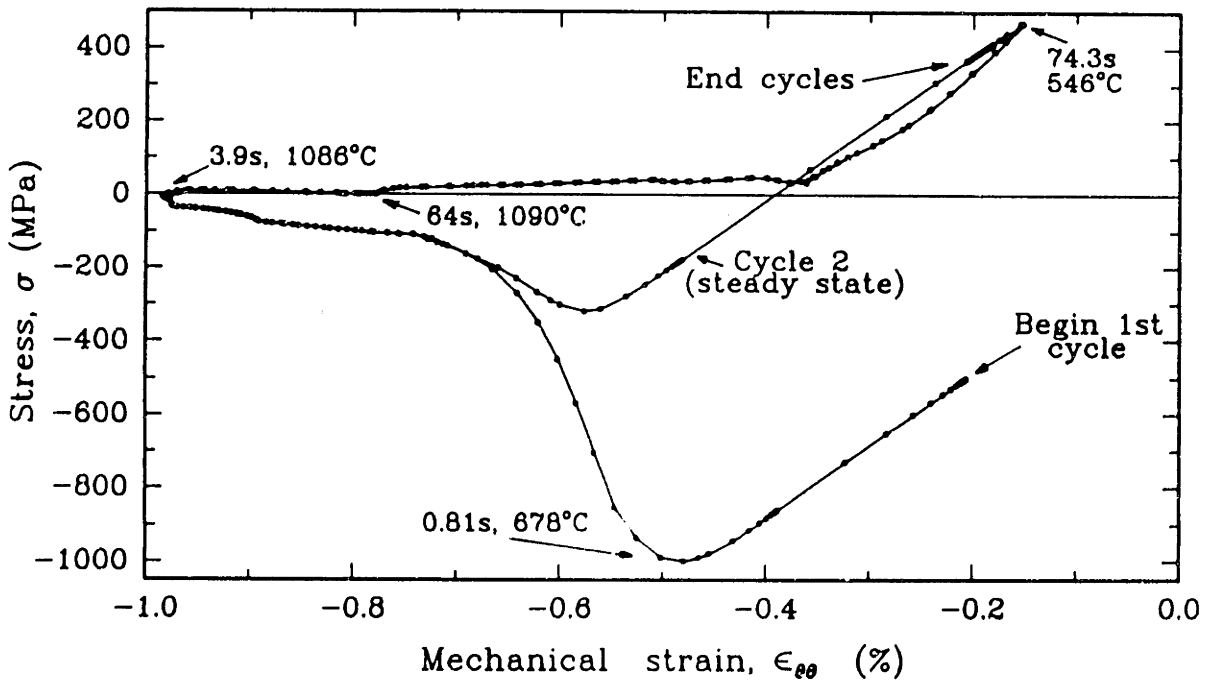

(b) Hysteresis loops for the NiCoCrAlY isotropic coating with imposed displacement from <100> substrate

Fig. 2.7 **Inelastic stress–strain histories for the 4.5s heating, 60s hold, and 15s cooling thermal history**

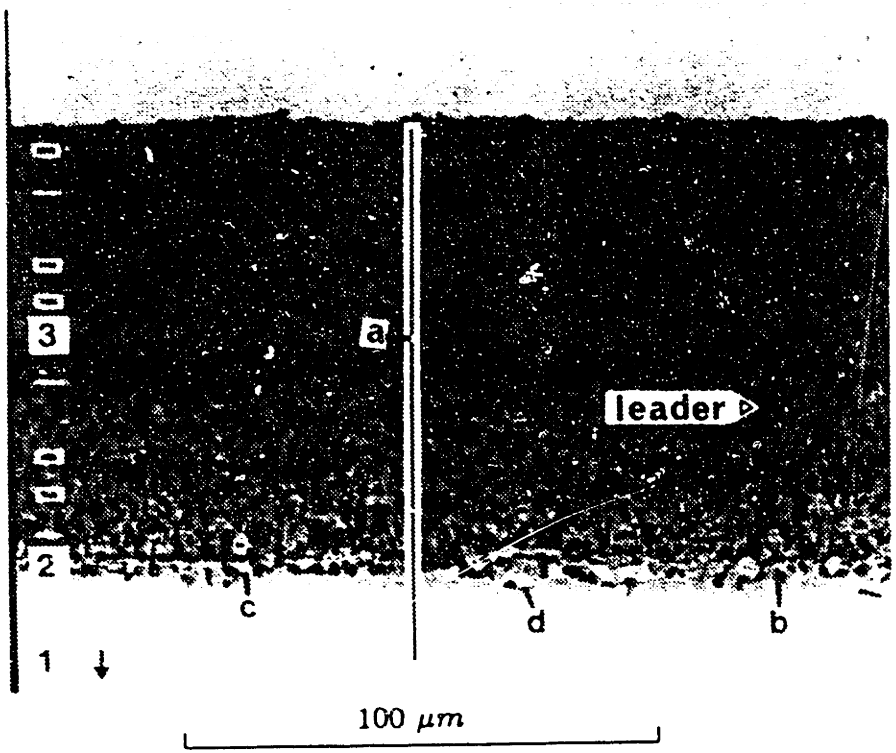

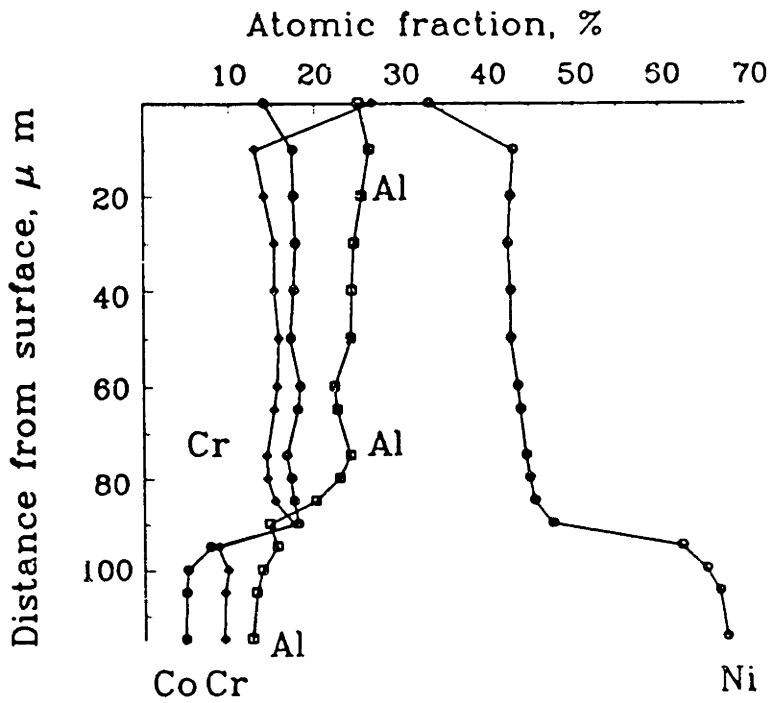

Point	Ni	Co	Cr	Al	Ti	Ta	Mo	W	Y
a	42.8	17.1	15.7	24.2	0.12	0.04	0.01	0.07	< 0.05
b	49.4	10.6	5.8	34.1	0.20	0.00	0.01	0.00	< 0.05
c	5.6	3.9	83.5	0.6	0.06	0.10	0.50	4.70	1.13
d	32.2	7.1	6.4	7.6	13.6	25.6	0.10	4.90	1.34

Fig. 2.8 Backscattered electron micrograph of the NiCoCrAlY coating after peening and diffusion bonding heat treatment, with results of microprobe analysis

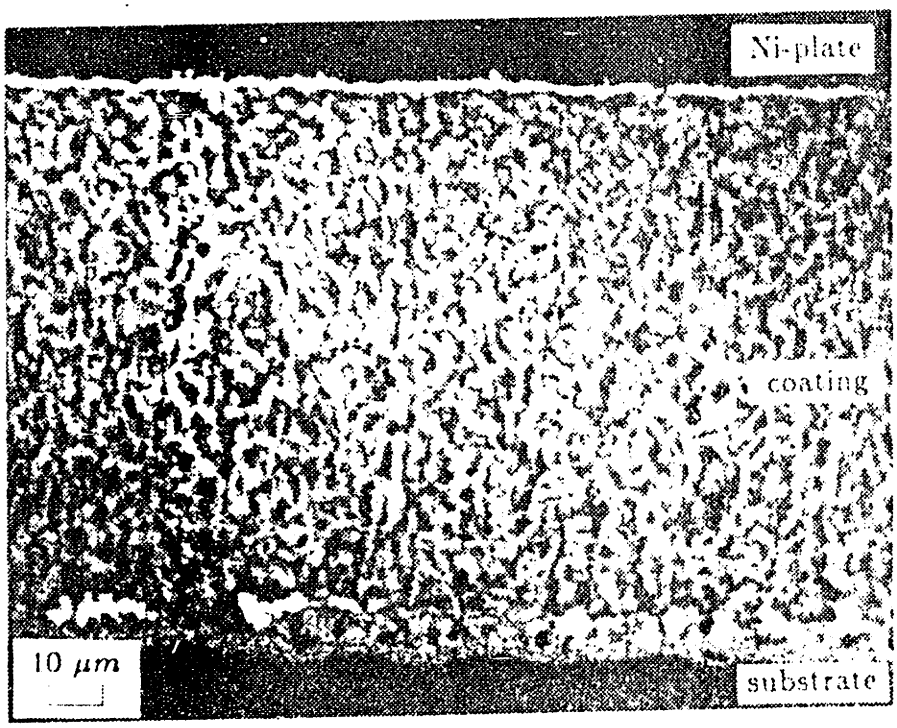

(a) Cr dot-map

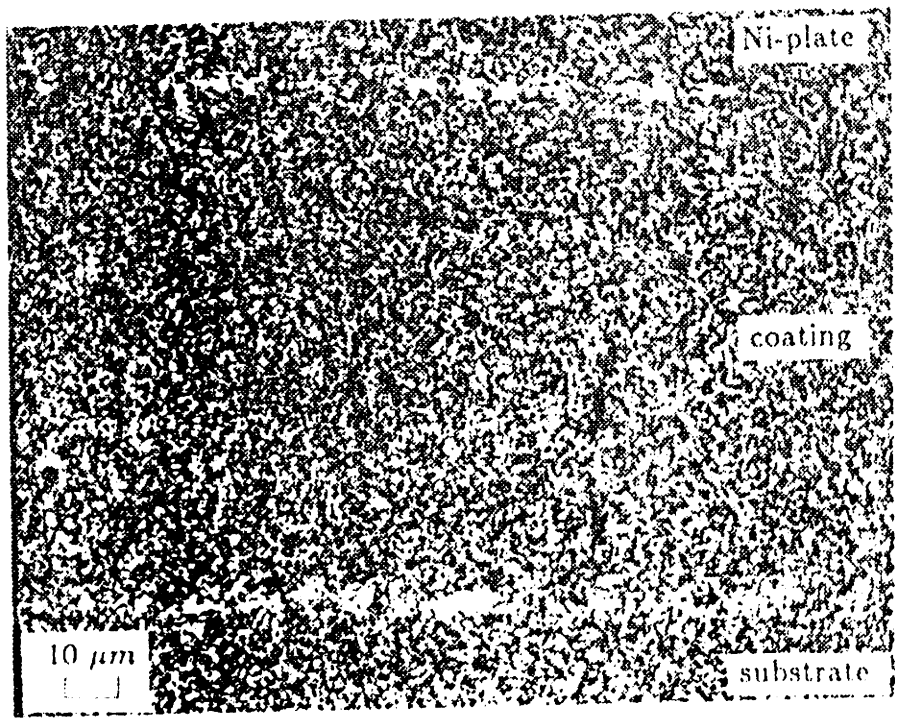

(b) Y dot-map

Fig. 2.9 Coating microprobe dot-maps of Cr and Y [illegible] section shown in Fig. 2.8)

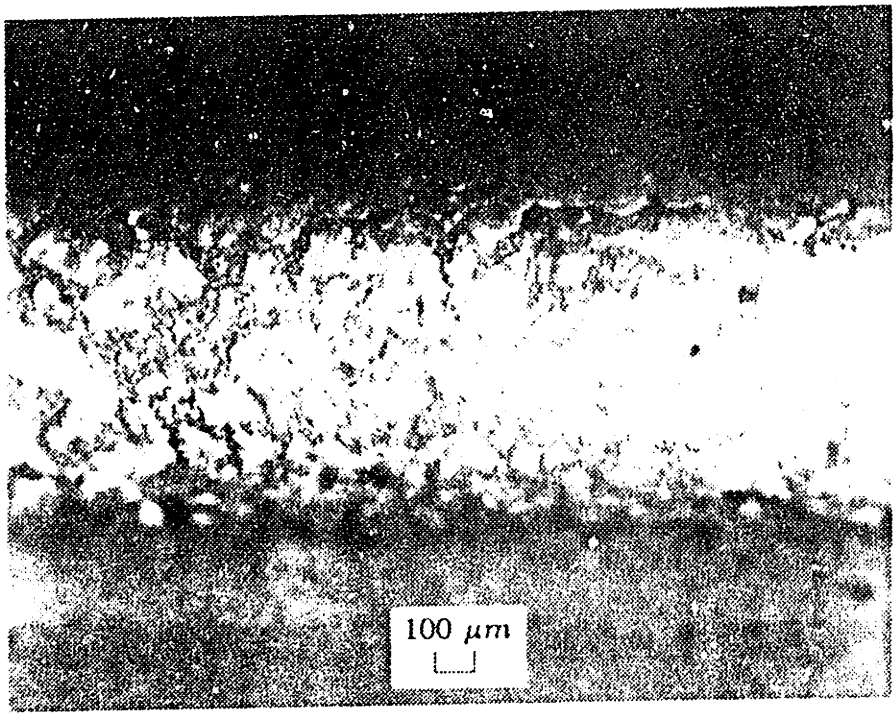

(a) Oxide spalling on the rim of the specimen

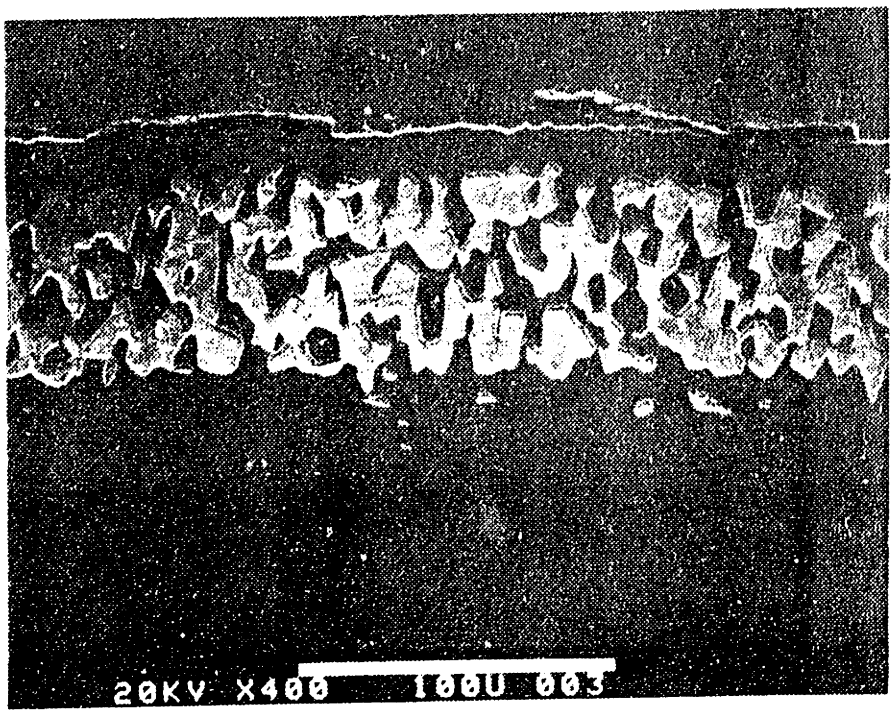

(b) Cross-sectional view of (a) showing coating and transition zone oxidation

[illegible] SEM micrograph of the coating after *isothermal* exposure [illegible] at 1090 °C

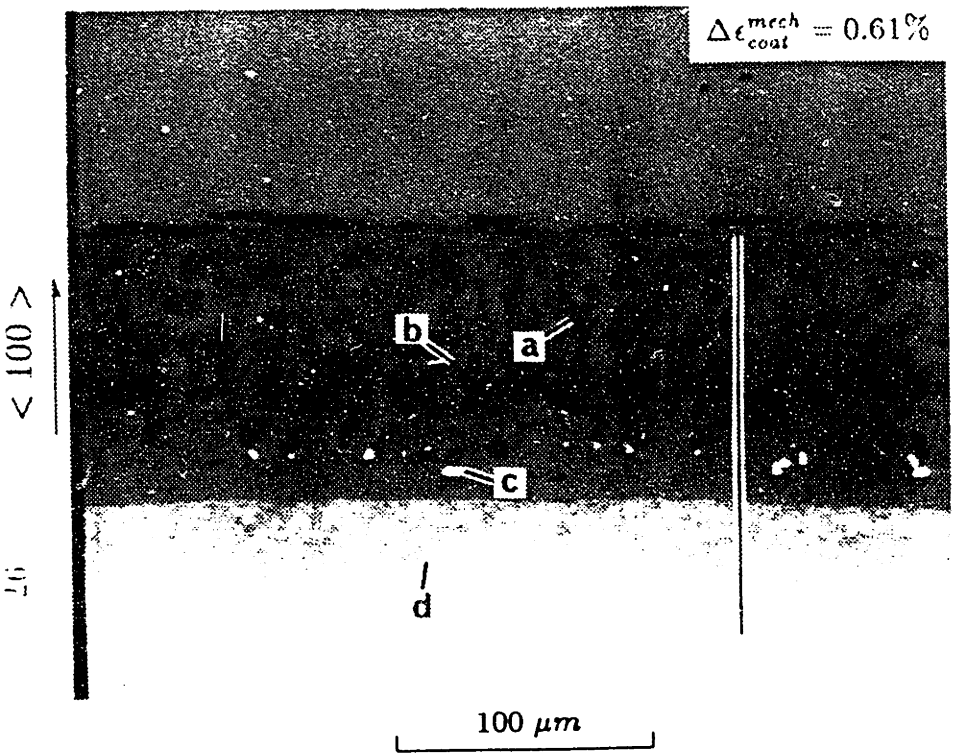

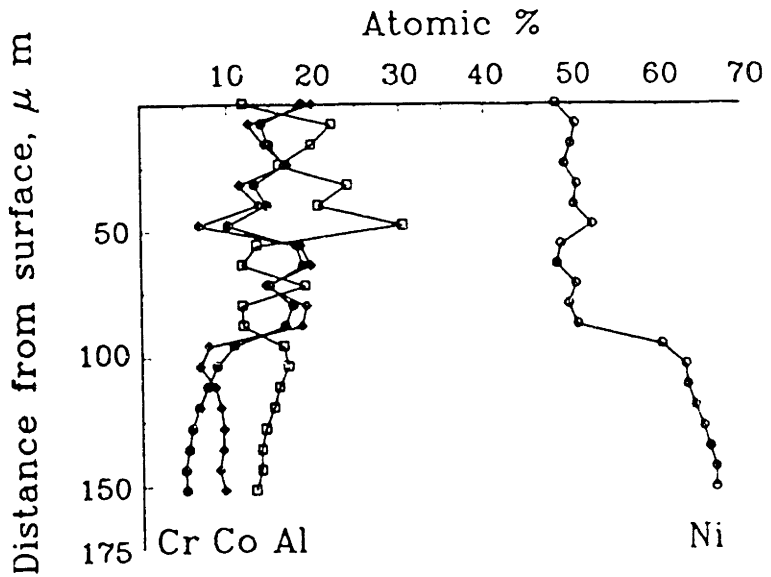

Point	Ni	Co	Cr	Al	Ti	Ta	Mo	W	Y
a	52.6	9.9	6.5	30.5	0.1	0.4	0.0	0.1	< 0.05
b	48.7	18.4	19.6	11.7	0.3	0.4	0.2	0.8	< 0.05
c	7.3	3.3	2.5	0.4	0.3	31.0	52.0	1.5	1.73
d	38.5	8.4	16.4	7.8	2.6	1.1	3.8	20.9	0.55

(a) after cyclic exposure to 20s heating – 15s cooling cycles

Fig. 2.11 **Backscattered electron micrograph of NiCoCrAlY coating with results of microprobe analysis**

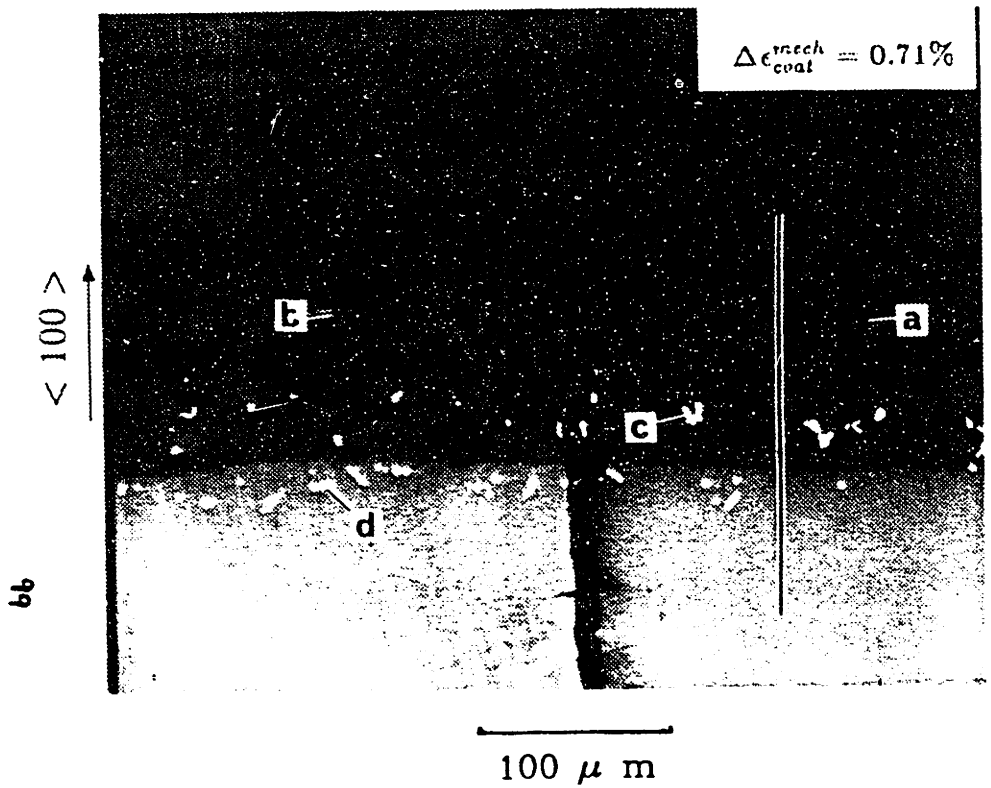

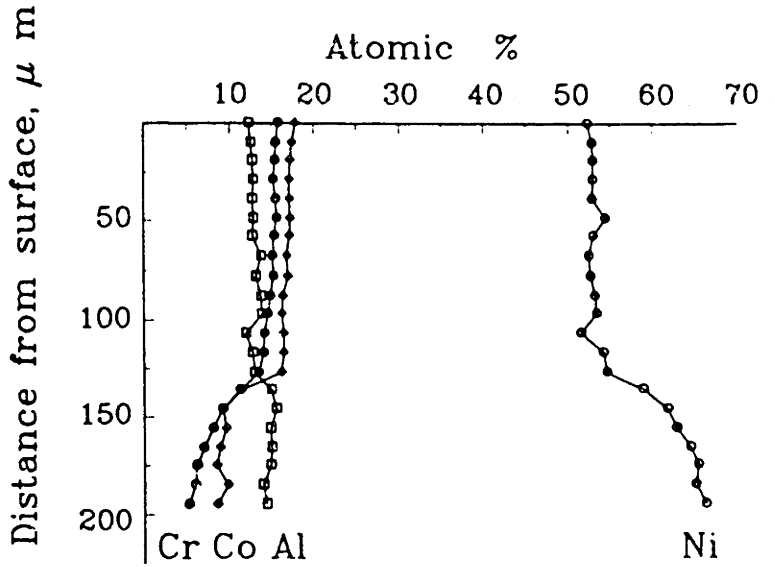

Point	Ni	Co	Cr	Al	Ti	Ta	Mo	W	Y
a	54.5	8.9	6.4	29.5	0.1	0.6	0.1	0.1	< 0.05
b	52.8	15.4	16.9	12.8	0.2	0.5	0.4	1.0	< 0.05
c	7.2	2.6	2.0	0.4	0.3	27.8	54.4	1.5	1.80
d	32.9	9.6	15.9	5.6	3.3	1.2	5.7	24.7	1.14

(b) after cyclic exposure to 6s heating – 15s cooling cycles

Fig. 2.11 continued

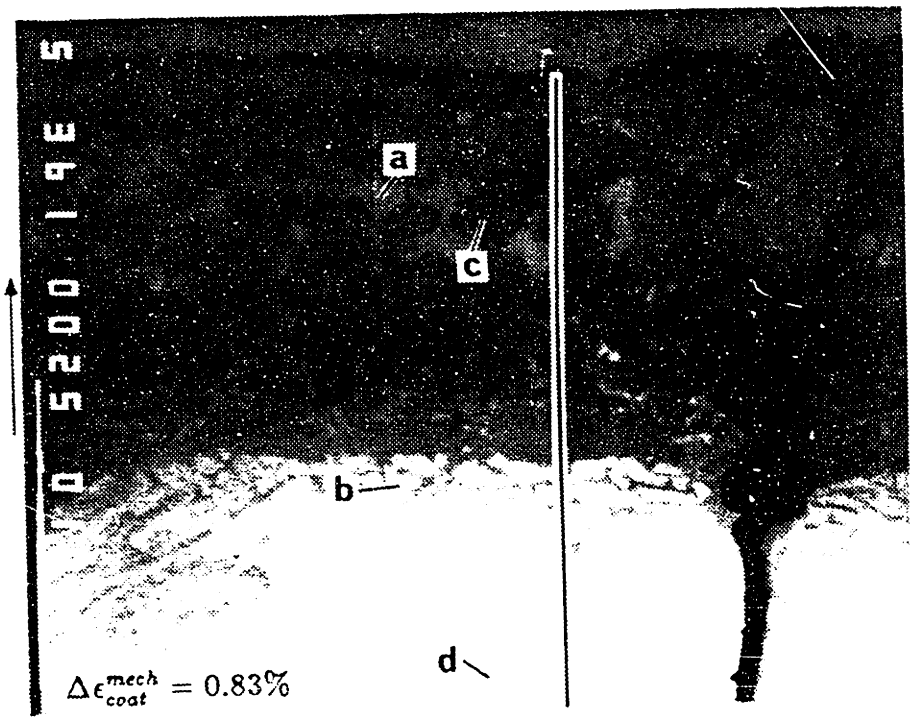

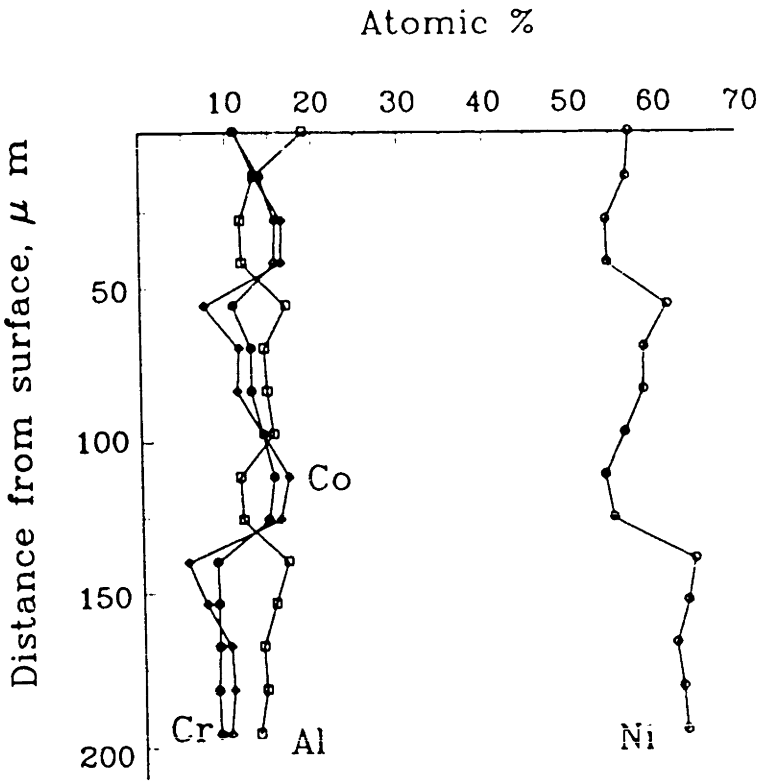

Point	Ni	Co	Cr	Al	Ti	Ta	Mo	W	Y
a	63.4	9.8	5.7	18.1	0.1	1.2	1.3	0.6	< 0.05
b	64.7	8.6	5.1	17.2	0.1	1.3	1.9	1.2	< 0.05
c	54.3	15.7	16.5	12.3	0.2	0.4	0.0	0.6	< 0.05
d	54.2	15.9	16.4	12.3	0.4	0.1	0.2	0.7	< 0.05

(c) after cyclic exposure to 4.5s heating – 15s cooling cycles

Fig. 2.11 continued

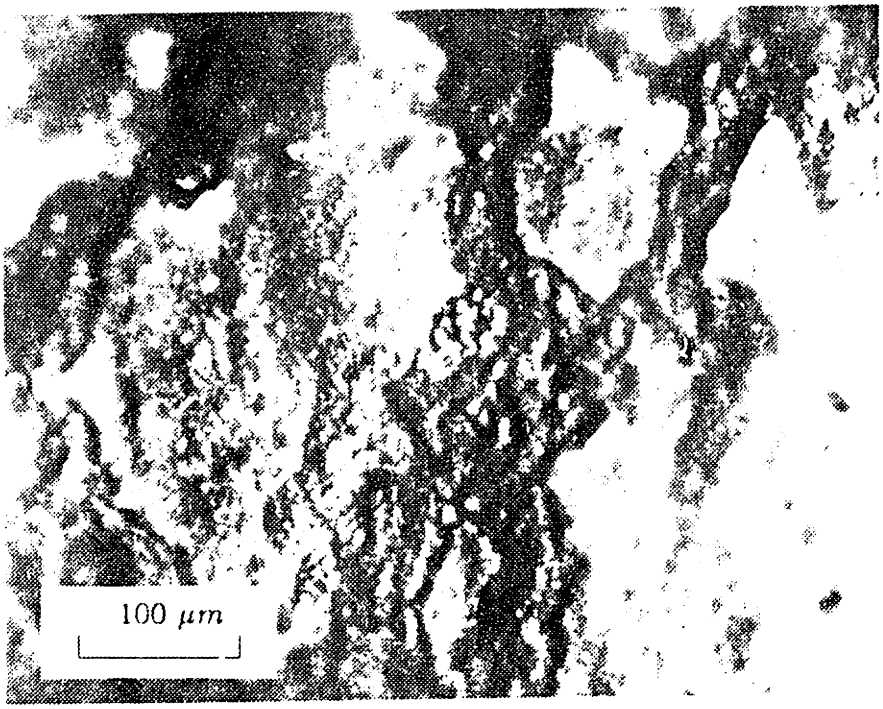

(a) Primary and secondary oxide scale on the coating surface

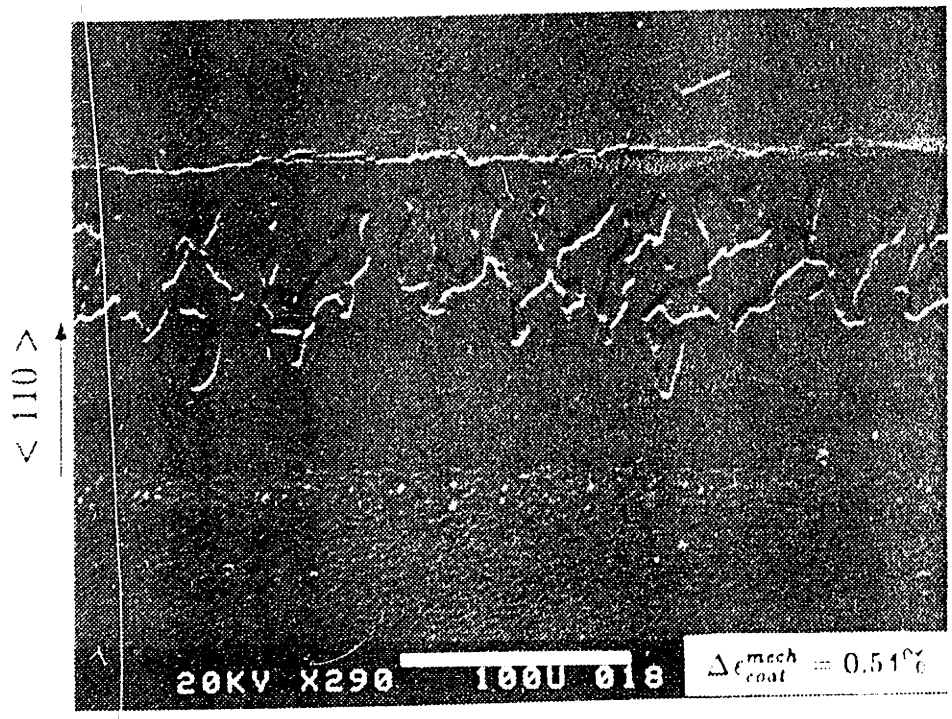

(b) Cross-sectional view of (a) showing substrate ($\gamma - \gamma'$), transition zone (γ), and NiAl depletion in coating

Fig. 2.12 Coating degradation after 6000 cycles of 6s heating - 15s cooling history

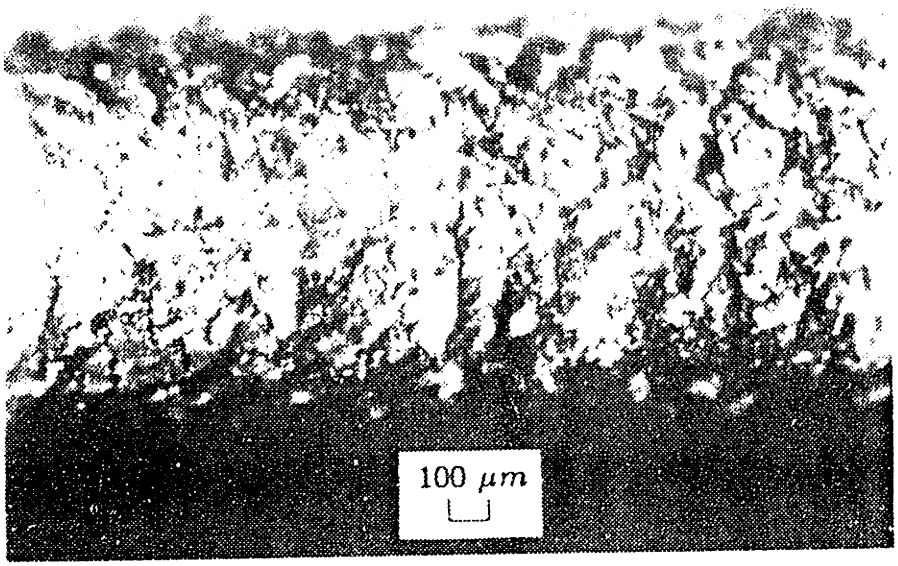

(a) Intermediate cracking and oxide spalling on specimen rim

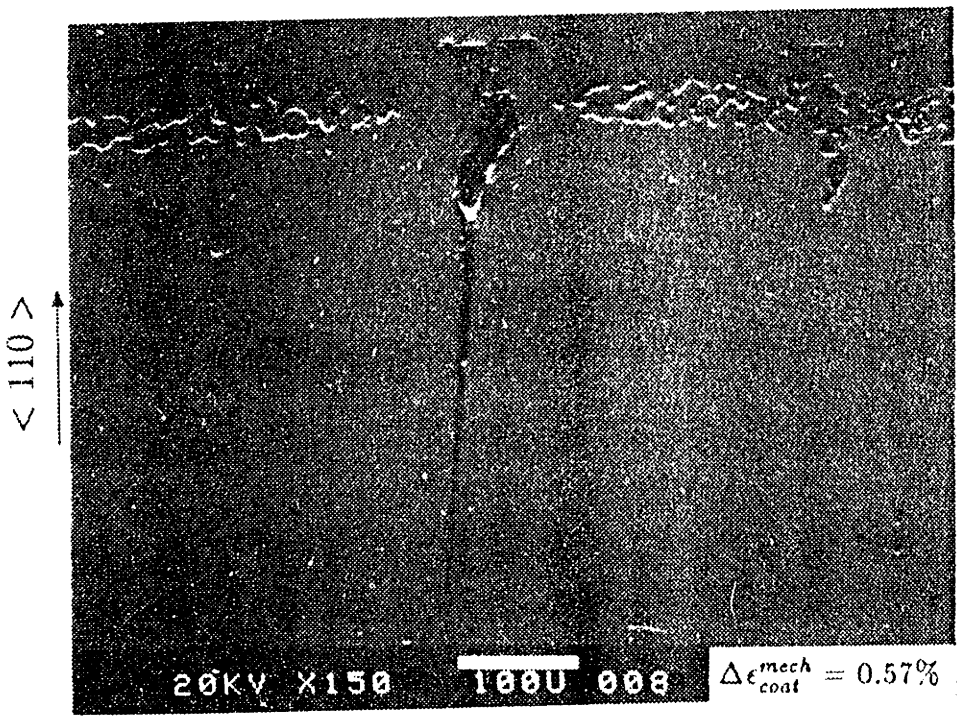

(b) Coating cross-section of (a) showing coating oxidation and crack propagation into the substrate

Fig. 2.13 Coating degradation after 6000 cycles of 1.5s heating - 15s cooling history

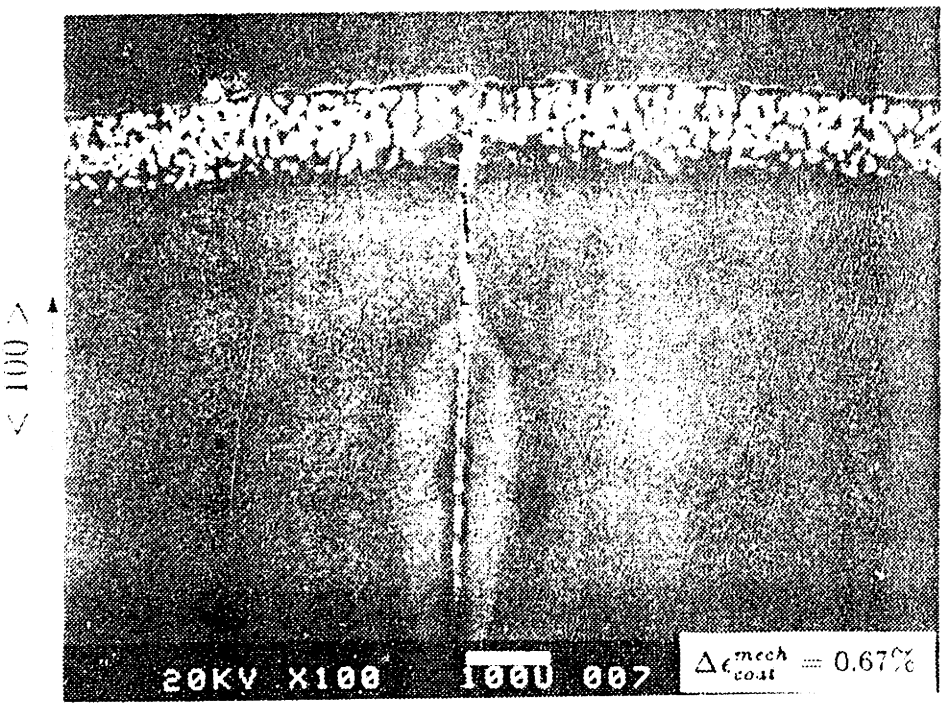

Fig. 2.14 Coating degradation after 6000 cycles of 20s heating - 7s forced cooling histories

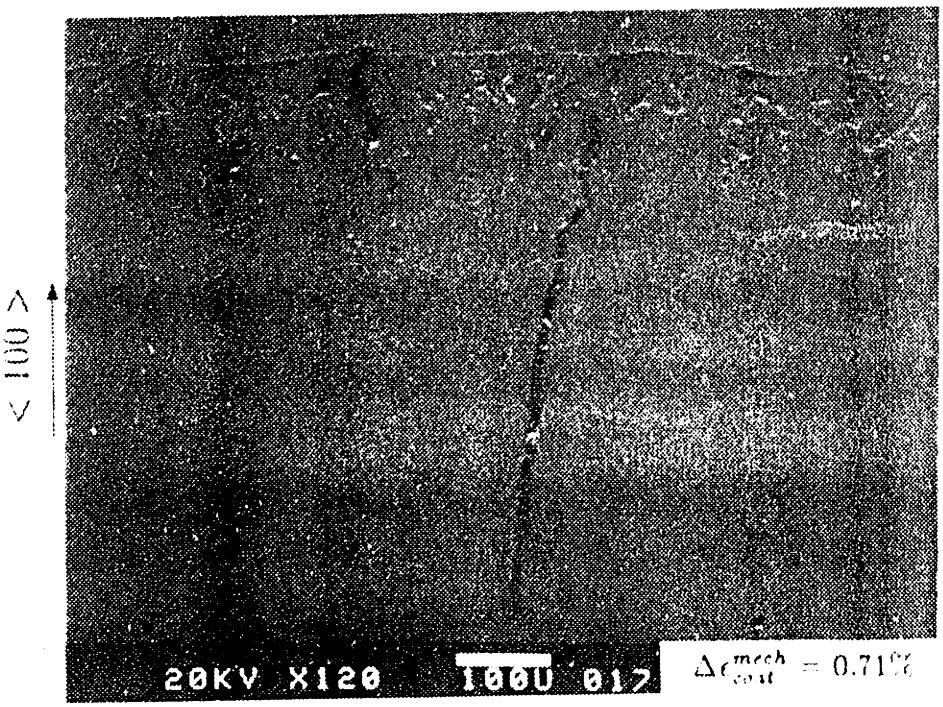

Fig. 2.15 Coating degradation after 6000 cycles of 6s heating - 15s cooling histories

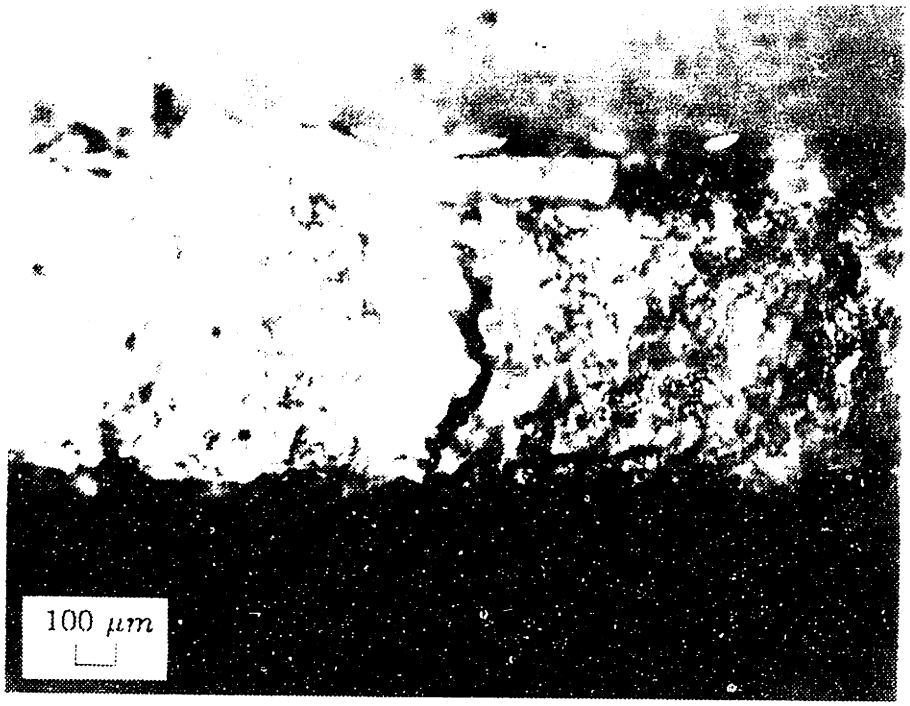

(a) Cracking and severe oxide spalling on specimen rim.

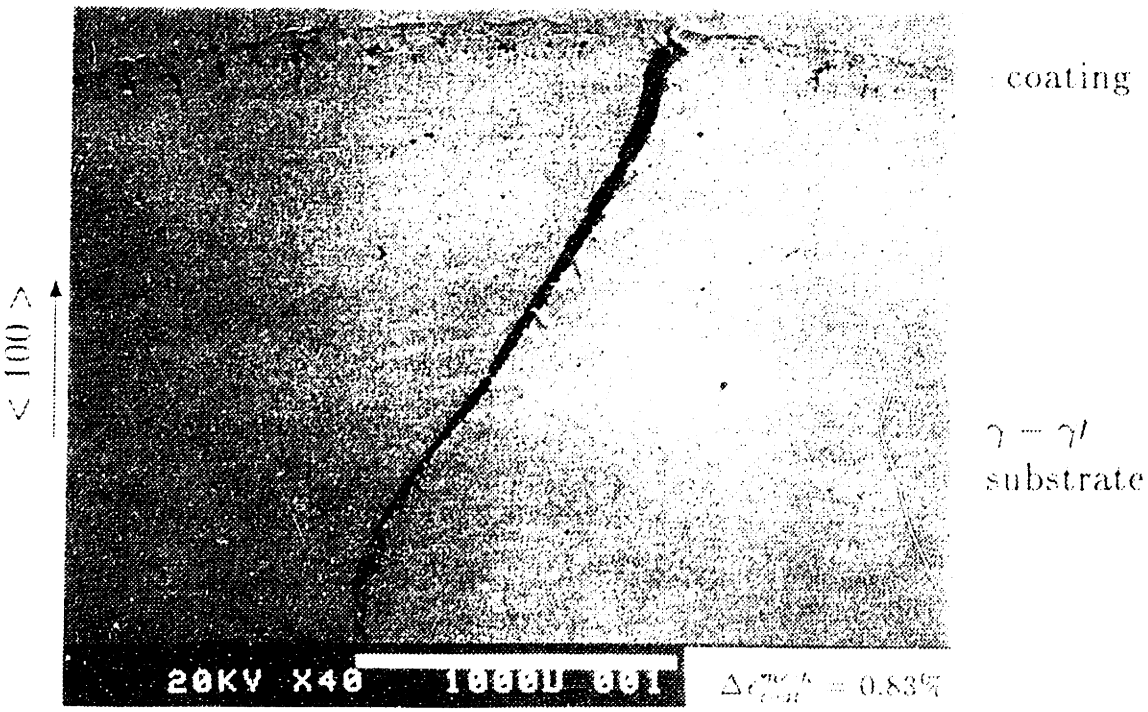

(b) Coating cross-section of (a) with large crack propagating into the substrate

Fig. 2.16 Coating degradation after 6000 cycles of 1.5s heating - 15s cooling history

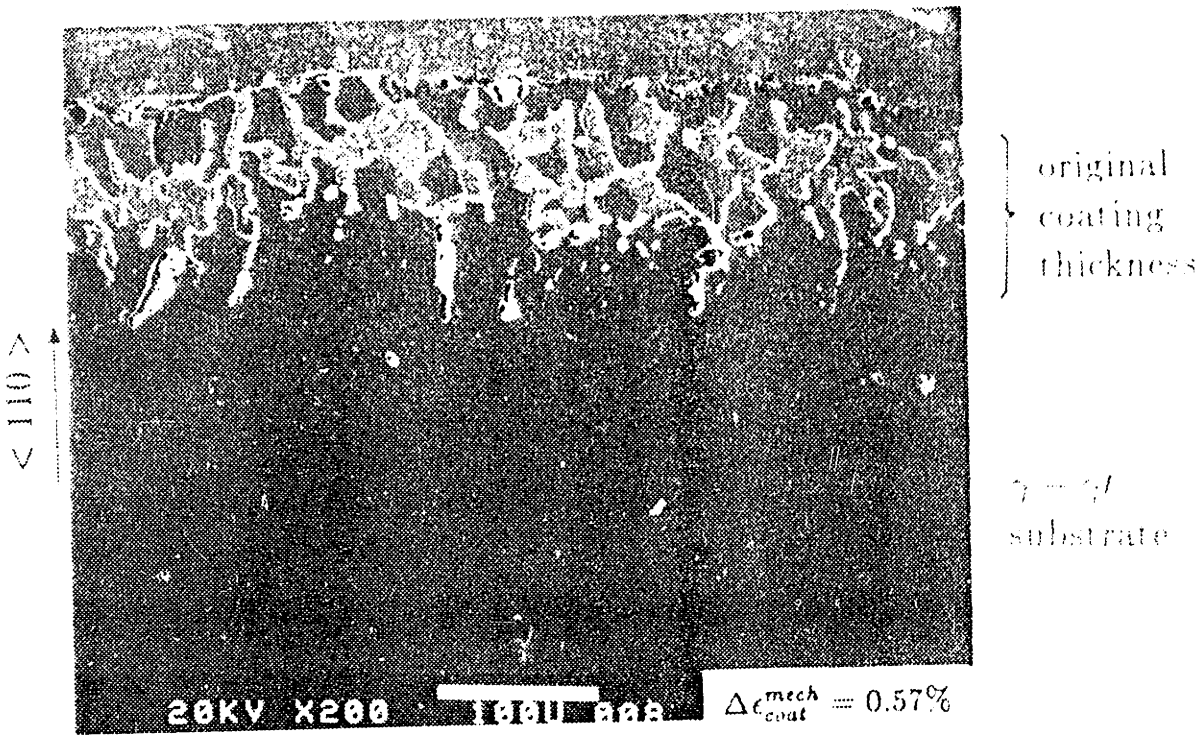

(a) Small strain range

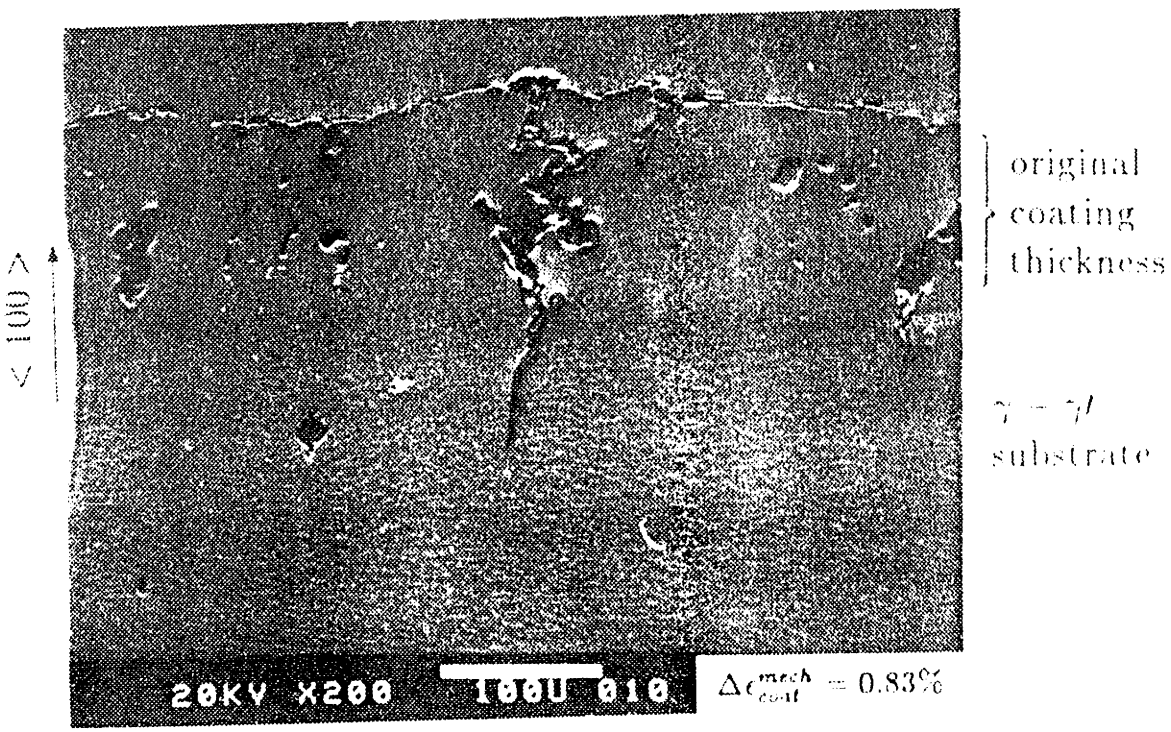

(b) Large strain range

Fig. 2.17 Stages of interface (Kirkendall) void development

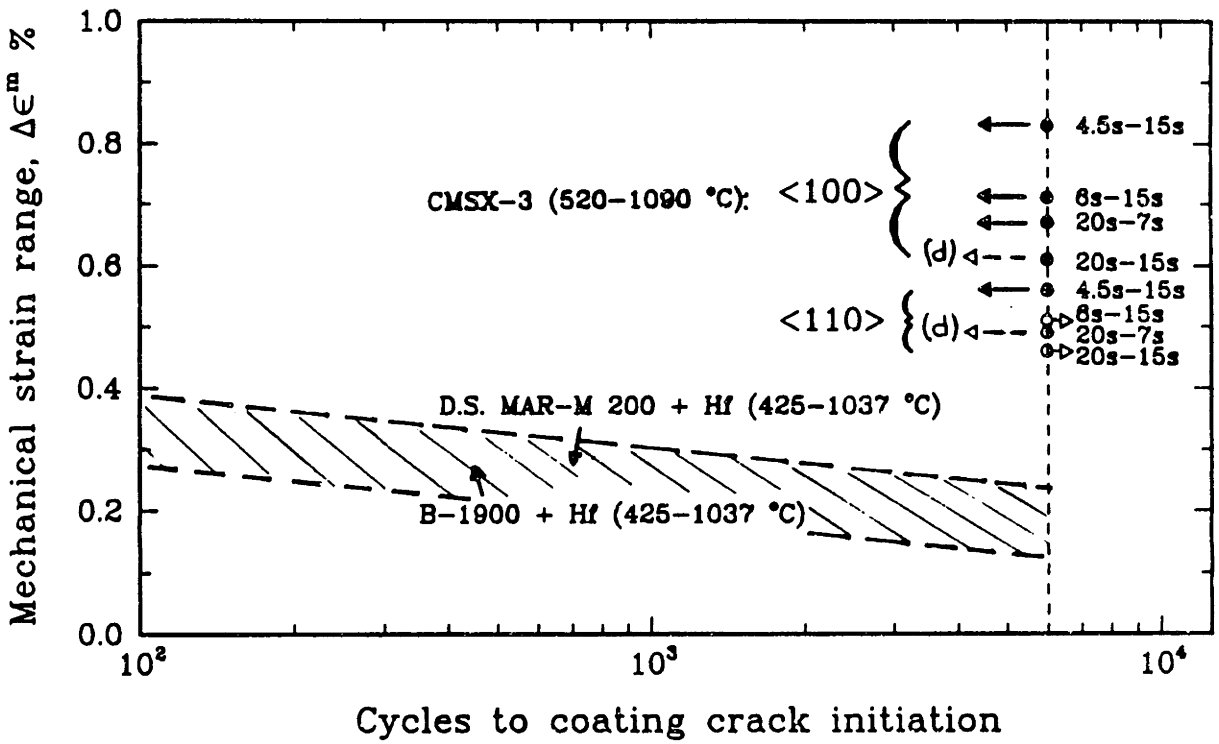

(d) indicates cracks which originated from surface defects or pits

Fig. 2.18 **Crack initiation in a NiCoCrAlY coating on different substrates**

Appendix 2.A Oxide Layer Stress at a Given Temperature

2.A.1 Plane stress analysis of the oxide layer

Consider a plane stress model of the thin oxide layer such that the through-the-thickness stress component is $\sigma_{rr} = 0$, and the in-plane normal stresses $\sigma_{\theta\theta}$, $\sigma_{zz} \neq 0$. The elastic strain components, expressed in terms of the oxide Poisson's ratio ν and elastic modulus E at a given temperature, are

$$\epsilon^e_{\theta\theta} = \frac{\sigma_{\theta\theta}}{E} - \nu \frac{\sigma_{zz}}{E}, \tag{2.A.1}$$

$$\epsilon^e_{zz} = \frac{\sigma_{zz}}{E} - \nu \frac{\sigma_{\theta\theta}}{E}, \tag{2.A.2}$$

$$\epsilon^e_{rr} = -\frac{\nu}{E}(\sigma_{zz} + \sigma_{\theta\theta}). \tag{2.A.3}$$

Solve for σ_{zz} in Eq. 2.A.2 and substitute in Eq. 2.A.1. Then,

$$\epsilon^e_{\theta\theta} = \frac{\sigma_{\theta\theta}}{E} - \nu \left(\epsilon^e_{zz} + \nu \frac{\sigma_{\theta\theta}}{E}\right). \tag{2.A.4}$$

The elastic strains in Eq. 2.A.4 can, in turn, be given as a function of the total and thermal components,

$$\begin{aligned} \epsilon^e_{\theta\theta} &= \epsilon^{total}_{\theta\theta} - \epsilon^{th}, \\ \epsilon^e_{zz} &= \epsilon^{total}_{zz} - \epsilon^{th}. \end{aligned} \tag{2.A.5}$$

(Due to the isotropy of the oxide thermal expansion coefficient, $\epsilon^{th}_{zz} = \epsilon^{th}_{\theta\theta} = \epsilon^{th}$). Finally, substituting Eq. 2.A.5 into Eq. 2.A.4 and solving for $\sigma_{\theta\theta}$ leaves:

$$\sigma_{\theta\theta} = \frac{E}{(1-\nu^2)}\left[\epsilon^{total}_{\theta\theta} + \nu\,\epsilon^{total}_{zz} - (1+\nu)\,\epsilon^{th}\right]. \tag{2.A.6}$$

(2.A.7)

2.A.2 Oxide thermal strain

Define the oxide thermal strain, ϵ^{th}, due to a drop in temperature from $T_{hld}(= 1090\,^{\circ}C)$ to a temperature T in terms of,

$l_{T_{hld}} \rightarrow$ specimen length at T_{hld} ,

$l_T \rightarrow$ specimen length at T ,

as,

$$\epsilon^{th} = \frac{l_T - l_{T_{hld}}}{l_{T_{hld}}} . \tag{2.A.8}$$

Let T_0 be a reference temperature (usually room temperature) at which the specimen reference length l_0 is measured. Then, the average coefficient of thermal expansion at the temperature T is defined as:

$$\alpha_T = \frac{(l_T - l_0)}{l_0} \frac{1}{(T - T_0)} . \tag{2.A.9}$$

Solving for l_T in Eq. 2.A.9,

$$l_T = l_0 \left[1 + \alpha_T (T - T_0)\right] , \tag{2.A.10}$$

and making $T = T_{hld}$ in Eq. 2.A.10,

$$l_{T_{hld}} = l_0 \left[1 + \alpha_{T_{hld}} (T_{hld} - T_0)\right] . \tag{2.A.11}$$

Substituting Eqs. 2.A.10 and 2.A.11 into Eq. 2.A.8 yields

$$\epsilon^{th} = \frac{\alpha_T (T - T_0) - \alpha_{T_{hld}} (T_{hld} - T_0)}{1 + \alpha_{T_{hld}} (T_{hld} - T_0)} . \tag{2.A.12}$$

Chapter 3

Mechanisms of Void-Induced Cracking in a High Temperature Protective Coating

Abstract

The mechanisms of nucleation and growth of microvoids which nucleate at the interface of NiCoCrAlY overlay coatings and monocrystalline Ni-base superalloys have been described. Interface voids, which in this work were associated with coating strain ranges higher than 0.51% at normal cooling rates, form due to vacancies clustering together under the influence of a tensile stress (applied or diffusion induced), and nucleate at junctions between γ grain boundaries and β grains or other hard phases. These voids grow by diffusion or localized plastic flow, depending on the grain size, follow the receding NiAl (β) grains of the coating and eventually open up to the coating surface.

3.1 Introduction

The work presented in the previous chapter showed that under certain loading conditions, namely for mechanical strain ranges larger than 0.51 % and normal cooling rates, the observed cracks appeared to have originated from voids located at

the coating/substrate interface. In this chapter, the mechanisms of nucleation and growth of these interface voids will be investigated further.

After a description of different crack initiation mechanisms common to high temperature protective coatings, the relation between concentration profiles and vacancy supersaturation is described. The mechanism of void nucleation from vacancy clusters and stable growth into macrovoids is then discussed.

3.2 Crack Initiation Mechanisms: Prior Observations.

Perhaps the most widely reported mechanism is coating cracking due to oxide breakdown (cracking or spalling). The failure of the protective oxide scale, often referred as breakaway oxidation (Nesbitt, 1982) results in a higher rate of Al consumption from the coating. In general, oxide breakdown can be associated not only with imposed cyclic strains and tensile stresses, but also with the oxide composition per se (Wallwork et al., 1971). The optimum conditions for oxidation resistance occur when a compact protective Al_2O_3 forms on the coating surface. However, when the oxide deviates from stoichiometric Al_2O_3, as on NiCoCrAlY, it may form simultaneously with less protective oxides, such as Cr_2O_3 or NiO (Goward, 1979). Its overall mechanical and diffusion properties are affected, becoming more susceptible to cracking (Wallwork et al., 1971); as a contrast, c.f. the thicker stoichiometric oxide that forms on an aluminide (NiAl) coating (Holmes et. al., 1987). In the limit, when the Al content in the coating decreases below a certain level (e.g. from 28 to 8 at.% at 1100°C depending on the Cr content of the alloy), the coating no longer forms alumina (Barret and Lowell, 1978). An increase in oxide spalling with increasing cooling rates was reported by Lowell et al. (1983) and Holmes (1987). Finally, scale cracking could presumably lead to coating cracking by causing localized oxidation due to

highly localized cyclic deformation on the coating surface (Coffin, 1963). Holmes also observed that when the cooling rate was increased (to 520°C / 8s), not only crack-like defects extended from the coating surface into the substrate, but also that cracks appeared to nucleate within the (aluminide) coating and its diffusion zone.

Another coating failure under thermal fatigue is the formation of surface waviness or *scalloping*, which can eventually penetrate the coating, as observed by Holmes and McClintock (1987) on an aluminide coating.

Coating deposition processes can also play an important role in the failure mechanism. Busso (1987) tested a sputtered-PVD NiCoCrAlY coating which showed a high density of columnar voids not successfully closed by glass pinning (Fig. 3.1a). When the coating was subjected to strain ranges higher than 0.31 %, it degraded by crack propagation from the bottom of the columnar voids, as well as by transforming the coating and nearby substrate into a single γ phase, as shown in Fig. 3.1b.

3.3 The Mechanism of Void-induced Cracking

3.3.1 Vacancy supersaturation due to interdiffusion.

Consider the concentration profiles resulting from interdiffusion across the coating - substrate interface, as shown schematically in Fig. 3.2a for Ni and Al (with others elements omitted for simplicity).

Vacancy supersaturation in the coating-substrate interface region is possible due to the Kirkendall effect: migration through a lattice of a section (marked by a surface scratch, for example) due to an inequality in atom fluxes across the section, which gives rise to an equal and opposite vacancy flux. At the interface, the diffusion of Ni to the coating occurs at a greater rate than the migration of Al to the substrate due to its higher diffusivity (Janssen, 1973), and to its higher concentration gradient (see Fig. 3.2a). The interface will therefore move into the original substrate.

The element fluxes in Fig. 3.2a could in principle be determined from the phenomenological description of multi-component diffusion based on Onsager's formulation of Fick's law extended to ternary system diffusion (Shewmon, 1963). The equation which relates the flux J_i of element i, to its concentration gradient $\partial C_i/\partial x$ is given, when applied to components 1 and 2 in a ternary system in one dimension in which component k represents the solvent, in terms of the direct diffusion coefficients, D^k_{ii}, D^k_{jj}, and the indirect diffusion coefficients, D^k_{ij}, D^k_{ji}:

$$J^k_i = -\sum_{j=1}^{2} D^k_{ij} \frac{\partial C_i}{\partial x} \qquad (i = 1 \ to \ 2) \tag{3.1}$$

More approximately, the fluxes of Al and Ni can be determined from the planar description of a one-dimensional diffusion problem in a binary system, where the possibility of a flux of vacancies (due to Kirkendall diffusion) is allowed (Shewmon, 1963). In addition to gradients in chemical potentials of Al and Ni across the interface (associated with their concentration gradients) there is also a corresponding difference in vacancy chemical potential due to a deviation of vacancy concentration from its equilibrium value. Then for an isobaric and isothermal system, the fluxes of Al (J_{Al}) and Ni (J_{Ni}) along the diffusion path are given in terms of the diffusivities and concentrations of Ni and Al, D_{Ni}, D_{Al}, C_{Ni}, C_{Al}, and of the chemical potentials of Ni, Al, and vacancies, $\mu_{Ni}, \mu_{Al}, \mu_v$ (Anthony, 1969):

$$J_{Al} = -\frac{C_{Al} D_{Al}}{kT} \frac{\partial(\mu_{Al} - \mu_v)}{\partial x}$$

$$J_{Ni} = -\frac{C_{Ni} D_{Ni}}{kT} \frac{\partial(\mu_{Ni} - \mu_v)}{\partial x} \tag{3.2}$$

For vacancy controlled diffusion, the vacancy flux J_v across a section is the difference between J_{Ni} and J_{Al}: (e.g. Fig. 3.2b):

$$-J_v = J_{Ni} + J_{Al} \tag{3.3}$$

With a positive gradient of vacancy flux, e.g. on the coating side of the interface in Fig. 3.2c, the concentration between two sections dx apart will tend to decrease with time, $dC_v/dt < 0$, due to the net outflow of vacancies. This decrease will be partly offset by the generation of vacancies within this region, at N_S vacancy sources per unit volume, increasing the vacancy concentration at the rate $N_S\, dN_v/dt$:

$$\frac{dC_v}{dt} - N_S \frac{dN_v}{dt} = -\frac{\partial J_v}{\partial x} = \frac{\partial J_{Ni}}{\partial x} + \frac{\partial J_{Al}}{\partial x} \tag{3.4}$$

For example, on the substrate side of the interface, the flux gradient is negative. If the vacancy concentration is initially in equilibrium there is no net activity from vacancy sources and sinks ($dN_v/dt = 0$). The negative flux gradient initially gives a corresponding increase in the vacancy concentration, $dC_v/dt > 0$. As C_v increases from its equilibrium value, vacancies begin to condense at the sinks according to an equation of the form

$$\frac{dN_v}{dt} = -F\,(C_v - C_{vo}) \tag{3.5}$$

where C_{vo} is the vacancy concentration at equilibrium and F is a coefficient which depends on temperature and the nature of sinks and sources (e.g. dislocation density, grain size). As the vacancy concentration increases, a steady state may be reached, which is found by setting $dCv/dt = 0$ in Eq. 3.4 and introducing Eq. 3.5:

$$C_v - C_{vo} = -\frac{1}{N_S F}\frac{\partial J_v}{\partial x} \tag{3.6}$$

Balluffi (1954) reported that the excess vacancy concentration or supersaturation $(C_v - C_{vo})$ for void formation due to Kirkendall diffusion (no applied stresses) must be about $0.01 \times C_{vo}$. Values of N_S and F are not known. Among those who have observed Kirkendall voids, as noted above, Gedwill et al. (1982) found voids at the interface of a NiCrCoAlY coating with the substrate having the lower of two Al contents (which resulted in a more negative vacancy gradient $\partial J_v/\partial x$ in Eq. 3.6).

3.3.2 Mechanism of void nucleation.

The rate of nucleation of voids can be analyzed as being due to vacancies clustering together and nucleating a cavity under the influence of an applied tensile stress. This nucleation is likely to happen at grain boundary under tension because the free energy required to form a critical cluster size is smaller here than within a grain. Raj and Ashby (1975) also found that the free energy barrier for void nucleation is the smallest when the void formed at a triple junction between a grain boundary and a second phase particle. For our particular case, this implies that the Kirkendall voids will most likely nucleate at junctions between γ grains and Cr, Ti, Ta, or W precipitates (Fig. 3.3) or β (NiAl) grains (Fig. 3.4a).

The formation of such voids by vacancy aggregation was modeled using the classical Becker-Döring theory of nucleation (Raj and Ashby, 1975; Raj, 1978; Argon, 1983). The models predict that it can occur only above a threshold stress, $\sigma_{\theta\theta}^{th}$, and that above this stress an incubation time is needed for the formation of a stable void. The change in free energy in the system due to the formation of a void (at constant temperature and pressure) arises from the change in surface and interface energy, from the change in stored elastic energy in the system, and from the work done by the local stress on the surroundings when the void forms. The critical radius at which the change in free energy reaches a maximum, r_c, and the magnitude of this maximum energy barrier ΔG^* (with the change in stored strain energy negligible), is given in terms of the stress $\sigma_{\theta\theta}$, the surface free energy per unit area of the void γ_s, and a constant F_c, which when multiplied by r_c^3 yields the volume of the critical void and varies depending on where the cavity forms (Raj and Ashby, 1975):

$$r_c = \frac{2\,\gamma_s}{\sigma_{\theta\theta}} \tag{3.7}$$

$$\Delta G^* = \frac{r_c^3\,F_v\,\sigma_{\theta\theta}}{2} \tag{3.8}$$

For a fixed r_c, voids that form at triple junctions give the smallest critical volume (or smallest F_v). Above this volume, the cluster becomes stable and nucleates a void.

An incubation time t^* per nucleus or site is required to reach the critical size $r_c(\sigma_{\theta\theta})$. A good estimate of this incubation time (Raj and Ashby, 1975; Argon et al., 1980) is the time necessary for the required vacancies making up the critical size void to diffuse into this cluster along the incoherent boundary. An increase in the local tensile stress will decrease the critical radius and the incubation time. Similarly, an increase in the temperature will increase the diffusion rate and therefore decrease the incubation time.

If under certain circumstances grain boundary sliding occurs, it will produce a stress concentration at triple junction between the hard precipitates or NiAl (β) grains and the boundary (Fig. 3.4a), decreasing the incubation time. In our case, due to the cyclic nature of the coating stresses, the stress concentration will be a transient during the cooling part of the cycle which generates the tensile stresses in the coating, and if the void is to grow at all, it will need to do so mainly by diffusion before the diffusion coefficient drops practically to zero at the lower temperatures. Extremely high stress concentrations would be needed to radically decrease the incubation time to within the cooling time of the cycle.

Without Kirkendall diffusion, threshold stresses for void nucleation were found to be of the order of $0.01 \times E$ by Argon (1983). Since tensile stresses of the order of 5×10^{-4} E at 990°C develop in the coating, we could be tempted to conclude that stress concentration of the order of 20 due to sliding grain boundaries at the triple junctions between γ grain boundaries and relatively coarse β grains will be needed to initiate voids (similar values of stress concentrations have been determined by others (Evans, 1982). However note that although the stress singularities at triple junctions will be smoothed down by diffusional flow, the stress concentrations will

not be washed out completely by diffusional flow because a typical β grain size is greater than the critical diffusion length[1] defined by Argon (1983).

There is also a possibility of having a higher far-field stress than the applied stress considered up to here. This additional stress field can arise from the local stresses generated as a consequence of volume misfit due to Kirkendall diffusion. This can be explained as follows. Kirkendall diffusion creates a state of vacancy supersaturation, as discussed above, and could create local tensile stresses generated by diffusion (Ballufi et al., 1957). The tensile stresses arise due to the restraining effect of the bulk of the material (away from the interface) on the volume contraction in the interface region losing atoms. This establishes a predominantly 2-D stress field parallel to the plane of the interface of magnitude up to the coating flow strength. Away from this region, vacancy sinks (e.g. grain boundaries, dislocations) eliminate the excess of vacancies deposited in their vicinity to maintain approximate equilibrium. The additional effect of this interface stress field is added to the effect of the applied stress discussed above, then making void formation and growth more likely by decreasing the needed stress concentration to produce a stable void.

It is interesting to note that the Kirkendall voids observed at the interface of a coating in the as-received condition by Gedwill et al. (1982) imply that the stresses generated due to Kirkendall diffusion might by themselves suffice to nucleate voids, and that they must somehow correlate directly with the level of vacancy supersaturation.

3.3.3 Growth of stable voids into macrovoids.

The growth pattern of the voids, that is, following the receding β phase (Fig. 3.5a and schematically in Fig. 3.4b), suggests that there is a continuous growth of an

[1] Distance over which diffusion smooths down stress singularities, as calculated from pure Ni data.

elongated void at the junctions of γ grain boundaries and β grains (at this stage we can expect the interface precipitates to have gone into solution into the γ phase). We would then expect, in the absence of β phase in the coating, some of the voids to stall their growth, as shown in Fig. 3.5b. However, some may eventually open up to the coating surface, e.g. the center crack in Fig. 3.5b. Once this stage is reached, not only will the crack driving force increase considerably, but the oxidation rate will also be increased.

Voids can grow not only by diffusion but also by localized plastic flow due to dislocation segments entering voids whose sizes have reached the order of the dislocation network spacing. An indication that dislocation creep can be a possible mechanism of plastic deformation is given by deformation mechanism maps for pure Ni of 1 and 10μm grain size (Frost et al., 1982). With the stresses found in the inelastic finite element analysis of the coating at high cycle temperatures, e.g. of the order of 25 MPa at 950°C (T/T_m=0.8), which yields a strain rate of 4.5 x $10^{-3}s^{-1}$, dislocation creep will be added to boundary diffusion creep (Coble creep) when the grains coarsen above 5 μm.

Although this analysis offers only a qualitative discussion of the damage mechanisms observed in overlay coatings, it shows that interdiffusion can be a critical mechanism, so that fluxes of associated elements in and out of the substrate play a dominant role in the life of the coating. An important conclusion from this mechanism is that Kirkendall void formation could be avoided by imposing barriers between substrate and coating, or by controlling the aging process to reduce concentration gradients before cyclic straining.

3.4 Conclusions and Recommendations

The degradation of an EB-PVD NiCoCrAlY overlay coating in an oxidizing environment under cyclic loading ($0.51\% < \Delta\epsilon_{coat}^{mech} \leq 0.83\%$) consisted of severe cracking, which under normal cooling rates and a coating strain range $> 0.51\%$ cracks appeared to originate from internal (Kirkendall) voids which grew from the original coating-substrate interface towards the coating surface.

Internal voids form due to vacancies clustering together under the influence of a (applied or diffusion-induced) tensile stress, and nucleate at junctions between γ grain boundaries and Cr, Ta, Ti, or W precipitates or β grains. These voids grow by diffusion or localized plastic flow, depending on the coating grain size, following the receding β grains.

Kirkendall void formation could be avoided by imposing barriers between substrate and coating to reduce interdiffusion, and by controlling aging such as to reduce the concentration gradients. As is known, thermal expansion mismatch strains should be minimized to reduce the level of the tensile stresses and strain ranges. Beyond that, further crack initiation and propagation data for the coating, with realistic stress-strain histories, are necessary to accurately correlate realistic strain ranges with the development of damage.

Bibliography

[1] Anthony, T.R. (1969), 'Solute segregation in vacancy gradients generated by sintering and temperature changes', *Acta Met.* **17**, 603-609.

[2] Argon, A.S., I.W. Chen, and C.W. Lau (1980), 'Intergranular cavitation in creep: theory and experiments', *Creep-Fatigue Environment Interactions*, edited by R.M. Pelloux and N.S. Stoloff, AIME: New York, p. 46.

[3] Argon, A.S. (1983), 'Intergranular cavitation in creeping alloys', *Scripta Met.* **17**, 5-12.

[4] Balluffi, R.W. (1954), 'The supersaturation and precipitation of vacancies during diffusion', *Acta Met.* **2**, 194-202.

[5] Balluffi, R.W., and L.L. Siegle (1957), 'Growth of voids in metals during diffusion and creep', *Acta Met.* **5**, 449-454.

[6] Barret, C.A., and C.A. Lowell (1978), 'The cyclic oxidation resistance of CoCrAl alloys at 1100 and 1200°C, and a comparison with the NiCrAl alloy system', *Oxid. Met.* **12**, 293-311.

[7] Busso, E.P. (1987), *Thermal Fatigue of an Overlay Coating for Single Crystal Nickel-Base Superalloys*, MSc Thesis, Dept. Mech. Eng., M.I.T., May.

[8] Coffin Jr., L.F. (1963), 'Cyclic-strain-induced oxidation of high temperature alloys', *Trans. of A.S.M.*, **56**, 339-344.

[9] Evans, A.G. (1982), in *Recent Advances in Creep and Fracture of Engineering Materials and Structures*, B. Wilshire and D.R. Owen (eds.), Pineridge Press, U.K., p. 53.

[10] Frost, H.J., and M.F. Ashby (1982), *Deformation Mechanism Maps*, Pergamon Press, pp. 20-22.

[11] Gedwill, M.A., T.K. Glasgow, and S.R. Levine (1982), 'A new diffusion oxidation resistant coating for superalloys', *Thin Solid Films* **95**, 65-72.

[12] Goward, G.W. (1979), 'Protective coatings for high temperature alloys', *Source Book on Materials for Elevated Temperature Applications*, ASM Eng. Bookshelf, E.F. Bradley (ed.), pp. 369-384.

[13] Holmes, J.W., and F.A. McClintock, K.S. O'Hara, and M.E. Conners (1987), 'Thermal fatigue testing of coated monocrystalline superalloys, *Low-Cycle Fatigue*, ASTM STP 942, H.D. Salomon, G.R. Halford, L.R. Kaisand, and B.N. Leis (eds.), pp. 672-691.

[14] Janssen, M.M.P. (1973), 'Diffusion measurements in NiAl systems', *Met. Trans. A* **4**, 1623-1632.

[15] Lowell, C.A., C.A. Barret, and R.W. Palmer (1983), 'Development of a cycle oxidation spall model', *Oxide Deposition and Hot Corrosion in Combustion Turbine Engine Conf.,* NASA Lewis Research Center, April.

[16] Nesbitt, J.A. (1982),'Solute transport during the cyclic oxidation of Ni-Cr-Al alloys', *NASA Report 165544.*

[17] Raj, R., and M.S. Ashby (1975), 'Intergranular fracture at elevated temperature', *Acta Met.* **23**, 653-666.

[18] Raj, R. (1978), 'Nucleation of cavities at second phase particles in grain boundaries', *Acta Met.* **26**, 995-1005.

[19] Shewmon, P.G. (1963), *Diffusion of Solids*, McGraw-Hill (ed.).

[20] Wallwork, G.R., and A.Z. Hed (1971), 'Some limiting factors in the use of alloys at high temperatures', *Oxid. Met.* **3**, 171-184.

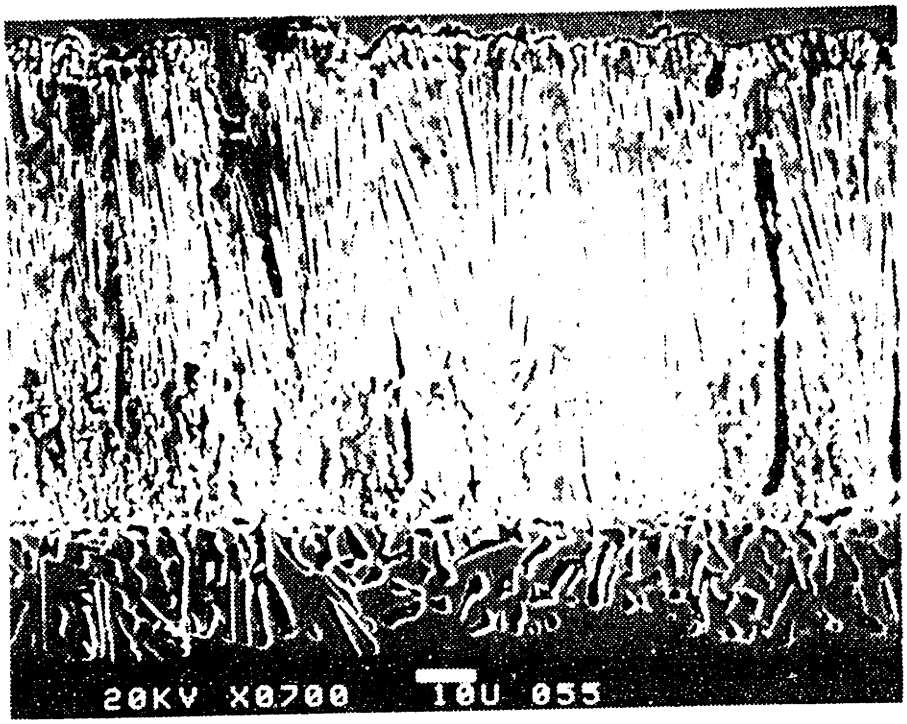

(a) In the as coated condition after peening and heat treatment with columnar voids open to the surface

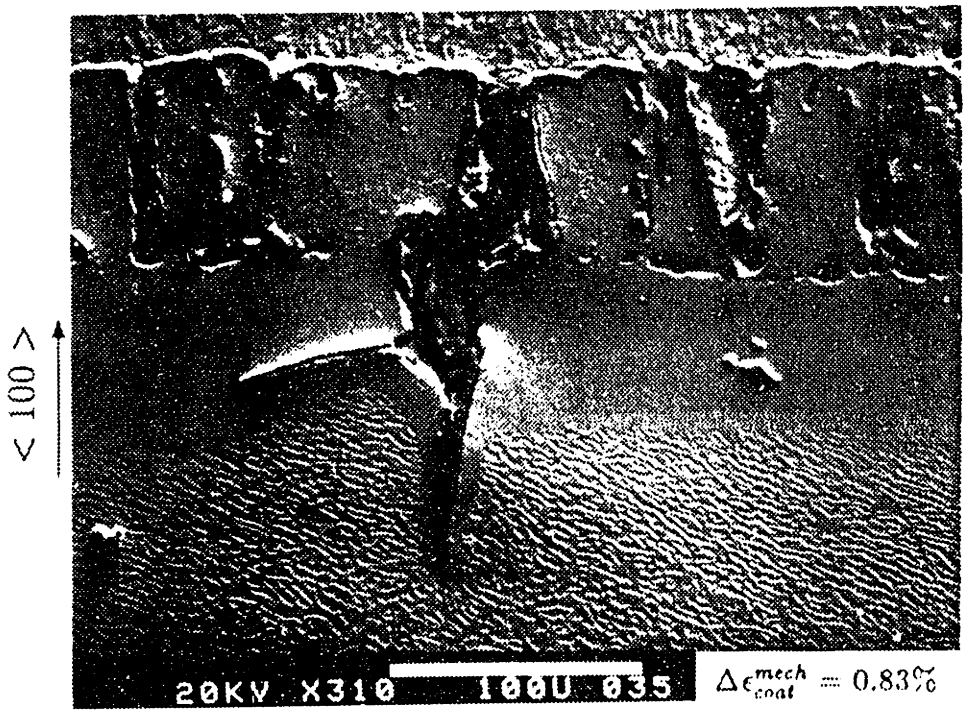

(b) After *cyclic* exposure (6000 4.5s heating cycle) showing grain boundary oxidation, and crack propagation into the substrate

Fig. 3.1 Sputtered-PVD NiCoCrAlY coating

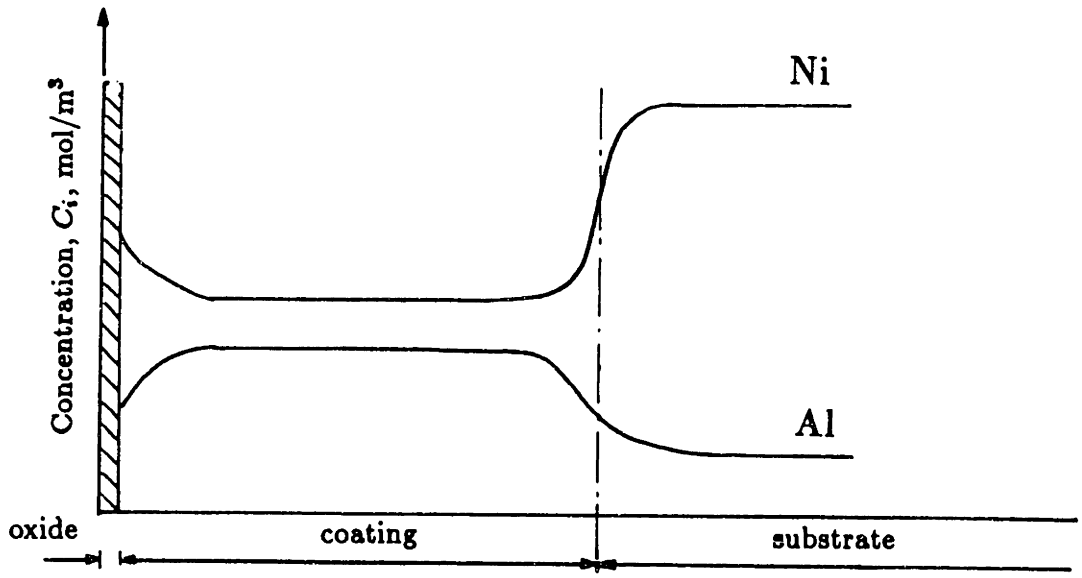

(a) Schematic concentration profiles

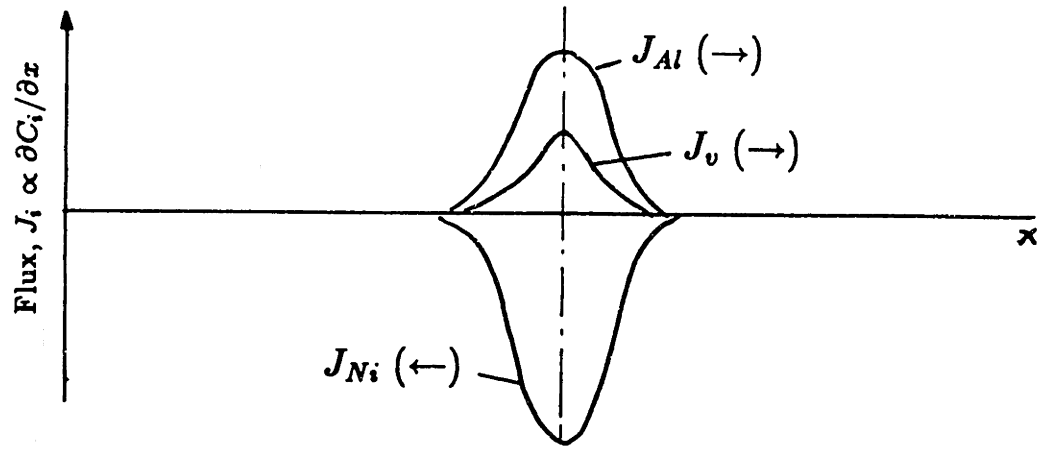

(b) Fluxes

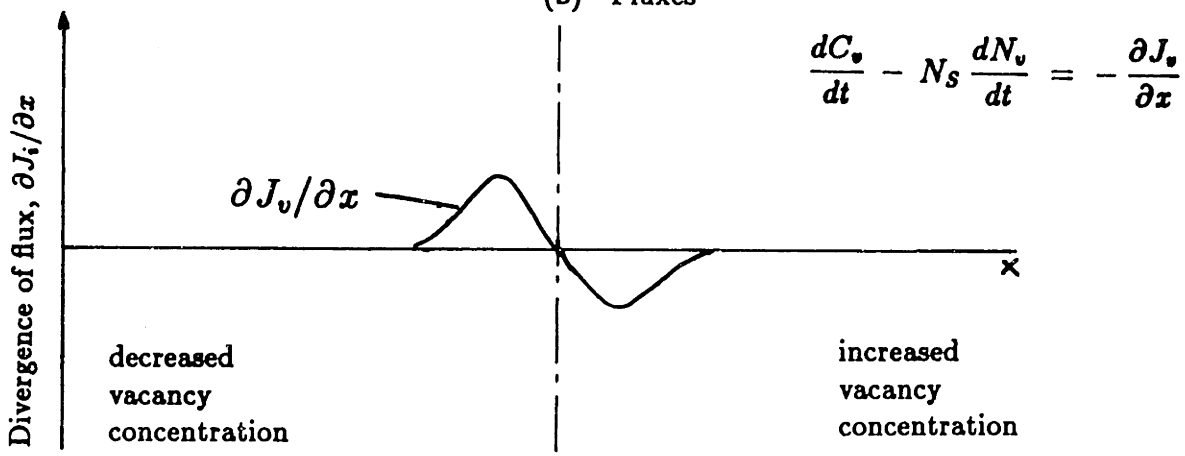

(c) Divergence of flux

Fig. 3.2 Change in vacancy concentration due to Ni and Al concentration gradients

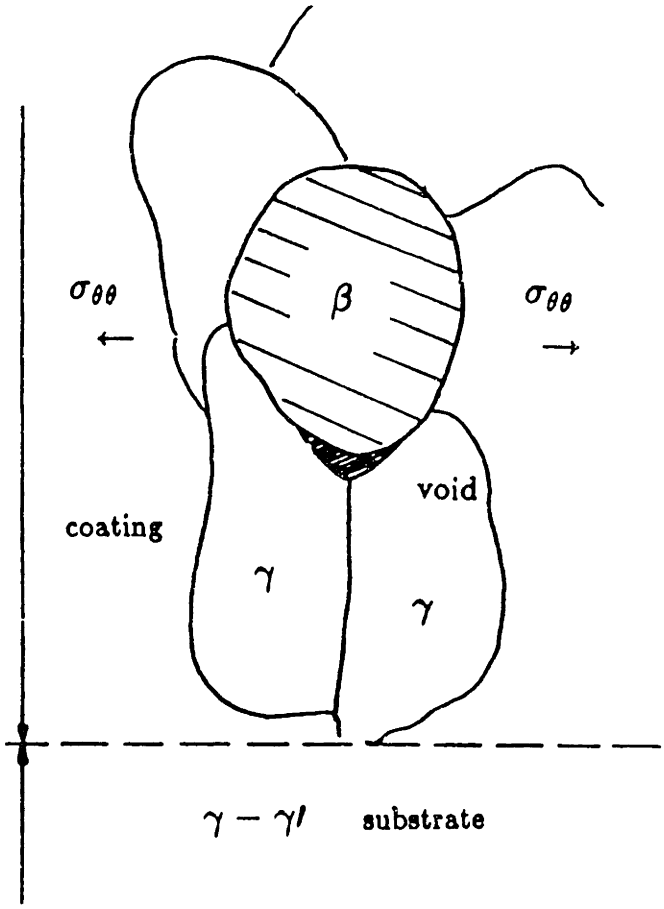

(a) Nucleation at t_1

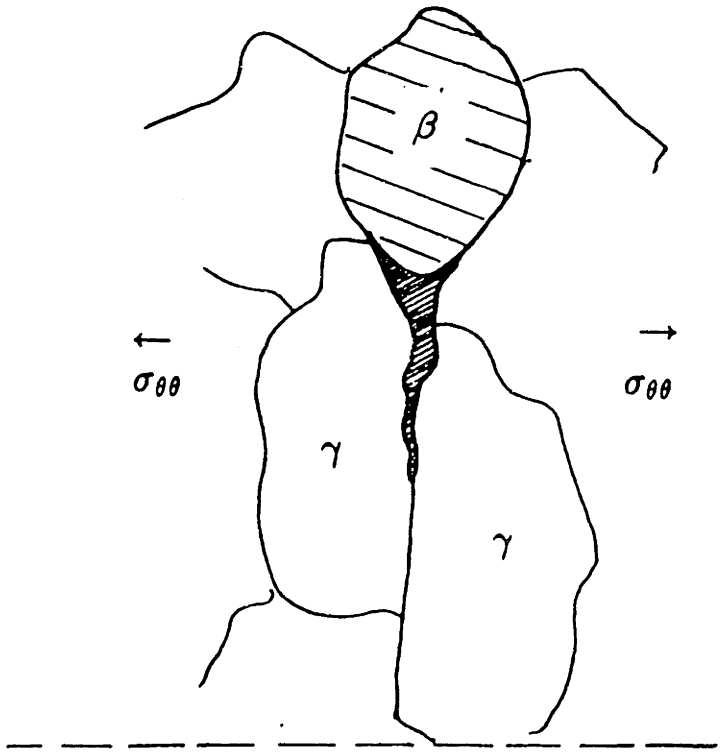

(b) Void growth at $t_2 > t_1$

Fig. 3.4 Void growth mechanism

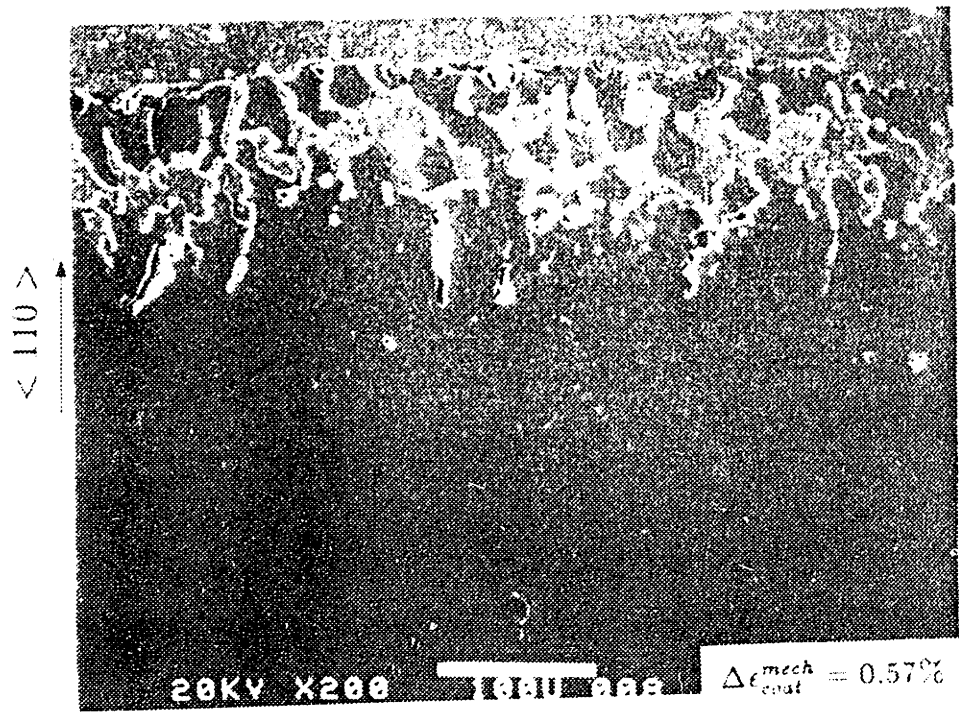

(a) Small strain range

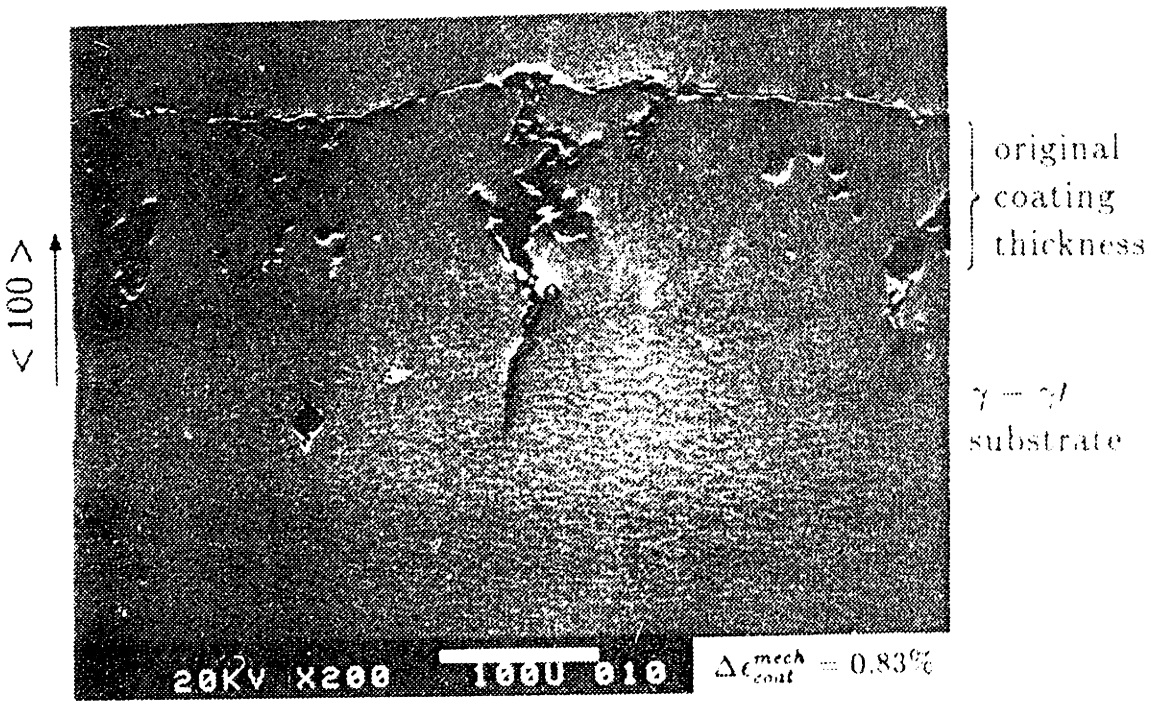

(b) Large strain range

Fig. 3.5 Stages of interface (Kirkendall) void development

Part II
Cyclic Deformation of Monocrystalline Nickel Aluminide

Chapter 4

Stable Configurations of Dislocations in Homogenized Nickel-aluminide Single Crystals

Abstract

Dislocations produced in quasi-stoichiometric NiAl ($\approx$ 50.6 *at.*% Ni) by homogenizing and slow cooling have been analyzed. The observed dislocations were primarily on {100} planes with < 100 > Burgers vectors in one of three structures: vacancy-fed edge concentric loops and spiral dislocations, and zig-zag dislocations having screw resultants. The orientations of the edges of vacancy loops and spiral dislocations correspond to those for which the dislocations have the minimum line energy in a $\pm$ 34° stable zone either side of < 100 > directions. The line orientations of the zig-zag dislocations conform to the predicted stable directions.

4.1 Introduction

Several studies have shown that a large number of vacancies can be retained in NiAl after cooling from high temperatures leading to the formation of dislocation loops and spiral dislocations (Ball and Smallman, 1968, Parthasarathi and Fraser, 1984). However, little or no attention has been paid to the effect of anisotropic elasticity in shaping such dislocation configurations. Thus, the work presented in this chapter is aimed at determining the effect of elastic anisotropy on the dislocation structure of undeformed NiAl crystals in its as-grown homogenized state. Such understanding will help the study, in the next chapter, of the subsequent behavior of the crystal under cyclic deformation along a preferred crystallographic orientation.

After a description of the crystallography and elasticity of NiAl single crystals, the relationship between these properties and the formation and shapes of the observed dislocation structure is described. First, spiral dislocations, dislocation loops, and dislocation segments are characterized by determining their edge or screw components, orientation, and for the two first groups, their interstitial or vacancy character. Second, the crystallographic orientations of the dislocation lines are compared with theoretically expected orientations computed from the variation of dislocation line energy with crystallographic directions and the inverse Wulff construction (Head, 1967).

4.2 Properties of NiAl Single Crystals

4.2.1 General observations

The attraction of the single phase intermetallic compound NiAl as a structural alloy is based on its low density, high melting point (1640°C for its stoichiometric composition), as well as on its excellent high temperature oxidation and corrosion resistance.

Although these properties have made NiAl a widely used protective (polycrystalline) coating of gas turbine airfoils, its structural applications have remained limited due to its inherent low temperature brittleness. After initial improvements in its high temperature strength and ductility were obtained by eliminating grain boundaries, most of the research effort focussed on monocrystalline NiAl. Studies, such as that of Polvani et al. (1976) on polycrystalline β' (Ni_2AlTi) - β (NiAl), have also shown that alloying improves the high temperature resistance to equal that of superalloys, although the achievement of ductility has remained a problem. Only recently, there has been a resurgence of interest in the structural applications of NiAl and new research programs have started to develop new materials on the basis of NiAl phases, such as the matrix material in either fiber-reinforced (e.g. Al_2O_3) or particle reinforced (e.g. TiB_2) metal-matrix composites (e.g. see reviews by Stephens and Nathal, 1988, Busso, 1989).

4.2.2 Crystallographic structure

Intermetallic phases are stoichiometric compounds which occupy an intermediate position between metallic alloys and ceramics. NiAl (β) is one of these compounds, with the B2 crystallographic structure (also referred as CsCl, and $L2_0$ structures), in which Ni atoms occupy the cube corners of the unit cell and Al atoms reside at the cube centers. For stoichiometric NiAl, there is practically complete atomic order up to the melting point (Sauthoff, 1986). Their outstanding high temperature stability, better than the L_{12} compound Ni_3Al (Jung et al., 1987), results from the tight binding between the unlike metal atoms[1]. The equilibrium phase diagram for

[1]The ratio of the atomic radii in the NiAl lattice, $R_{Al}/R_{Ni} = 0.847$, is somewhere in between their ionic radii (0.069 nm and 0.051 nm for Ni^{+2} and Al^{+3} respectively) and their metallic radii (0.124 nm and 0.143 nm for Ni and Al respectively) due to the covalent bonding from some exchange of the covalent electrons that exist between the unlike atoms (Lautenschlager et al., 1967).

the Ni-Al system of Fig. 4.1 shows that single phase NiAl can be obtained over a 14 at.% range of compositions around stoichiometry. Departures from stoichiometry can however result in accompanying changes in vacancy concentrations promoting diffusion and thermally activated dislocation motion at high temperatures (Sauthoff, 1986). Thus, in a Ni-rich compound, the excess Ni atoms will occupy either vacancy sites or Al sites in the Al sublattice, whereas an excess of Al atoms leads to vacancies in the Ni sublattice.

Further ordering from the NiAl phase, which is considered too soft at high temperatures when compared to commercial superalloys, see Fig. 4.2, can be achieved by alloying it with Ti. This leads to the Heusler-type alloy Ni_2AlTi (β'), obtained by the substitution of half the Al atoms by Ti, with much higher stability and strength and therefore with a higher creep resistance than NiAl, see Fig. 4.2. The creep resistance can still be further increased by precipitating a second phase. Furthermore, the creep resistance of the Ni_2AlTi with precipitated particles of the softer NiAl reaches that of the $\gamma - \gamma\prime$ superalloys.

4.2.3 Elastic constants

Since NiAl single crystals exhibit cubic symmetry, their elastic properties are fully characterized by three independent elastic constants. The elastic constitutive equation, expressed in a reference frame normal to the planes of symmetry, $\{100\}$[2], is

[2]Note that a general rotation of the coordinates away from the cube axes fully populates the matrix. Hereafter, a set of directions related by symmetry are all represented by the symbol $< >$, e.g. the diagonals of a cube, [111],[11$\bar{1}$], [1$\bar{1}$1], and [1$\bar{1}\bar{1}$], are all represented by $< 111 >$. Similarly, a set of equivalent lattice planes related by symmetry, e.g. the faces of a cube (100), (010),($\bar{1}$00),(0$\bar{1}$0), (001), and (00$\bar{1}$), are planes represented by the symbol $\{100\}$.

written in terms of the elastic stiffnesses as,

$$\begin{Bmatrix} \sigma_{11} \\ \sigma_{22} \\ \sigma_{33} \\ \sigma_{23} \\ \sigma_{31} \\ \sigma_{12} \end{Bmatrix} = \begin{bmatrix} C_{11} & C_{12} & C_{13} & 0 & 0 & 0 \\ C_{12} & C_{22} & C_{23} & 0 & 0 & 0 \\ C_{13} & C_{23} & C_{33} & 0 & 0 & 0 \\ 0 & 0 & 0 & C_{44} & 0 & 0 \\ 0 & 0 & 0 & 0 & C_{55} & 0 \\ 0 & 0 & 0 & 0 & 0 & C_{66} \end{bmatrix} \begin{Bmatrix} \epsilon_{11} \\ \epsilon_{22} \\ \epsilon_{33} \\ \epsilon_{23} \\ \epsilon_{31} \\ \epsilon_{12} \end{Bmatrix}, \tag{4.1}$$

where

$$C_{11} = C_{22} = C_{33}; \quad C_{12} = C_{13} = C_{23}; \quad C_{66} = C_{44} = C_{55}. \tag{4.2}$$

The elastic stiffnesses of NiAl for temperatures between -196°C and 600°C were measured by Rusović and Warlimont (1977) using an ultrasonic pulse-echo technique at 10 MHz. Their composition dependence around stoichiometry was also investigated. The temperature dependence of all the elastic constants was found to be linear within the temperature range tested, and to cover the temperature range of interest in later chapters, they were linearly extrapolated to 850°C , as shown in Fig. 4.3. For almost stoichiometric NiAl (50.6 at.% Ni) the C_{ij} are given by:

$$\begin{aligned} C_{11} &= 0.2039 \times 10^6\,[MPa] - 21.547\ T\ [^0C/MPa], \\ C_{12} &= 0.1361 \times 10^6\,[MPa] - 14.167\ T\ [^0C/MPa], \\ C_{44} &= 0.1144 \times 10^6\,[MPa] - 26.882\ T\ [^0C/MPa]. \end{aligned} \tag{4.3}$$

In order to verify the accuracy of the data and the validity of extrapolating it to 850°C , a comparison was carried out between the uniaxial moduli $E_{<100>}, E_{<110>}$, and $E_{<111>}$ measured by Wasilewski (1966) at 850°C and those calculated from the stiffness coefficients given by Eq. 4.3. The uniaxial moduli can be calculated from the elastic constants C_{ij} by first calculating the elastic compliances S_{ij}. See procedure in Appendix 4.A. Table 3.1 shows the uniaxial moduli calculated from the corresponding compliances according to Eq. 4.A.4-6 in Appendix 4.A, and those given by Wasilewsky (1966), $E^w_{<100>}, E^w_{<110>}$, and $E^w_{<111>}$. Comparison between the

moduli at 850°C shows the two sets of data to be within 2% of each other, which can be regarded as being in very good agreement, validating the linear extrapolation of Fig. 4.3.

As a final verification of the accuracy of the elastic data, published Young's modulus for polycrystalline NiAl and values computed from the single crystal data were compared. For the latter, Hashin and Shtrikman's bounds (1962) for a random isotropic aggregate of cubic crystals were used. (By using these bounds, the difference between Voigt (1928) and Reuss (1929) lower and upper bounds was improved by an order of magnitude).

Hashin and Shtrikman's bounds for shear can be expressed in terms of the bulk modulus

$$k = \frac{C_{11} + 2\,C_{12}}{3}\,, \tag{4.4}$$

and $C \equiv (C_{11} - C_{12})/2$:

$$G^{l} \;=\; C + 3\left[\frac{5}{C_{44} - C} + 12\left(\frac{k + 2C}{5\,C\,(3\,k + 4\,C)}\right)\right]^{-1},$$

and

$$G^{u} \;=\; C_{44} + 2\left[\frac{5}{C - C_{44}} + 18\left(\frac{k + 2\,C_{44}}{5\,C_{44}\,(3\,k + 4\,C_{44})}\right)\right]^{-1}. \tag{4.5}$$

Upper and lower bounds for Young's modulus, E^{u}_{YM} and E^{l}_{YM} respectively, based on the isotropic bulk modulus given by Eq. 4.4 and the shear modulus bounds of Eq. 4.5 can be obtained from

$$E_{YM} = \frac{9\,k\,G}{3\,k + G}\,. \tag{4.6}$$

The bounds for the modulus can now be compared with E_{YM} for polycrystalline stoichiometric NiAl also measured by Rusović and Warlimont (1979). Fig. 4.4 shows that there is also a reasonably good correlation between polycrystalline modulus E_{YM} and its bounds, specially at temperature above 400°C .

4.3 Experimental Procedure

NiAl single crystal ingots of approximately 5 by 2 by 1.5 in. were grown by General Electric Co. - Evendale using the floating zone method. The chemical composition of the ingots was determined with an atomic absorption method, giving Ni and Al contents of 50.6 $\pm$ 0.6 at. % and 48.4 $\pm$ 0.2 at. % respectively. The as-grown ingots were homogenized at 1315 °C for 50 hr and subsequently cooled down slowly inside the furnace, at $\approx$ 150°C / hr, to room temperature. Crystallographic orientations were determined by the standard Laue back-reflection method. Rectangular cross-section bars oriented along cubic axes were cut and sectioned for transmission electron microscopy (TEM) using electric-discharge machining.

Next, thin films approximately 0.40 mm thick were ground and polished to a thickness of 0.08 - 0.10 mm, and were then electro-polished with a 10 % perchloric acid - 90 % methanol solution using a 20 A current and a 8-12 V voltage. The films were examined in a JEOL 200 electron microscope at an accelerating voltage of 200 kV. [3].

4.4 Results and Analysis

4.4.1 Observed Dislocation Structure

Under TEM, the films exhibited grown-in dislocations in one of three different structures, all lying on cube planes: straight or sharply kinked dislocations, concentric dislocation loops (Fig. 4.5) and spiral dislocations (Fig. 4.6), with the last two groups having their straight sides aligned with the cubic directions. The dislocation density was approximately 0.2 $\mu m/\mu m^3$.

The dislocation segments, mostly lying on cubic planes, made up almost 50 %

[3]The TEM pictures shown in this chapter have been taken by Y.P. Liu, of the Department of Materials Science and Engineering at MIT. See also Liu (1990).

of the total density. 3/4 of them were found to be straight edge segments lying along cube directions and are mostly debris from dislocation loops and spiral dislocations, Fig. 4.7. The remaining segments have curved or zig-zag configurations, e.g. dislocation 1 in Fig. 4.6, and have screw resultants with $< 100 >$ type Burgers vectors.

The $\mathbf{g}.\mathbf{b} = 0$ invisibility criterion, plus the additional $\mathbf{g}.\mathbf{b}\times\mathbf{u} = 0$ criterion when the line direction vector $\mathbf{u}$ is parallel to the diffraction vector $\mathbf{g}$ for edge dislocations, was used to determine the Burgers vectors. The contrast behavior of the dislocation loops of Fig. 4.7 using a two beam condition confirms that, as the two invisibility conditions are met, the loops have a pure edge character with a slip direction, $\mathbf{b} = [001]$, perpendicular to their planes. As Fig. 4.7 (a) and (b) shows, the opposite pairs of dislocation segments become invisible when [100] and $[0\bar{1}0]$ reflections are used respectively. On the other hand, a strong residual contrast is obtained in (c) with $\mathbf{g} = [1\bar{1}0]$.

Furthermore, the observed shift in image position after changing the sign of the reflection vector $\mathbf{g}$ was used to verify that the loops are vacancy in nature. This indicates that they formed due to the collapse of vacancy disks which collected as the result of a large excess concentration of vacancies trapped in the material during cooling from high temperatures.

The contrast experiments of Fig. 4.8 (a) and (b) also confirms a slip vector $\mathbf{b} = [001]$ and pure edge type spiral dislocations. A strong image contrast in (c) and (d) was obtained when $\mathbf{g} = [1\bar{1}0]$ and $\mathbf{g} = [110]$ respectively. The formation of spiral dislocations follows the well known process (e.g. see Hirth and Lothe, 1982) of screw dislocation climb due to vacancy condensation around the screw dislocation, which lies along the axis of the spiral. Initially, vacancies gather and form a vacancy disc on a $\{100\}$ plane normal to the screw dislocation. The subsequent collapse of

the vacancy disc is followed by continuous vacancy precipitation forming new loops, which due to the helical structure of atom planes along a screw dislocation connect each other to form the spiral dislocation.

The intervals between successive dislocation loops as well as the decreasing loop radius (at the juncture of any two adjacent straight sides) is related to the relative mobility of vacancies at different temperatures. As the cooling progresses, the decreasing temperatures limit the number of vacancies that can nucleate and precipitate at any given location resulting in smaller dislocation loops. The reduction in diffusion and climbing will also limit the amount of curvature that each loop can adopt, thus yielding more square-shaped loops as they decrease in size.

Fig. 4.9 can be used to determine the Burgers vector of zig-zag dislocations. In (a), they show a very strong contrast when a reflection parallel to their line orientation is used, whereas in (b) they become nearly out of contrast with $\mathbf{g} = [010]$. (The presence of a weak residual contrast even though the invisibility criterion is satisfied is a feature associated with the elastic anisotropy of B2 compounds. Computed image matching can often facilitate identification (Head et al. 1987)). It can be concluded from these images that the slip direction of the zig-zag dislocations is $\mathbf{b} = [100]$.

The tendency of most dislocations to adopt straight configurations and for some to be oriented along particular directions, even to the extend of forming sharply kinked or zig-zag configurations is an attempt to minimize their line energy in the highly elastically anisotropic matrix. The next section will discuss this effect in detail.

4.4.2 Stable configurations of dislocations

It has been shown that some orientations of dislocations in unstressed elastic anisotropic crystals are elastically unstable and unlikely to occur (Head, 1967). Two different criteria exist to determine if a dislocation will be unstable (Friedel, 1964). First, if $E(\theta)$ is the line energy of a straight dislocation per unit length as a function of the angle θ defining its line direction in a given plane, then it will be unstable if it rotates towards a direction for which a negative effective line tension τ may result:

$$\tau \equiv E + \frac{d^2E}{d\theta^2} < 0 \ . \tag{4.7}$$

The second is an analogy to the Wulff plot used to determine the equilibrium shape of a crystal under an orientation-dependent surface energy (Frank, 1963), which predicts that the final equilibrium shape of a dislocation will be composed of quasi-straight segments.

These two criteria are satisfied by the inverse Wulff plots, viz. reciprocal line energy versus orientation plots, which give regions of forbidden line directions whenever the closed curve is concave. On the other hand, the dislocations are stable for those orientations where the closed curve is convex.

Determination of $E(\theta)$. The energy of a straight dislocation can be calculated following the anisotropic elasticity theory of straight dislocations developed by Eshelby et al. (1953). The elastic energy per unit length of a dislocation is given in terms of its Burgers vector **b**, the core radius of the dislocation r_o, the outer cut-off radius r_1, and the anisotropic or energy coefficient K: which itself is a function of the Burgers vector, the single crystal elastic constants (Eq. 4.3), and the orientation of the dislocation line in the crystal:

$$E = \frac{K\, b^2}{4\, \pi}\, ln\left(\frac{r_1}{r_o}\right) \ . \tag{4.8}$$

A general relation for the energy coefficient K of a dislocation in a cubic crystal can only be obtained analytically if the dislocation lies along either $< 100 >$ or $< 110 >$ crystallographic directions. This relation was given by Foreman (1955) in terms of an arbitrary Burgers vector with its components $\mathbf{b} = (b_1, b_2, b_3)$ given on an orthogonal system aligned with the dislocation and satisfying a two-fold symmetry, the elastic stiffness coefficients in a rotated frame from the cubic reference frame aligned with the dislocation, C'_{ij}, and $C' = (C'_{11}\, C'_{22})^{1/2}$:

$$K = \frac{1}{b^2}\,(K_1\, b_1^2 + K_2\, b_2^2 + K_3\, b_3^2)\ , \tag{4.9}$$

where

$$\begin{aligned} K_1 &= (C' + C'_{12}) \left[\frac{C'_{66}\,(C' - C'_{12})}{C'_{22}\,(C' + C'_{12} + 2\,C'_{66}}\right]^{1/2}, \\ K_2 &= K_1 \left[\frac{C'_{22}}{C'_{11}}\right], \\ K_3 &= (C'_{44}\, C'_{55})^{1/2}\ . \end{aligned} \tag{4.10}$$

For other orientations, it is necessary to solve the relevant equations outlined by Foreman (1955) entirely numerically.

The coefficients C'_{ijkl}[4] can be calculated in terms of the single crystal elastic constants C_{ijkl} and the direction cosines l_{ij} by using the following relation (McClintock and Argon, 1966):

$$C'_{ijkl} = C_{ijkl} - (2\,C_{2323} + C_{1122} - C_{1111}) \left(\sum_{n=1}^{3} l_{in}\, l_{jn}\, l_{kn}\, l_{ln} - \delta_{ij}\, \delta_{kl}\, \delta_{ik}\right) \tag{4.11}$$

The δ_{ij}'s are the Kronecker delta.

[4]The pair of indexes ij or kl of the elastic coefficients reduce to the single index notation as follows:

ij or kl	11	22	33	23	31	12
m or n	1	2	3	4	5	6

Stable shapes of dislocation loops and spiral dislocations. All the observed spiral dislocations and dislocation loops were lying on cubic planes and found to be edge dislocations belonging to the same $\{100\}< 100 >$ slip system family. To find the stable configurations of these dislocations, it is necessary to determine their elastic energy per unit length at different orientations in a plane normal to their Burgers vectors.

Consider the variation of the energy per unit length of a straight edge dislocation lying on a (010) plane with a $\mathbf{b} = [010]$ normal to that plane. Then, with $\mathbf{b} = [0, b, 0]$, Eq. 4.9 gives $K = K_2$, which can be determined analytically according to Eq. 4.10 for dislocations aligned with any of the $< 100 >$ and $< 110 >$ crystallographic directions.

Fig. 4.10 shows the computed energies, normalized by the energy at cubic orientations, $E_{<100>}$, for (010)[010] dislocations as a function of their orientations on the (010) plane in NiAl (at 850°C) and β Brass (Morton, 1984). Here, θ is defined from [001] towards [100] and, due to symmetry only 180° are shown. In NiAl, the deviations from isotropy (e.g. given by $E/E_{<100>} - 1$ in Fig. 4.11) of the intermediate values of E for $0^o < \theta < 45^o$ and similar symmetric regions were determined by scaling the deviations exhibited by similar dislocations in β brass with the ratio of the isotropy deviations of NiAl and brass at $< 110 >$ orientations (e.g. $= 1/3.85$ in Fig. 4.10). As expected, it is approximately of the same order of magnitude than the ratio of their Zener's parameters. [5] The latter is defined as,

$$A = \frac{2\,C_{44}}{C_{11} - C_{12}}\,. \tag{4.12}$$

Here, $A_{Brass}/A_{NiAl}(850^oC) = 8.45/2.98 = 2.83$ (for isotropy, $A = 1$).

[5]The deviations from isotropy and instability ranges for the same type of dislocations in different materials are expected to be the same if the elastic ratios which characterized cubic anisotropy in cubic crystals, namely Zener's parameter and the ratio $(C_{11} + 2C_{12})/C_{44}$, are the same (Head, 1967).

The corresponding inverse Wulff plots for both NiAl and β brass are given in Fig. 4.11. For NiAl, it shows wide regions with convex shapes at $\pm 34^{\circ}$ either side of each cubic orientation. As stated earlier, dislocations with orientations within these regions will have stable configurations. It is also evident in Fig. 4.11 how the higher anisotropy of brass increases its instability regions. In the limit, the inverse Wulff plot becomes a perfect circle for isotropic elasticity.

The NiAl stable regions exhibit a rather sharp 10% drop in E between $< 100 >$ and $< 101 >$ orientations with a minimum at cubic directions, Fig. 4.11. This seems to imply that dislocations which adjust their line orientations during vacancy disc condensation or climb will tend to lie along these directions of minimum energy. These results are consistent with the observed tendency of the sides of the loops and spiral dislocations to remain straight, and strongly suggest that the elastic anisotropy in NiAl plays a dominant role in determining the shapes of loops and spiral dislocations.

Stability ranges of zig-zag dislocations. It is also of interest to determine whether the sharply kinked or zig-zag dislocations observed in this study can also be related to the elastic anisotropy of NiAl. While all the observed zig-zag dislocations have also been found to belong to the same family of $\{100\}< 100 >$ slip systems, it is now necessary to determine the energy of these dislocations oriented at different angles in a plane parallel to their Burgers vectors.

Consider dislocations of edge character with a [100] Burgers vector, lying on a (010) cubic plane at an angle θ from the pure edge position, [001]. Then, $\mathbf{b}$ in Eq. 4.9 becomes,

$$\mathbf{b} = b\,[cos\ \theta,\ 0,\ sin\ \theta], \tag{4.13}$$

and the resulting K,

$$K = K_1 \cos^2\theta + K_3 \sin^2\theta \ . \tag{4.14}$$

Fig. 4.10 shows the computed energy at 850°C , normalized by $C_{44}\, b^2 /(4\pi)\, ln(r_1/r_o$, for (010)[100] dislocations as a function of their line orientations. The angle θ is measured from [001] towards [100]. The values of K for dislocations aligned with [001], [101], and [100] directions were analytically determined from Eq. 4.9. Since the values of E plotted in Fig. 4.10 for NiAl showed only a discrepancy of up to 3% with those obtained from Eq. 4.9, it was decided to approximate the intermediate values of K for $0^o < \theta < 45^o$ and for $45^o < \theta < 90^o$, from Eq. 4.9. Due to symmetry, similar variations were assumed every 90^o.

The corresponding inverse Wulff plot showing the variation of the reciprocal of the elastic line energy with θ given in Fig. 4.13. Note that the pure edge and screw positions correspond to $\theta = 0^o$ and $\theta = 90^o$ respectively. Fig. 4.13 reveals that, in a 180^o region, there are three regions which show concave shapes or concavities. Then dislocations with orientations within these regions will therefore be unstable. On the other hand, orientations for which the curve in Fig. 4.13 is convex will yield stable configurations.

The predicted instability ranges are between 8^o and 48^o, 63^o and 117^o centered at 90^o, and between 132^o and 172^o. Thus, screw dislocations, are expected to have unstable configurations over a wide range. The observed sharply kinked or zig-zag dislocations conform to the predictions of this analysis. For instance, in Fig. 4.6, dislocations A and B are in the predicted $\pm 8^o$ directions, and the arms of the V formed by dislocations C and D agree with the boundaries of the $63^o - 117^o$ region.

4.5 Summary

This study has shown how the energy of $\{100\}< 100 >$ dislocations in NiAl varies with line directions in planes normal and parallel to their Burgers vectors. As a consequence, edge vacancy loops and spiral dislocations lying on a (001) plane with $\mathbf{b} = a[001]$ show a wide range around the cubic axes for which their orientations result in stable configurations. However, these stable regions are characterized by a steep decrease of the dislocation energy towards a minimum at the cubic directions. This result seems to explain their square shape with their edges aligned along $< 100 >$ axes. Similarly, the presence of sharply kinked dislocations lying on a (001) plane and having screw resultant with $\mathbf{b} = a[100]$ can also be explained by the wide ranges of unstable configurations of $\{100\}< 100 >$ screw dislocations.

Bibliography

[1] Ball, A. and Smallman R.E. (1968), 'Vacancy defects in the ordered compound NiAl', *Acta Metall.*, **16**, 233.

[2] Busso, E.P. (1989), 'High temperature materials in Japan: an overview of their research, development, and life prediction work', *MIT-Japan Program Technical Publication Series'*, MITJP89-14, Center for International Studies, MIT, Cambridge, MA.

[3] Eshelby, J.D., W.T. Read, and W. Shockley (1953), 'Anisotropic elasticity with applications to dislocation theory', *Acta Met.*, **1**, 251.

[4] Frank F.C. (1963), *Metal Surfaces*, American Society for Metals, Ohio, US, p. 1.

[5] Friedel J. (1964), *Dislocations*, Pergamon Press, Oxford, p. 32.

[6] Foreman A.J.E. (1955), 'Dislocations energies in anisotropic crystals', *Acta Met.*, **3**, p. 322.

[7] Hanson, M. (1958), *Constitution of Binary Alloys*, 2nd Ed., McCgraw Hill eds., p. 119.

[8] Hashin, Z., and S. Shtrikman (1962), 'A variational approach to the theory of the elastic behavior of polycrystals', *J. Mech. and Phys. of Solids*, **10**, 343.

[9] Head, A.K. (1967), 'Unstable dislocations in anisotropic crystals', *Phys. Stat. Sol.*, **19**, 185.

[10] Head, A. K. et al. (1973), *Computed Electron Micrographs and Defect Identification*, North Holland eds., Amsterdam, Holland.

[11] Hearmon, R.F.S. (1945), 'The elastic constants of anisotropic materials', *Review of Modern Physics*, **18**, 3, 409.

[12] Hirth, J.P., and J. Lothe (1982), *Theory of Dislocations*, 2nd Ed., J. Wiley & Sons, p. 626.

[13] Jung, I., M. Rudy, and G. Sauthoff (1987), 'Creep in ternary B2 aluminides and other intermetallic phases', *High Temp. Ordered Intermetallic Alloys II*, Mat. Res. Soc., N.S. Stoloff et al. eds., 263.

[14] Lautenschlager, E.P, T. Hughes, and J.O. Brittain (1987), 'Slip in hard-sphere CsCl models', *Acta Met.*, **15**, 1347.

[15] Liu, Y.P. (1990),'Dislocation loops in single crystal NiAl', *Proceedings of the XIIth Int. Congress for Electron Microscopy,* San Francisco Press. Inc., San Francisco, CA, USA. In press.

[16] McClintock, F.A. and A.S. Argon (1966), *Mechanical Behavior of Materials,* Addison-Wesley eds., p. 78.

[17] Morton, A.J. (1984),'Dislocation loops in anisotropic materials II. Formation and equilibrium shapes of vacancy loops in $\beta-$ Brass, *Phil. Mag.,* **52**, 99.

[18] Parthasarathi, A, and H.L. Fraser (1984), 'The annealing of vacancy defects in β-NiAl', *Phil. Mag.,* **50**, No. 1, 89.

[19] Polvani, R.S, W.S. Tzeng, and P.R. Strutt (1976), ' High temperature creep in a semi-coherent NiAl-Ni_2AlTi alloy', *Met. Trans. A*, **7**, 33.

[20] Reuss, A. (1929), 'Berechnung der fliessgrenze von mischkristallen anf grund der plastizitatsbedingung fur einkristalle', *Z. Angew Math. Mech.*, **9**, 49.

[21] Rusović, N., and H. Warlimont (1977), 'The elastic behavior of B2-NiAl alloys', *Phys. Sta. Sol. (a)*, **44**, 609.

[22] Rusović, N. and Warlimont, H. (1979), 'Young's modulus of B2-NiAl alloys', *Phys. Sta. Sol. (a)*, **53**, 283.

[23] Sauthoff, G. (1986), 'Intermetallic phases as high temperature materials', *Z. Metallkde,* **77**, 654.

[24] Stephens, J.R., and M.V. Nathal (1988), 'Status and prognosis for alternative engine materials', *Superalloys 88*, S. Reichman et al. eds., The Met. Society, 183.

[25] Strutt, P.R., and B.H. Kear (1987), 'Creep in ordered Nickel base alloys', *High Temp. Ordered Intermetallic Alloys II*, Mat. Res. Soc., N.S. Stoloff et al. eds., 280.

[26] Wasilewski, R.J. (1966), 'Elastic constants and Young's modulus of NiAl', *Trans. Met. Soc. AIME*, **236**, 455.

[27] Voigt, W. (1928), *Lehrbuch der krystallphysik*, B.G. Teubner, Leipzig.

Table 4.1 Elastic compliances[1] S_{ij} from Rusović, and uniaxial moduli[1] $E_{<>}$ from them, and measured by Wasilewsky, $E^w_{<>}$

T (°C)	0	200	400	600	850
S_{11}	105.3	107.6	110.0	112.8	115.9
S_{12}	-42.2	- 43.0	- 44.1	- 45.3	- 46.4
S_{44}	87.4	91.7	96.5	1.010	1.093
$E_{<100>}$	95.0	92.9	90.9	88.7	86.3
$E_{<110>}$	187.2	181.1	175.1	169.0	161.1
$E_{<111>}$	276.7	264.9	253.3	242.1	226.7
$E^w_{<100>}$	97.4	94.8	92.3	89.7	87.1
$E^w_{<110>}$	192.5	185.5	178.5	171.6	164.6
$E^w_{<111>}$	286.6	272.4	258.2	244.0	229.8

(1) Units of S_{ij} : $\times 10^{-4}$ [GPa^{-1}]. Units of E, E^w: $[GPa]$

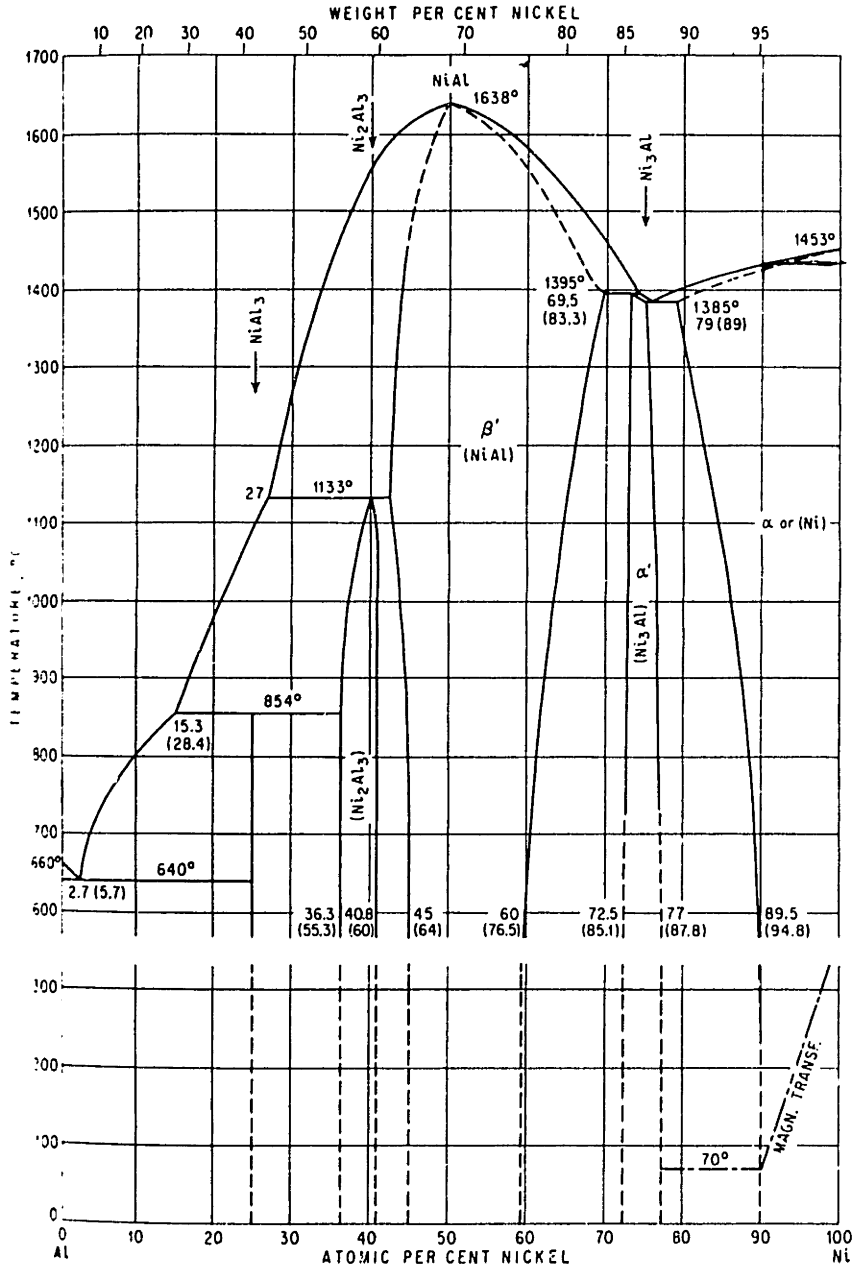

Fig. 4.1 Equilibrium phase diagram for Al-Ni (Hanson, 1958)

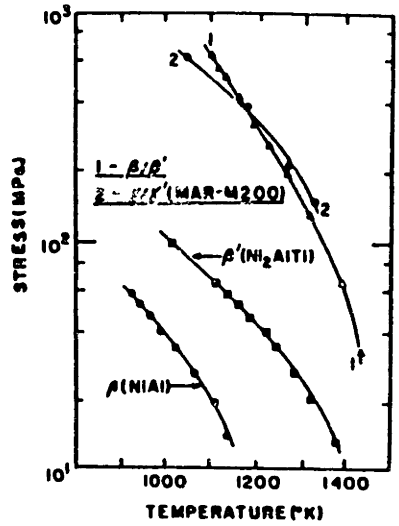

Fig. 4.2 Stress to maintain a creep rate of $10^{-7}\,s^{-1}$ vs. temperature in different Ni-base alloys (Strutt and Hear, 1987)

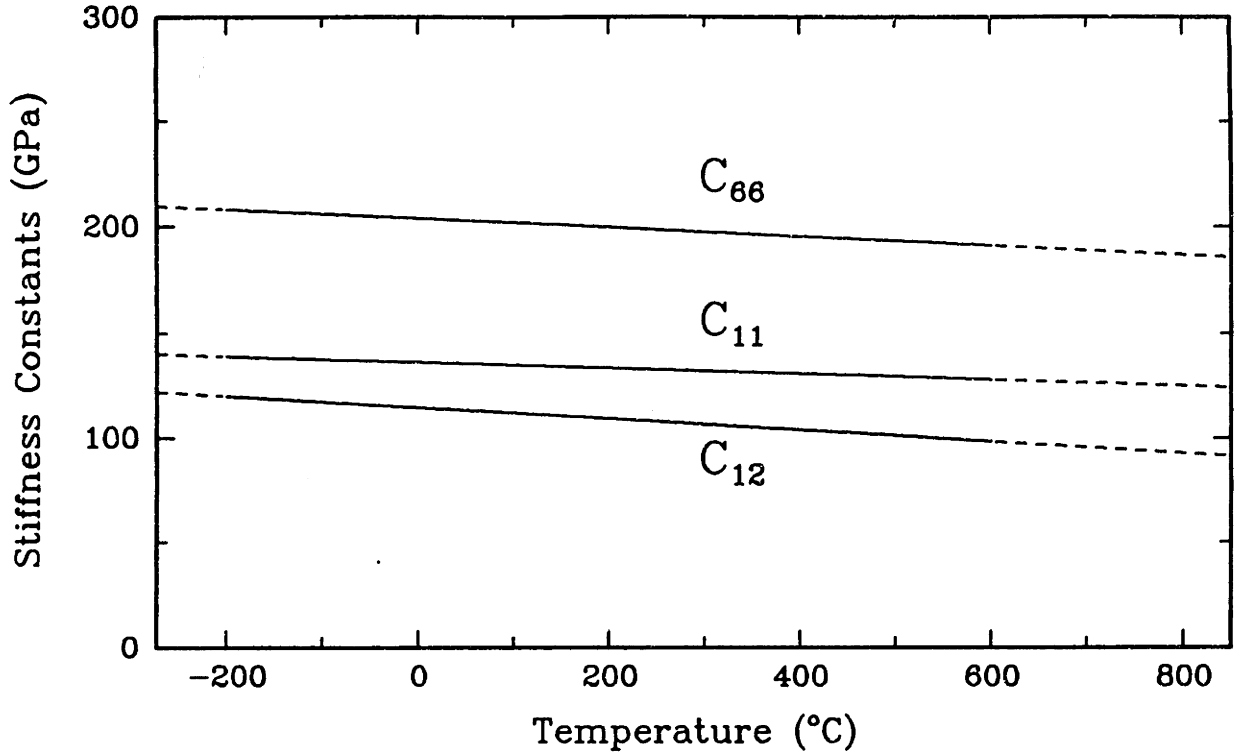

Fig. 4.3 Stiffness constants C_{ij} versus Temperature for NiAl

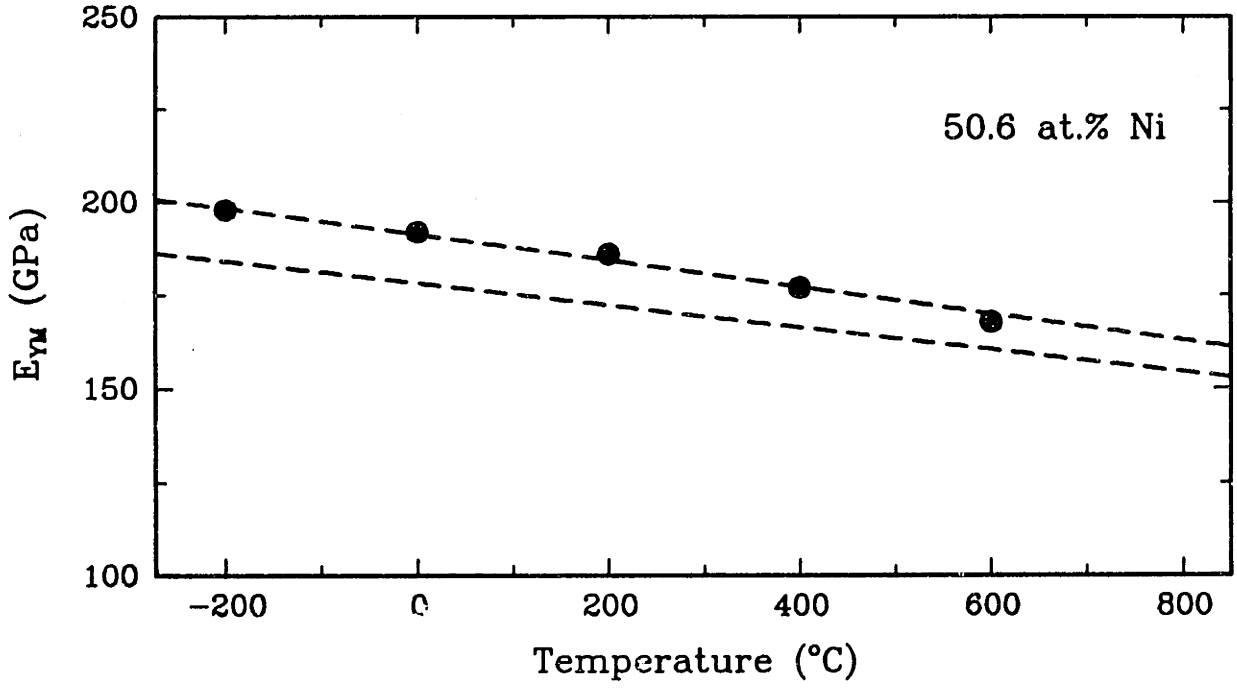

Fig. 4.4 Young's Modulus for NiAl: (– – –) Hashin and Shtrikman's bounds computed from single crystal data, (●) pollycrystalline data

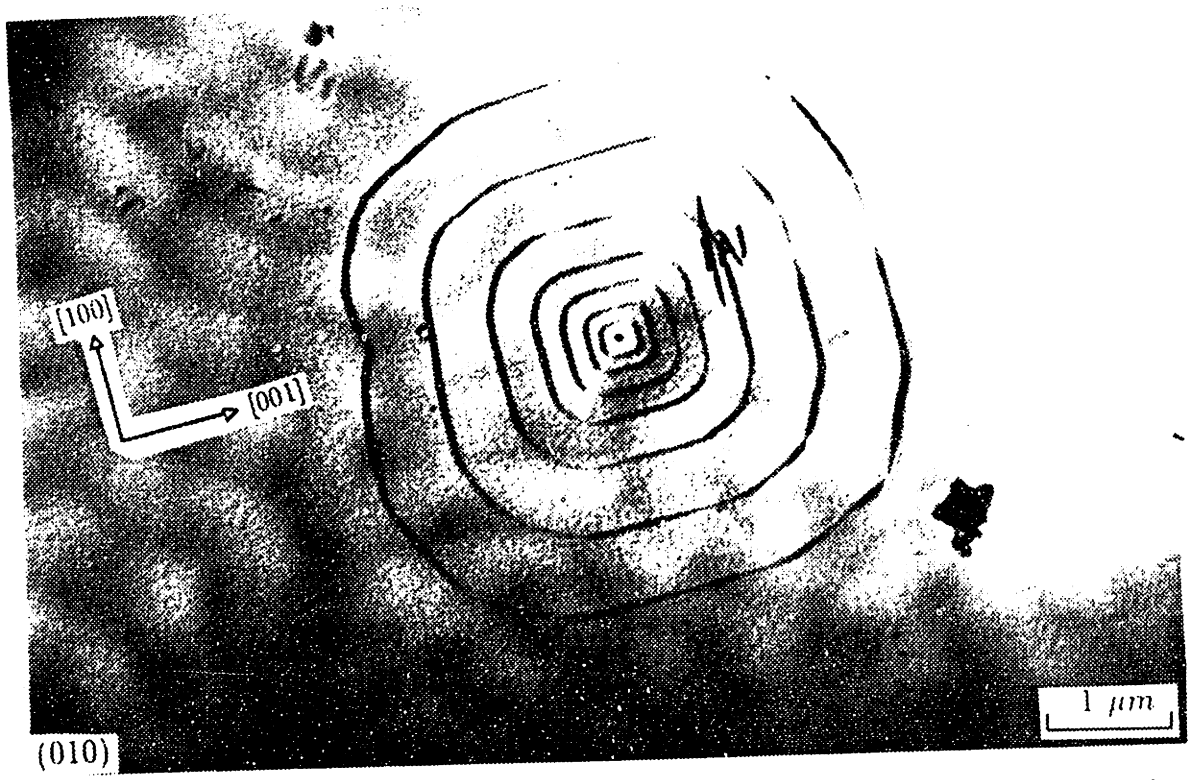

Fig. 4.5 Electron micrograph of typical concentric dislocation loops in NiAl

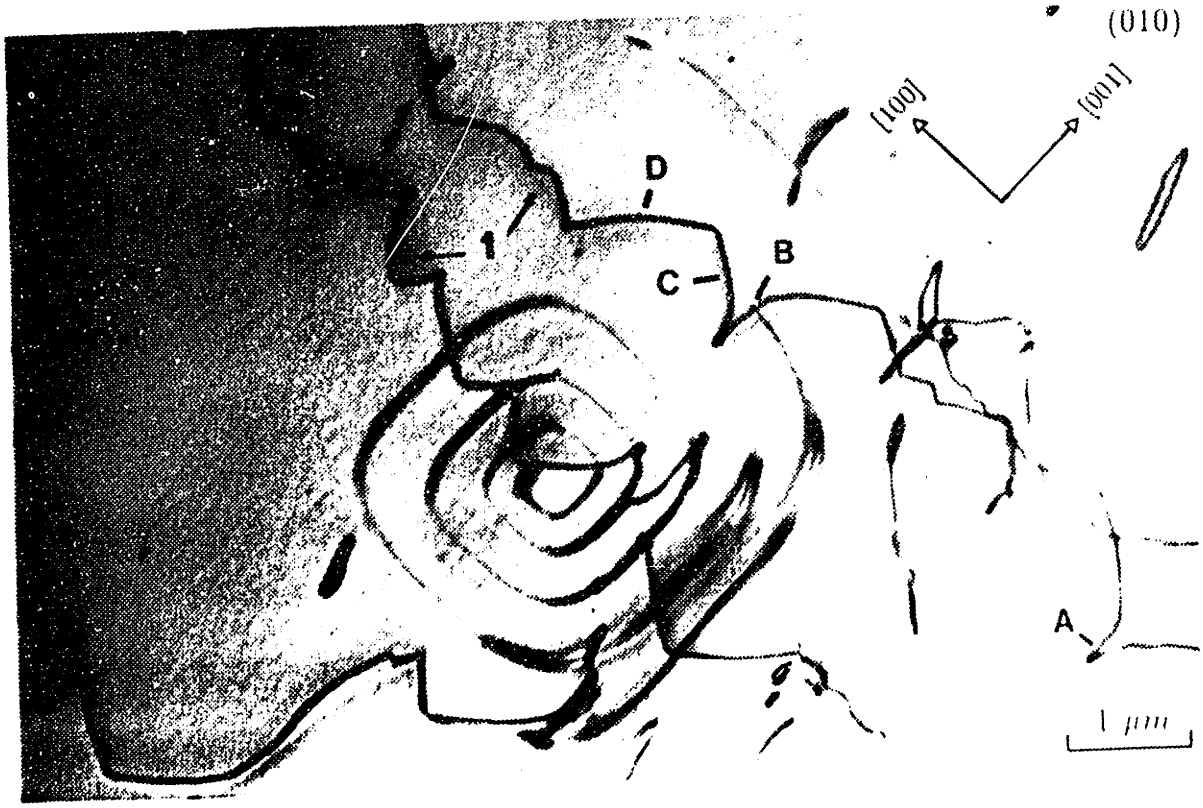

Fig. 4.6 Electron micrograph showing a helical dislocation and sharply kinked or zig-zag dislocations

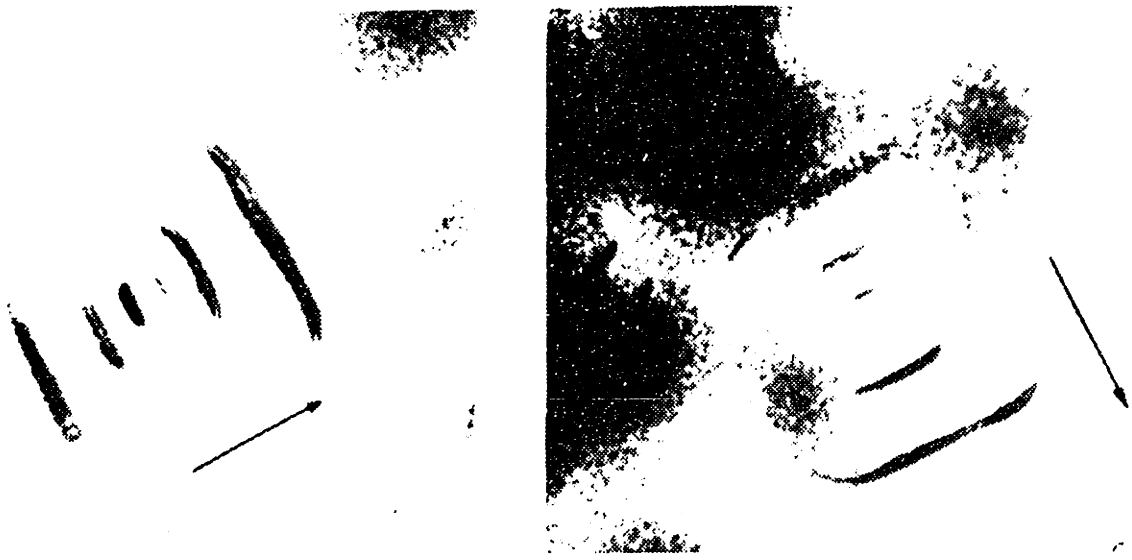

(a) $\mathbf{g} = [100]$ (b) $\mathbf{g} = [0\bar{1}0]$

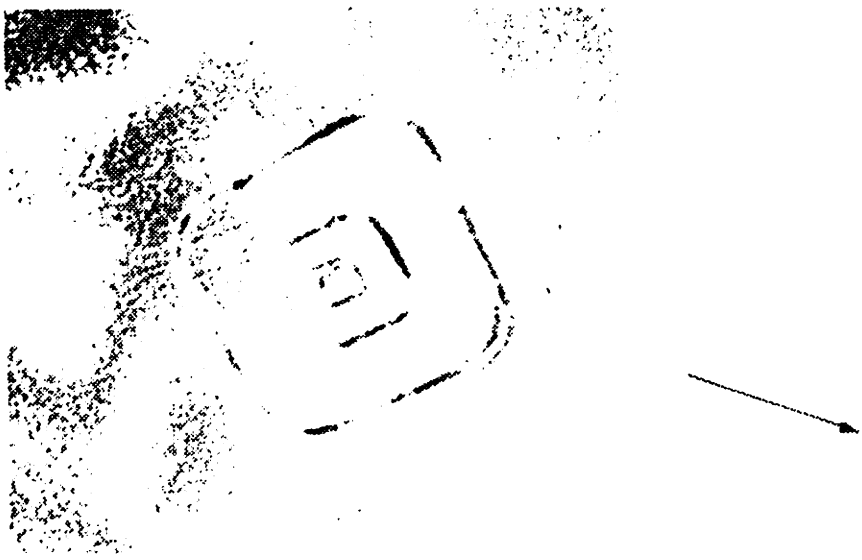

(c) $\mathbf{g} = [1\bar{1}0]$

Fig. 4.7 Determination of the Burgers vector of dislocation loops lying on a (001) plane

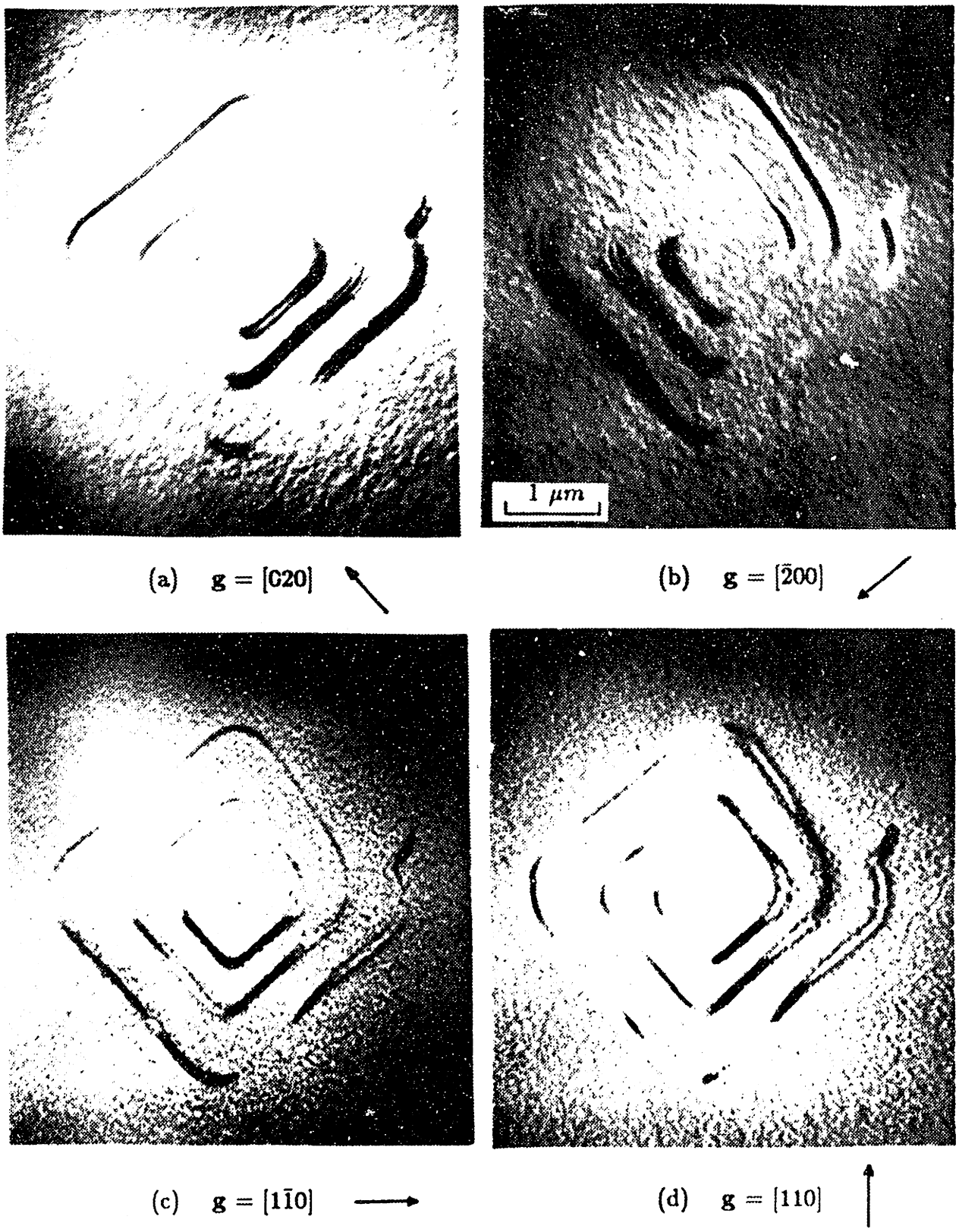

Fig. 4.8 Determination of the Burgers vector of spiral dislocations lying on a (001) plane

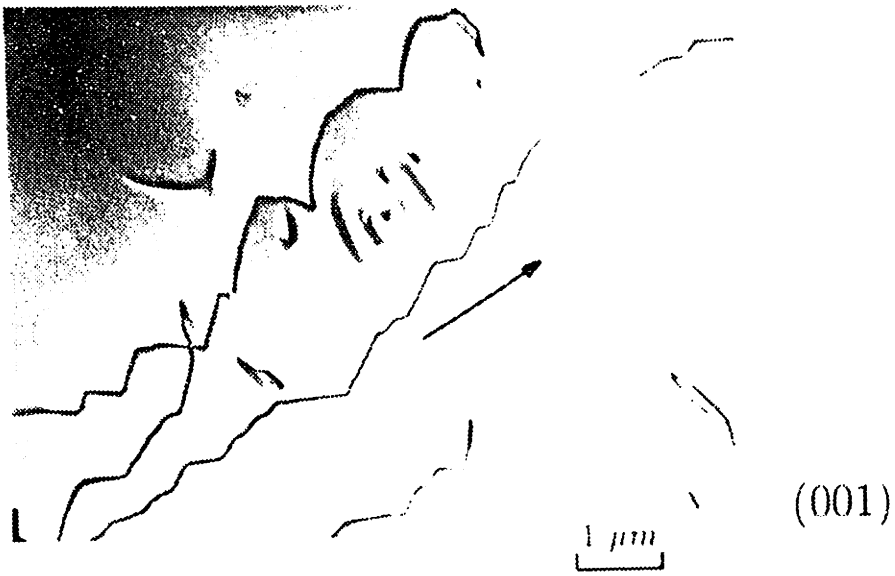

(a) $\mathbf{g} = [100]$

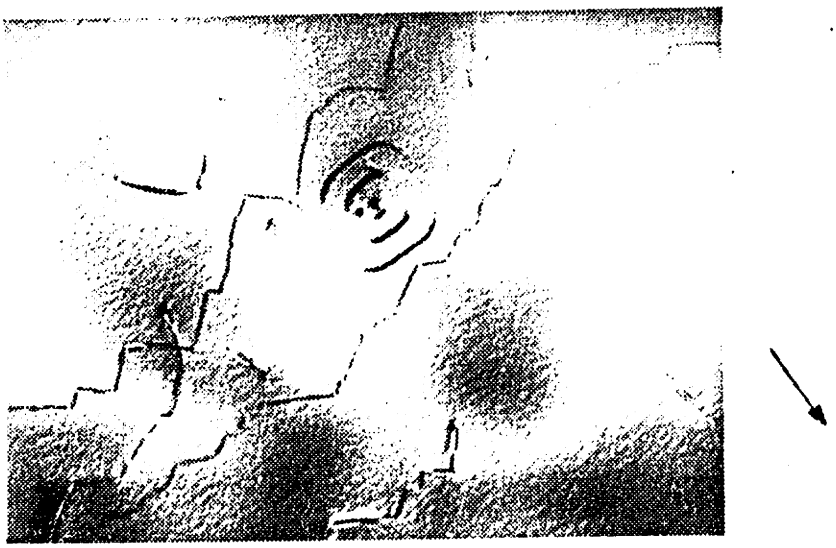

(b) $\mathbf{g} = [0\bar{1}0]$

Fig. 4.9 Image contrast of zig-zag dislocations lying on a (001) plane

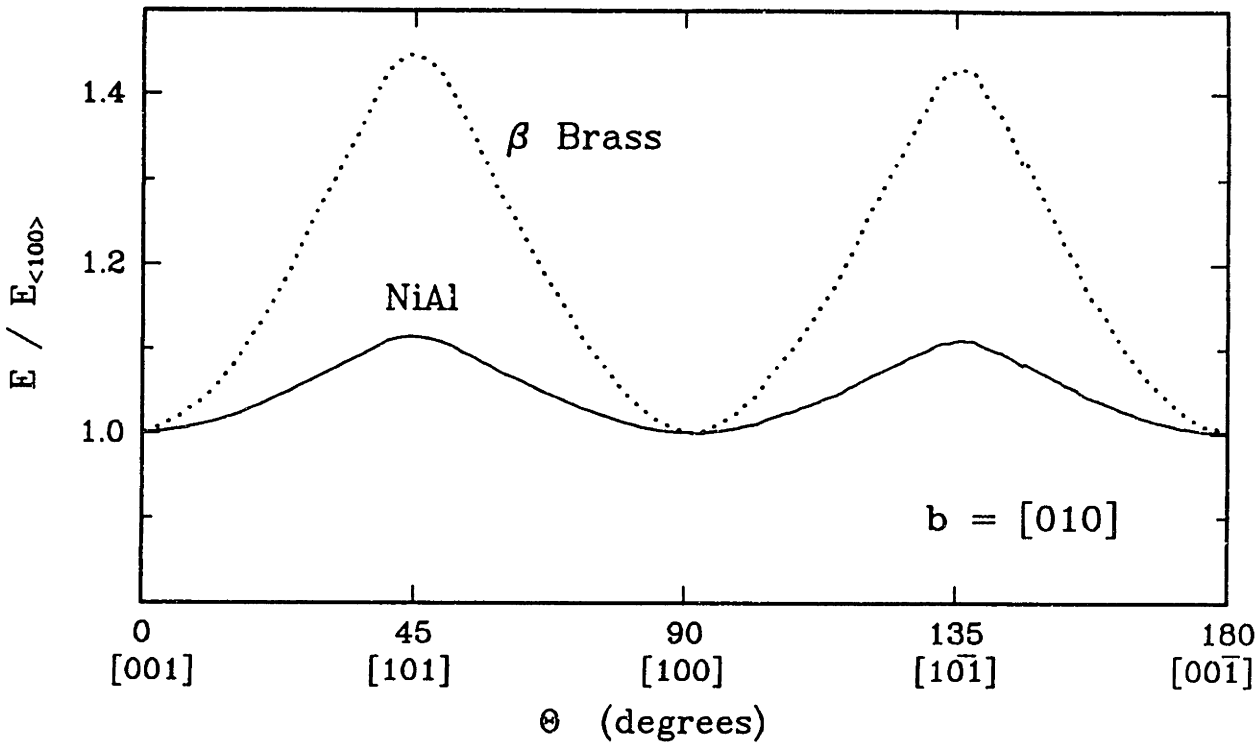

Fig. 4.10 Energy of a dislocation on a (010) plane normal to its Burgers vector in NiAl and β brass

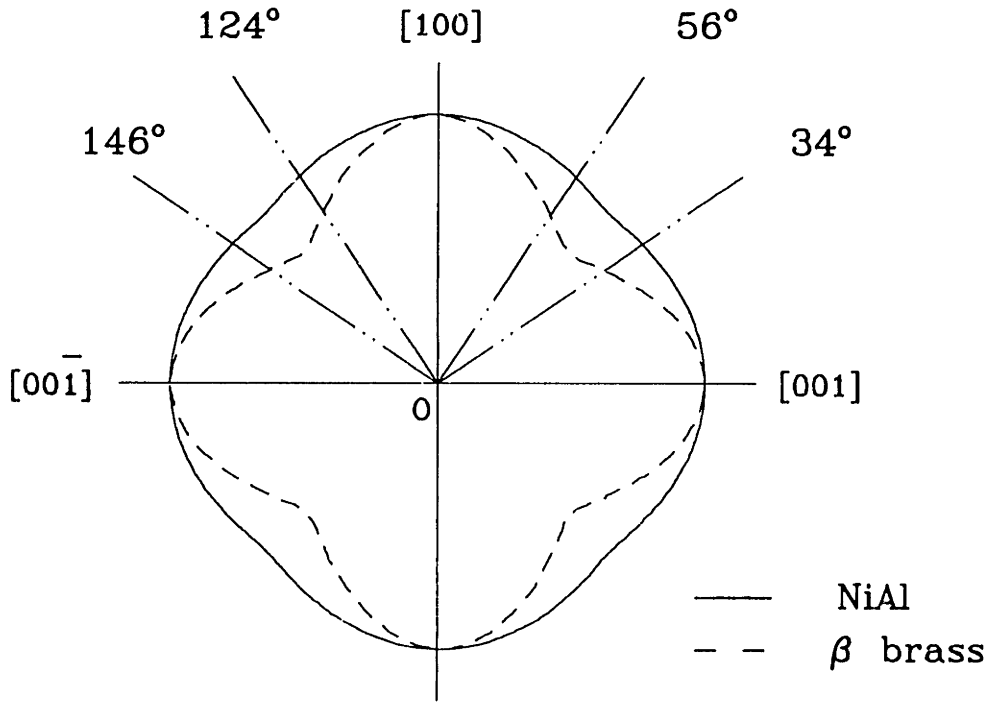

Fig. 4.11 Inverse Wulff plot showing the variation of the reciprocal of the elastic line energy of Fig. 4.10

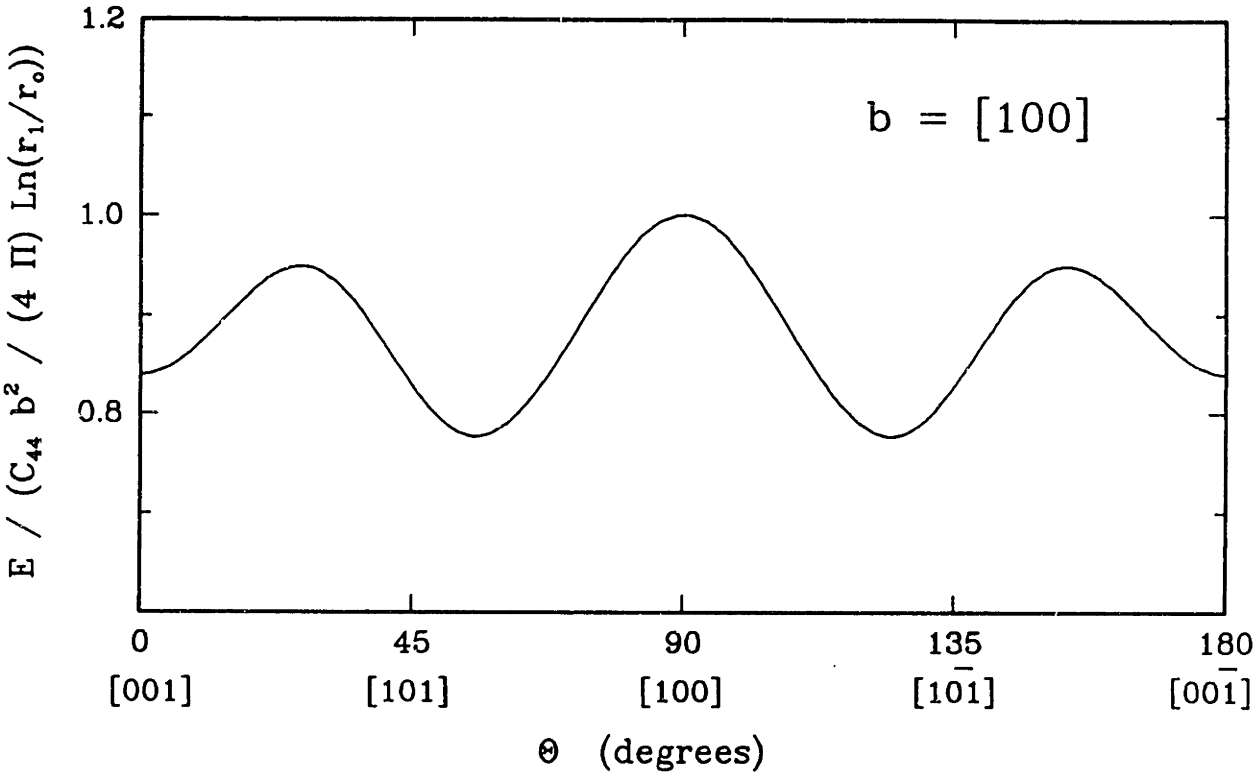

Fig. 4.12 Energy of a dislocation on a (010) plane in NiAl

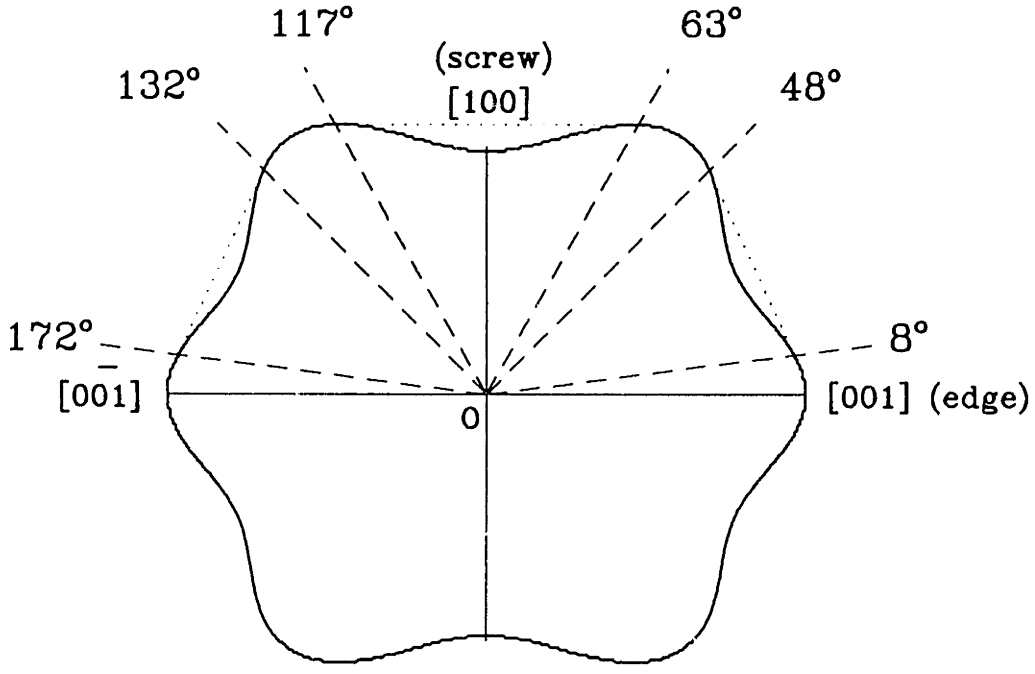

Fig. 4.13 Inverse Wulff plot showing the variation of the reciprocal of the elastic line energy of Fig. 4.12

Appendix 4.A Calculation of Cubic Elastic Compliances and Uniaxial Moduli from Single Crystal Data

The uniaxial moduli can be obtained from the elastic constants C_{ij} by first calculating the elastic compliances S_{ij}. Assume a uniaxial state of stress, with $\sigma_{11} \neq 0$ and $\epsilon_{22} = \epsilon_{33}$, then, from Eq. 4.1:

$$\sigma_{11} = C_{11}\,\epsilon_{11} + 2\,C_{12}\,\epsilon_{22}\,, \tag{4.A.1}$$

$$\sigma_{22} = 0 = C_{12}\,\epsilon_{11} + (C_{11} + C_{12})\,\epsilon_{22}\,. \tag{4.A.2}$$

Solve for ϵ_{22} in Eq. 4.A.2, and substitute it in Eq. 4.A.1,

$$\sigma_{11} = \left(C_{11} - \frac{2\,C_{12}^2}{C_{11} + C_{12}}\right)\epsilon_{11} = E_{<100>}\,\epsilon_{11}\,. \tag{4.A.3}$$

The inverse of $E_{<100>}$ in Eq. 4.A.3 and C_{44} give two of the compliances:

$$S_{11} = \frac{1}{E_{<100>}} = \frac{C_{11} + C_{12}}{(C_{11} - C_{12})(C_{11} + 2\,C_{12})};\quad S_{44} = \frac{1}{C_{44}}. \tag{4.A.4}$$

To find S_{12} in term of the coefficients C_{ij}, make use of the following relation (Hearmon, 1945),

$$C_{11} = \frac{S_{11} + S_{12}}{(S_{11} - S_{12})\,(S_{11} + 2\,S_{12})}\,, \tag{4.A.5}$$

and obtain S_{12} by solving the following quadratic equation derived from Eq. 4.A.5:

$$-S_{12}^2\,2\,C_{11} + S_{12}\,(C_{11}\,S_{11} - 1) + C_{11}\,S_{11}^2 - S_{11} = 0\,. \tag{4.A.6}$$

The uniaxial moduli are found from the inverse of the normal compliances along each of the three crystallographic orientations $<100>$, $<110>$, and $<111>$, and their direction cosines:

$$E_{<100>} = \frac{1}{S_{<100>}} = \frac{1}{S_{11}}\,,$$

$$E_{<110>} = \frac{1}{S_{<110>}} = \{S_{11} - \frac{1}{2}\,(S_{11} - S_{12} - \frac{1}{2}\,S_{44})\}^{-1}\,, \tag{4.A.7}$$

$$E_{<111>} = \frac{1}{S_{<111>}} = \{S_{11} - \frac{2}{3}\,(S_{11} - S_{12} - \frac{1}{2}\,S_{44})\}^{-1}\,.$$

Chapter 5

Mechanisms of Cyclic Deformation of NiAl Single Crystals at High Temperatures

Abstract

Cubic-oriented single crystals of the intermetallic NiAl were subjected to $\epsilon = \epsilon_m \pm 0.5\%$ cyclic strain histories at 750 and 850 ^oC. For $\epsilon_m = 0\%$, the material initially strain-softened for about 15 cycles, with re-arrangement of the dislocation structure. From the steady state cyclic response, excursions turn out to be transients lasting a fraction of a cycle. TEM analysis showed $\{110\} < 110 >$ slip systems to be operative, with a low dislocation density (e.g. $\rho = 3\ \mu m^{-2}$).

Stable cyclic responses obtained at different temperatures, strain rates, and mean strains revealed two dominant modes of deformation: kinematic hardening for $\Delta\epsilon = 1\%$, and isotropic hardening during monotonic deformation of 35%.

The types of interactions between dislocations in a given slip plane and forest dislocations penetrating that slip plane were studied for the $\{110\}< 110 >$ slip systems and the dislocation configurations observed in TEM foils. From this study and the role that thermal activation has in lowering the lattice resistance to dislocation

motion, it was found that the total slip plane glide resistance is due to lattice resistance and to forest dislocations, 58% of which were found to be impenetrable within the temperature and flow stress ranges studied here.

An idealized dislocation model describing the motion of gliding dislocations through a random network of impenetrable obstacles in the presence of lattice resistance shows that appreciable plastic flow is not observed until these obstacles can be bypassed. During kinematic hardening, obstacle bypassing can occur without a noticeable increase in dislocation density. As dislocations travel larger distances, they develop $< 111 >$ sessile segments and tangles, causing the dislocation density to increase over the level needed to balance recovery. The measured dislocation density at $\epsilon_m = 35\%$ of $\rho = 13.8\,\mu m^{-2}$ was predicted within 5% by the theoretical model.

5.1 Introduction

The operating conditions of high temperature structural components usually lead to complex histories of stress, inelastic strain, and temperature. Intermetallic compounds in general, and NiAl in particular, have been considered for such applications based on low density, high melting point, and good oxidation and corrosion resistance. Nevertheless, their actual structural applications have remained limited due to their inherent low temperature brittleness. There has recently been a renewed interest on NiAl and new research programs have been or are being started to develop new structural materials on the basis of NiAl phases, such as metal-matrix composites using NiAl as the matrix material in either fiber reinforced (e.g. Al_2O_3) or particle reinforced (e.g. TiB_2) composites (e.g. see reviews by Stephens and Nathal, 1988; Busso, 1989).

Although numerous studies of the high temperature behavior of monocrystalline NiAl have been published, the work found has been performed under monotonic or steady-state creep conditions. The present and future applications of NiAl require,

however, an understanding of its mechanical behavior under varying loads and temperatures. As a step in that direction, this work deals with the study of the high temperature steady-state cyclic and monotonic behavior of cubic-oriented NiAl single crystals. This analysis will be the basis for a micromechanics model to be introduced in the next chapter.

After a brief review of the known high temperature behavior of NiAl, the material response to small and large deformation histories and the resulting dislocation structures are described. A detailed analysis of dislocation motion in visco-plastic deformation is presented and its mechanistic implications for the observed macroscopic response are discussed.

5.2 Reported High Temperature Behavior of NiAl Single Crystals

5.2.1 Slip modes

The particular combination of slip plane and direction that could serve as a slip system usually arises from atomic density considerations. Strong directional bonding may make some atomic movements energetically unfavorable. In those alloys with covalent bonding and a relatively high anti-phase boundary energy, such as NiAl (APB energy = 0.4 J/m^2 = $0.07 \times 10^{-18} J/b^2$, Jung 1987), the predominant glide plane is the closest-packed plane, {110} for NiAl.

Plastic deformation of crystals compressed along any other direction than $<100>$ is caused by the operation of the $\{110\} <100>$ and $\{100\} <100>$ slip systems at all temperatures (see Table 5.1).

For NiAl crystals with a tensile or compressive axis within 8^o of $<100>$, conflicting data exist. The systems have been reported to be mainly $\{110\}<110>$ but sometimes also $\{211\} <111>$. Frazer et al. (1973a,b) observed $\{101\}<100>$ slip,

but this could not hold for a perfectly aligned < 100 > crystal.

5.2.2 High temperature strength and creep behavior

An interesting characteristic of the plastic deformation of NiAl is the difference in behavior between single crystal specimens loaded along < 100 > (so called 'hard' crystals) and those loaded away from < 100 > ('soft' crystals) at low and intermediate temperatures. The decreasing difference with temperature between the yield strengths of hard and soft crystals is shown in Fig. 5.1. The yield strengths for both crystals become equal at around 850°K (577°C).

Jung et al. (1987) recently discussed creep mechanisms in NiAl and concluded that the beneficial effect of atomic order (e.g. preferred vacancy sites) in reducing the diffusion rates during creep will be counteracted by the large number of vacancies arising from the lower energies of vacancies on preferred sites. Thus, the diffusion aspects of creep mechanisms do not differ much from those of b.c.c. metals and should not lead to special creep effects. It has also been reported (Strutt et al., 1970)(Hocking et al., 1971) that creep in NiAl above 950°C leads to the formation of well defined subgrain boundaries with a low dislocation density within the subgrains. The activation energy for creep of stoichiometric NiAl single crystals is constant within the range 850°C < T < 1050°C at 310 kJ.mole^{-1} (or 0.5×10^{-18} J) (Bevk et al., 1973). This is 10 % higher than that of β' (Ni_2AlTi) (Strutt et al., 1976). The creep exponent for hard < 100 > crystals from 527°C < T < 777°C was estimated by Fraser et al. (1973b) to lie in the range $6 < m < 12$.

Fig. 5.2 shows creep curves for compression specimens oriented along [101] and [001] axes tested at 850°C and four different stress levels, with the < 100 > orientation stronger by a factor of 2 to 3. (The steady-state creep rates in Fig. 5.2 are irregular giving exponents of 5 to 12). The low creep strength of < 100 >, e.g. 25 MPa for a

steady state creep rate of $\approx 10^{-7}\ s^{-1}$ at 850°C , is only about one twentieth of the strength of a typical $\gamma - \gamma'$ superalloy at the same temperature, see Fig. 4.2.

5.3 Specimens, Apparatus, and Procedure

5.3.1 Specimens

The chemical composition of NiAl was reported in Chapter 4. Rectangular cross-section bars oriented along cubic axes were machined into 100 mm long uniaxial specimens with button-head ends (Fig. 5.3) using electric-discharge machining. All single crystal specimens were electro-polished prior to testing, with a 10% HCl - 90% methanol solution (see Section 4.3).

Crystallographic orientations were determined by the standard Laue back-reflection method. The final orientations of the machined specimens were within $\pm 2°$ of $< 100 >$. The dislocation structure of deformed NiAl specimens was observed and analyzed using transmission electron microscopy (TEM) (see Chapter 4).

5.3.2 Apparatus and procedure

An apparatus was assembled to perform cyclic tests of the cubic NiAl single crystals at temperatures of up to 850 °C . The tests were done with a uniaxial servo-hydraulic system (Instron 1350) of a 100 kN capacity. Grip alignment was accomplished with a dial gauge to check that both the flatness of the horizontal grip surface and the grip concentricity with the axis of the servo-hydraulic piston were within 0.025 mm. No evidence of buckling was found on visually inspecting deformed specimens.

As shown in Fig. 5.4, the specimens were heated with two-turn concentric insulated induction coils made of 3 mm diameter Cu tubes connected to a high frequency (80 - 200 kHz) solid state induction generator (5 KW) through an impedance matching transformer. This coil configuration was needed to increase its inductance and

allow magnetic coupling between the coil and the low-magnetic-permeability NiAl specimen. Measurement of the temperature distribution along the specimen gauge length and calibration of the desired test temperature was performed with an optical fiber pyrometer with a measurement spot size on the specimen surface of 1.6 mm. The coil design was optimized so that the temperature difference along the 11.4 mm. gauge length never exceeded 6°C , up to 850 °C . Temperature control during the test was achieved by a Pt/Pt-10% Rd thermocouple (0.20 mm diameter) positioned on the specimen shoulder 1 mm away from the gauge length.

Water-cooled heat shields made of 3 mm copper sheets were placed between the induction coils and the grips to avoid excessive heating of the water-cooled grips. Strain measurements were done with a 15 % water-cooled high temperature extensometer (MTS-632.51) with a shortened 11.4 mm gauge length.

Control of the cyclic tests, loading histories, and data collection was done using the software package LabTech Notebook on a DELL 310 personal computer. Oscillations of $\pm$ 0.015% in strain and of $\pm$ 3 MPa in stress associated with the dynamic of the control system were smoothed out from some of the data reported in this chapter. A Fortran 77 computer program to generate loading commands for arbitrary loading histories is given in Appendix 5.D.

5.4 Small Cyclic Deformation Histories

Strain-controlled cyclic tests at 750 °C and 850 °C and stress drop and hold tests at 850 °C were performed to characterize < 100 > oriented single crystal behavior.

The temperature, strain and stress ranges were selected so as to obtain practically measurable stresses (50 - 200 MPa), and strains ($\pm$ 0.5%) and strain rates (0.01 to 0.001 S^{-1}) encountered during service in leading and trailing edges of gas turbine airfoils (Busso and McClintock, 1988). Preliminary experiments showed that, within

the temperature range tested, it was possible to return the material to its initial state (i.e. *structure*) after subjecting it to different strain histories and strain rate excursions within the $\pm$ 0.5 % strain range. As a result, different types of deformation histories were run on a single specimen, allowing not only a large number of tests with a limited number of single crystal specimens, but also verification of test results.

5.4.1 Cyclic test results

Fig. 5.5 shows that, for T = 850 °C and $\dot{\epsilon} = 10^{-3}\,s^{-1}$, the material appears to harden more than isotropically during the first cycle (stress at Point B, 8 % greater than stress at Point A), but on the second reversal it begins to soften by 5 %. This softening progresses until the steady-state cyclic response is reached with 20 % softening in about 15 cycles. Similar softening (including the anomalous hardening on first reversal) was observed in specimens tested at the other temperatures and rates. The strain hardening modulus decreases from h/E = 0.023 after the first reversal to the steady-state h/E = 0.007. The average modulus $E_{<100>}$ at 850°C measured from the hysteresis loops, $\approx$ 81 GPa, was consistent with the 86 GPa calculated from the elastic constants given in Chapter 4.

Stable cyclic responses obtained at 750 °C and 850 °C for three strain rates, $\dot{\epsilon} = 10^{-3}$, 3.2×10^{-3}, and $10^{-2}\,s^{-1}$, are shown in Fig. 5.6. The main characteristics of the resulting stress-strain hysteresis loops are their sharp yield followed by a purely kinematic hardening behavior[1]. The inverse strain-rate sensitivity of the flow stress,

$$n = \left.\frac{\partial ln\,\dot{\epsilon}}{\partial ln\,\sigma}\right|_T , \tag{5.1}$$

was approximately equal to 9.5 at 750°C and 7.3 at 850 °C , consistent with Fraser et al.'s data (1973b) (see Section 5.2.2).

[1] Here, the concept of kinematic hardening refers to the fact that despite the material hardening after yielding, it recovers its stabilized initial strength level after each reversal.

Tests with arbitrary strain reversals and increasing strain ranges within the $\pm 0.5\%$ strain region are shown in Figs. 5.7 and 5.8 respectively. Note that the small *roundness* at yielding (over $\Delta\epsilon \approx 0.05\%$) is present even after small strain reversals of 0.1%.

Stress drop and hold tests were performed to determine the average macroscopic internal or back stress which balances an applied stress giving zero subsequent strain rate. As Fig. 5.9 shows, the stress was cycled between ± 60 MPa, dropped from its maximum amplitude to successively decreasing fractions of it, and then held for 3 sec. The test objective is to probe the material with different driving forces (proportional to the difference between the applied stress during the holding period and an effective average internal or back stress) at constant structure and measure the resulting inelastic strain rates. The resulting stress-strain curves are shown in Fig. 5.10. (A similar test on an INCONEL 750 specimen at 850°C exhibited similar cyclic creep or ratchetting behavior). From the change of sign of the slope of the inelastic strain vs. time curves (e.g. see Fig. 5.9), the back stress was between 0.30 to 0.05 σ_{max}. (A value of the order of 5 to 7 per cent of the macroscopic stress was measured from the kinematic hardening exhibited by the hysteresis loops of Fig. 5.6). The constancy of the cyclic response to $\pm 0.5\%$ strain before and after the stress drop and hold test served to verify that any state change during the test was negligible.

Finally, strain rate change tests were performed. After a steady state cyclic response had been established, excursions from this steady state to a higher (Point A in Fig. 5.11) or lower (Point B) rate resulted in brief transients of $\approx$ 0.1 to 0.3% strain. The elastic slopes, $d\sigma/d\epsilon$, at the beginning of the transients are found from the $< 100 >$ elastic modulus $E_{<100>}$ and the elastic strain rate, which is the difference between the total (applied) strain rate $\dot{\epsilon}$ and the prior inelastic strain rate

$\dot{\epsilon}^{in}_{prior}$:

$$\frac{d\sigma}{d\epsilon} = E_{<100>}\left(1 - \frac{\dot{\epsilon}^{in}_{prior}}{\dot{\epsilon}}\right) . \qquad (5.2)$$

Before a change in rate $\dot{\epsilon}^{in}_{prior} \cong \dot{\epsilon}$, then a ten-fold increase in $\dot{\epsilon}$ at Point A should give an elastic slope of $0.9\, E_{<100>}$ (Eq. 5.2). Various specimens gave $\approx 0.7 - 0.9\, E_{<100>}$ slopes. Similarly, a ten-fold decrease in the rate at Point B should result in a negative slope of $-9\, E_{<100>}$, with -3 to $-8 E_{<100>}$ observed. This variability is consistent with the oscillations of the displacement response about the command signal of the control system (already smoothed out in the data shown in Fig. 5.11). Finally, the slope of $2.9\, E_{<100>}$ or more observed at a load reversal, where $\dot{\epsilon}^{in}_{prior} \cong -\dot{\epsilon}$, is consistent with the prediction of $2\, E_{<100>}$, Eq. 5.2.

5.4.2 Dislocation structure of cyclically deformed specimens

TEM films of cyclically deformed specimens ($\epsilon = \pm 0.5\,\%$) sectioned parallel to {100} and {110} planes revealed the {110}< 110 > systems to be the operative ones. For a <100> oriented specimen, there are four active {110}<110> systems (Fig. 5.12). Thus, deformation is symmetric double slip, which in NiAl gives uniform deformation without slip traces.

The Burgers vector of the observed dislocations[2] with tangent vector $\mathbf{t}$ was determined using the $\mathbf{g} \cdot \mathbf{b} = 0$ invisibility criterion[3] for screw dislocations, and the additional $\mathbf{g} \cdot \mathbf{b} \times \mathbf{t} = 0$ for edge dislocations (or altogether $\mathbf{g} \times \mathbf{t} = 0$). As the contrast images of an (001) foil in Fig. 5.13 show, a strong contrast is obtained for the generally edge dislocations parallel to those at A and B and the generally screw dislocations parallel to those at C and D in Fig. 5.13 (a) when a $\mathbf{g} = [\bar{1}\bar{1}0]$ diffraction

[2]The atomic size of a unit cell in NiAl is $a_{NiAl} = 0.288\, nm$ (Lautenschlager et al., 1987), giving $b_{<110>} = \sqrt{2}\, a_{NiAl} = 0.407\, nm$.

[3]A dislocation will be invisible if the diffracting plane with normal g is parallel to the dislocation-induced displacements.

is used. In contrast, the edge and screw dislocations A and D become invisible when a $\mathbf{g} = [100]$ diffraction is used in (b). Similarly, dislocations B and C are not visible in (c) for a $\mathbf{g} = [0\bar{1}0]$ diffraction.

The dislocation network was found to be composed mostly of edge and screw dislocations of nearly equal densities ($\approx 55\%$ screw). The dislocation structure was inhomogeneous with some regions showing a density of half or less of that of others. Fig. 5.14 shows a typical structure of the more dense regions. The total dislocation density, measured from a range of representative regions from different TEM films, was $3\,\mu m^{-2}$.

5.4.3 Transition from initial to cyclic dislocation structures

A comparison between the dislocation structures of undeformed and cyclically deformed NiAl reveals that the initial strain softening was accompanied by the re-arrangement of the initial dislocation structure, namely that resulting from solidification and homogenization treatment described in Chapter 4. This re-arrangement was associated with an increase in the dislocation density from 0.2 to 3 μm^{-2}.

Foils obtained after one $\epsilon = \pm 0.5\,\%$ strain cycle showed that some of the edge loops grew, changed plan-form due to climb, and distorted by out-of-plane glide. Furthermore, the number of dislocation loops decreased substantially during softening, possibly by diffusion mechanisms such as dislocation core diffusion (Frost and Ashby, 1982). With cycling, these $\{100\}<100>$ dislocations become less important as $\{110\}<110>$ dislocations are somehow generated.

5.4.4 Dislocation interactions in $\{\ 110\ \}<110>$ systems

A study of the dislocation interactions that can occur between edge and screw dislocations with $<110>$ Burgers vectors gliding on $\{110\}$ planes in NiAl will help

to identify the sources contributing to the overall slip plane glide resistance or flow stress.

Cubic NiAl single crystals slip as do ionic crystals having the sodium chloride crystal structure (Kear et. al, 1959), so similar dislocation interaction modes should be expected. When dislocations cut through each other, each dislocation acquires a jog or a kink[4] parallel to the others' Burgers vector. Three possible types of interactions can be identified in cubic NiAl.

Jog formation in screw dislocations. Consider a moving $(101)[\bar{1}01]$ screw dislocation, A-B Fig. 5.15a, which intersects a stationary edge dislocation D-C on an oblique 60° $(01\bar{1})$ plane. As the moving dislocation passes through the stationary one, the two parts of its glide plane beyond the intersected dislocation suffer a relative displacement K-J parallel to the Burgers vector of C-D. (Note that the intersected dislocation C-D will, at the same time, also acquire a jog parallel to A-B). The interpretation of the nature of the jog J-K can be simplified by resolving the jog in and normal to the slip plane of dislocation A-B. As can be deduced from Fig. 5.15a, the only jog that cannot be accommodated either by shear or by increasing the length of A-B is the jog normal to the glide plane, of magnitude $\mathbf{b}/2$. Furthermore, a screw dislocation with a jog component normal to its glide plane can only glide forward by dragging the jog along with it and leaving a trail of vacancies or interstitial atoms behind, depending on the sign of the dislocation and Burgers vector, a *non-conservative* process. This can also be seen by considering the screw to wrap around the intersecting dislocation, leaving a trail of parallel edge dislocations of opposite sign on glide planes $\mathbf{b}/2$ apart. Note that similar non-conservative jogs

[4] A jog is a short line of dislocation that connects a dislocation line in a certain crystallographic plane with another lying on an adjacent parallel glide plane. A kink, on the other hand, is a short dislocation segment that connects the ends of two parallel dislocations lying on the same glide plane.

will also be produced as the result of screw-screw dislocation interaction.

Jog formation in edge dislocations. A similar analysis can be followed to describe the intersection of a gliding edge dislocation, A-B in Fig. 5.15b, and a screw dislocation C-D on an orthogonal plane. The resulting jog, K-J, is normal to the glide plane of the dislocation and will glide in the cubic plane, $(0\bar{1}0)$. The jogged edge dislocation can move conservatively but to do so, it must drag the jog with it. This type of jogs, however, can lie on planes where there is little or no shear, as in Fig. 5.15b, and where the lattice friction resistance is higher than in the active {110} planes. A more complete analysis of whether or not the plane glide resistance can be overcome by the dislocation line tension will be given in the next section. The same type of jogged edge dislocations are formed as the result of edge - edge dislocation interaction.

The above two interactions are two of those possible between moving edge and screw $\{110\}<110>$ dislocations. All others can be worked out in a similar manner. Table 5.2 summarizes the jog characteristics for all interactions.

Sessile segments in screw dislocations. A third type of interaction takes place between screw dislocations gliding on oblique planes (Kear, 1959). Consider the two expanding loops in Fig. 5.16. The screw components of the loops glide towards each other and first intersect at Point A. As previously described, this intersection will result on the formation of non-conservative jogs in both gliding dislocations. As the unjogged upper parts of the dislocations continue their glide, they converge towards the line of intersection of the glide planes $< 111 >$ under the applied stress and attractive interaction forces developing an edge segment with a $< 110 >$ Burgers vector.

The contrast experiment of a $(0\bar{1}1)$ foil obtained from a cyclically deformed spec-

imen in Fig. 5.17 shows a [011] Burgers vector for the [111] dislocation segments [5], e.g. parallel to dislocation A in (a). A strong image contrast is obtained in (a) with $\mathbf{g} = [0\bar{1}\bar{1}]$, whereas the $< 111 >$ segments become invisible in (b) according to $\mathbf{g} \times \mathbf{t} = 0$ when $\mathbf{g} = [100]$.

5.4.5 Contributions to the flow stress

Among the possible contributions to the overall flow stress of NiAl single crystals, only two mechanisms appear to play dominant roles:

1. Lattice friction resistance to dislocation motion,

2. Obstacle-producing forest dislocations.

Other sources considered but less important are the following. Possible point defect solid solution hardening (e.g. see Kocks et al, 1975) mainly due to the positive elastic misfit caused by larger Ni atoms occupying Al lattice spacings in the Ni-rich alloy of the present study. It is however likely to be negligible in comparison to the mechanisms discussed above. Another possible strengthening source would be cross slip, such as a $< 110 >$ screw dislocation from a $\{110\}$ to a $\{111\}$ plane (Schmid factor of $\{111\} < 110 > = 0.41$ vs. 0.5 for $\{110\} < 110 >$). This could take place if pinning points developed on the cross-glide $\mathbf{t} =< 112 >$ dislocations, so the screw after cross-gliding could act as a Frank-Read source. However, no evidence of cross-slip was found in the microstructure.

Dislocation motion is only possible after the lattice friction resistance can be overcome. This mechanism (e.g. see Kocks et al., 1975), which arises due to the periodicity of the core energy of a dislocation as it moves through the lattice, and to the directionality of atomic bonding, takes place by nucleating small bulges of

[5]Note in proof: the Burgers vector seems to be inconsistent with the expected $[\bar{1}10]$ or [110]. Time, however, does not allow resolving the question.

one Burgers vector, **b**, along a dislocation line (if aligned with the lattice) which subsequently propagate and merge moving the dislocation line one **b**. For bowed dislocations, the small bulges (30 to 40 **b** long for NiAl, as calculated from a double-kink model using a quasi-parabolic potential) will be nucleated only where aligned with the lattice, and will then propagate towards the pinning points, with the jog motion along the dislocation easily activated.

After the lattice resistance is overcome, a gliding dislocation encounters forest dislocations along its path where it can be held back as the unsupported part of the dislocation bows out. The resistance to penetration that each obstacle offers to the gliding dislocation is governed by the characteristics of the resulting jog, e.g. see Table 5.2. This resistance is often characterized by a resistive force-penetration distance curve with a maximum resistive force $\hat{F}$ (Kocks et al., 1975). Since the maximum force that can act on an obstacle by the bowing of a dislocation segment around it (when interactions are neglected) is twice the line tension of the dislocation E, viz. twice the average elastic energy of an isolated straight dislocation per unit length, the maximum resistive force is usually normalized by $2\,E$:

$$\beta \equiv \frac{\hat{F}}{2\,E}\,. \tag{5.3}$$

Previous work (e.g. Argon and East, 1982) has shown that discrete obstacle resistance due to forest dislocations is due to some forest dislocations which can be penetrated and some which will be bypassed rather than being penetrated. Gliding dislocations will be interacting with both types of obstacles at all times. The strength of the penetrable forest will be greatest at 0 K and will decrease with increasing temperatures as more thermal energy becomes available.

In what follows, the nature and number fraction of obstacle-producing forest dislocations in cubic NiAl will be determined and their contributions to the total slip plane glide resistance established. (The $< 111 >$ sessile segments, Fig. 5.17, which

were found to make up only 5 to 10 % of the total dislocation density, will not be accounted for). The lattice resistance will subsequently be obtained by subtracting the discrete obstacle resistance due to forest dislocations from the total glide resistance.

5.4.6 Obstacle strength characterization

In principle, the total density of strong and weak obstacles could be calculated by studying each particular intersection between active dislocations. To that effect, interactions between gliding and forest dislocations will be studied based on energy considerations, and those which give strong reactions identified. An estimate of the forest resistance will be obtained from this analysis.

Under $< 100 >$ loading, only 3/4 of the total dislocation density ρ will interact with either $< 100 >$ edge or $< 110 >$ screw dislocations in a given $\{110\}$ plane. As previously discussed (see Table 5.2), gliding screw and edge dislocations which intersect any forest dislocations acquire non-conservative and conservative jogs respectively.

Conservative jogs could either be dragged along by the rest of the dislocation, or be overcome when the dislocation wraps around the obstacle, leaves a screw trail that cross-glides pinching off the obstacle leaving a dislocation loop behind, and continues to glide. Two factors support the possibility of a high dragging force on jogs in edge dislocations. *i*) These jogs lie on planes where the interplanar distance, e.g. the spacing between successive planes parallel to the glide plane of the jog (IPD in Table 5.2), is considerably smaller than that of $\{110\}$ active slip planes ($IPD_{(101)} = 0.707a$). A smaller interplanar distance usually translates into a higher associated lattice resistance. *ii*) The magnitude of the Burgers vector for $< 110 >$ slip, b = 0.4 nm, is 40% greater than that for $< 100 >$ slip; this requires dislocations to have a higher initial activation for complete lattice order to be restored when they

begin to glide. This high drag force is compounded by the low Schmid factor of the jog (SF in Table 5.2). It is then possible that, even though jogged edge dislocations can move conservatively, they can be held back at these points due to being unable to overcome the high glide plane resistance associated with their jogs. Fig. 5.18a shows experimental evidence of the existence of pinned screw dislocation segments (those parallel to $[\bar{1}01]$) in the cyclically deformed NiAl specimens. Fig. 5.18b, on the other hand, shows pinned edge segments aligned with the cubic axes. Here as elsewhere, the bowed configurations of the dislocation segments were preserved by switching off the induction heating immediately after stopping the tests at the point of maximum load in the cycle.

On the other hand, whether or not a non-conservative jog will be dragged along with the rest of the dislocation and leave a trail of defects behind will depend on the relative magnitude of the work done by the line tension E on the jog and the energy of formation of the defect E_f. If the obstacles could be overcome by a configuration of the dislocations in which the bowed segment is bent by an angle θ at each side of the obstacle, then

$$2\, E\, b \sin\theta \;\lesssim\; E_f\,. \tag{5.4}$$

Approximating E by $\mu b^2 / 2$, gives the angle θ at which the work done by the line tension equals the defect energy E_f :

$$\sin\theta \;=\; \beta \;=\; \frac{E_f / b}{\mu\, b^2}\,. \tag{5.5}$$

The formation energy of a vacancy at a jog for undissociated dislocations, e.g. that required to remove an atom from the lattice and place it on the surface of the crystal, has been measured by Parthasarathi et al. (1984) as $E_f = 0.23 \times 10^{-18}\, J$, or equivalently 140 KJ/mol. Considering that the non-conservative motion of a jog in $\{110\}< 110 >$ screw dislocations will leave 8 vacancies per unit b, with $\mu = 91{,}540$

MPa, Eq. 5.5 gives,

$$sin\,\theta = \beta = \frac{8\ 0.23 \times 10^{-18}}{91.54 \times 10^{9}\,(0.4 \times 10^{-9})^{3}} = 0.309\ ;\ \theta = 18^{o}\ . \qquad (5.6)$$

The energy to nucleate an interstitial atom is approximately five times higher than that for vacancies. Then the corresponding angle in Eq. 5.6 will be $\approx 90^{o}$. In either case, the interaction will result in the formation of a defect trail defect after intersection.

The weak or strong nature of the resulting jog will be greatly affected by whether or not the reaction between the interacting dislocations will be energetically favorable. Table 5.3s and 5.4 characterize the strengths of the jogs on gliding screw and edge dislocations respectively as they intersect $\{110\}< 110 >$ forest dislocations. [6].

The Burgers vector of the reacted dislocation ($\mathbf{b}_{12}$) and the ratio between the energy of the reacted dislocation and the sum of the individual dislocation energies is shown. When this ratio is less than unity, the reaction will be energetically favorable and will therefore take place. As it has been shown (Saada, 1957), when undissociated dislocations (as in NiAl) react at the point of contact with other dislocations, the applied stress σ_{lock} needed to force the interacting dislocations through one another and undo the reacted configuration can be higher than that needed to bypass the obstacle for a given forest density [7], $\rho_I = l_I^{-1/2}$. The corresponding σ_{lock} normalized by the Orowan stress ($\mu\ b / l_I$) are shown in Tables 5.3 and 5.4. Following the 2-D modeling work of Bacon, Kocks, and Scattergood (1973), bypassing will occur when $\sigma_{lock}/(\mu\, b/l_I > 0.6$.

The last criterion to identify those intersections which would not develop strong

[6]The interaction of the parallel $(101)[\bar{1}01]$ and $(\bar{1}01)[101]$ edge dislocations in Table 5.2 seems very unlikely since the reaction $a\ [\bar{1}01] + a\ [101] = 2a\ [001]$ is energetically unbiased. This is compounded by the fact that there is no shear stress on cubic planes to drive any reacted [001] dislocations in cross-slip.

[7]The role that thermal activation has in the *unlocking* process was found to be negligible (Saada, 1957).

obstacles to dislocation motion is the relative motion between gliding and forest dislocations. Unless the dislocations are being driven against (*opposed* in Tables 5.3 and 5.4) each other, the strength of the resulting obstacles are considered negligible.

Maximum resistive force of weak obstacle-producing forest dislocations neglecting lattice resistance.

A different approach to characterize the forest density based on the force to penetration of weak forest obstacles to gliding edge dislocations will be outlined. The main limitation of this approach is that since only the overall flow stress is known at this stage, it is not clear what fraction of the thermally activated flow stress corresponds to lattice friction and what to the thermally activated weak obstacles. Then, an accurate account of the weak obstacle strength cannot be done until the magnitude of the lattice friction is known. To provide a comparison to the first analysis, lattice friction will be neglected as a source of thermal activation and the strength of the weak obstacles under this assumption will be determined.

To obtain the desired force-distance curve of weak obstacles, values of the apparent or experimental activation area at different stress levels, and the dependence of the forest-resistance contribution to the flow stress on the normalized weak obstacle strength, Eq. 5.3, must be found first (Argon and East, 1982).

Next, a procedure will be followed to obtain an estimate of the weak obstacle strength when lattice friction contribution to the overall flow stress is neglected.

Apparent activation area. By definition, the stress derivative of the activation energy ΔG at constant structure gives the apparent activation area a^* through the Burgers vector b (Kocks et al., 1975),

$$a^* = -\frac{1}{b}\frac{\partial \Delta G}{\partial \tau} . \tag{5.7}$$

Express ΔG in terms of the inelastic strain rate $\dot{\gamma}$ at a temperature T through

$$\dot{\gamma} = \dot{\gamma}_R \, exp\left(-\frac{\Delta G}{k\,T}\right), \tag{5.8}$$

where k is the Boltzmann constant and $\dot{\gamma}_R$ the strain rate pre-exponential factor. For small stress changes $\tau_2 - \tau_1$, assuming that the pre-exponential factor $\dot{\gamma}_R$ is unaffected by stress, gives

$$a^* = \frac{k\,T}{b}\,\frac{ln(\dot{\gamma}_2/\dot{\gamma}_1)}{\tau_2 - \tau_1}\,, \tag{5.9}$$

where $\dot{\gamma}_1$ and $\dot{\gamma}_2$ are the strain rates immediately before and after the stress change. Fig. 5.19 gives the apparent activation area versus the total flow stress τ_R, calculated from Eq. 5.9 with the strain rate sensitivity exhibited by the stabilized loops of Fig. 5.6 at 750 and 850°C . (The short transients measured during strain rate drop and jump tests, e.g. Fig. 5.11, were neglected in obtaining $\tau_2 - \tau_1$, discussed in Section 5.5). τ_R in Fig. 5.19 was defined as the average of the flow stresses before and after the strain rate change. The scaling of the flow stress with the ratio of the shear modulus at 0 K and that at the test temperature allowed reducing all elastic interactions to a common reference level of 0 K. The apparent activation area for a given τ_R, a^* was related to the flow stress in Fig. 5.19 through an empirical relation of the form,

$$a^* = A\ ln\left[\frac{B}{\tau_R\,(\mu_0/\mu) - S_o}\right], \tag{5.10}$$

where $A = 1.935 \times 10^{-18}\,m^2$ and $B = 584$ MPa are constants chosen to fit the data, and $S_0 (= 38$ MPa) the experimentally measured flow stress, corrected for the shear modulus dependence on temperature, which becomes independent of temperature[8], Fig. 5.1. The assumed form of Eq. 5.10, plotted in Fig. 5.8, makes the apparent activation area infinity as the flow stress approaches the athermal flow stress S_0.

[8]The concept that a fraction of the flow stress could be considered athermal is consistent with data up to the highest tested temperatures, e.g. 1230 K by Pascoe and Newey (1968a). At higher temperatures, additional recovery processes may produce a softening effect whose effect on S_0 would have to be investigated.

Calculation of the normalized strength of weak obstacles. An estimate of the slip plane glide resistance for two or more different obstacles of different peak strengths for dislocation glide through a random mixture of obstacles has been obtained by Hanson and Morris (1975a,b), using a numerical model of dislocation glide. This resistance, τ_p, for a case of weak and strong obstacles with normalized strengths β_W, β_S, and fractions C_W, C_S, and expressed in terms of the random average total obstacle spacing l_I and the anisotropic line tension E_a is,

$$\tau_p = \alpha' \left(\frac{2\,E_a}{l_I\,b}\right) \left\{\left[C_W\,(sin^{-1}\,\beta_W)^3 + C_S\,(sin^{-1}\,\beta_S)^3\right]\right\}^{1/2} , \qquad (5.11)$$

where $\alpha' \cong 0.887$ is a statistically determined factor.

Assume that the strong obstacle fraction C_S is determined by the fraction of the total forest density which is impenetrable to gliding screw dislocations. Then, from Table 5.2, since 6/11 of the forest density will be intersected by gliding screw dislocations, $C_S = 0.55$. From the 2-D modeling work of Bacon, Kocks, and Scattergood (1973), the bypass stress for the forest spacings and obstacle diameter of interest here is $\beta_S \approx 0.6$.

Fig. 5.20 shows the dependence of the flow stress τ_R on the normalized weak obstacle strength β_W for cubic NiAl according to Eq. 5.11 with $\tau_p^* = \tau_p / (2\,E_a/b\,l)$ and $C_W = 1 - C_S$. Note the considerable decrease in strength for low β_W when the fraction of weak obstacles is increased to 87 % of the total forest density, as in pure Cu crystals (Argon and East, 1982).

The ratio of the total flow stress to the flow stress at which $\beta_W \rightarrow 0$ obtained from Eq. 5.10 should equal the ratio $\tau_p^*(\beta_W, \beta_S)/\tau_p^*(0, \beta_S)$ obtained from Fig. 5.20:

$$\frac{\tau_R\,\mu_o/\mu}{S_o} = \frac{\tau_p^*(\beta_W, \beta_S)}{\tau_p^*(0, \beta_S)} . \qquad (5.12)$$

The normalized weak obstacle strength β_W at each temperature can be obtained from Eq. 5.12 after substituting $\tau_p^* = \tau_p / (2\,E_a/b\,l)$ from Eq. 5.11. The computed

values of β_W corresponding to the flow stress range measured during the present experiments are shown in Table 5.5.

Based on the computed values of β_W, (Eq. 5.12) and on the impenetrability criterion, namely that $\beta \geq 0.6$ for any obstacle to be regarded as impenetrable, if lattice friction were negligible, jogs in gliding edge dislocations will develop into pinning points rather than being dragged along by the rest of the dislocation. This conclusion, however, leads to the following contradiction. Barring any other mechanisms , without weak obstacles and lattice friction there cannot be any mechanisms that can be thermally activated. Since the experimental results show that not to be the case (e.g. strain rate and temperature sensitivity of hysteresis loops of Fig. 5.6), then lattice friction should not be ignored.

5.4.7 Final obstacle strength characterization

From the analysis summarized in Tables 5.3 and 5.4, and from the knowledge that 3/4 of the total dislocation density ρ could interact with a given slip system, the density of strong and weak obstacles are,

$$\begin{aligned} \rho_{I\,strong} &= \frac{12}{24}\frac{3}{4}\rho = 0.375\,\rho\,, \\ \rho_{I\,weak} &= \frac{5}{24}\frac{3}{4}\rho = 0.156\,\rho\,. \end{aligned} \tag{5.13}$$

The small fraction of weak obstacles, the previous conclusions about the important role of lattice friction during thermal activation, and the absence of rounding (given by the amount of plastic flow before steady-state hardening) in the cyclic hysteresis loops justify neglecting the flow stress contribution from the weak obstacles. From here on, they will therefore be ignored.

Furthermore, as nearly 2/3rds of the dislocation forest intersect a given slip plane

at an oblique angle[9], take as an approximation the strong obstacle density as,

$$\rho_I \;=\; 0.8\,\rho_{I\,strong} \;=\; 0.3\,\rho\,. \tag{5.14}$$

The contribution to the total flow stress by the *strong* dislocation forest of density ρ_I regarded as being impenetrable discrete obstacles can be expressed, according to the statistical work of Kocks (1967), as

$$S_0 \;=\; 0.85\;\mu_0\;b\;\rho_I^{1/2}\,, \tag{5.15}$$

where μ_0 is the single crystal shear modulus at 0 K. Note that Eq. 5.11 can lead to Eq. 5.15 with $E_a = \mu_0 b^2/2$, $C_W = 0$, $C_S = 1$, and $\beta_S = 0.83$. The mean spacings of the entire dislocation forest, $l_I = \rho_I^{-1/2}$, that have to be cut by either edge or screw dislocation segments calculated from the total measured dislocation density are tabulated in Table 5.6.

The athermal component of the flow stress, Eqs. 5.14 and 5.15, can be expressed in terms of the total density ρ as,

$$S_0 \;=\; 0.85\;\mu_0\;b\;(0.3\,\rho)^{1/2}\,. \tag{5.16}$$

Fig. 5.21 shows the athermal flow stress S_0 for $\rho = 3\,\mu m^{-2}$ and the total flow stresses obtained by resolving the macroscopic yield strength of the stabilized cubic responses of Fig. 5.6 into the active $\{110\}<110>$ systems (Schmidt factor = 0.5). Once again, all elastic interactions were reduced to 0 K. Note the good agreement between the predicted S_0, according to Eq.5.16, and the experimentally measured athermal flow stress data under monotonic loading conditions (Pascoe and Newey, 1968a). Due to the permanent initial cyclic softening exhibited by NiAl, the resolved monotonic yield strength should be regarded as an upper bound to the flow stress.

[9]Given a total dislocation density per unit volume, the forest density will be the highest, the highest the fraction of dislocations piercing the slip plane at 90°.

Since only the lattice resistance is thermally dependent, its contribution to the total flow stress at constant structure and strain rate $\dot{\epsilon}$, and at a temperature T can then be determined directly from Fig. 5.21:

$$\tau_l(T) = \tau_R(T) - S_0 \frac{\mu(T)}{\mu_0} . \tag{5.17}$$

5.4.8 Mechanistic Implications

Contrary to what was expected, plastic flow was not observed (less than 0.01 %) at stresses immediately above the lattice resistance, Eq. 5.17, but instead occurred when the applied stress reached the overall glide resistance. To explain this behavior, consider the idealized model of Fig. 5.22 which describes the motion of a $(101)[\bar{1}01]$ screw dislocation in NiAl through a random network of impenetrable obstacles in the presence of lattice resistance. Here, the composition of the forest dislocations was obtained from to Table 5.2 and regarded as stationary for simplicity, and the repulsive or attractive character of the forest trees determined from the analysis presented in Appendix 5.A. The resolved shear stress-strain hysteresis loop measured experimentally at $\dot{\epsilon} = 0.01\, s^{-1}$ and T = 850 °C is included for reference.

While it is assumed that the interaction between gliding dislocation segments and forest dislocations occurs at the point of contact, the repulsive or attractive nature of screw forest dislocations piercing the slip plane will likely play a role in determining the equilibrium configurations of gliding screw dislocation segments. It can be shown, see Appendix 5.A, that although the integrated interaction force between two perpendicular screw dislocations will be constant and independent of their separation, those at 60° from each other will exhibit a distance-dependent interaction force. A more detailed study of the local equilibrium of dislocations when line tension, interaction forces, and lattice resistance are present is expected to yield results similar to those summarized in Tables 5.3 and 5.4, and should not alter

the semi-quantitative understanding to be gained from the present model.

As mobile dislocations overcome the lattice resistance they release the curvature which they had at the last reversal point (Position A in Fig. 5.22). As the applied stress τ is increased, they start bowing in the opposite direction until the stress needed to bow the dislocation segments or *bowing stress* τ_{bow}, (inversely proportional to the radius of curvature of bowed dislocations), reaches a critical value at the level of the flow stress, Position B. The rounding at B is due to the range of dislocation configurations.

For a given forest density, there are different arrangements by which some of the obstacles may be bypassed at a constant $|\tau_{bow}|_y$ (Kocks, 1967). This is likely to occur for a value of $|\tau_{bow}|_y \propto l_I^{-1}$, where l_I is the average forest spacing in the glide plane previously introduced. Since the bowing of a dislocation will be affected by anisotropy, its curvature will vary along its length. Assume for simplicity, however, that all dislocation segments bow out with a constant radius of curvature R. Thus, bypassing is expected to occur when R reaches a critical value of the order of half the mean random spacing of the forest trees in the slip plane, viz. $l_I/2 \approx 0.5\,\mu m$ (see Table 5.6).

The bowing stress at yielding, $|\tau_{bow}|_y$, is equal to the total flow stress less the lattice resistance τ_l (Eq. 5.17):

$$|\tau_{bow}|_y = |\tau| - \tau_l = S_0 \frac{\mu}{\mu_0}. \tag{5.18}$$

Eliminating S_0 in terms of the forest density ρ_I (Eq. 5.15) and taking $\rho_I = 0.3 \times 3\,\mu m^{-2}$ (see Table 5.6) gives

$$|\tau_{bow}|_y = 0.85\,\mu\, b\, \rho_I^{1/2} = 30.7\ MPa\,. \tag{5.19}$$

In Eq. 5.19, the elastic energy of a dislocation has been approximated by $\mu\, b^2\,/\,2$. However, a more accurate relation for the bowing stress at yielding should be ex-

pressed in terms of the anisotropic line energy E_a of a dislocation loop (Appendix 5.B):

$$|\tau_{bow}|_y = \frac{E_a}{b\,\rho_I^{-1/2}/2}\,, \tag{5.20}$$

where

$$E_a = (E_{screw}\,E_{edge})^{1/2}\,. \tag{5.21}$$

The energies per unit length of screw and edge dislocations are given in Table 5.7. Then, for an average gliding dislocation, $E_a = 7.24 \times 10^{-9}$ J/m, and with $\rho_I = 0.9\,\mu m^{-2}$, Eq. 5.20 gives $|\tau_{bow}|_y = 34.5MPa$, above that of Eq. 5.19.

Gliding dislocations comprising 1/4 of the total length per unit volume ρ can, by bypassing obstacles and traveling a small distance Δy, accommodate a small shear strain $\Delta\gamma$,

$$\Delta y = \frac{\Delta\gamma}{b\,\rho\,/\,4}\,, \tag{5.22}$$

(see Appendix 5.C). The steady-state trapezoidal shape of the hysteresis loop means that the increase in hardness is counteracted by recovery processes. One possible recovery mechanism is related to dislocation trails or dipoles formed after a gliding screw dislocation intersects a forest dislocation, see Fig. 5.22. These dipoles, which form immediately after obstacles are bypassed and consist of a trail of either vacancies or interstitial atoms depending on the sign of the gliding screw dislocation, impose a higher curvature on the dislocation from which they originated. The resulting higher stress, responsible for the hardening seen after yielding in Fig. 5.22, can be associated to the continued bowing of dislocations connected mainly to interstitial trails. Since it is expected that interstitial trails will act as vacancy sinks after they formed, breaking of interstitial trails from the rest of a dislocation by diffusion can take place either between B and C, or C and reversed yielding. This process,

which constitutes a kind of recovery, could remove most of the trails between a load reversal and yielding. Then, the process of dipole formation and recovery will again be repeated between C and A in Fig. 5.22.

The second recovery process is associated with the unpinning of clusters of redundant dislocations being held by small sessile segments which are removed by gliding dislocations (Argon and Deng, 1987, Prinz et al., 1982). (A few of them are shown in Fig. 5.14). Since there is steady state cyclic response, the number of dislocations which are constantly being stored into clusters must be close to the number which are being unpinned.

While bearing in mind the limitations of using a schematic dislocation network to describe such a complex process, we can learn from Fig. 5.22 that obstacle bypassing is likely to give much more strain than that given by the reversal of bowing before bypassing. This can be seen from the average motion of the gliding dislocation segment between Positions A and B as a fraction of the distance traveled between A and C in Fig. 5.22 (Eq. 5.22), approximately 3 % for the strain history considered in Fig. 5.22.

If the load is reversed at Point C, the process is then repeated until the next reversal point is reached and so on. In addition, should the deformation progress monotonically, the dislocation density will remain approximately unchanged for as long as the number of gliding dislocations being stored at clusters and sessile segments, and possible new dislocation loops generated by active sources, does not overcome the softening effects of recovery. Until that happens, the macroscopic deformation can be described as being purely kinematic.

5.5 Small Stress Transients

The undershoots and overshoots in strength during the transients (beyond the dynamics of the control system) can best be understood by analyzing the Orowan relation for the inelastic shear strain rate in terms of the magnitude of the slip vector b, the mobile dislocation density ρ_m, and the average velocity of the mobile dislocations v,

$$\dot{\gamma} = b\,\rho_m\,v\,. \tag{5.23}$$

Consider, for instance, the ten-fold increase in the imposed deformation rate at Point A in Fig. 5.11. At first, the resulting sudden increase in $\dot{\gamma}$ results in an increase in the elastic strains and the stress τ. A higher stress leads to a higher initial v. Furthermore, a higher stress should increase ρ_m by releasing new dislocations. This mechanism will however require small transients since, due to the too high v for the imposed $\dot{\gamma}$, they will be pinned or stored soon after the stress drops. Thus, the mobile dislocation velocity v and the structure will stabilize at the end of the transient. An analogous argument could be pursued for a strain rate drop to explain the undershoot in strength at Point D in Fig. 5.11.

5.6 Large Deformation Histories: Isotropic Hardening

From the mechanisms of cyclic deformation described in the previous section, it is expected that the overall dislocation density should eventually increase for larger strain amplitudes or monotonic deformation. A cubic oriented specimen was first cyclically stabilized at $\epsilon = 0\,\% \pm 0.5\,\%$, loaded monotonically to 35% strain and then cycled at $\epsilon = 35\,\% \pm 0.5\%$ strain.

5.6.1 Test results and observed dislocation structure

The test result for $\dot{\epsilon} = 0.01\, s^{-1}$, T = 850 °C , showed that steady state cyclic response following the monotonic deformation was achieved immediately after the first cycle (no cyclic relaxation observed). The $\pm$ 0.5% hysteresis loops before and after the mean strain of 35% are shown in Fig. 5.23. Here, the stress-strain loop retained the same sharp yield characteristics of the zero mean strain test, but with a 65% increase in the slip plane glide resistance τ_R, Table 5.8.

TEM observations of cubic and {110} films showed similar types of {110} < 110 > dislocations as the specimens with $\epsilon_m = 0\%$, with a higher density of sessile < 111 > segments, Fig. 5.24a. Bowing of some of the dislocation segments was apparent, such as the edge segments in Fig. 5.24b.

The dislocation density was measured at four sections normal to the [001] loading direction spaced 1 mm to one side of the center of the specimen. The two-beam condition for $\mathbf{g} =<$ 110 > refraction was used as the imaging condition to reveal all dislocations of the {110}< 110 > slip system family. The densities were obtained from more than ten different regions representative of the structures in each of the four [001] TEM films and were found to be within $\rho = 13.8 \pm 3.3\ \mu m^{-2}$.

The dislocation structure exhibited regions which appeared dense with dislocation tangles, which sometimes seem to form strands with dense tangles aligned preferentially parallel to the orientation of pure edge and screw dislocations (Fig. 5.25a). Other regions, however, showed less dense regions of untangled dislocations interrupted by dislocation cell walls spaced at 50 to 100 times the mean dislocation spacing, Fig. 5.25b.

5.6.2 Estimate of discrete obstacle resistance due to forest dislocations

An estimate of the athermal forest resistance S_0 for the $\epsilon = 35\,\% \pm 0.5\,\%$ strain history can be found from the new dislocation forest density, $\rho_I = 0.3\,\rho$, according to Eq. 5.15. Then, with $\rho = 13.8\,\mu m^{-2}$, $S_0(\rho) = 87.3$ MPa. Since the lattice resistance can be safely assumed to depend only on temperature and strain rate for the scale of the obstacle spacings considered in this work, another value of S_0 can be obtained from the experimentally measured flow stress τ_R at $\epsilon_m = 35\,\%$ and the lattice resistance τ_l measured at $\epsilon_m = 0\%$. Then, from Eq. 5.17:

$$S_0(\tau_R) = \frac{\mu_0}{\mu}\,(\tau_R - \tau_l)\,. \tag{5.24}$$

Table 5.8 summarizes these results and shows the excellent agreement, within 3 %, between $S_0(\tau_R)$ and $S_0(\rho)$.

5.7 Summary and Conclusions

1. This study has shown that cyclic deformation of monocrystalline NiAl is dominated by two different deformation modes, namely kinematic hardening in the small strain range regime ($\epsilon = \pm 0.5\%$), and isotropic hardening during monotonic deformation or large strain amplitudes ($\epsilon_m \approx 35\%$).

2. Due to the small deformations and no net state change involved in the cyclic tests, it was possible to run several tests on a single uniaxial specimen.

3. It was implicitly assumed that an increase in the number of retained dislocation loops will translate into an increase in forest density.

4. Initially, before settling into a steady-state cyclic response, the material strain cyclicly softens due to the re-arrangement of the initial dislocation structure.

$\{110\}< 110 >$ were found to be the active slip systems during cyclic deformation, and a low dislocation density (e.g. 3 μm^{-2} for $\pm$ 0.5% strain). After a steady state cyclic response is achieved, excursions from this state are only transients characterized by overshoots or undershoots in stress. They are associated with temporary excess or deficiency of mobile dislocations during a jump or drop in the imposed deformation rate respectively.

5. The contribution to the total flow stress by the fraction of the dislocation forest which gives rise to impenetrable discrete obstacles (58 %) was estimated from the total forest density. In summary, the total slip plane glide resistance was approximated by an athermal discrete obstacle resistance due to forest dislocations and the lattice resistance that can be both thermally and stress activated.

6. The role of $< 111 >$ oriented sessile dislocation segments formed as the result of screw dislocation intersections was found to be important in the formation of stable dislocation clusters for strain amplitudes larger than 0.5 %.

7. A mechanistic interpretation of the observed macroscopic behavior shows that appreciable plastic flow is not observed until the discrete obstacles can be bypassed. During kinematic hardening, obstacle bypassing results in the formation of dipoles in gliding screw dislocations which aid in kinematic hardening. These dipoles are constantly being sectioned or removed by diffusion-assisted recovery. Dislocations have to travel distances larger than 13 times the forest spacing to develop sessile dislocations and dislocation clusters so that the dislocation density can increase over the level needed to balance recovery processes. The measured dislocation density for $\epsilon_m = 35\,\%$ was found to be within 5 % of the predictions of the theoretical model.

8. This study makes progress towards understanding the cyclic and monotonic deformation of an ordered single crystal structure from known operative slip systems, dislocation interactions, and observed dislocation configurations. There are still unresolved problems in need of further study, such as vacancy-assisted recovery and possible thermal activation of weak obstacles.

Bibliography

[1] Argon, A.S. and G.H. East (1979), 'Forest dislocations in stage I deformation of Copper single crystala', *Proc. 5th Intnl. Conf. Strength of Metals and Alloys*, Aug. 1979, P. Haasen et al. eds, Pergamon Press, 9.

[2] Argon, A.S. and D. Deng (1984),'Mechanisms of Inelastic Deformation of Solids', *Materials Forum*, **11**, 91.

[3] Bacon, D.J., U.F. Kocks, and R.O. Scattergood (1973), 'The effect of dislocation self-interaction on the Orowan stress', *Phil. Mag.*, **28**, 1241.

[4] Ball, A. and R.E. Smallman (1966), 'The operative slip system and general plasticity of NiAl - II', *Acta Met.*, **14**, 1517.

[5] Bevk, J., R.A. Dodd, and P.R. Strutt (1973), 'The orientation dependence of deformation mode and structure in stoichiometric NiAl single crystals deformed by high temperature steady-state creep', *Met. Trans. A*, **4**, 159.

[6] Busso, E.P. (1989), 'High temperature materials in Japan: an overview of their research, development, and life prediction work', *MIT-Japan Program Technical Publication Series,* MITJP89-14, Center for International Studies, MIT, Cambridge, MA.

[7] Eshelby, J.D., W. T. Read, and W. Shockley (1953),'Anisotropic elasticity with applications to dislocation theory', *Acta Met.*, **1**, 251.

[8] Foreman, A.J.E. (1955),'Dislocations energies in anisotropic crystals', *Acta Met.*, **3**, 322.

[9] Fraser, H.L., R.E. Smallman, and M.H. Loretto (1973a), 'The plastic deformation of NiAl single crystals between 300 and 1050°K II. The mechanism of kinking and uniform deformation', *Phil. Mag. A,* **28**, 651.

[10] Fraser, H.L., R.E. Smallman, and M.H. Loretto (1973b), 'The plastic deformation of NiAl single crystals between 300 and 1050°K I. Experimental evidence on the role of kinking and uniform deformation in crystals compressed along $< 001 >$', *Phil. Mag. A,* **28**, 667.

[11] Frost, H.J., and M.F. Ashby (1982),'Deformation Mechanisms Maps', Pergamon Press.

[12] Hanson, K. and J.W. Morris (1975a),'Limiting configurations in dislocation glide through a random array of point obstacles', *J. Appl. Phys.*, **46**, 983.

[13] Hanson, K. and J.W. Morris (1975b),'Estimation of the critical resolved shear stress for dislocation glide through a random array of point obstacles', *J. Appl. Phys.*, **46**, 2378.

[14] Hartley, C.S., and J.P. Hirth J. P. (1965), 'Interaction of nonparallel, noncoplanar dislocations', *Acta Met.*, **13**, 79.

[15] Hirth, J.P., and J. Lothe (1982), *Theory of Dislocations*, 2nd ed. (J. Wiley pub.).

[16] Hocking, L.A., P.R. Strutt, and R.A. Dodd (1971), 'Comparison of steady-state creep behavior in stoichiometric CoAl and NiAl single crystals between 850 and 1050°C ', *J. Inst. Met.*, **99**, 98.

[17] Jung, I., M. Rudy, and G. Sauthoff (1987), 'Creep in ternary B2 aluminides and other intermetallic phases', *High Temp. Ordered Intermetallic Alloys II*, Mat. Res. Soc., N.S. Stoloff et al. eds., 263.

[18] Kanne, W.R., P.R. Strutt, and R. A. Dodd (1969), 'Nature of slip and substructure deformation during creep in stoichiometric NiAl at temperatures between 475 and 775°C', *Trans. Met. Soc. AIME*, **245**, 1259.

[19] Kear, B.H., A. Taylor, and P.L. Pratt (1959), 'Some dislocation interactions in simple ionic crystals', *Phil. Mag.*, **5**, 665.

[20] Kocks, U.F. (1966),'A statistical theory of flow stress and work hardening', *Phil. Mag.*, **13**, 541.

[21] Kocks, U.F. (1967),'Statistical treatment of penetrable obstacles', *Canadian J. of Physics*, **45**, 737.

[22] Kocks, U.F., A.S. Argon, and M.F. Ashby (1975), *Thermodynamics and Kinetics of Slip*, Progress in Mat. Sci., V. 19, Pergamon Press eds..

[23] Lautenschlager, E.P, T. Hughes, and J.O. Brittain (1967),'Slip in hard-sphere CsCl models', *Acta Met.*, **15**, p. 1347.

[24] McClintock, F.A., and A.S. Argon (1966), *Mechanical Behavior of Materials* (Addison-Wesley pub.).

[25] Parthasarathi, A. and H.L. Fraser (1984), 'The annealing of vacancy defects in β-NiAl', *Phil. Mag. A*, **50**, No. 1, 89.

[26] Pascoe, R.T. and C.W. Newey (1968a), 'The mechanical behavior of the intermediate phase NiAl', *Met. Sci. J.*, **2**, 138.

[27] Pascoe, R.T. and C.W. Newey (1968b), 'Deformation modes of the intermetallic phase NiAl', *Phy. Stat. Sol.*, **29**, 357.

[28] Prinz, F.B. and A.S. Argon (1984),'The evolution of plastic resistance in large strain plastic flow of single phase subgrain forming metals', *Acta Metall.*, **32**, No. 7, 1021.

[29] Saada, G. (1960),'Sur le durcissement dû à la recombinaison des dislocations', *Acta Metall.*, **8**, 841.

[30] Stephens, J.R., and M.V. Nathal (1988), 'Status and prognosis for alternative engine materials', *Superalloys 88*, S. Reichman et al. eds., The Met. Society, 183.

[31] Strutt, P.R., R.A. Dodd,and G.M. Rowe (1970), *Proc. 2nd Int. Conf. on the Strength of Metals and Alloys*, Metals Park, OH, 1057.

[32] Strutt, P.R., R.S. Polvani, and J.C. Ingram (1976), 'Creep behavior of the Heusler type structure alloy Ni_2AlTi', *Met. Trans. A*, **7A**, 23.

[33] Strutt, P.R. and B.H. Kear (1987), 'Creep in ordered Nickel base alloys', *High Temp. Ordered Intermetallic Alloys II*, Mat. Res. Soc., N.S. Stoloff et al. eds., p. 280.

[34] Teutonico, L.J. (1963), 'The dissociation of dislocations in the FCC structure', *Acta Met.*, **11**, 1283.

[35] Wasilewski, R.J., S.R. Butler, and J.E. Hanlon (1967), 'Plastic deformation of single-crystal NiAl', *Trans. Met. Soc. AIME*, **239**, 1357.

Table 5.1 Reported operative slip systems in stoichiometric NiAl single crystals

Slip system	*Deviation of loading axis from* $< 100 >$	*Temp. range* (°C)	*Ref.*
Crystals with tensile axis away from $< 100 >$			
$\{100\} < 100 >$ $\{110\} < 100 >$	45^0 45^0 $\approx 35^o$ $18^o - 45^o$	T < 1055°C ↓	Ball and Smallman (1966) Wasilewski et al. (1967) Kanne et al. (1969) Bevk et al. (1973)
Crystals with tensile axis on or close to $< 100 >$			
$\{211\} < 111 >$	$\approx 5^0$	$20 \leq T < 727$ ↓	Pascoe and Newey (1968a,b)
$\{110\} < 110 >$	$\approx 5^0$		Pascoe and Newey (1968a,b)
$\{110\} < 110 >$	8^0	$750 < T < 1055$	Bevk et al. (1973)
$\{110\} < 110 >$	?	$T \approx 850$	Strutt et al. (1970)
$\{110\} < 100 >$	2^0	$27 < T < 777$	Fraser et al. (1973a,b)

Table 5.2 Jog characteristics in gliding dislocations of the (101)[$\bar{1}$01] system resulting from their interactions with stationary ones of system i piercing the (101) plane

	Stationary System i :	(0$\bar{1}$1)[011]		($\bar{1}$01)[101]		(011)[0$\bar{1}$1]	
Active System:	*Dislocation Type*	*Edge* t= [100]	*Screw* t= [011]	*Edge* t= [0$\bar{1}$0]	*Screw* t= [101]	*Edge* t= [$\bar{1}$00]	*Screw* t= [0$\bar{1}$1]
(101) [$\bar{1}$01]	*Edge* t= [010]	t_{jog} = [011] SP_{jog} = (1$\bar{1}$1) IPD_{jog} = 0.29a SF_{jog} = 0.41 CON^1	t_{jog} = [011] SP_{jog} = (1$\bar{1}$1) IPD_{jog} = 0.29a SF_{jog} = 0.41 CON^1	– Do not intersect –	t_{jog} = [101] SP_{jog} = (0$\bar{1}$0) IPD_{jog} = 0.5a SF_{jog} = 0. CON^1 (Fig. 5.15b)	t_{jog} = [0$\bar{1}$1] SP_{jog} = ($\bar{1}\bar{1}\bar{1}$) IPD_{jog} = 0.29a SF_{jog} = 0.41 CON^1	t_{jog} = [0$\bar{1}$1] SP_{jog} = ($\bar{1}\bar{1}\bar{1}$) IPD_{jog} = 0.29a SF_{jog} = 0.41 CON^1
	Screw t= [10$\bar{1}$]	t_{jog} = [011] SP_{jog} = (1$\bar{1}$1) NON-CON^2 (Fig. 5.15a)	t_{jog} = [011] SP_{jog} = (1$\bar{1}$1) NON-CON^2	t_{jog} = [101] SP_{jog} = (0$\bar{1}$0) NON-CON^2	t_{jog} = [101] SP_{jog} = (0$\bar{1}$0) NON-CON^2	t_{jog} = [0$\bar{1}$1] SP_{jog} = ($\bar{1}\bar{1}\bar{1}$) NON-CON^2	t_{jog} = [0$\bar{1}$1] SP_{jog} = ($\bar{1}\bar{1}\bar{1}$) NON-CON^2

Note: t_{jog} : chosen positive direction along the jog for a right-handed Burgers circuit
SP_{jog} : slip plane of jog = $t_{jog} \times b_{jog} = t_{jog} \times [\bar{1}01]$
IPD_{jog} : interplanar distance. Spacing between sucessive planes parallel to SP_{jog} in terms of the lattice parameter a (the smaller IPD is, the higher the associated lattice resistance will be)
SF_{jog} : Schmid Factor of jog relative to [001] stressing (SF active system = 0.5)
CON^1 : conservative motion of the jog (it can leave Orowan loops behind)
NON-CON^2 : non-conservative motion of jog (glide plane of screw is different from that of the jog), it can leave vacancy or intersticial trails behind.

Table 5.3 Intersection between a (101)[$\bar{1}$01] gliding screw gliding dislocation and {110}< 110 > forest dislocations

Gliding Screw Dislocation	*Forest Dislocations*	$(0\bar{1}1) < 011 >$				$(\bar{1}01) < 101 >$				$(011) < 011 >$			
		Edge		*Screw*		*Edge*		*Screw*		*Edge*		*Screw*	
	$\mathbf{b}_2$ $\mathbf{t}_2$	a[011] [100]	a[0$\bar{1}\bar{1}$] [100]	a[011] [011]	a[0$\bar{1}\bar{1}$] [011]	a[$\bar{1}$0$\bar{1}$] [010]	a[101] [010]	a[$\bar{1}$0$\bar{1}$] [101]	a[101] [101]	a[0$\bar{1}$1] [100]	a[01$\bar{1}$] [100]	a[0$\bar{1}$1] [0$\bar{1}$1]	a[0$\bar{1}$1] [0$\bar{1}$1]
	$\mathbf{b}_{12} = \mathbf{b}_1 + \mathbf{b}_2$	a[$\bar{1}$12]	a[$\bar{1}\bar{1}$0]	a[$\bar{1}$12]	a[$\bar{1}\bar{1}$0]	a[$\bar{2}$00]	a[002]	a[$\bar{2}$00]	a[002]	a[$\bar{1}\bar{1}$2]	a[$\bar{1}$10]	a[$\bar{1}\bar{1}$2]	a[$\bar{1}$10]
$\mathbf{b}_1 = a[\bar{1}01]$	$E_{12}/(E_1 + E_2)$	0.56	0.35	0.56	0.35	1.00	1.00	1.00	1.00	0.56	0.35	0.56	0.35
$\mathbf{t}_1 = [10\bar{1}]$	*Angle between* $\mathbf{t}_1$ *and* $\mathbf{t}_2$	45°	45°	60°	60°	90°	90°	90°	90°	45°	45°	60°	60°
	$\sigma_{lock}/(\mu b/l_I)$	0.80	0.80	0.72	0.72	0.62	0.62	0.62	0.62	0.80	0.80	0.72	0.72
	Relative motion of gliding and forest disl.	Along	Opposed	Opposed	Opposed	Opposed	Opposed	Opposed	Along	Opposed	Along	Opposed	Opposed
	Obstacle	Negligible	Strong	Strong	Strong	Weak	Weak	Weak	Negligible	Strong	Negligible	Strong	Strong

Note: $E_{12}/(E_1 + E_2) = b_{12}^2/(b_1^2 + b_2^2)$

Table 5.4 Intersection between a (101)[$\bar{1}$01] gliding edge gliding dislocation and {110}< 110 > forest dislocations

Gliding Edge Dislocation	*Forest Dislocations*	(0$\bar{1}$1) < 011 >				($\bar{1}$01) < 101 >				(011) < 011 >			
		Edge		*Screw*		*Edge*	*Screw*			*Edge*		*Screw*	
	$\mathbf{b}_2$ $\mathbf{t}_2$	a[011] [100]	a[0$\bar{1}\bar{1}$] [100]	a[011] [011]	a[0$\bar{1}\bar{1}$] [011]		a[$\bar{1}$0$\bar{1}$] [101]	a[101] [101]		a[0$\bar{1}$1] [100]	a[01$\bar{1}$] [100]	a[0$\bar{1}$1] [0$\bar{1}$1]	a[0$\bar{1}$1] [0$\bar{1}$1]
	$\mathbf{b}_{12} = \mathbf{b}_1 + \mathbf{b}_2$	a[$\bar{1}$12]	a[$\bar{1}\bar{1}$0]	a[$\bar{1}$12]	a[$\bar{1}\bar{1}$0]		a[$\bar{2}$00]	a[002]		a[$\bar{1}\bar{1}$2]	a[$\bar{1}$10]	a[$\bar{1}\bar{1}$2]	a[$\bar{1}$10]
	$E_{12}/(E_1 + E_2)$	0.56	0.35	0.56	0.35		1.00	1.00		0.56	0.35	0.56	0.35
$\mathbf{b}_1$ = a[$\bar{1}$01]	*Angle between*					DO NOT							
$\mathbf{t}_1$ = [010]	$\mathbf{t}_1$ *and* $\mathbf{t}_2$	90°	90°	45°	45°		90°	90°		90°	90°	45°	45°
	$\sigma_{lock}/(\mu b/l_f)$	0.62	0.62	0.80	0.80		0.62	0.62		0.62	0.62	0.80	0.80
	Relative motion of gliding and forest disl.	Along	Opposed	Opposed	Opposed	INTERSECT	Opposed	Opposed		Along	Opposed	Opposed	Opposed
	Obstacle	Negligible	Strong	Strong	Strong		Weak	Weak		Negligible	Strong	Strong	Strong

Table 5.5 Activation parameters for dislocation glide through a random field of weak and strong point obstacles ($\beta_S = 0.6$)

τ_R [MPa]	S_0 [MPa]	a^* [nm^2]	$(\tau\,\mu_o/\mu)/S_0$	$\tau_p^*(\beta_W,\beta_S)$ (Eq. 5.11)	$\tau_p^*(0,\beta_S)$ (Eq. 5.11)	β_W (Eq. 5.12)
28.7	38.0	∞	1.000	0.340	0.340	0.000
37.5	↓	7.53	1.313	0.446	↓	0.579
43.9		6.49	1.537	0.522		0.691
51.4		5.72	1.800	0.611		0.783
55.7		5.50	1.895	0.644		0.811
63.7		4.99	2.166	0.736		0.874
70.9		4.62	2.411	0.819		0.917

Table 5.6 Area density and mean spacing of the dislocation forest piercing any active {110} slip plane

	Mean strain = 0 %		*Mean strain = 35 %*	
Obstacle type:	*No. of forest disl.*[1]*/ unit area,* ρ_I	*Mean spacing*[2]*,* $l_I = \rho_I^{-1/2}$ [μm]	*No. of forest disl.*[1]*/ unit area,* ρ_I	*Mean spacing*[2]*,* $l_I = \rho_I^{-1/2}$ [μm]
Strong	$\frac{3}{8} \cdot \rho\|_{\epsilon_m=0\%}$	0.94	$\frac{3}{8} \cdot \rho\|_{\epsilon_m=35\%}$	0.44
Weak	$\frac{15}{96} \cdot \rho\|_{\epsilon_m=0\%}$	1.46	$\frac{15}{96} \cdot \rho\|_{\epsilon_m=35\%}$	0.68

1. $\rho|_{\epsilon_m=0\%} = 3 \cdot 10^{12}\ m^{-2}$, $\rho|_{\epsilon_m=35\%} = 1.38 \cdot 10^{13}\ m^{-2}$ 2. Unit volume $= l_I \cdot l_I \cdot l_I$
3. The number of screw and edge segments is assumed to be equal

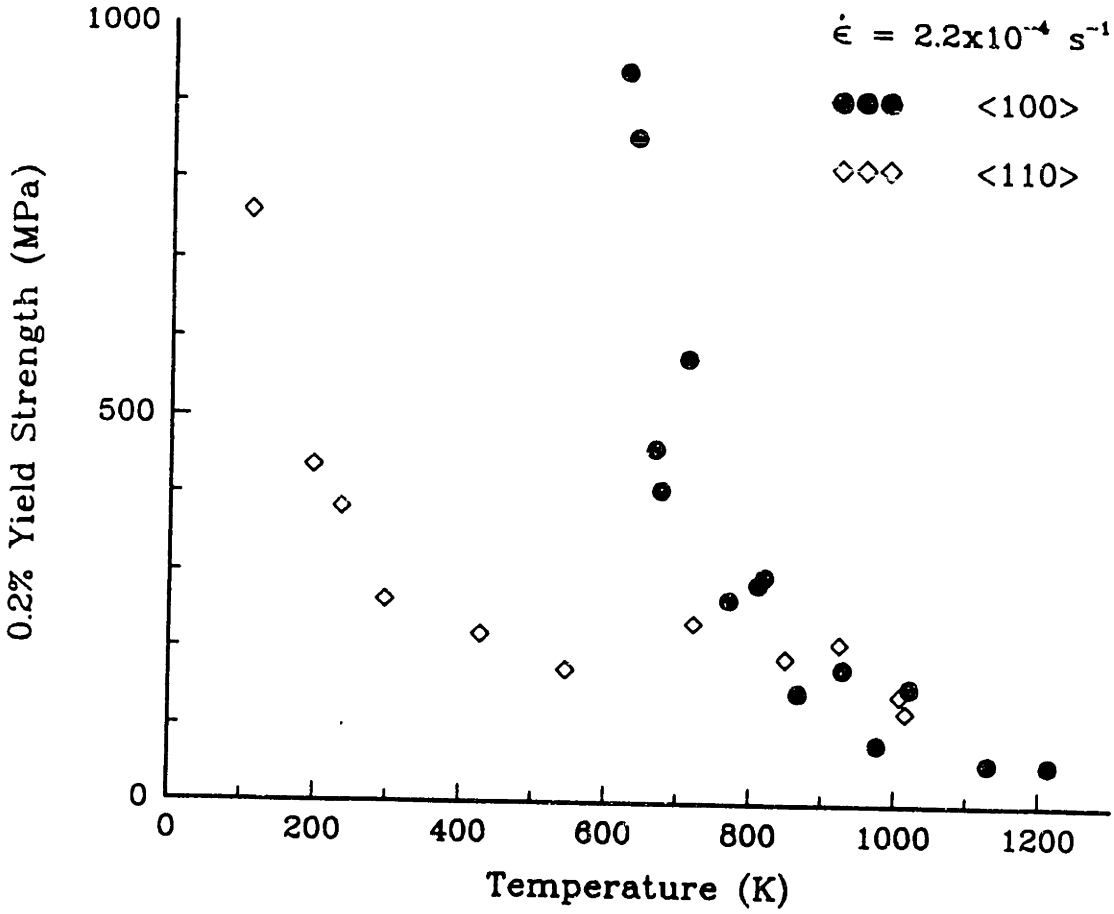

Fig. 5.1 Temperature dependence of the monotonic 0.2% yield strength of stoichiometric NiAl single crystals (Pascoe et al.,1968a)

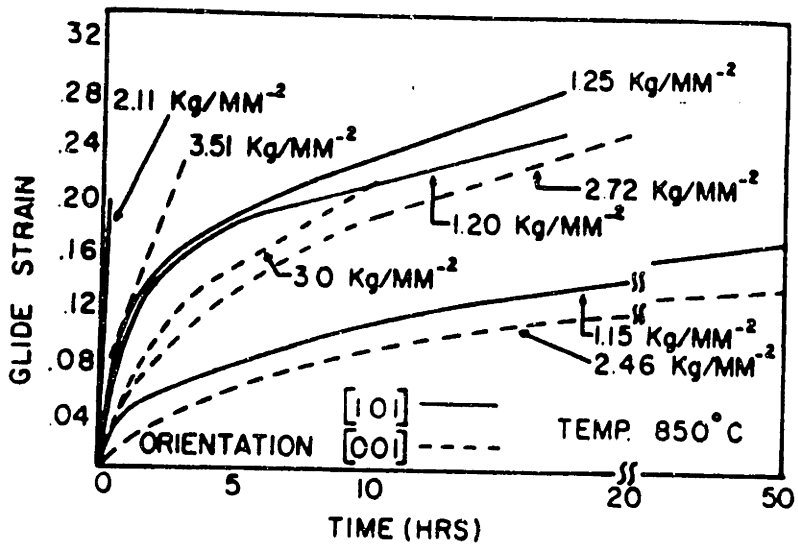

Fig. 5.2 Creep curves for NiAl single crystals obtained from compression specimens (Strutt et al., 1970)

Table 5.7 Total anisotropic energy of a straight dislocation for $\rho = 3\ \mu m^{-2}$

	K [MPa]	α_c	E [J/m]
Edge	76,845	3.24	8.529×10^{-9}
Screw	53,069	4.69	6.149×10^{-9}

Table 5.8 Estimates of the athermal flow stress from the measured flow stress and dislocation density

($T = 850°C$, $\dot{\epsilon} = 10^{-2}\ s^{-1}$)

Mean strain %	τ_R [MPa] (Fig. 5.21)	τ_l [MPa] (Fig. 5.21)	$S_o(\tau_R)\,\mu/\mu_o \equiv \tau_R - \tau_l$ [MPa] (Eq. 5.17)	$S_o(\rho)\,\mu/\mu_o$ [MPa] (Eq. 5.16)
0	51.4	20.7	30.7	$\equiv S_0(\tau_R)\mu/\mu_0$
35	84.8	↓	64.1	65.6

(Scale 1:1)

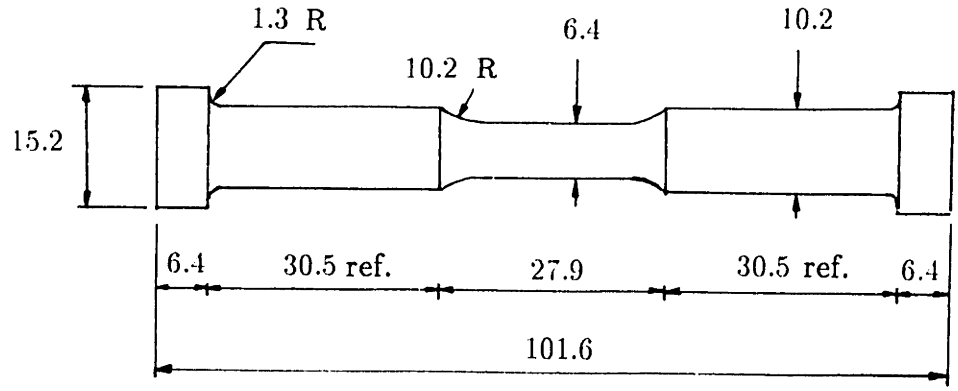

Fig. 5.3 Detailed drawing of uniaxial specimen with button-head ends (all dimensions in mm)

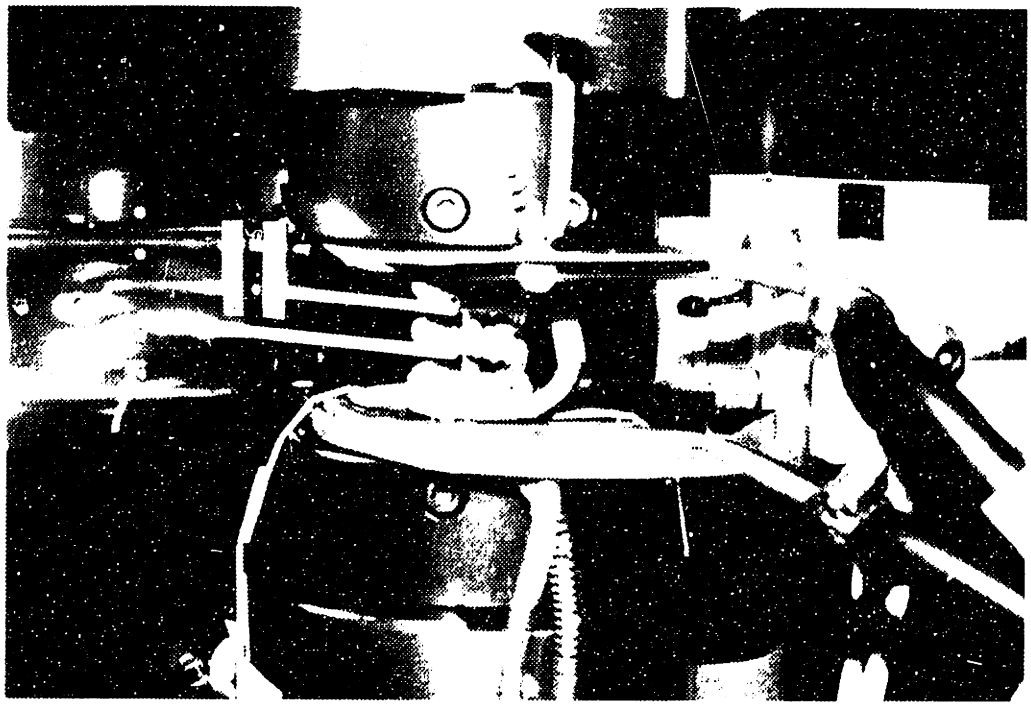

Fig. 5.4 Side view of apparatus showing insulated induction coil, high temperature extensometer rods, refrigerated Cu heat sinks, and water cooled grips

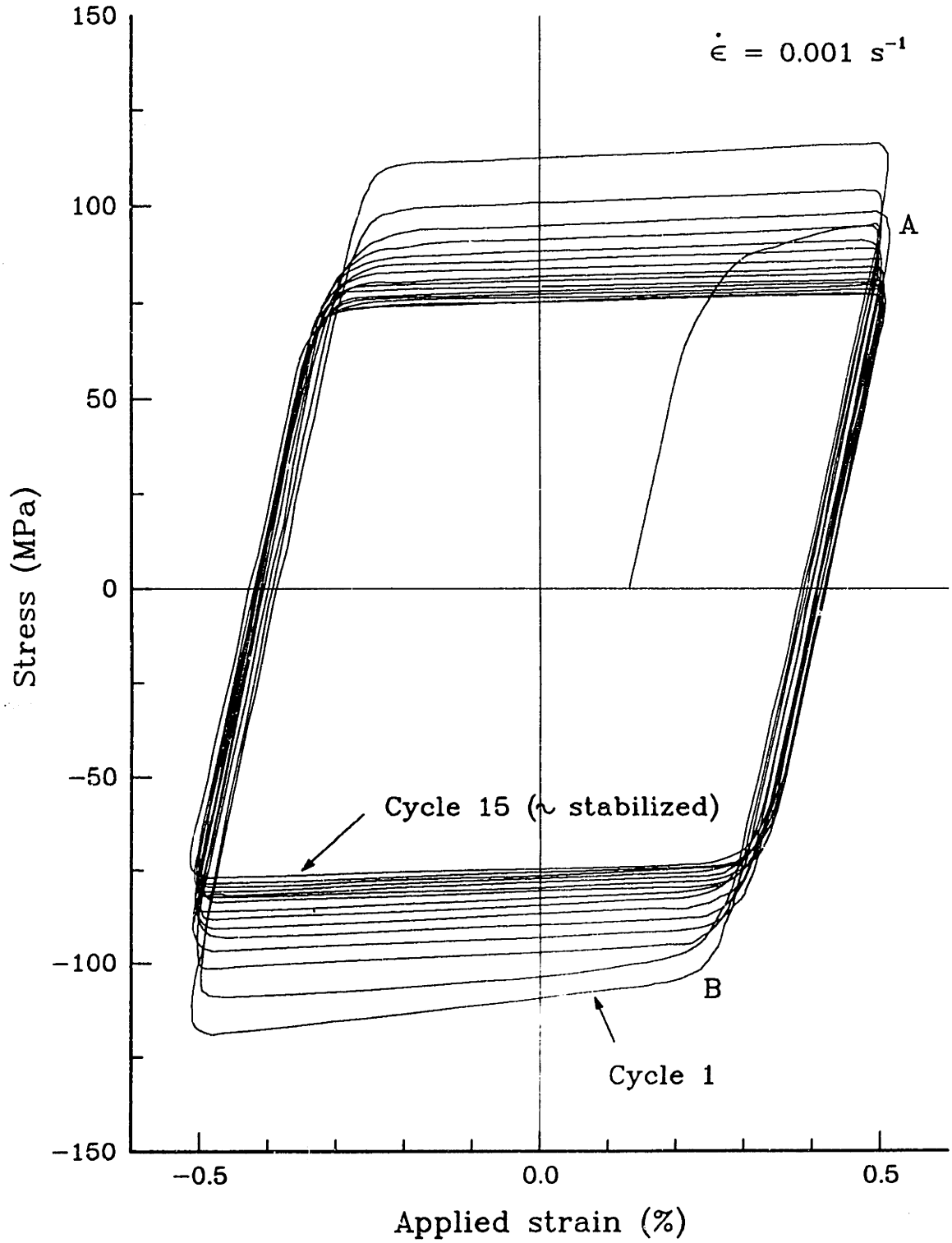

Fig. 5.5 Cyclic strain softening shown by <100> oriented NiAl single crystals at 850°C

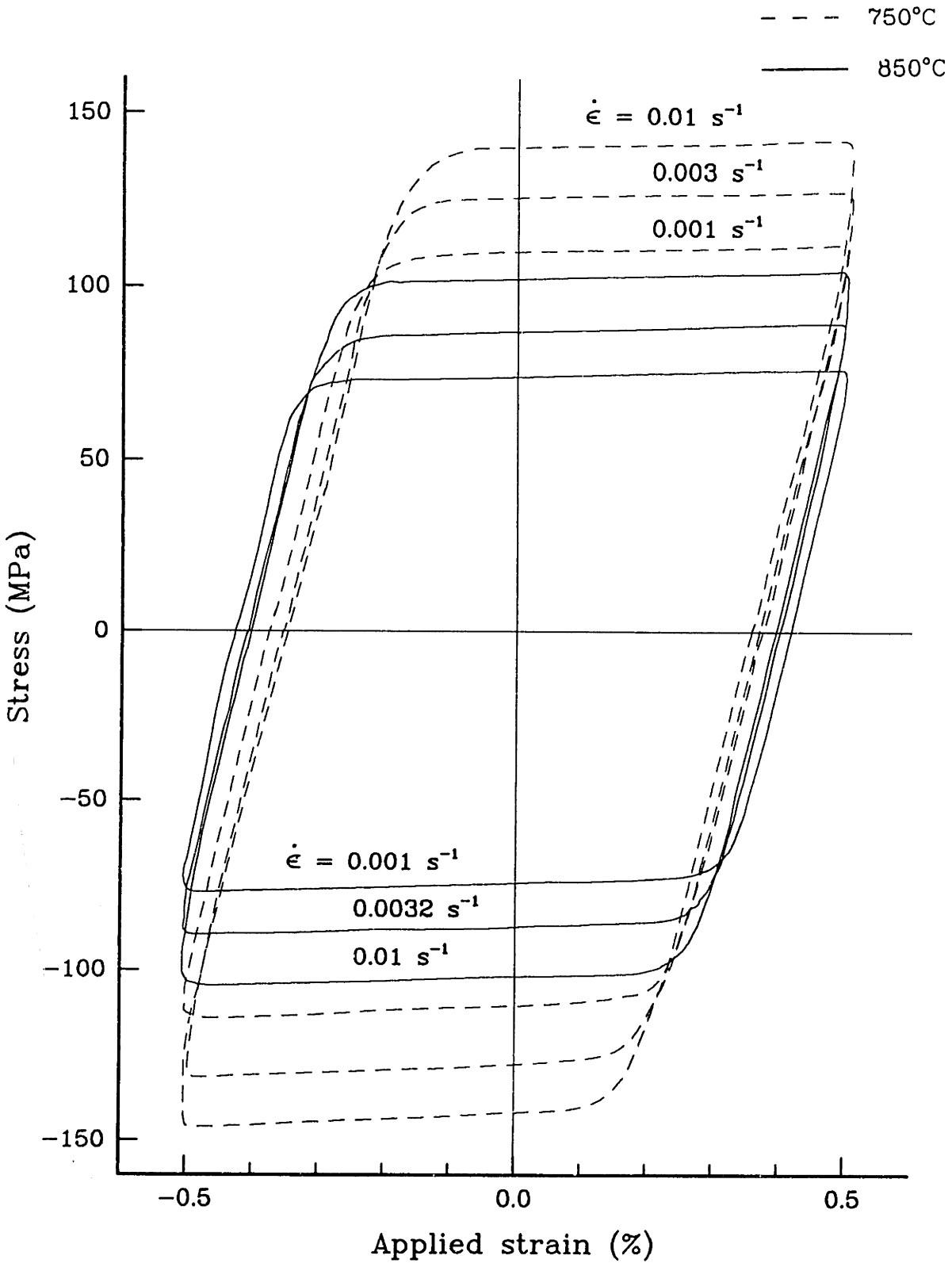

Fig. 5.6 Temperature and strain rate effects of <100> NiAl single crystals

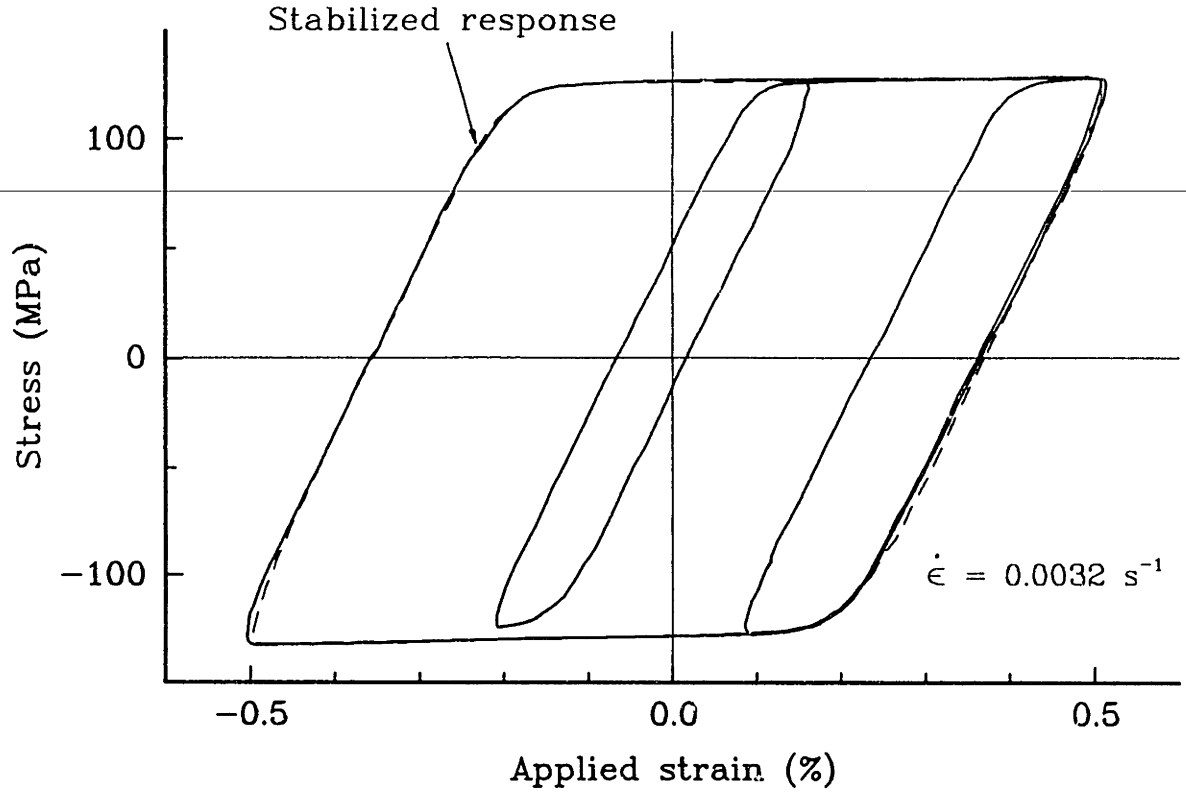

Fig. 5.7 Arbitrary strain reversals at 750°C

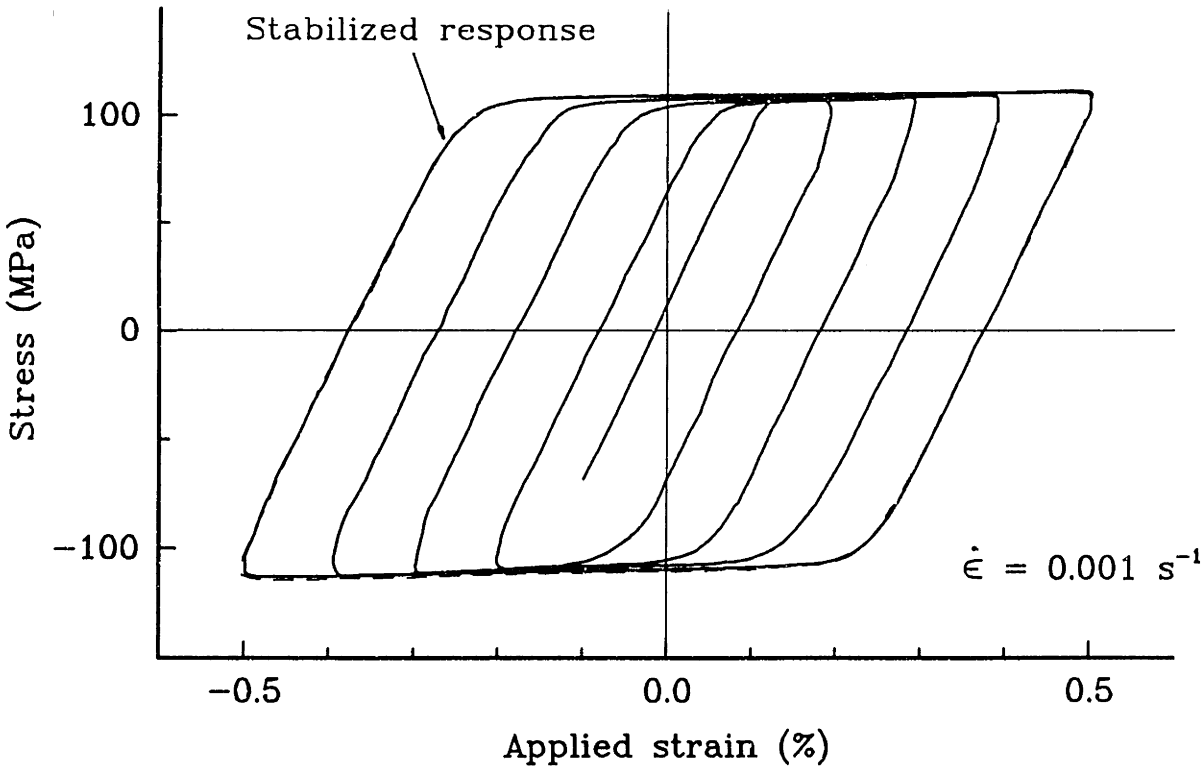

Fig. 5.8 Increasing strain range test at 750°C

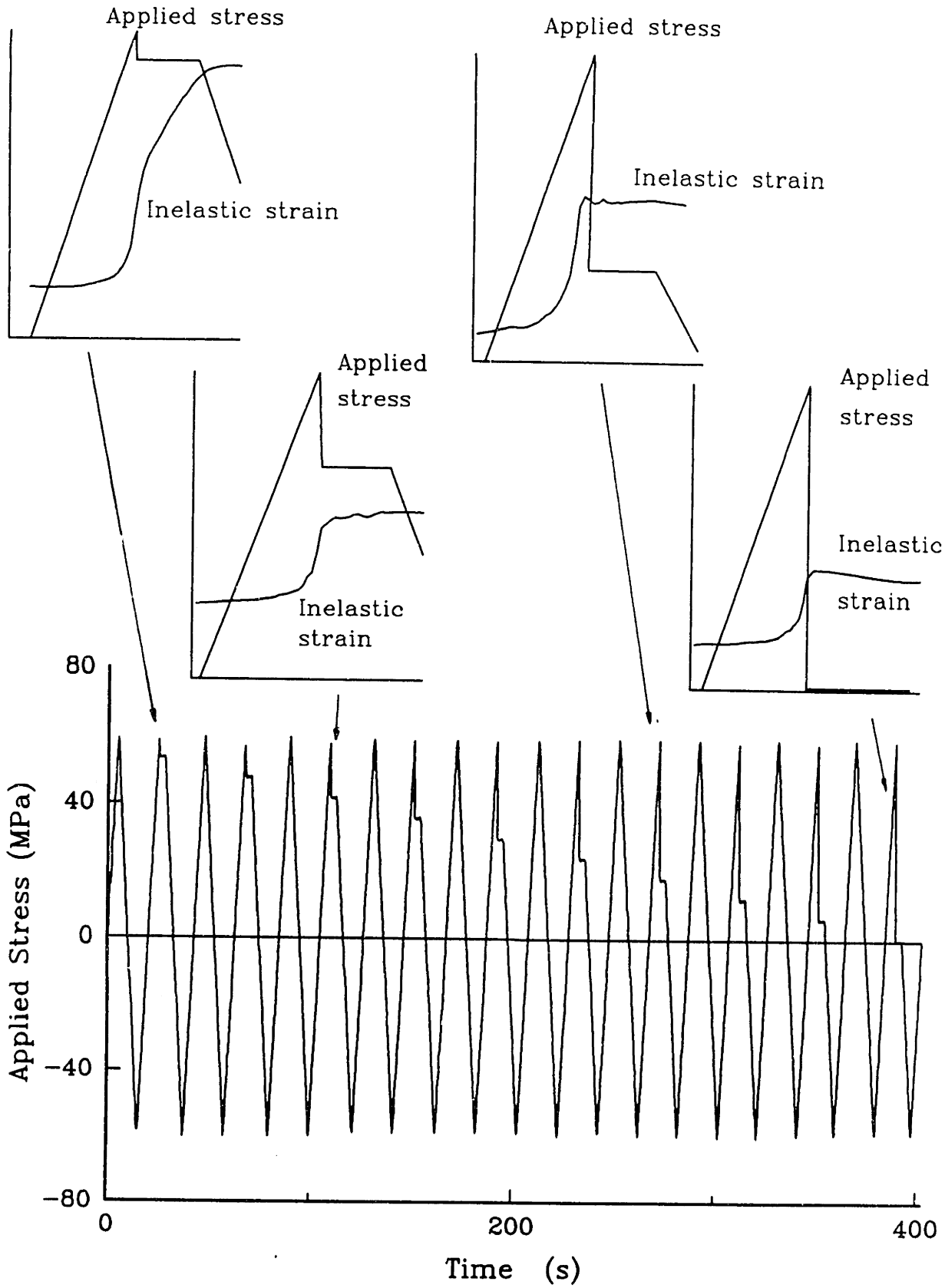

Fig. 5.9 Stress drop and hold test: imposed stress path and resulting inelastic strain versus time curves

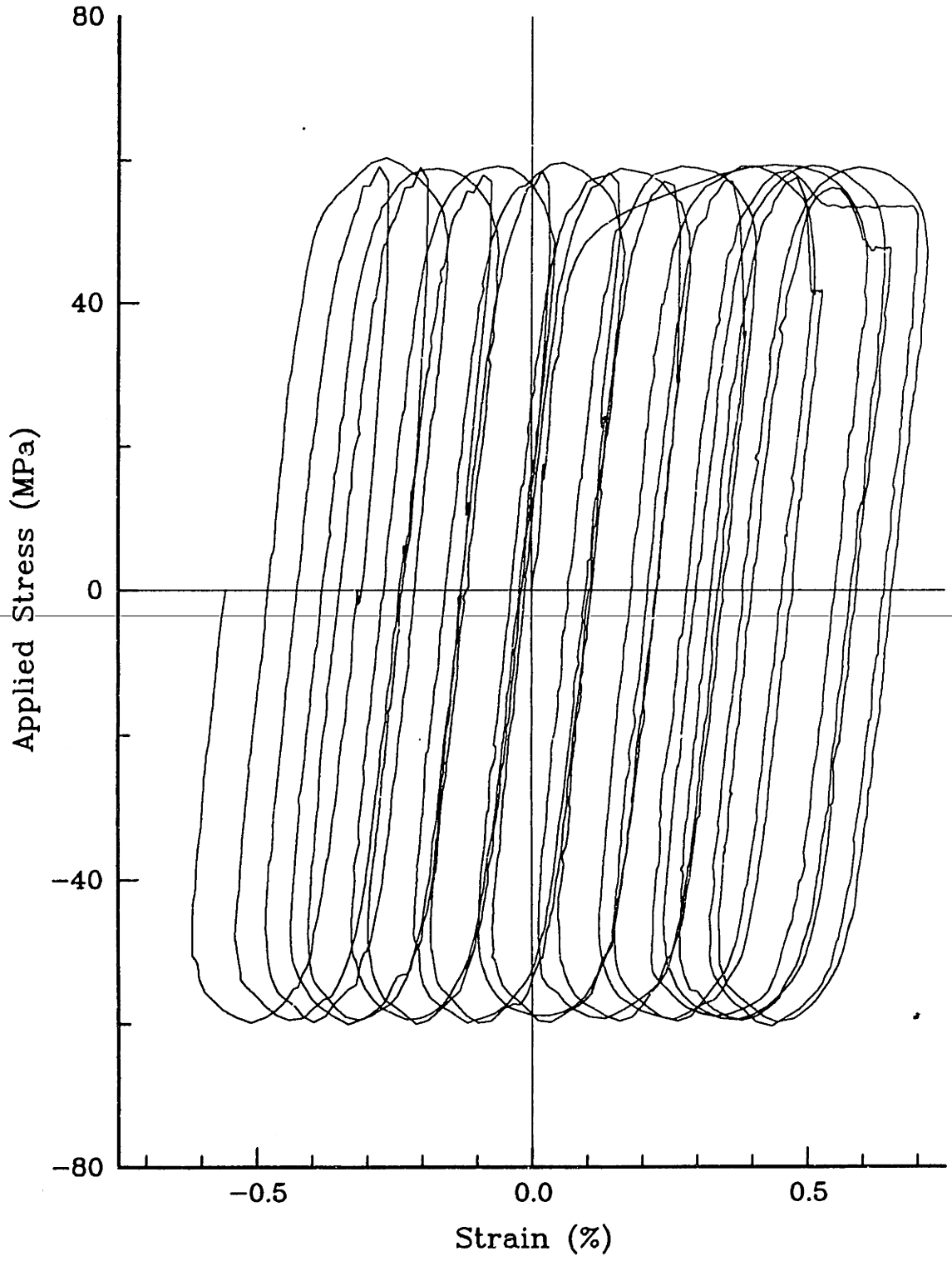

Fig. 5.10 Stress–strain response of <100> NiAl crystals to a stress drop and hold at 850°C

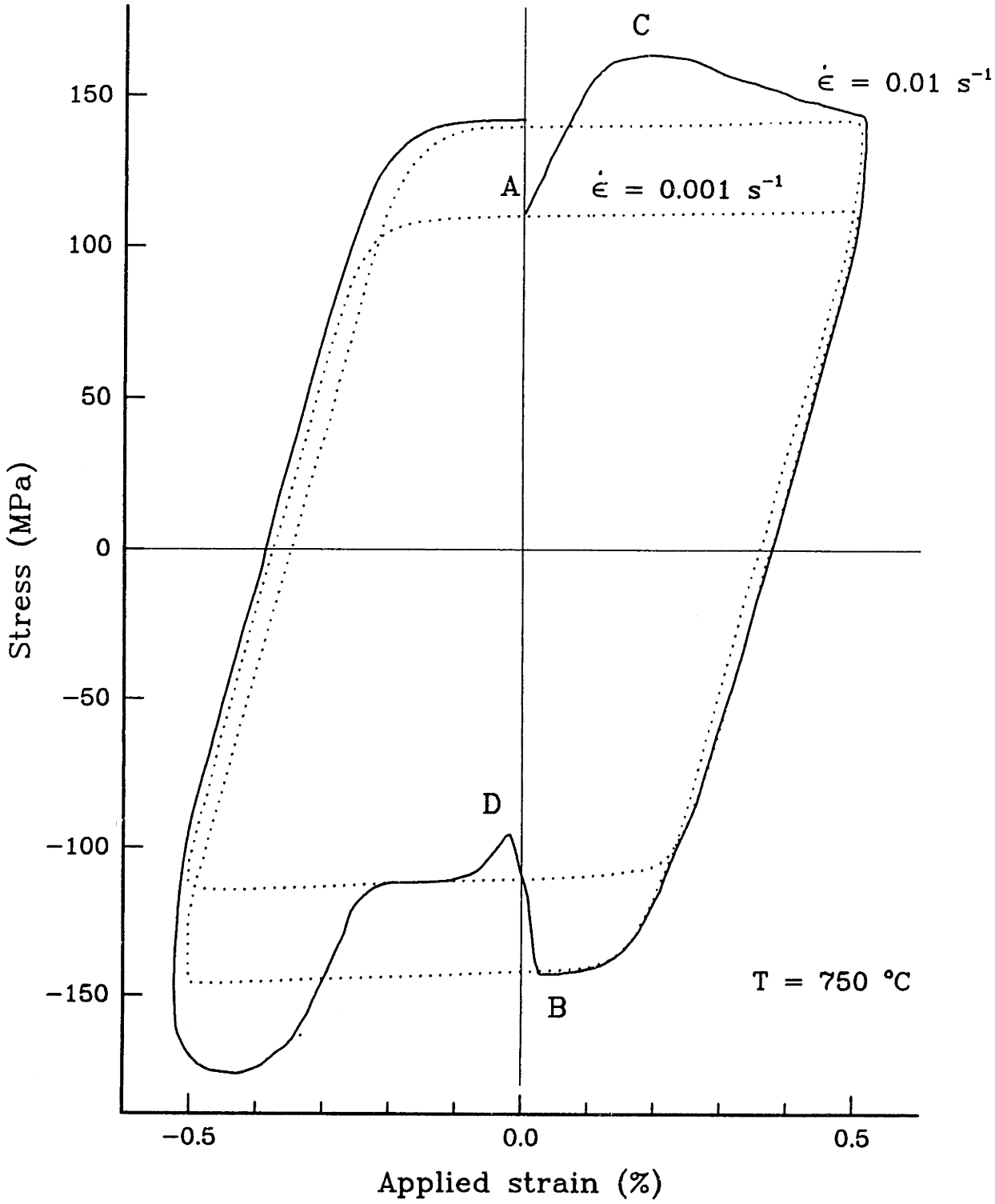

Fig. 5.11 Strain rate jump and drop test from stabilized <100> cycles (shown in dotted lines)

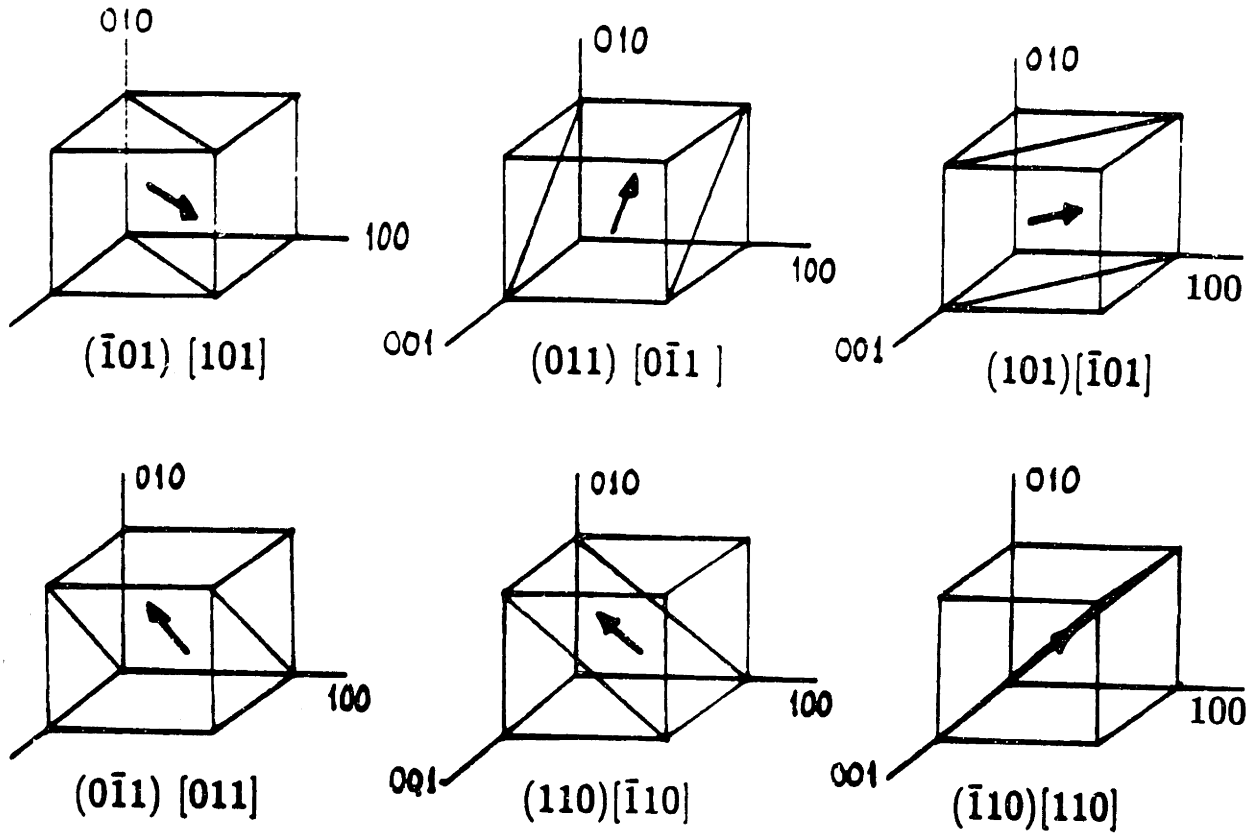

Fig. 5.12 Slip planes and directions for $\{110\}< 110 >$ slip systems

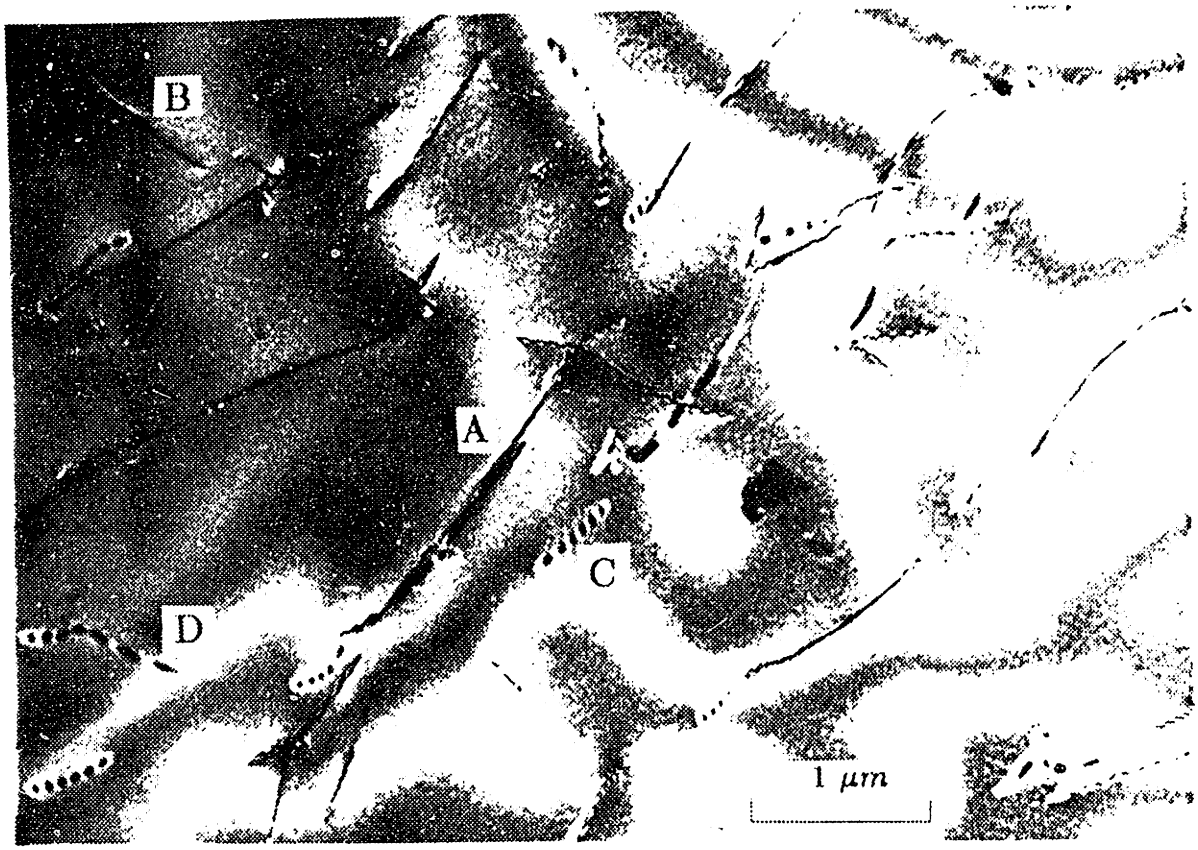

(a) $\mathbf{g} = [\bar{1}\bar{1}0]$

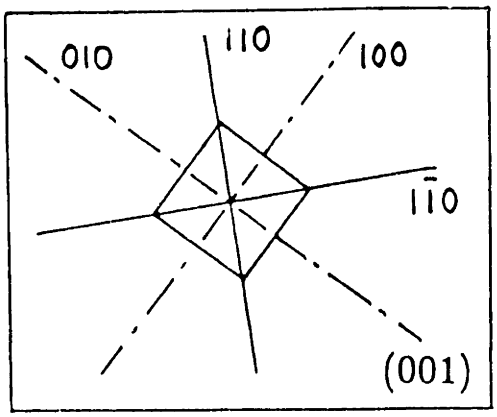

Orientation of pictures

Disl. A = (011) [01$\bar{1}$]

Disl. B = (10$\bar{1}$) [101]

$\rho = 3\ \mu m^{-2}$

Fig. 5.13 TEM contrast images of a (001) foil from a cycled [001] oriented NiAl specimen: Burgers vector determination. (T= 850°C, $\epsilon = 0.4\ 0.5\%$)

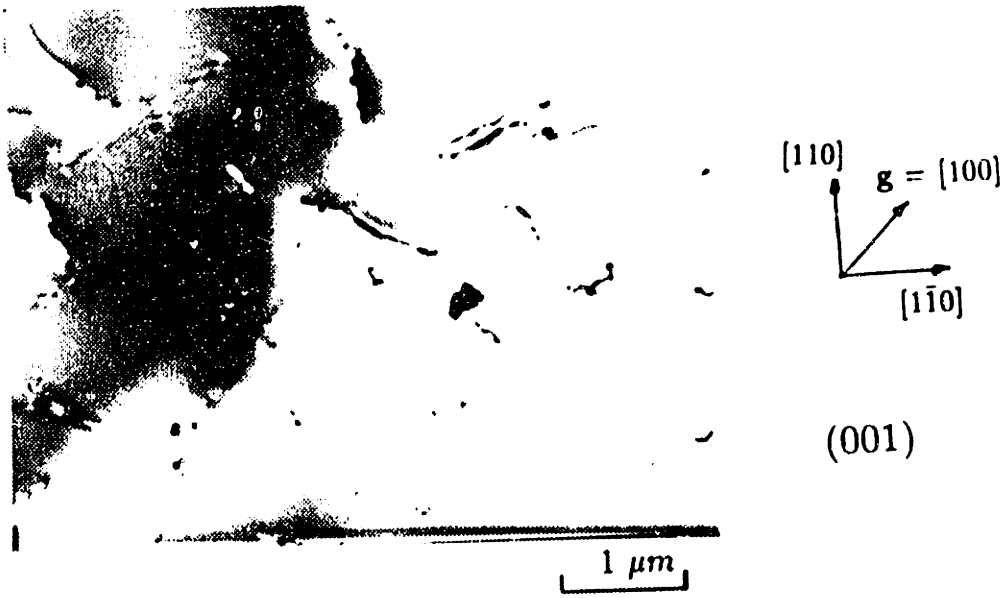

(b)

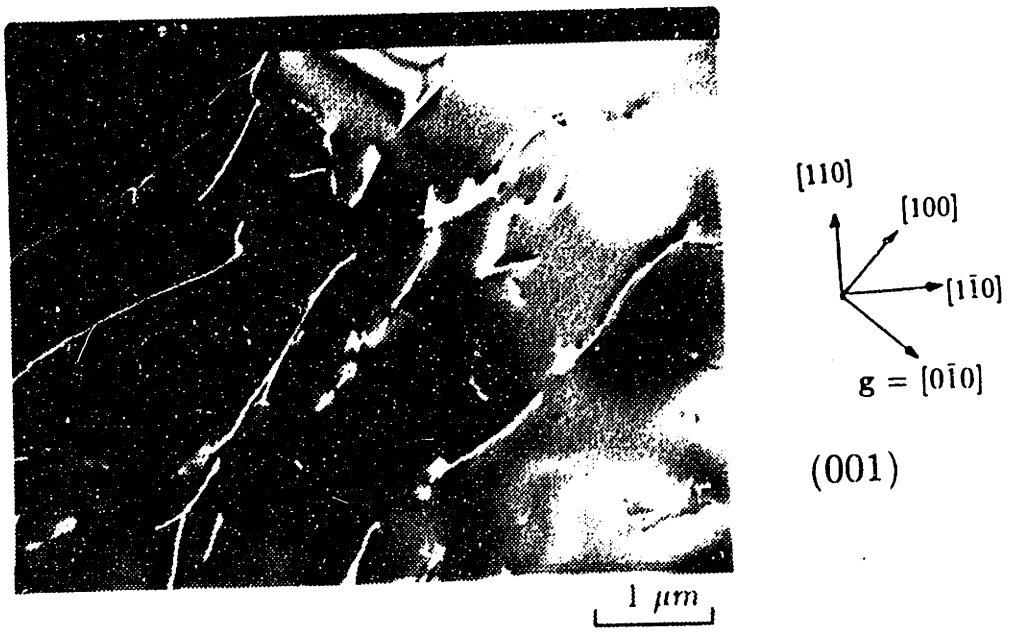

(c) (dark field)

Fig. 5.13 (contd.)

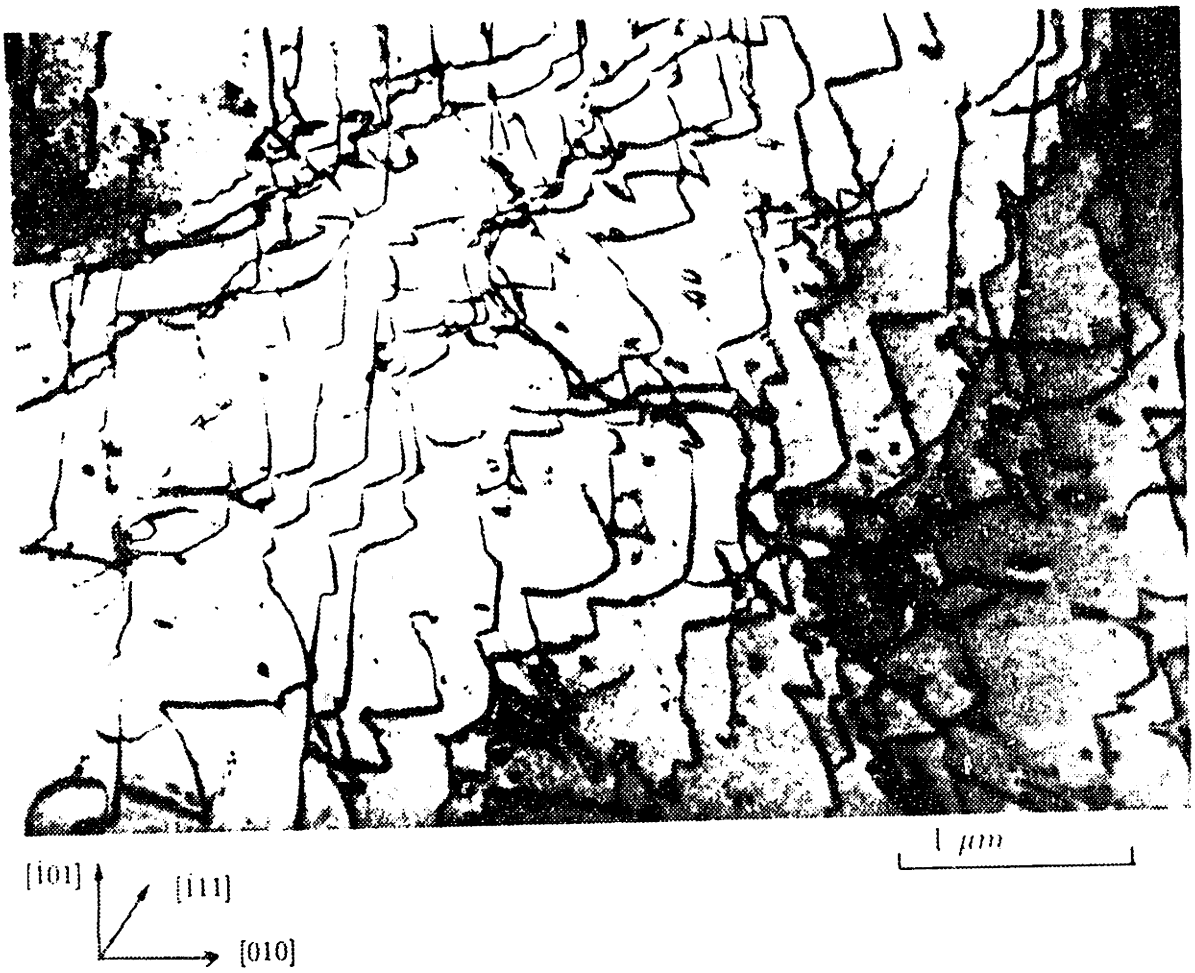

Fig. 5.14 Typical dense dislocation region in a (101) glide plane of cyclically deformed NiAl with $\epsilon = 0 \pm 0.5\,\%$. ($g = [0\bar{1}\bar{1}]$)

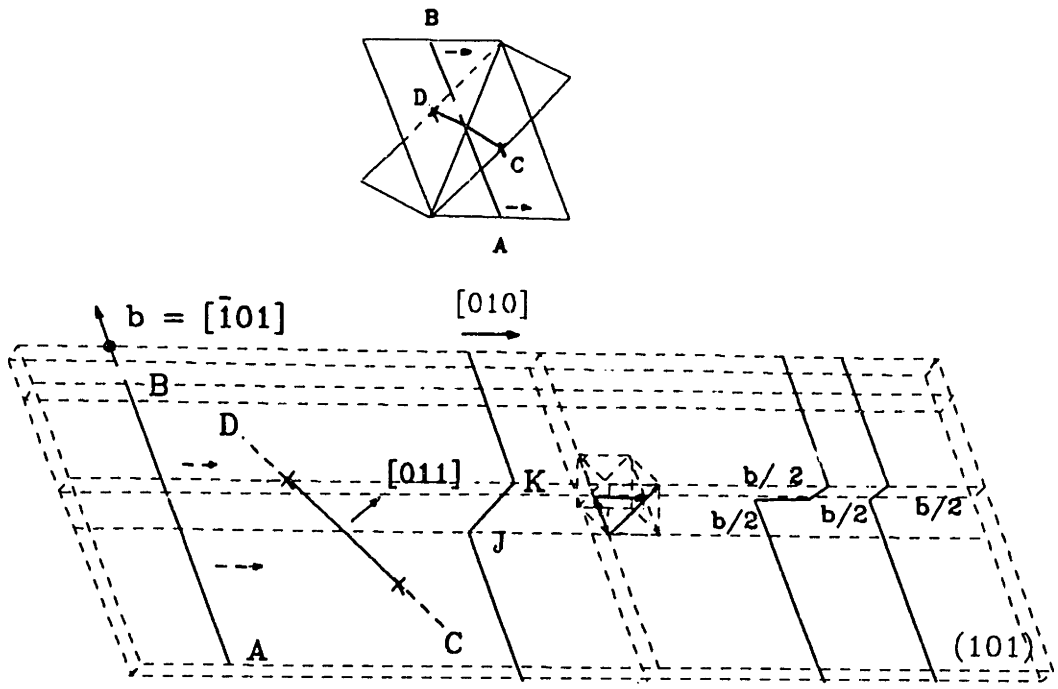

(a) Intersection between a screw and an edge dislocation on {110} planes at 60°. (After Kear et al., 1959)

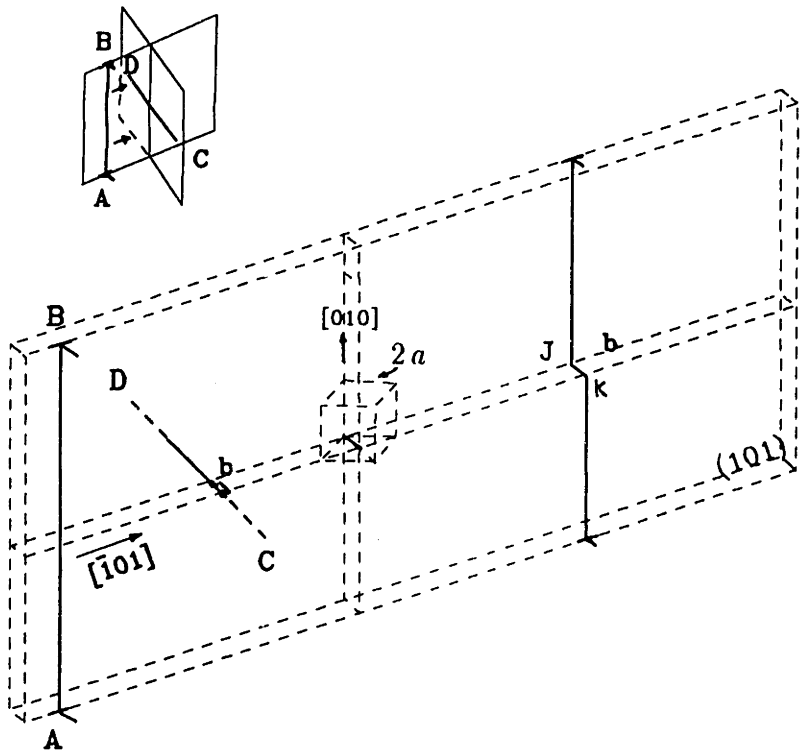

(b) Intersection between edge and screw dislocations in orthogonal planes

Fig. 5.15 Jog characteristics of {110}<110> dislocations

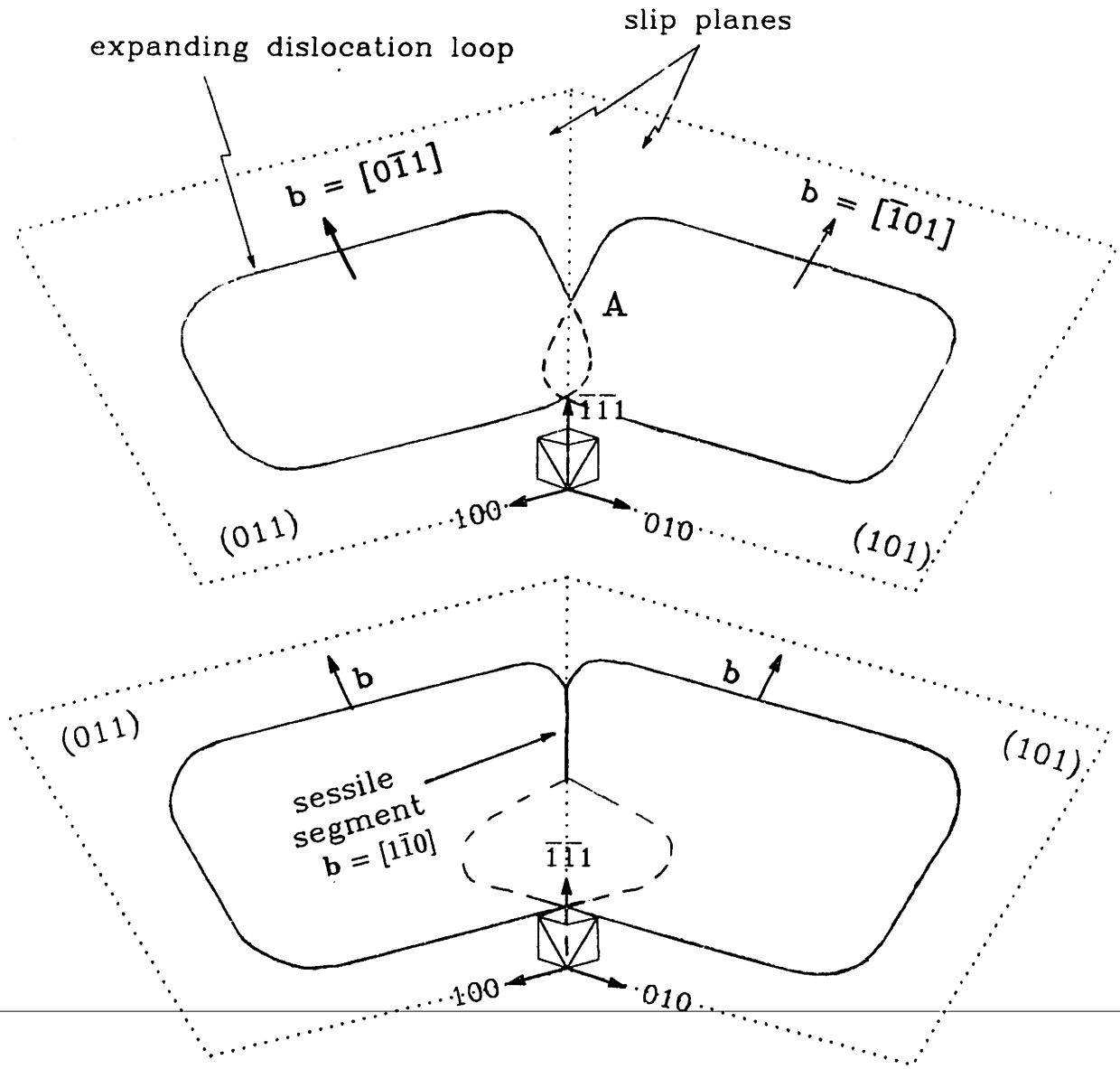

Fig. 5.16 Formation of <111> sessile dislocation segments as the result of screw dislocation intersection on oblique planes

(a)

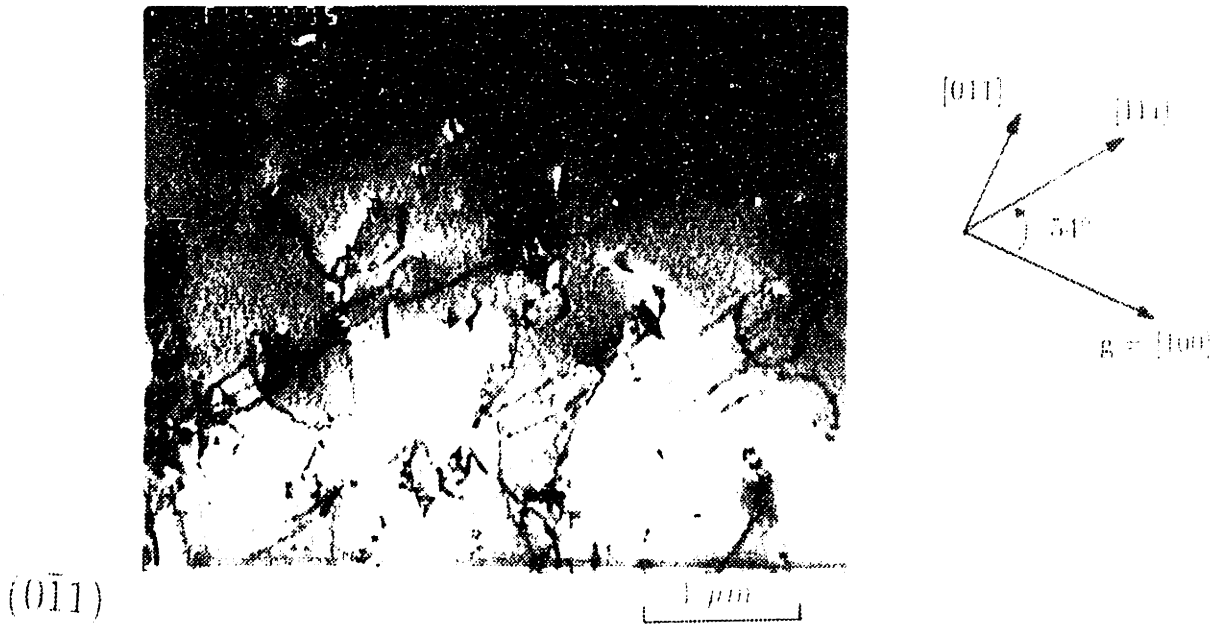

(b)

Fig. 5.17 TEM image contrasts of t = < 111 > dislocation segments lying on a $(0\bar{1}1)$ plane ($\epsilon = 0 \pm 0.5\%$)

(a) (101) foil, $\mathbf{g} = [0\bar{1}\bar{1}]$

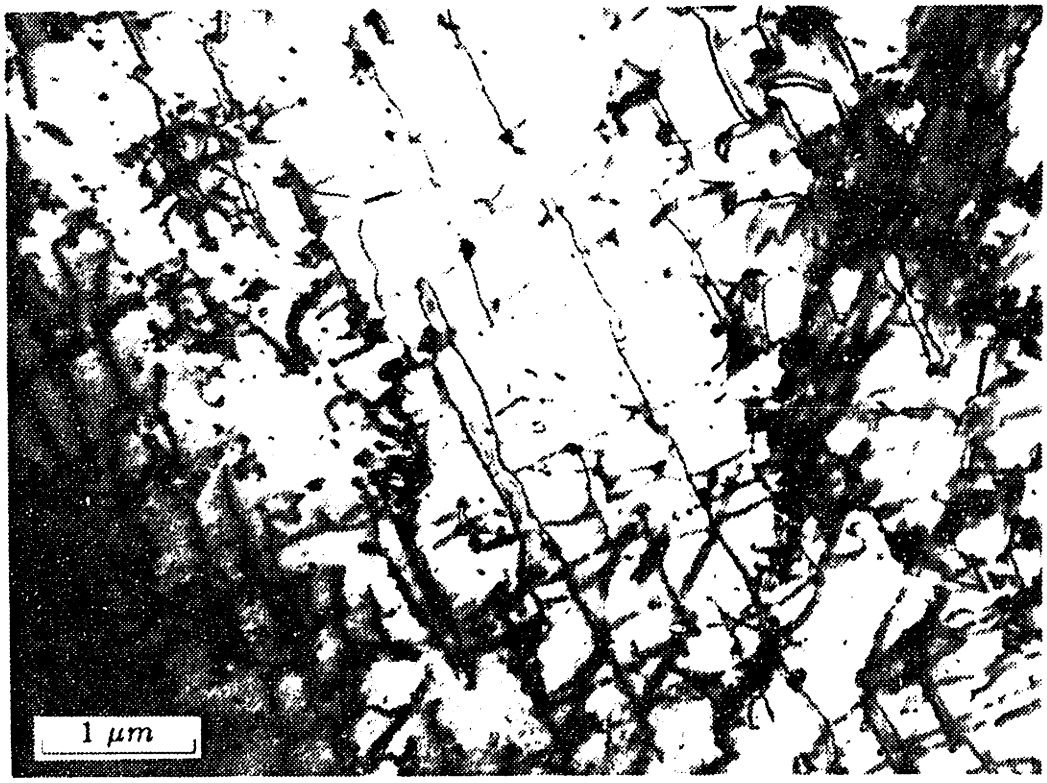

(b) (001) foil, $\mathbf{g} = [\bar{1}\bar{1}0]$

Fig. 5.18 Dislocation segments in cycled NiAl for $\epsilon = 0 \pm 0.5$ % history. Note some bowing

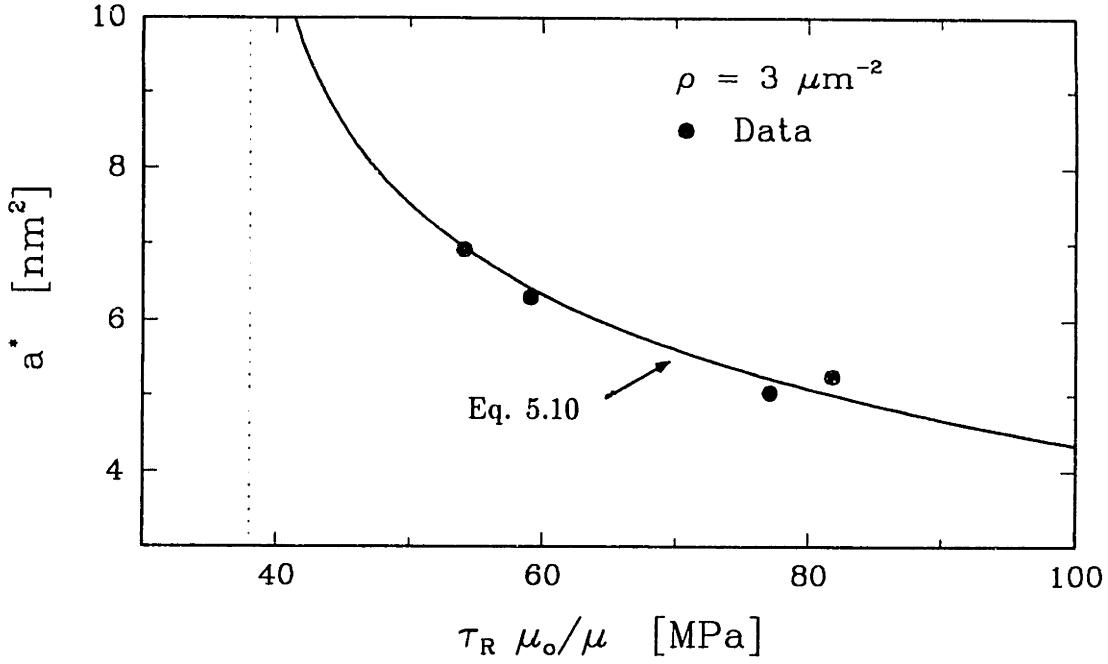

Fig. 5.19 **Calculated activation area dependence on the overall flow stress**

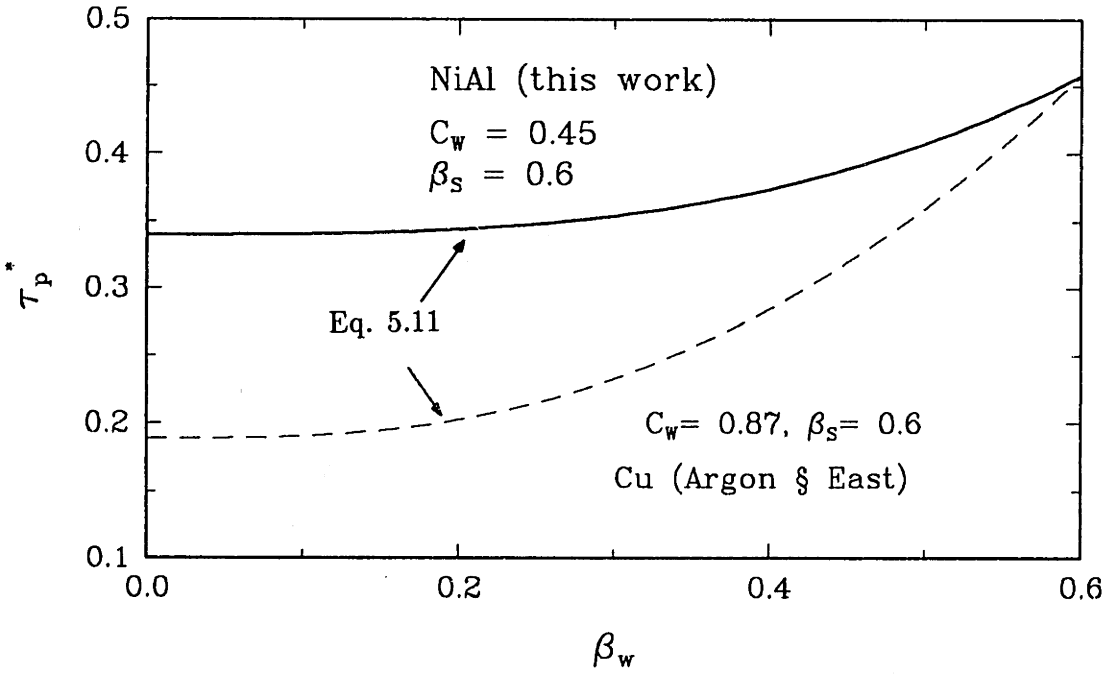

Fig. 5.20 **Flow strength dependence on the normalized weak obstacle strength (β_w) of fraction C_w. Strong obstacles are regarded as impenetrable for $\beta_S \geqslant 0.6$**

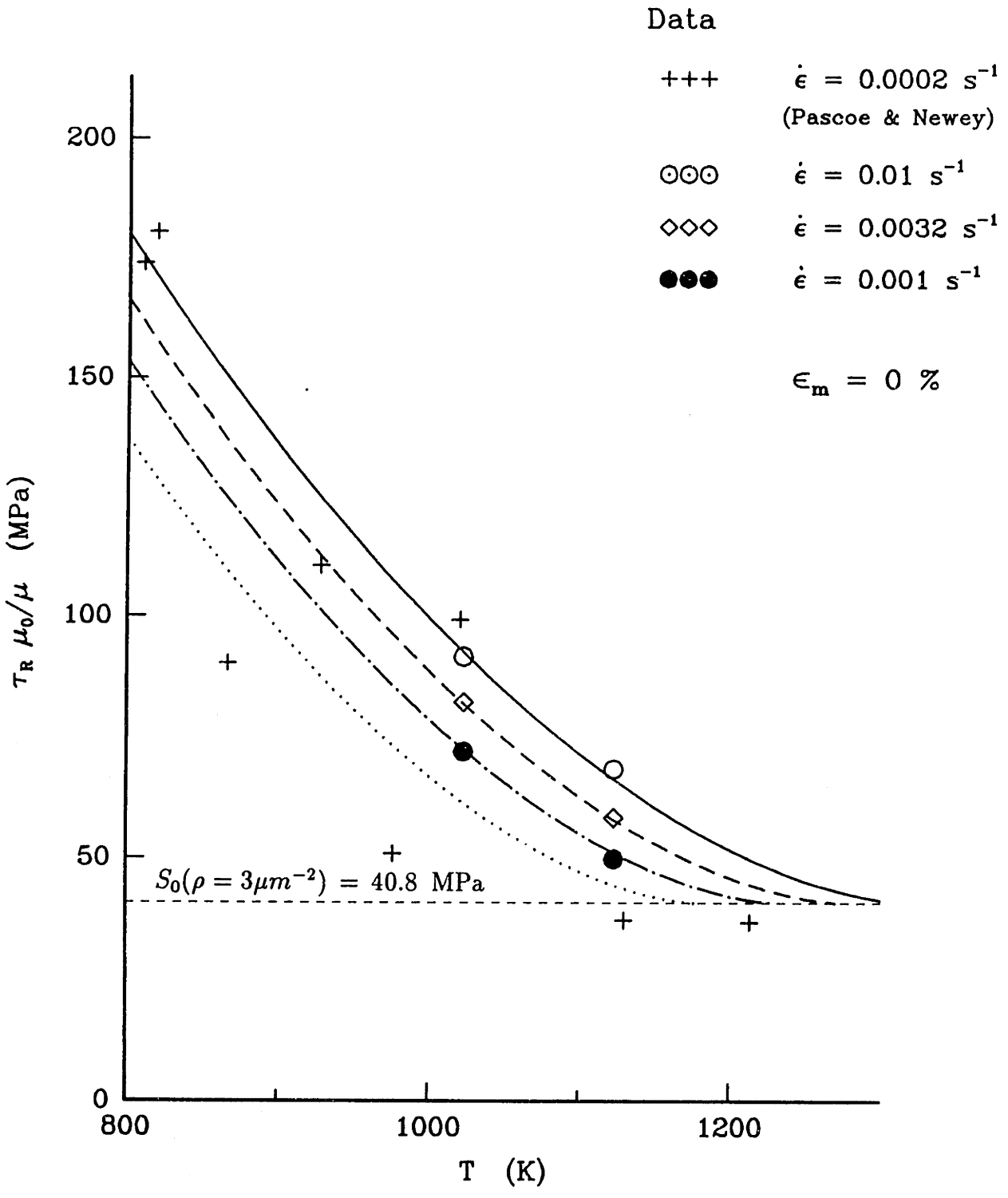

Fig. 5.21 Temperature and strain rate dependence of the flow stress of {110}<110> slip systems at constant structure

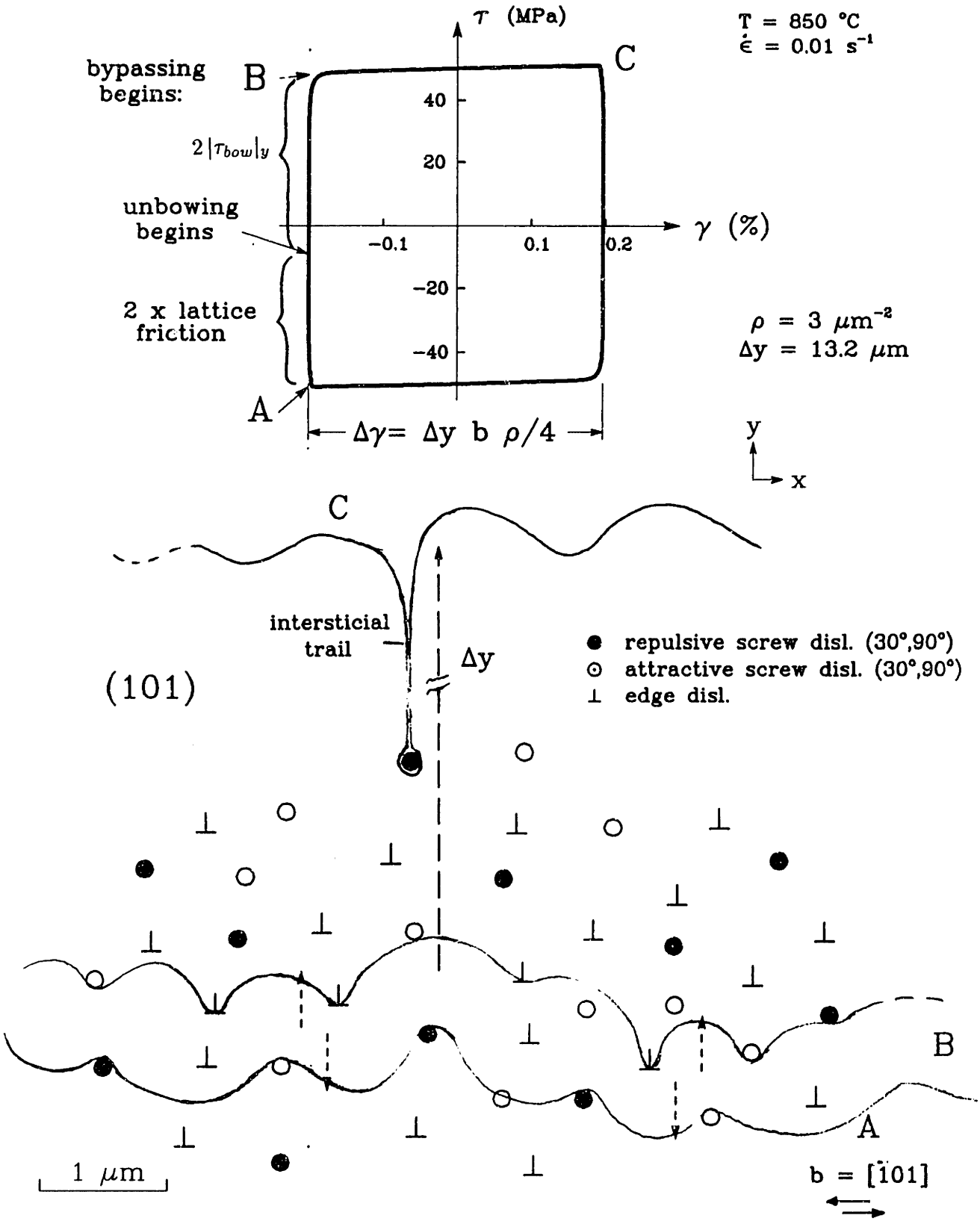

Fig. 5.22 Schematic equilibrium configurations of a screw dislocation interacting with a dislocation forest: (A) at a reversal point, (B) at the onset of plastic flow and (C) after accommodating a shear strain increment of $\Delta\gamma$

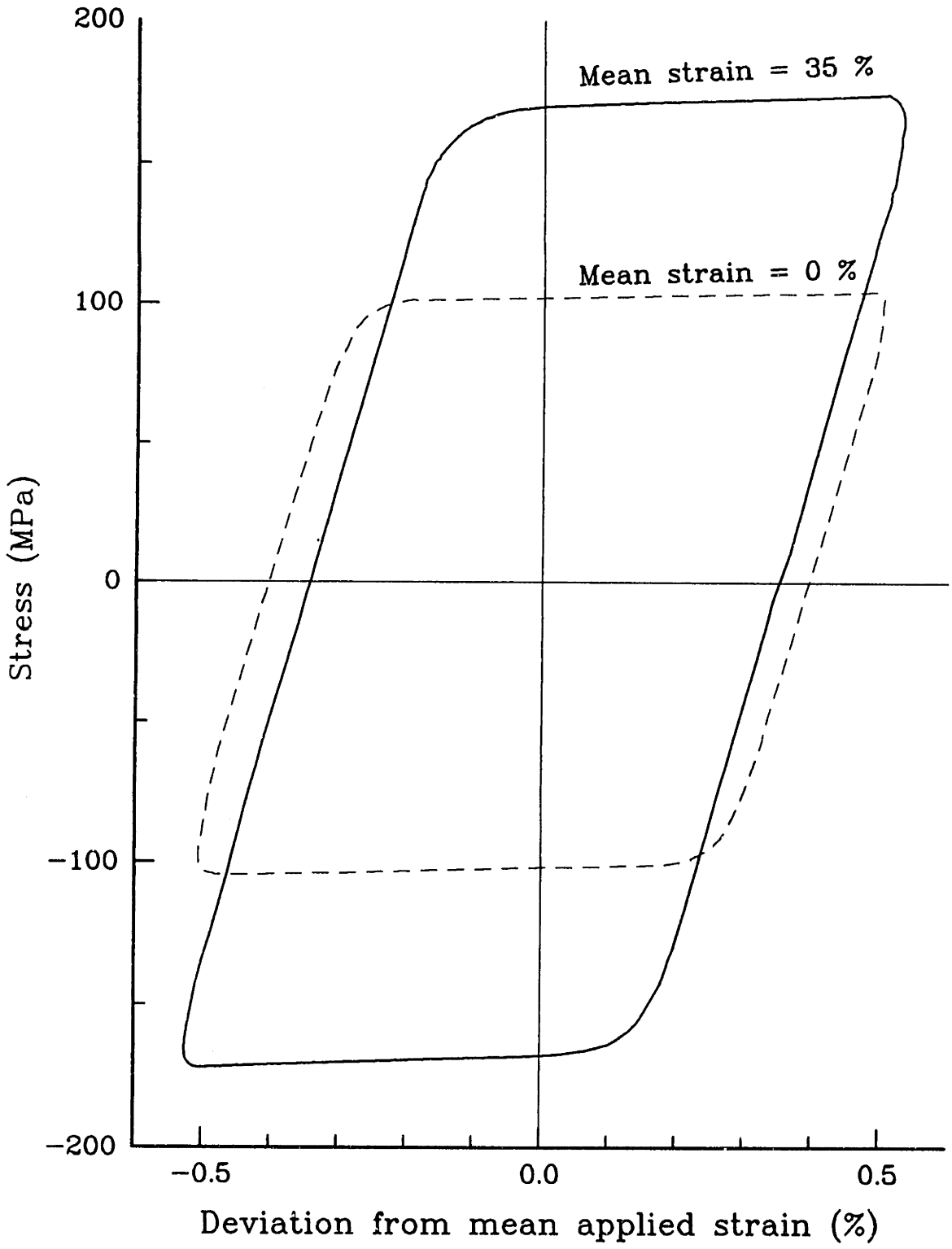

Fig. 5.23 Stabilized cyclic response with two different mean strains at 850°C (ϵ = 0.01 s^{-1})

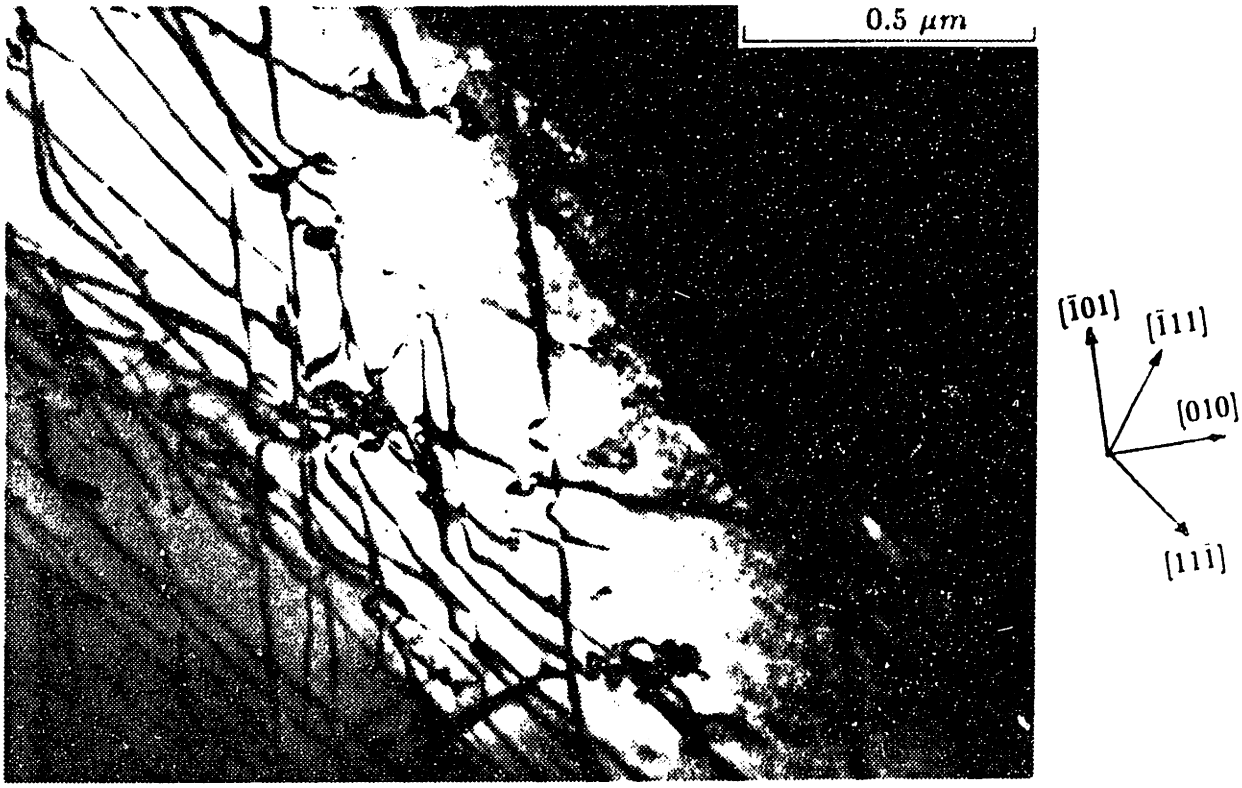

(a) (101) foil, $\mathbf{g} = [0\bar{1}\bar{1}]$

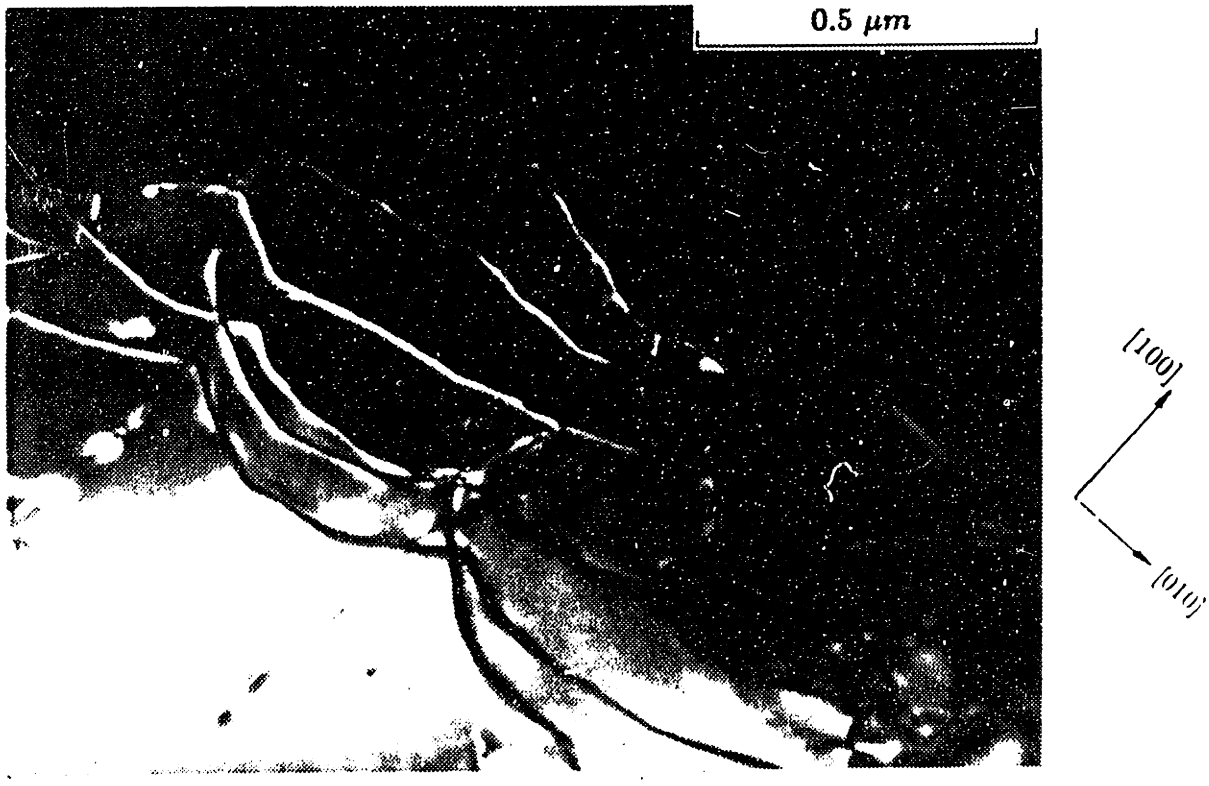

(b) (001) foil, $\mathbf{g} = [\bar{1}\bar{1}0]$

Fig. 5.21 $\mathbf{t} = \langle 111 \rangle$ sessile segments (a) and bowed ($\approx$ edge) segments (b) from a $\langle 100 \rangle$ cycled specimen, subjected to the $\epsilon = 35 \pm 0.5$ % history

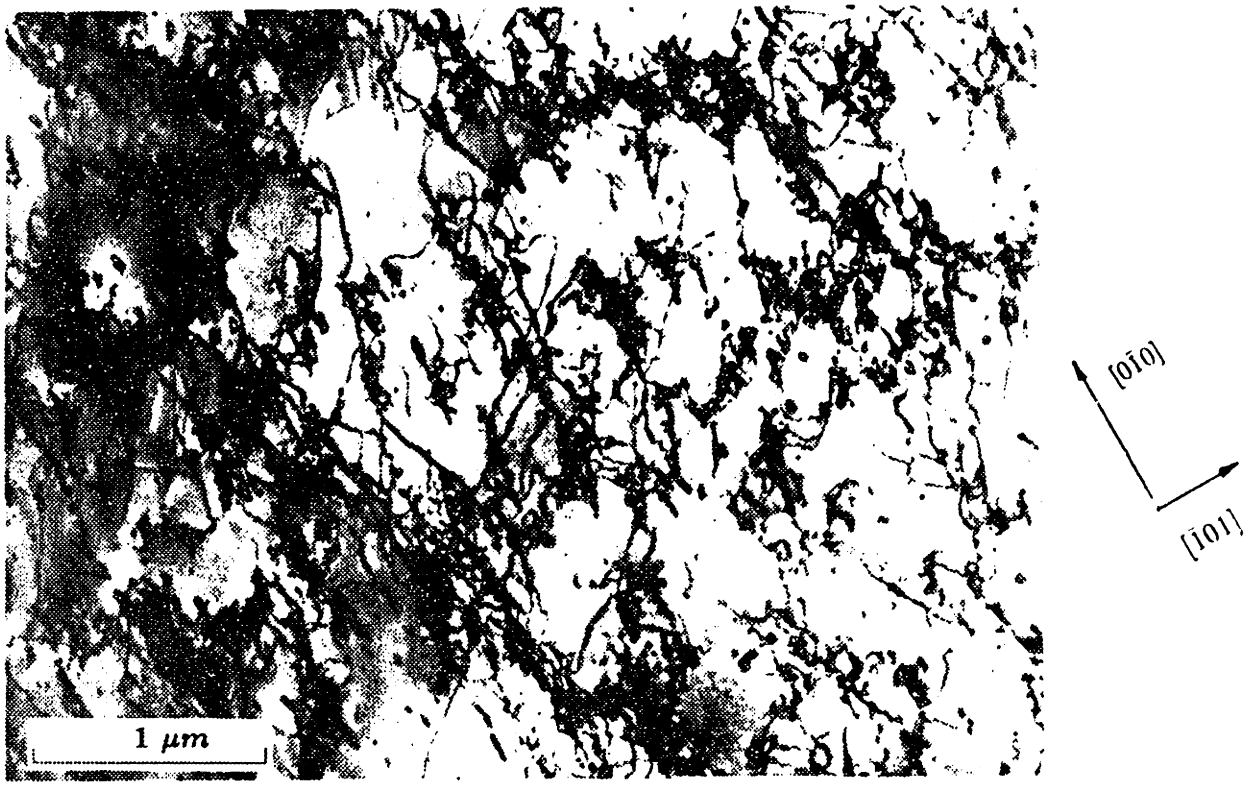

(a) Typical region showing dense dislocation tangles forming strands. (101) foil, $\mathbf{g} = [0\bar{1}\bar{1}]$

(b) Dense band of dislocations forming cell walls. (001) foil, $\mathbf{g} = [\bar{1}\bar{1}0]$

Fig. 5.25 Dislocation structure resulting from the $\epsilon = 35 \pm 0.5$ % history

Appendix 5.A Interaction forces between two screw dislocations which form an angle α with one another in an anisotropic body

There has been extensive work in determining the interaction forces between pairs of dislocations. However, most of this work has concentrated on studying the interaction between dislocations in isotropic media (see Hartley and Hirth [1965] for a complete study). The only analysis on anisotropic media found by the author was that of Tectonico [1962] who studied the interaction forces between extended parallel dislocations. Here, an extension of dislocation interactions in an isotropic solid to an anisotropic solid will be presented.

5.A.1 Forces acting on a straight dislocation

Two approaches are usually followed to determine the interaction forces between dislocations of relatively simple configurations, such as infinite straight dislocations segments. The first one consists in calculating the interaction energy and differentiating it with respect to the coordinate in the direction of the dislocation motion. The second approach, to be followed here, consists in determining the stress field of one of the dislocations and transforming it into the coordinates corresponding to the other dislocation.

The forces acting in the latter due to the stress field of the first dislocation can be calculated using the relation introduced by Peach and Koehler and Nabarro. This relation gives the force per unit length of a dislocation defined by its Burgers vector $\mathbf{b}$ and its positive line direction vector $\mathbf{s}$ under a stress field σ which is not originating from the dislocation under consideration:

$$\mathbf{F} = (\sigma \cdot \mathbf{b}) \times \mathbf{s} \, . \tag{5.A.1}$$

Eq. 5.A.1 can also be expressed in indicial form as

$$F_k = -\epsilon_{ijk}\, s_i\, \sigma_{jl}\, b_l, \tag{5.A.2}$$

where ϵ_{ijk} is the permutation operator with components

$$\begin{aligned} \epsilon_{123} &= \epsilon_{231} = \epsilon_{312} = 1, \\ \epsilon_{132} &= \epsilon_{213} = \epsilon_{321} = -1, \\ \epsilon_{ijk} &= 0 \quad \text{for any two subscripts equal or otherwise.} \end{aligned} \tag{5.A.3}$$

Consider two screw dislocations of different type[1], hereafter referred to as 1 (right-handed) and 2 (left-handed), which form an angle α with one another, as shown in Fig. 3.A.1. Assume that the stress field σ in Eq. 5.A.1 is due to Dislocation 1 and let $\mathbf{F}$ be the corresponding force on Dislocation 2 due to the stress field of Dislocation 1. The forces acting on Dislocation 2 will first be determined in the coordinate frame attached to Dislocation 1 (x_1, x_2, x_3 in Fig. 3.A.1), and will then be rotated an angle α to the frame fixed in Dislocation 2 (x_1', x_2', x_3' in Fig. 3.A.1) through the rotation matrix $\mathbf{R}$:

$$\mathbf{F}' = \mathbf{R}\,\mathbf{F} \longrightarrow \begin{Bmatrix} F_1' \\ F_2' \\ F_3' \end{Bmatrix} = \begin{bmatrix} 1 & 0 & 0 \\ 0 & cos\alpha & -sin\alpha \\ 0 & sin\alpha & cos\alpha \end{bmatrix} \begin{Bmatrix} F_1 \\ F_2 \\ F_3 \end{Bmatrix} \tag{5.A.4}$$

The origins of the triads attached to each dislocation are determined such that they are connected by a vector d (see Fig. 3.A.1) which defines the shortest possible vector connecting the two dislocations (Hartley and Hirth, 1965). In the limiting case, as the applied stress needed to make the dislocations approach each other increases, d tends to be of the order of one Burgers vector. At the point of contact, it has been shown that the dislocations will react into a different type of dislocation (Saada, 1957).

[1]The type of a screw dislocation is defined by the relative orientation of its Burgers vector and the direction of its positive Burgers circuit according to the right hand rule.

Let $\mathbf{s}^{(1)}$, $\mathbf{s}^{(2)}$, and $\mathbf{b}^{(1)}$, $\mathbf{b}^{(2)}$ refer to the direction of the positive Burgers circuit, and to the Burgers vectors of Dislocations 1 and 2 respectively. Then, Eq. 5.A.1 becomes:

$$\mathbf{F} = (\sigma \cdot \mathbf{b}^{(2)}) \times \mathbf{s}^{(2)}. \tag{5.A.5}$$

Note that Eq. 5.A.5 is also valid for anisotropic crystals within the asumptions of linear elasticity (Hirth and Lothe [1982]).

Then, an expansion of Eq. 5.A.2 using Eq. 5.A.3 yields,

$$\begin{aligned} F_1 &= -\epsilon_{ij1}\, s_i^{(2)}\, \sigma_{jl}\, b_l^{(2)} \\ &= -\epsilon_{2j1}\, s_2^{(2)}\, \sigma_{jl}\, b_l^{(2)} - \epsilon_{3j1}\, s_3^{(2)}\, \sigma_{jl}\, b_l^{(2)} \\ F_1 &= -s_2^{(2)}\,(\sigma_{31}\, b_1^{(2)} + \sigma_{32}\, b_2^{(2)} + \sigma_{33}\, b_3^{(2)}) + s_3^{(2)}\,(\sigma_{21}\, b_1^{(2)} + \sigma_{22}\, b_2^{(2)} + \sigma_{23}\, b_3^{(2)}) \end{aligned} \tag{5.A.6}$$

$$\begin{aligned} F_2 &= -\epsilon_{ij2}\, s_i^{(2)}\, \sigma_{jl}\, b_l^{(2)} \\ &= -\epsilon_{1j2}\, s_1^{(2)}\, \sigma_{jl}\, b_l^{(2)} - \epsilon_{3j2}\, s_3^{(2)}\, \sigma_{jl}\, b_l^{(2)} \\ F_2 &= s_1^{(2)}\,(\sigma_{31}\, b_1^{(2)} + \sigma_{32}\, b_2^{(2)} + \sigma_{33}\, b_3^{(2)}) - s_3^{(2)}\,(\sigma_{11}\, b_1^{(2)} + \sigma_{12}\, b_2^{(2)} + \sigma_{13}\, b_3^{(2)}) \end{aligned}$$

$$\begin{aligned} F_3 &= -\epsilon_{ij3}\, s_i^{(2)}\, \sigma_{jl}\, b_l^{(2)} \\ &= -\epsilon_{1j3}\, s_1^{(2)}\, \sigma_{jl}\, b_l^{(2)} - \epsilon_{2j3}\, s_2^{(2)}\, \sigma_{jl}\, b_l^{(2)} \\ F_3 &= -s_1^{(2)}\,(\sigma_{21}\, b_1^{(2)} + \sigma_{22}\, b_2^{(2)} + \sigma_{23}\, b_3^{(2)}) + s_2^{(2)}\,(\sigma_{11}\, b_1^{(2)} + \sigma_{12}\, b_2^{(2)} + \sigma_{13}\, b_3^{(2)}) \end{aligned} \tag{5.A.7}$$

When the above equations are expressed in the x_1, x_2, x_3 frame for a right-handed screw dislocation $\mathbf{b}^{(2)}$ and $\mathbf{s}^{(2)}$ are given as:

$$\begin{aligned} \mathbf{b}^{(2)} &= b^{(2)}\,(0, -sin\,\alpha, -cos\,\alpha), \\ \mathbf{s}^{(2)} &= (0, -sin\,\alpha, -cos\,\alpha). \end{aligned} \tag{5.A.8}$$

The final stage in evaluating Eq. 5.A.4 consists in determining the stress components σ_{ij}.

Stress field of a screw dislocation in an anisotropic cubic crystal. The stress field of a dislocation can be determined following the anisotropic elasticity theory of straight dislocations developed by Eshelby et al. [1953]. Define a left-handed screw dislocation away from free surfaces in a cubic single crystal by its positive Burgers circuit vector along he positive x_3 direction and by a Burgers vector given by $\mathbf{b}^{(1)} = (0, 0, -b^{(1)})$ (Fig. 3.A.1), where $b^{(1)}$ is its magnitude. Its stress field is then given by:

$$\sigma = \begin{bmatrix} 0 & 0 & \sigma_{13} \\ 0 & 0 & \sigma_{23} \\ \sigma_{31} & \sigma_{32} & 0 \end{bmatrix}. \tag{5.A.9}$$

The stress components are expressed in terms of $b^{(1)}$, the elastic stiffness components relating stress to strain tensors in a rotated frame from the cubic reference frame aligned with the screw dislocation, C'_{ij}, and the anisotropic or energy coefficient K, introduced in Section 4.4.2:

$$\begin{aligned} \sigma_{13} = \sigma_{31} &= -\frac{b^{(1)}}{2\,\pi} K \frac{C'_{55}\, x_2}{C'_{44}\, x_1^2 + C'_{55}\, x_2^2}, \\ \sigma_{23} = \sigma_{32} &= \frac{b^{(1)}}{2\,\pi} K \frac{C'_{44}\, x_1}{C'_{44}\, x_1^2 + C'_{55}\, x_2^2}. \end{aligned} \tag{5.A.10}$$

The coefficients C'_{ijkl} for cubic single crystals can be calculated in terms of the single crystal elastic constants C_{ijkl}, and the direction cosines by using the relation given in Section 4.4. Since our particular interest is on screw dislocations of $\{110\} < 110 >$ slip systems of NiAl single crystals, we must rotate the reference frame 45° about the i axis of the cubic crystal to reach the $< 110 >$ orientation of the screw dislocation. Then, the elastic moduli expressed in the rotated frame becomes:

$$\mathbf{C}' = \begin{bmatrix} C'_{11} & C'_{12} & C'_{12} & 0 & 0 & 0 \\ C'_{12} & C'_{22} & C'_{23} & 0 & 0 & 0 \\ C'_{12} & C'_{23} & C'_{22} & 0 & 0 & 0 \\ 0 & 0 & 0 & C'_{44} & 0 & 0 \\ 0 & 0 & 0 & 0 & C'_{55} & 0 \\ 0 & 0 & 0 & 0 & 0 & C'_{55} \end{bmatrix}, \tag{5.A.11}$$

where

$$
\begin{aligned}
C'_{11} &= C_{11}, \quad C'_{12} = C_{12}, \quad C'_{55} = C_{44}, \\
C'_{22} &= C_{11} + \frac{1}{2}(2\,C_{44} + C_{12} - C_{11}), \\
C'_{23} &= C_{12} - \frac{1}{2}(2\,C_{44} + C_{12} - C_{11}), \\
C'_{44} &= C_{44} - \frac{1}{2}(2\,C_{44} + C_{12} - C_{11}).
\end{aligned}
\tag{5.A.12}
$$

The energy coefficient K for a pure screw dislocation lying along a $< 110 >$ orientation was derived in Appendix 5.B,

$$K = (C'_{44}\,C'_{55})^{1/2}, \tag{5.A.13}$$

with the elastic constants C'_{ij} given by Eq. 5.A.12.

Final expresions for the interaction forces F'. Express the forces acting on Dislocation 2 (Eq. 5.A.4), using Eq. 5.A.6-5.A.8 and 5.A.10 (we will set aside the component F'_3 since it does not affect the motion of Dislocation 2):

$$
\begin{aligned}
F'_1 &= F_1 \ , \\
&= -\,s_2^{(2)}\,(\sigma_{31}\,b_1^{(2)} + \sigma_{23}\,b_2^{(2)}) + s_3^{(2)}\,\sigma_{32}\,b_3^{(2)}, \\
&= \sigma_{32}\,b^{(2)}\,(-\,sin^2\alpha + cos^2\alpha), \\
F'_1 &= \sigma_{32}\,b^{(2)}\,cos\,2\alpha,
\end{aligned}
\tag{5.A.14}
$$

$$
\begin{aligned}
F'_2 &= F_2\,cos\,\alpha - F_3\,sin\,\alpha, \\
&= [s_1^{(2)}(\sigma_{31}b_1^{(2)} + \sigma_{32}b_2^{(2)}) - s_3^{(2)}\sigma_{13}b_3^{(2)}]cos\,\alpha + [s_1^{(2)}\sigma_{23}b_3^{(2)} - s_2^{(2)}\sigma_{13}b_3^{(2)}]\,sin\,\alpha, \\
&= -\,\sigma_{13}\,b^{(2)}\,cos\,\alpha\,(cos^2\alpha + sin^2\alpha), \\
F'_2 &= -\,\sigma_{13}\,b^{(2)}\,cos\,\alpha\,.
\end{aligned}
\tag{5.A.15}
$$

Define $x_1 = d$ as the closest distance between the dislocations and express x_2 in terms of d, a normalized dislocation coordinate $\bar{x}'_3 (= x'_3/d)$, and the angle α as:

$$x_2 = \bar{x}'_3\,d\,sin\,\alpha. \tag{5.A.16}$$

Substitute these new expressions for x_1 and x_2 into Eq. 5.A.10, and then Eq. 5.A.10 into Eq. 5.A.14, 5.A.15 to obtain the final local expressions for the interaction forces per unit length of Dislocation 1:

$$F_1' = -\frac{b^{(1)}\, b^{(2)}}{2\,\pi\, d}\, \frac{cos\, 2\,\alpha}{(C_{44}'\, C_{55}')^{-1/2} + \frac{C_{55}'^{\,1/2}}{C_{44}'^{\,3/2}}\, (\bar{x}_3'\, sin\,\alpha)^2}\ , \tag{5.A.17}$$

$$F_2' = -\frac{b^{(1)}\, b^{(2)}}{4\,\pi\, d}\, \frac{sin\, 2\alpha\ \ \bar{x}_3'}{\frac{C_{44}'^{\,1/2}}{C_{55}'^{\,3/2}} + (C_{44}'\, C_{55}')^{-1/2}\, (\bar{x}_3'\, sin\,\alpha)^2}\ . \tag{5.A.18}$$

As Fig. 3.A.1 shows, F_1' is a force which acts along the direction given by the closest distance between the dislocations d. When the dislocations are of different types, as in Fig. 3.A.1 it is an attractive force when $0 \leq \alpha < 45^o$, zero for $\alpha = 45^o$ and a repulsive one when $45^o < \alpha \leq 90^o$. This force is maximum when the angle between screw dislocations is either 90^o (perpendicular dislocations) or 0^o (parallel dislocations). F_2' is a component of the interaction force which acts along x_2'. Since it has different signs at each side of $x_3' = 0$, it acts as a torque tending to twist the dislocation 90^o away from its original the screw position.

If the dislocations are of the same type, F_1' will change sign and act in such a way that the dislocations will repel each other when $0 \leq \alpha < 45^o$, and will attract each other when $45^o < \alpha \leq 90^o$. The sign of F_2' will also be reversed.

For isotropy, C_{44}' and C_{55}' are equal to the elastic shear modulus of the material, G, and Eq. 5.A.17 and 5.A.18 give the isotropic interaction forces obtained by Hartley and Hirth [1965]:

$$F_1' = -\frac{b^{(1)}\, b^{(2)}\, G}{2\,\pi\, d}\, \frac{cos\, 2\,\alpha}{1 + (\bar{x}_3'\, sin\,\alpha)^2}\ , \tag{5.A.19}$$

$$F_2' = -\frac{b^{(1)}\, b^{(2)}\, G}{4\,\pi\, d}\, \frac{sin\, 2\alpha\ \ \bar{x}_3'}{1 + (\bar{x}_3'\, sin\,\alpha)^2} \tag{5.A.20}$$

The only possible angles between gliding screw segments and forest dislocations piercing a {110} gliding plane are 60^o and 90^o. As it has been shown (Hartley

and Hirth, 1965), the integral interaction force between two perpendicular screw dislocations ($\alpha = 90°$), is a constant value independent of d. The remaining case, e.g. screw dislocations at $60°$ from each other, will be analized next in more detail for NiAl.

Interaction forces between $\{110\} < 110 >$ screw dislocations at $60°$ in NiAl. Let d be the distance at which the maximum *attractive* interaction force per unit length F_1' equilibrates that due to the applied effective stress, τ, in a moving dislocation:

$$F_{applied} = \tau\, b^{(1)}\,. \tag{5.A.21}$$

Thus, obtain d by equating Eq. 5.A.17 and Eq. 5.A.21 and solve for d with $\bar{x}_3' = 0$:

$$d \;=\; -\frac{b^{(2)}}{2\,\pi\,\tau_E}\,\frac{cos\,2\,\alpha}{(C_{44}'\,C_{55}')^{-1/2}}\quad. \tag{5.A.22}$$

At 850°C , the elastic stiffnesses for stoichiometric NiAl (see Section 4.2.3) are:

$$C_{11} \;=\; 185.6\,GPa, \qquad C_{12} = 124.0\,GPa, \qquad C_{44} = 91.5\,GPa. \tag{5.A.23}$$

Evaluating Eq. 5.A.12 with these values gives,

$$C_{11}' \;=\; 185.554\,GPa, \qquad C_{12}' = 124.024\,GPa, \qquad C_{55}' = 91.543\,GPa, \tag{5.A.24}$$

$$C_{22}' \;=\; 246.332\,GPa, \qquad C_{23}' = 63.246\,GPa, \qquad C_{44}' = 30.765\,GPa. \tag{5.A.25}$$

With $\alpha = 60°$, an effective stress of 51.5 MPa (measured in a cycle at $\gamma = 0\%$, with $\dot{\epsilon} = 0.01 s^{-1}$), and with $b^{(1)} = b^{(2)} = b = 0.407 \times 10^{-9}$ m, Eq. 5.A.26 yields:

$$d|_{\alpha=60°} \;=\; 3.34\,10^{-8}\ \text{m} \;=\; 82\,b. \tag{5.A.26}$$

Fig. 3.A.1 shows the interaction forces evaluated from Eq. 5.A.17 and 5.A.18 using the value of d from Eq. 5.A.26. Note that the maximum attractive force in the

direction of the closest approach is overestimated by a factor of 1.7 when isotropy is assumed using 5.A.19 and 5.A.20.

Here, it has been shown how the magnitud of the interaction forces per unit length depends on the relative distance bewteen the dislocations, which should play a role in determining the equilibrium configurations of gliding dislocations in NiAl. A more detailed study of the local equilibrium when line tension and lattice resistance are included, outside the scope of the present work, should elucidate some of the effects that repulsive and attractive dislocation forests on gliding dislocations.

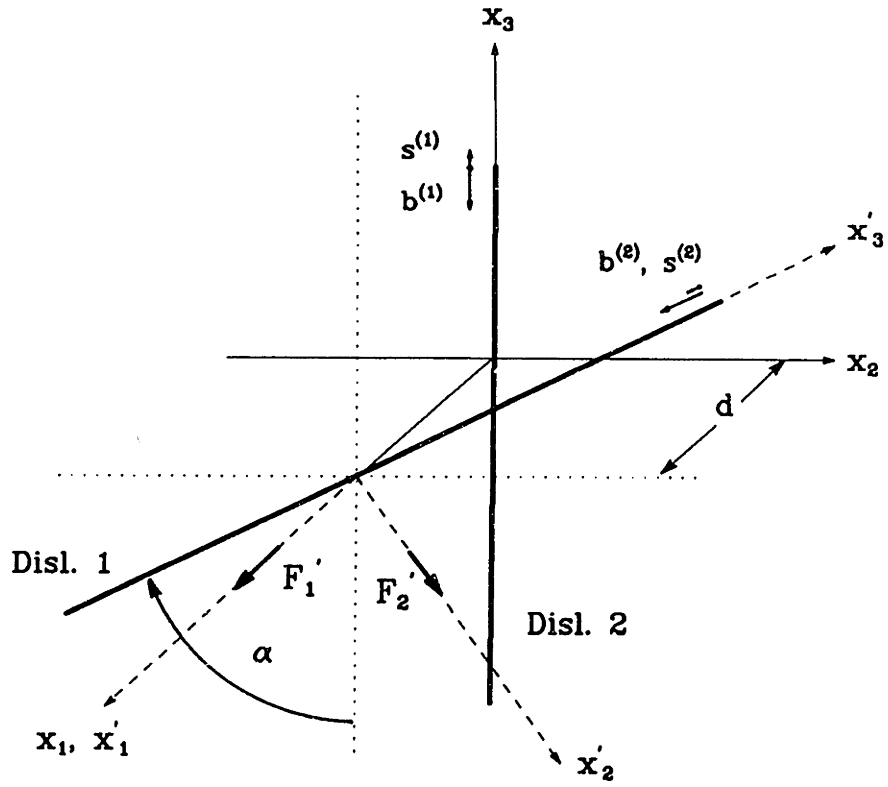

Fig. 5.A.1 Non–planar screw dislocations forming an angle α

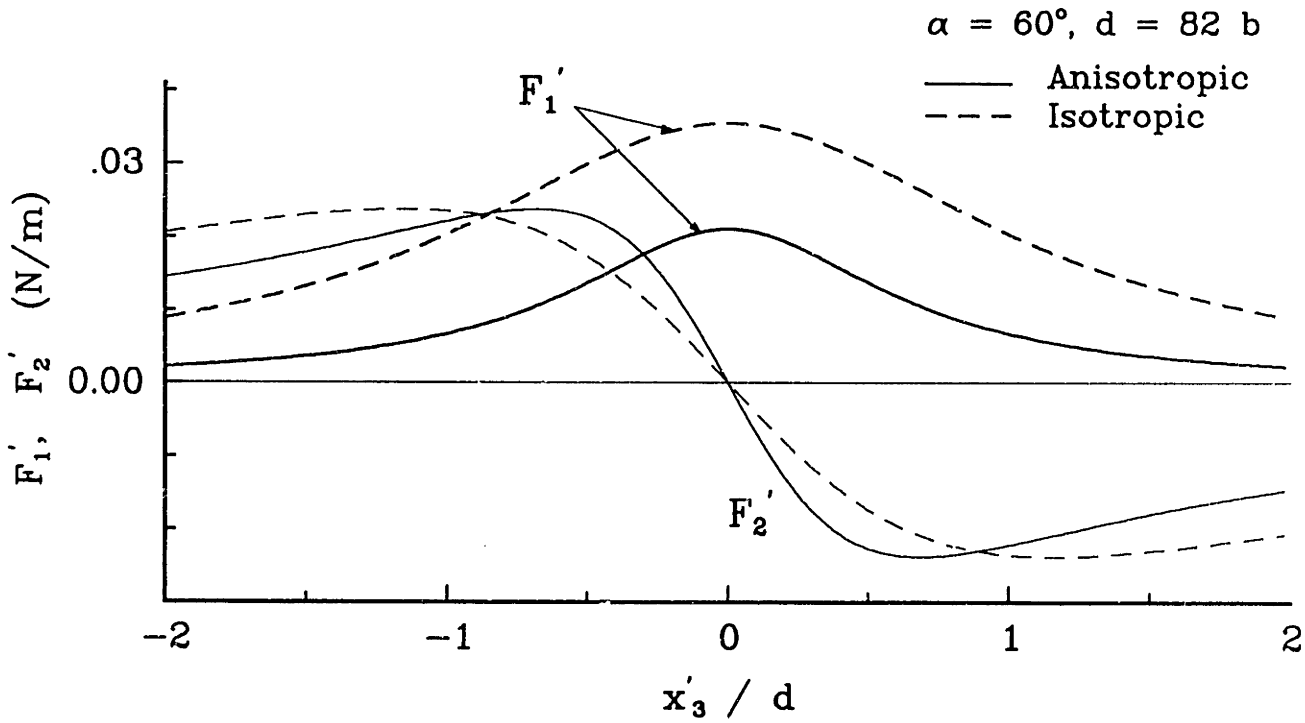

Fig 5.A.2 Interacting gliding and twisting forces per unit length between {110}<110> screw dislocations at 60° in NiAl

Appendix 5.B Average Anisotropic Energy of a Dislocation Loop

5.B.2 Total anisotropic energy of a dislocation

The total anisotropic energy of a straight dislocation of either mixed, edge or screw character is given in terms of the radius of the dislocation strain field r_1 , an effective core radius r_0, and a factor K which is itself a function of the single crystal elastic constants, the crystallographic orientation of the dislocation line and its Burgers vector b (Foreman, 1955):

$$E = \frac{K\, b^2}{4\,\pi}\; Ln\left(\frac{r_1}{r_0}\right) . \tag{5.B.1}$$

While r_1 can be easily approximated by the mean spacing between dislocations in the crystal, r_0 is more difficult to determine since it depends on the interatomic forces acting on the dislocation core.

The energy contribution from the dislocation core, inside which linear elasticity theory breaks down, can be estimated from a Peierls-Nabarro type dislocation model (Foreman, 1955) defined by a interatomic-force displacement law, which yields the shear displacement of neighboring planes of atoms. Eshelby (1953) extended the original Peierls - Nabarro model to an anisotropic elastic media and expressed r_0 as,

$$r_0 = \frac{F\, K}{C} , \tag{5.B.2}$$

where F is the interplanar distance or atomic spacing between parallel slip planes ($\approx\ b$), and C the shear elastic coefficient C_{44} for crystals with cubic symmetry. Eshelby's expression for E is given as,

$$E = \frac{K\, b^2}{4\,\pi}\left[Ln\left(\frac{C_{44}}{K}\frac{r_1}{b}\right) + 1\right] . \tag{5.B.3}$$

Eq. 5.B.3 can be shown in a more conventional form if the core width is defined as a factor α_c of its Burgers vector b:

$$E = \frac{K\,b^2}{4\,\pi}\,Ln\left(\alpha_c\,\frac{r_1}{b}\right) . \tag{5.B.4}$$

To find the expression defining α_c, equate Eq. 5.B.3 and 5.B.4,

$$Ln\left(\frac{C_{44}}{K}\,\frac{r_1}{b}\right) + 1 = Ln\left(\alpha_c\,\frac{r_1}{b}\right) , \tag{5.B.5}$$

and solve for α_c :

$$\alpha_c = \frac{b}{r_1}\;exp\left[Ln\left(\frac{C_{44}}{K}\,\frac{r_1}{b}\right) + 1\right] . \tag{5.B.6}$$

With the mean spacing between dislocations l defined in terms of the total measured dislocation density ρ as $l = \rho^{-1/2} \equiv r_1$, Eq. 5.B.6 becomes:

$$\alpha_c = \frac{b}{\rho^{-1/2}}\;exp\left[Ln\left(\frac{C_{44}}{K}\,\frac{\rho^{-1/2}}{b}\right) + 1\right] . \tag{5.B.7}$$

Following the analysis introduced in Section 4.4.2, the anisotropy factor K for a $\{110\}< 110 >$ edge dislocation oriented along a $< 100 >$ direction, given in terms of the elastic stiffness coefficients C_{ij}, can be shown to be,

$$K_{edge} = (C_{11} + C_{12})\left[\frac{C_{44}\,(C_{11} - C_{12}}{C_{11}\,(C_{11} + C_{12} + 2\,C_{44})}\right]^{1/2} . \tag{5.B.8}$$

Similarly, for a $\{110\}< 110 >$ screw dislocation oriented along a $< 110 >$ orientation,

$$K_{screw} = \left[\frac{1}{2}\,C_{44}\,(C_{11} - C_{12}\right]^{1/2} . \tag{5.B.9}$$

Table 5.5 shows the values of K calculated with the elastic moduli given in Section 4.2.3 at 850°C , α_c and E calculated according to Eq. 5.B.7 and 5.B.4 respectively. Here, $b = 4.07 \times 10^{-10}\,m$, and $\rho = 3\mu m^{-2}$ corresponds to that measured in the cyclically deformed specimens with $\pm$ 0.5 strain history.

When the core contribution to the total energy is neglected, e.g. when $\alpha_c = 1$, 14 % and 18% lower energies than those of the above table were obtained for edge and screw dislocation respectively.

5.B.3 Average elastic energy of a dislocation loop

Since the line tension of a dislocation varies with its orientation, the local line tension E can be made to depend on an angle θ. The line tension under an applied stress τ is proportional to the local curvature κ as follows:

$$E(\theta) = \frac{\tau\, b}{\kappa}. \tag{5.B.10}$$

The non-circular equilibrium shape of a dislocation loop resulting from Eq. 5.B.10 is often to a good approximation elliptical, with the ratio of the major (a_2) and minor (a_1) sides being equal to that of the energies of an edge and screw dislocations (Kocks, Argon, and Ashby, 1975):

$$\frac{a_2}{a_1} = \frac{E_{edge}}{E_{screw}}. \tag{5.B.11}$$

Then, the average line energy of a circle with the same area and total energy than those of an ellipsoidal loop will be:

$$E_a = (E_{screw}\ E_{edge})^{1/2}. \tag{5.B.12}$$

Using the values of $E_{screw/edge}$ of Table 5.7, $E_a = 7.242 \times 10^{-9}$ J/m.

Appendix 5.C Distance travelled by an average dislocation between reversal points

5.C.4 Formulation for multi-slip

Let $\mathbf{n}^i$ and $\mathbf{b}^i$ denote, respectively, the vector normal to a particular slip plane and a permissible slip direction. The shear strain rate for a family of m slip systems can be resolved into a particular orientation and added up to obtain the macroscopic inelastic strain rate tensor as follows:

$$\dot{\epsilon}^p_{ij} = \sum_{k=1}^{m} \frac{1}{2} \left(\mathbf{n}^k_i \, \mathbf{b}^k_j + \mathbf{b}^k_i \, \mathbf{n}^k_j\right) \dot{\gamma}^k \, . \tag{5.C.1}$$

For loading along the z axis in cubic NiAl single crystals, four $\{110\}< 110 >$ systems will be active and equally stressed. Consider any of the active systems, say the $(\bar{1}01)[101]$ system,

$$\begin{aligned} \mathbf{b}_{[101]} &= b\,[cos\,45^o,\, 0,\, cos\,45^o], \\ \mathbf{n}_{(\bar{1}01)} &= [-cos\,45^o,\, 0,\, cos\,45^o] \, . \end{aligned} \tag{5.C.2}$$

Express the normal component parallel to the z axis of Eq. 5.C.1 in incremental form as,

$$\Delta\epsilon^p_{zz} = \sum_{k=1}^{4} \frac{1}{2} \left(\mathbf{n}^k_z \, \mathbf{b}^k_z + \mathbf{b}^k_z \, \mathbf{n}^k_z\right) \Delta\gamma^k \, . \tag{5.C.3}$$

Then, substituting the z components of Eq. 5.C.2 into 5.C.3 gives the relation between the macroscopic inelastic strain range and the resolved shear strain in any of the four active $\{110\}< 110 >$ systems:

$$\Delta\epsilon^p_{zz} = \sum_{k=1}^{4} 0.5 \; \Delta\gamma^k \; = \; 2 \; \Delta\gamma^k \qquad \text{for} \quad k = 1, 2, 3, \; or \; 4 \, . \tag{5.C.4}$$

5.C.5 Inelastic shear strain range of slip system i.

Assume that there is no change in the total density of dislocations during the increment in strain.

Let ΔA_j^i be the area swept by an individual dislocation segment j of length l_j^i belonging to the slip system i . By definition, the increment in shear strain per unit volume V due to the sum of the areas swept by all the individual gliding dislocations of system i is given as,

$$\Delta\gamma^i = b \sum_{j=1}^{all\ seg.} \frac{\Delta A_j^i}{V} , \tag{5.C.5}$$

where b is the magnitud of the Burgers vector defined in Eq. 5.C.2. Define Δy as the mean free path of glide dislocations between sources and storage points, so that $\Delta A_j^i = \Delta y\ l_j^i$. Eq. 5.C.5 can now be written as,

$$\Delta\gamma^i = \Delta y\ b\ \frac{\sum_j l_j^i}{V} . \tag{5.C.6}$$

If $\sum_j l_j^i$ is the total line length that has moved in a volume V of the material, then $\rho^i = \sum_j l_i^j / V$ is the total dislocation density of moved and subsequently stored dislocations during the strain increment $\Delta\gamma^i$ in the slip system i. Eq. 5.C.6 becomes,

$$\Delta\gamma^i = \Delta y\ b\ \rho^i . \tag{5.C.7}$$

Substitute Eq. 5.C.7 into Eq. 5.C.4 to obtain,

$$\Delta\epsilon_{zz}^p = 2\ \Delta y\ b\ \rho^i . \tag{5.C.8}$$

The total measured dislocation density per unit volume is made up of the sum of the slip systems individual dislocation densities, namely $\rho = 4\,\rho^i$. The final expression for the macroscopically measured inelastic strain amplitude in a uniaxial test $\Delta\epsilon_{zz}^p$ in terms of the total mesured dislocation density ρ and Δy is:

$$\Delta\epsilon_{zz}^p = \frac{1}{2}\ \Delta y\ b\ \rho . \tag{5.C.9}$$

Appendix 5.D

```
C
C
C Program to generate the stroke command for constant engineering strain
C rate segments
C       Gauge length  (X0)                        = 11.43 mm. (0.45 in)
C       Strain conversion factor                  = 0.22108x10-2 Strain / Volt
C       Maximum sampling frequency (freqmax)=    0. samples/sec.
C
        IMPLICIT REAL*8 (A-H,O-Z)
        DIMENSION edot(100), STR0(100), STR1(100), freq(100)
        INTEGER  segsampl
        CHARACTER*(12) STROKE, ANS1, ANS2
C  Data
        DATA   FACTOR, freqmax  / 0.0022108,  80. /
        rndoff = 1.D-8
C  Input
        WRITE(6,*) 'DO YOU WANT POINT AT t=0 WRITTEN (Y/N) ? '
        READ(6,2) ANS1
        WRITE(6,*) ' AND AT  t=tmax (Y/N) ? '
        READ(6,2) ANS2
        WRITE(6,*) 'ENTER NUMBER OF LOADING SEGMENTS    '
        READ(6,*) nblocks
        DO 100 k=1, nblocks
           IF(k .EQ. 1) THEN
             WRITE(6,*)'  Segment >>>  1 :              EDOT = '
             READ(6,*) edot(1)
             WRITE(6,*)' Strains at begng. and end of segment 1  =  '
             READ(6,*) STR0(1), STR1(1)
             IF(nblocks .EQ. 1) emax = STR1(1)
           ELSE
             STR0(k) = STR1(k-1)
             WRITE(6,50) k
 50          FORMAT('   Segment',I2,' >>>> : ')
             WRITE(6,*)'                edot,  Strain1     : '
             READ(6,*) EDOT(k), STR1(k)
             IF(DABS(STR1(k)) .GT. DABS(STR1(k-1)))  emax=STR1(k)
         ENDIF
         SIGNedot = (STR1(k) - STR0(k)) / DABS(STR1(k)-STR0(k))
         edot(k)  = edot(k) * SIGNedot
100     CONTINUE
        WRITE(6,*) 'Segment # and sampling frequency (# samples/sec): '
        READ(6,*) n, freq(n)
        freq(1)   =   freq(n) / edot(n) * edot(1)
        freq0     =   freq(n)
        edot0     =   edot(n)
        IF(freq(1) .GT. freqmax)  freq(1) = freqmax
        WRITE(6,*) 'OUTPUT FILE NAME ? :  '
        READ(6,2) STROKE

    1   FORMAT(F11.5)
    2   FORMAT(4(A,F9.3))

        totaltime   = 0.
        ntotalsampl = 0
        DO 500 n=1, nblocks
          segtime  = DABS((STR1(n) - STR0(n)) / edot(n))
          IF(n .EQ. 1) THEN
            segsampl   = IDINT(freq(1) * segtime) + 1
            IF((freq(1) * segtime + 1.)-segsampl .GT. rndoff) THEN
             WRITE(6,51) n, freq(1) * segtime
51           FORMAT('*** ERROR *** non-integer sample number, SEG.',I2,
     +                '                    freq * time = ',F10.3)
             STOP
```

```
            ENDIF
          ELSE
            freq(n)  = DABS(freq0 / edot0 * edot(n))
            IF(freq(n) .GT. freqmax) freq(n) = freqmax
            segsampl =  IDINT(freq(n) * segtime)
            IF((freq(n)*segtime-segsampl) .GT. rndoff) THEN
              WRITE(6,51) n, freq(n) * segtime
              STOP
            ENDIF
          ENDIF

C         OPEN(UNIT=1,FILE='EST1.DAT')
          OPEN(UNIT=1,FILE=STROKE)
          WRITE(6,60) n
 60       FORMAT('"Segment >>>  ',I2,' : ')
          WRITE(6,65) edot(n)
 65       FORMAT('"                      edot = ',F11.5)
          WRITE(6,70) freq(n)
 70       FORMAT('"                      Freq = ',F6,1)
          WRITE(6,75) segtime
 75       FORMAT('"                   Segtime = ',F11.2)
         IF((n .EQ. 1).AND.((ANS1.EQ.'n').OR.(ANS1.EQ.'N'))) THEN
            WRITE(6,80) segsampl - 1
         ELSEIF((n.EQ.nblocks).AND.((ANS2.EQ.'n').OR.(ANS2.EQ.'N')))THEN
            WRITE(6,80) segsampl - 1
         ELSE
            WRITE(6,80) segsampl
         ENDIF
 80       FORMAT('"           Seg. samples = ',I10)
          WRITE(6,*) '-------------------------------------   '

            DO 300 I=1, segsampl
              IF((n .EQ. 1).AND.(I .EQ.1))  THEN
                strain = STR0(1)
                IF((ANS1 .EQ. 'N').OR.(ANS1 .EQ. 'n')) GOTO 300
                WRITE(UNIT=1,FMT=1) strain / FACTOR
              ELSE
                strain = strain + edot(n) / freq(n)
                IF(((ANS2.EQ.'N').OR.(ANS2.EQ.'n')).AND.(I.EQ.segsampl)
     +            .AND.(n.EQ.nblocks)) GOTO 300
                WRITE(UNIT=1,FMT=1) strain / FACTOR
              ENDIF
300         CONTINUE
400       CONTINUE
          totaltime   = totaltime + segtime
          ntotalsampl = ntotalsampl + segsampl
500       CONTINUE

          IF((ANS1.EQ.'N').OR.(ANS1.EQ.'n')) ntotalsampl=ntotalsampl-1
          IF((ANS2.EQ.'N').OR.(ANS2.EQ.'n')) ntotalsampl=ntotalsampl-1
          WRITE(6,600) totaltime
600       FORMAT('" Total time          = ',F11.3)
          WRITE(6,700) ntotalsampl
700       FORMAT('" Total # samples     = ',I7)
          WRITE(6,800)  emax / FACTOR
800       FORMAT('" Max. amplitude (V) =',F11.2)
          CLOSE(1)
          END
```

Chapter 6

Micromechanics Model of NiAl Single crystals

Abstract

A micromechanics model based on the observed dislocation structure successfully accounts for the steady-state macroscopic behavior of cubic oriented NiAl crystals subjected to strain histories within the range $\epsilon = \epsilon_m \pm 0.5\,\%$, for $\epsilon_m = 0, 35\,\%$, at 750 and 850 °C . The model properly predicts the flow stress dependence on temperature, strain rate, and structure arising from the lattice resistance to dislocation motion and from discrete obstacle resistance due to dislocation interactions.

The kinematic and isotropic hardening modes associated with defect trails left behind by gliding dislocations and dislocation storage, respectively, are properly represented. The average distance that dislocations have to glide for isotropic hardening to become the dominant mode of deformation was predicted by the model to be approximately 20 times the random dislocation forest spacing. The average measured dislocation density after a 35 % monotonic strain was found to be within 3 % of the prediction of the theoretical model.

Prediction of the brief stress transients caused by sudden strain rate changes, lasting $\approx$ 0.2% strain, would require an additional internal variable to those proposed here that could deal with the associated excess or defect mobile dislocation density.

6.1 Introduction

In the previous chapter, some of the complexities associated with forest dislocation cutting were discussed. In spite of these, a dislocation model was proposed which qualitatively accounted for the macroscopic cyclic behavior of $< 100 >$ oriented NiAl single crystals. Based on this acquired understanding and the original objectives of this work, a unified micromechanics approach will be followed to model the material behavior under this highly symmetric loading condition (e.g. $\{110\}< 110 >$ slip systems active).

This approach (e.g. see Bishop, 1952; Hill, 1966) has been extensively applied to a variety of applications such as localized deformation (e.g. Asaro and Rice, 1983) and high temperature structural applications (e.g. Paslay et al.,1970; Cailletaud et al., 1988; Busso, 1989). In a micromechanics approach, flow equations for individual slip systems and evolutionary equations for their internal variables, including cross-hardening effects, are formulated and the strain rate contributions from each of these systems are summed up to obtain the macroscopic inelastic strain rate of the single crystal. The driving force for the individual inelastic shear strain rates follows the basic assumption of Schmid's law, namely that, at a constant structure, slip on a particular system is a function of the applied stress resolved on the slip plane along the direction of slip.

The main advantage of this approach is that, since it is based on the physics of the deformation process, it offers enhanced predictive capabilities over more phenomenological approaches. Furthermore, if properly formulated and provided that a

new deformation mechanism is not encountered, the model should be able to predict accurately the material response outside the range for which it has been calibrated.

The effort in this work is primarily directed towards modeling the steady-state cyclic and monotonic response of the NiAl crystals studied in the previous chapter.

6.2 Summary of Observed Deformation Phenomena and Mechanisms

The observed dislocation structure, see Chapter 5, appeared to be composed mainly of edge and screw dislocations of approximately equal densities on stressed $\{110\}<110>$ slip systems. From the study of dislocation interactions and the approximate role that thermal and stress activation have in lowering the lattice resistance to dislocation motion and in obstacle bypassing, it was found that the flow stress in NiAl single crystals could be approximated as being due to the lattice resistance (both stress and thermally activated) and to a discrete obstacle resistance due to forest dislocations. 58 % of the total forest dislocations were found to be impenetrable within the temperature and flow stress ranges studied. When lattice friction was neglected, all forest obstacles were found to be impenetrable, thus leaving no mechanism left that could be thermally activated.

Although dislocation motion started as the stress since reversal reached twice the lattice resistance, appreciable plastic flow was not observed until forest dislocations could be bypassed at the level of the overall glide resistance or flow stress. For small strain amplitudes beyond yielding, kinematic hardening occurred due to the continued bowing of gliding screw dislocations connected to dislocation trails or dipoles formed as forest dislocations are bypassed. These defect trails promote reverse yielding. Some of the polarity due to the dipole formation process is removed by diffusion-assisted recovery, and new trails are formed every time obstacles are by-

passed during a reversal. Sudden changes in the imposed deformation rate resulted in short transients which lasted a fraction of the strain amplitude before the material returned to its steady state value.

After the structure develops dislocation tangles and sessile dislocations (for $\Delta\epsilon >$ 1.0 %), a steady-state cyclic response will be characterized by a balance between work hardening and dynamic recovery processes at a given strain rate, temperature, and stress. For large mean strains, dislocations became trapped due to being arrested by sessile dislocations or dislocation clusters. This resulted in an increased obstacle and dislocation density. Still, after 35 ± 0.5 % strain cycling, the material showed kinematic hardening, and similar rate and temperature dependence than at ± 0.5 % strain.

6.3 Model Formulation for a Slip System

In the light of the above observations, the main assumptions of the proposed micromechanics model will be:

1. The lattice resistance is stress and thermally activated.

2. Bypassing of forest dislocations by gliding dislocations is mainly a stress-activated process.

3. The form of the activation energy for lattice resistance and kinematic hardening for strain amplitudes of ± 0.5 % are also valid after isotropic hardening by 35 % strain.

6.3.1 Kinetics of the deformation process

An expression for the inelastic strain rate $\dot{\gamma}$ of a slip system under a resolved shear stress τ and a given temperature T and structure will require determining the rate

at which individual dislocations can overcome the lattice friction.

If every dislocation is supposed to start its motion from a position of constrained (metastable) equilibrium towards another configuration which also constitutes a stable position, then the energetic path between the two states can be characterized by a peak Gibbs free energy barrier, ΔG. The probability of an energy fluctuation at a given temperature that could allow the dislocation the overcome this barrier is given by the theory of kinetics in terms of Boltzmann constant k;

$$P_t = exp\left(-\frac{\Delta G}{kT}\right), \tag{6.1}$$

The rate of activation can then be found by multiplying P_t by an appropriate attempt frequency.

At any instant, the inelastic strain rate resulting from the release per unit time of a large number of dislocations facing similar energetic path barriers is given by,

$$\dot{\gamma} = \dot{\gamma}_R P_t. \tag{6.2}$$

Here, $\dot{\gamma}_R$ is the pre-exponential factor of the strain rate which represents the product of the dislocation frequency by the strain for successful activation. Eqs. 6.1 and 6.2 give the inelastic shear strain rate for the slip system:

$$\dot{\gamma} = \dot{\gamma}_R exp\left(-\frac{\Delta G}{kT}\right). \tag{6.3}$$

Since the activation energy, for the mechanisms of interest here, is far too complex to be obtained in closed form, it is necessary to utilize a more phenomenological relation that can successfully be used to account for the actual activation energy. Since the stress dependence of $\dot{\gamma}_R$ is expected to be small (p. 129, Kocks et al., 1975), important information about ΔG can be obtained from experimentally measured relations between strain rate and stress. A convenient form for the activation energy ΔG, proposed by Kocks et al. (1975), is given in terms of the strength $\hat{\tau}$

at which dislocations can be mobilized without the assistance of thermal activation, the total free energy of activation F_0 under a vanishingly small applied stress, and two parameters p and q chosen to produce the best fit to the stress dependence of the activation energy,

$$\Delta G = F_0 \left\{ 1 - \left(\frac{\tau}{\hat{\tau}} \right)^p \right\}^q . \tag{6.4}$$

The strength $\hat{\tau}$ can, in turn, be approximated by the product of the lattice friction stress at 0 K, $\hat{\tau}_0$, with the ratio of the shear modulus ($\equiv C_{44}$) at the temperature of interest to that at 0 K,

$$\hat{\tau} = \hat{\tau}_0 \frac{\mu}{\mu_0} . \tag{6.5}$$

The inelastic strain rate, Eq. 6.3, expressed in terms of Eqs. 6.4 and 6.5, becomes,

$$\dot{\gamma} = \dot{\gamma}_R \, exp \left\{ - \frac{F_0}{k\,T} \left[1 - \left(\frac{\tau}{\hat{\tau}_0 \, \mu/\mu_0} \right)^p \right]^q \right\} . \tag{6.6}$$

Since the model assumes that only the lattice resistance can be thermally and stress activated, the driving stress τ for the activation energy in Eq. 6.6 can be expressed in terms of the flow stress τ_R and the athermal discrete obstacle resistance due to forest dislocations S_0:

$$\tau \equiv \tau_l = \tau_R - S_0 \frac{\mu}{\mu_0} . \tag{6.7}$$

The final expression for the flow rate is then,

$$\dot{\gamma} = \dot{\gamma}_R \, exp \left\{ - \frac{F_0}{k\,T} \left[1 - \left(\frac{\tau_R - S_0 \, \mu/\mu_0}{\hat{\tau}_0 \, \mu/\mu_0} \right)^p \right]^q \right\} . \tag{6.8}$$

It is of practical interest to invert Eq. 6.8 so as to obtain the flow stress dependence on temperature, strain rate, and structure:

$$\tau_R = \hat{\tau}_0 \frac{\mu}{\mu_0} \left\{ 1 - \left(\frac{T}{T_0} \right)^{1/q} \right\}^{1/p} + S_0 \frac{\mu}{\mu_0} . \tag{6.9}$$

where,

$$T_0 \equiv \frac{F_0}{k} \frac{1}{ln(\dot{\gamma}_R/\dot{\gamma})} , \tag{6.10}$$

can be interpreted as an extrapolated temperature at which, for a given strain rate and no back activation, the thermal energy becomes large enough so as to provide the activation energy at zero applied stress.

6.3.2 Internal variables

To describe the observed cyclic behavior of NiAl, two internal variables per slip system are needed: (i) a kinematic hardening variable to account for the increased bowing after bypassing arising from dislocations connected to defect trails and the associated diffusion-assisted and reversed stress recovery of these trails and (ii) an isotropic hardening variable to describe the structure evolution as dislocation storage increases the forest density beyond the level needed to balance dynamic recovery processes.

The kinematic hardening variable B of a slip system, analogous to the back stress commonly used in continuum mechanics, can be obtained from the macroscopically measured average back stress resolved into one of the active slip systems. By definition, the absolute value of B should be the difference between the actual stress needed to bow gliding dislocations that have developed defect trails, or *bowing stress* τ_{bow}, and its value at initial yielding (after which massive obstacle bypassing occurs and new trails are formed):

$$|B| = |\tau_{bow}| - |\tau_{bow}|_{yield} . \tag{6.11}$$

The internal variable directly related to the structure or forest density on a slip plane is taken to be the athermal component of the flow stress S_0, whose relation to the density of the randomly distributed forest dislocations on a given slip plane, ρ_I,

is given by Eq. 5.16,

$$S_0 \;=\; \alpha\, \mu_0\, b\, \rho_I^{1/2}\;, \tag{6.12}$$

where $\alpha = 0.85$ is a statistical factor.

Expressing ρ_I in terms of the total measured dislocation density in the crystal ρ and the ratio $r = \rho_I/\rho$ gives

$$S_0 \;=\; \alpha\, r^{1/2}\, \mu_0\, b\, \rho^{1/2}\;. \tag{6.13}$$

Coupling between S_0 and B, needed to account for the back stress dependence on the current obstacle density on the slip plane, is obtained by recalling the definition of τ_{bow} at yielding from Eq. 5.15. Then, for the general case of forward and backward slip, Eq. 6.11 becomes,

$$B \;=\; \tau_{bow} \;-\; S_0 \frac{\mu}{\mu_0}\; sgn(\dot{\gamma})\;. \tag{6.14}$$

Fig. 6.1 shows the relation between the variables in the above equation during $\pm\, 0.5\,\%$ cyclic loading, as well as their relative magnitudes at different stages of the deformation process.

In order to extend Eq. 6.8 for the inelastic strain rate to cyclic loading, it will have to be modified accordingly and the flow stress, τ_R, be substituted by an *effective* stress defined by the difference between the resolved shear stress in the slip system and the back stress B. Hence,

$$\dot{\gamma} \;=\; \dot{\gamma}_R\; exp\left\{ -\frac{F_0}{k\,T} \left[1 \;-\; \left\langle \frac{|\tau - B| \;-\; S_0\, \mu/\mu_0}{\hat{\tau}_0\; \mu\,/\,\mu_0} \right\rangle^{p} \right]^{q} \right\}\; sgn(\tau - B)\;. \tag{6.15}$$

The brackets $<>$ imply that with $x = |\tau - B| - S_0\,\mu/\mu_0$, $< x >= x$ for $x > 0$, and $< x >= 0$ for $x \leq 0$. The $sgn(\tau - B)$ allows modeling both negative and positive slip on the system.

The resolved shear stress τ can be found from the stress component σ acting along the specimen axial direction **a**. Let **n** and **b** denote, respectively, the vector normal to a particular slip plane and a permissible slip direction. Then,

$$\tau = \sigma \, (\mathbf{a} \cdot \mathbf{n}) \, (\mathbf{a} \cdot \mathbf{b}) \ . \tag{6.16}$$

6.3.3 Evolution of the average internal or back stress

Since the actual material behavior during the transition between kinematic and isotropic hardening is not known, the back stress B will be assumed to evolve following a saturation hardening-recovery law in terms of the slope $h_b = dB/d\gamma$ at yielding, and a saturation parameter D,

$$\dot{B} = \{h_b - D \, B \, sgn(\dot{\gamma})\} \ \dot{\gamma} \, . \tag{6.17}$$

Physically, saturation should be the result of a competition between evolutionary equations for hardening and recovery. Here, an empirical equation is used for the combination. A linear hardening law for B was not used since it would have overestimated B for large deformations (e.g. 35 % strain).

The integrated form of the above equation in absolute value form,

$$|B| = \frac{h_b}{D} \, \{1 - exp(-D \, |\gamma|)\} \ , \tag{6.18}$$

is characterized by a saturation value (see Fig. 6.1),

$$|B|_{sat} = \frac{h_b}{D} \, . \tag{6.19}$$

D can be given in terms of physically representative quantities. Express the bowing stress τ_{bow} at saturation as a fraction f of the flow stress $\tau_{oro} = \mu \, b \, \rho_I^{1/2}$ (denoted the Orowan stress), which is the stress needed to drive a dislocation through an isolated pair of obstacles separated a distance $l_I = \rho_I^{-1/2}$. Then, from Eq. 6.14,

$$|B|_{sat} = |\tau_{bow}|_{sat} - S_0 \frac{\mu}{\mu_0} \ ,$$

$$= \quad f\,\tau_{oro} - S_0\frac{\mu}{\mu_0}\,. \tag{6.20}$$

A relation between τ_{oro} and S_0 can be obtained from Eq. 6.12,

$$\tau_{oro} = \mu\, b\, \rho_I^{1/2} = (S_0\,\mu/\mu_0)/\,\alpha\,. \tag{6.21}$$

Then, with this definition of τ_{oro}, solve for D after equating Eqs. 6.19 and 6.20,

$$D = \frac{h_b}{(f/\alpha - 1)\,S_0\,\mu/\mu_0}\,. \tag{6.22}$$

Finally, substitute D into Eq. 6.17 to express the evolution of B in terms of physically meaningful quantities:

$$\dot{B} = \left\{1 - \frac{B}{(f/\alpha - 1)\,S_0\,\mu/\mu_0}\,sgn(\dot{\gamma})\right\}\,h_b\,\dot{\gamma}\,. \tag{6.23}$$

A relation for f in terms of parameters obtained from experimental observations will be derived in Section 6.4.

6.3.4 Evolution of the athermal forest resistance

The change in the athermal glide resistance S_0, resulting from a strain-induced increment in the density of obstacle-producing forest dislocations, can be obtained by differentiating Eq. 6.12:

$$dS_0 = \frac{\alpha\,\mu_0\,b}{2}\,\frac{d\rho_I}{\rho_I^{1/2}}\,. \tag{6.24}$$

The strain increment that gives rise to this increase in obstacle density can be expressed in terms of the areas swept by individual gliding dislocations, ΔA_j, of length l_j. The increment in shear strain per unit volume V due to the sum of the areas swept by all the individual gliding dislocations is,

$$d\gamma = b\;d\left(\sum_{j=1}^{mobile\,seg.}\frac{\Delta A_j}{V}\right)\,. \tag{6.25}$$

Define Y as the mean free path of glide dislocations between sources and storage points, so that $\Delta A_j = Y\ l_j$. Eq. 6.25 can now be written as,

$$d\gamma = Y\ b\ d\left(\sum_{j}^{mobile\ seg.} \frac{l_j}{V}\right) . \tag{6.26}$$

$\sum_j l_j / V$ is the total dislocation density of moved and subsequently stored dislocations during the strain increment $d\gamma$. As expected from the mechanisms discussed in the previous chapter, stored dislocations will translate directly into an increased forest density resulting in a higher obstacle density by $d\rho_I = d\left(\sum_j l_j / V\right)$, Eq. 6.26 becomes,

$$d\gamma = Y\ b\ d\rho_I . \tag{6.27}$$

From the so-called principle of similitude (Kuhlmann-Wilsdorf, quoted by Argon and Deng, 1987, Kocks, 1966), Y can be related to the mean spacing of the randomly distributed obstacles in the slip plane, l_I, through a constant C:

$$Y = C\ l_I. \tag{6.28}$$

Then, making use of the definition $l_I = \rho_I^{-1/2}$, and substituting $d\rho_I$ from Eq. 6.27 (with Y as per Eq. 6.28) into Eq. 6.24 becomes:

$$dS_0 = \frac{\alpha\ \mu_0}{2\ C}\ |d\gamma| , \qquad \text{for} \quad \int d\gamma_{since\ rev.} > \Delta\gamma_{trans} . \tag{6.29}$$

The absolute value in Eq. 6.29 is needed to extend it to cyclic straining. $dS_0 > 0$ for strain reversals greater than a certain value $\Delta\epsilon_{trans}$ to be determined below.

Although Eq. 6.29 has not been modified to account for recovery processes likely to be present, such as the removal of tangled dislocations being held at clusters, a more complete physical model would have to include such effects (see Prinz et al., 1982, for ways of modeling recovery). As will be shown, neglecting dynamic recovery proved to be an adequate approximation.

6.4 Transition Configurations of Gliding Dislocations

In order to link the domains of kinematic and isotropic hardening, an approximation to the corresponding transition was made through the saturation hardening form of E, Eq. 6.23. Due to the infinite convergence associated with Eq. 6.18, namely that as,

$$B \rightarrow B_{sat}, \qquad \gamma \rightarrow \infty , \tag{6.30}$$

it is of particular interest to know how close to its saturated value (Eq. 6.19) the back stress B has to get for the athermal forest resistance to start increasing, viz. for $dS_0 > 0$. To that effect, define a parameter g_{tr} so that,

$$if \quad |B| \geq g_{tr}\,|B|_{sat} , \qquad then \qquad dS_0 > 0 . \tag{6.31}$$

If the transition per se is defined by *the strain accumulated (since the last load reversal) at which the dislocation density will start increasing over the level required to balance recovery,* then this transition strain amplitude can be obtained from Eq. 6.18 by eliminating B with Eq. 6.31, B_{sat} with Eq. 6.19, and D with Eq. 6.22:

$$\Delta\gamma_{trans} = \frac{-\,h_b \;\; ln(1 - g_{tr})}{(f/\alpha \;-\; 1)\; S_0\, \mu/\mu_0} . \tag{6.32}$$

Next, find f from Eq. 6.32 by eliminating $\Delta\gamma_{trans}$ from the total hardening measured after a strain increment beyond $\Delta\gamma_{trans}$. The strain change can be determined from the known evolution law for the athermal forest resistance with shear strain, Eq. 6.29, if both the initial and final states or structures are known. Consider an initial and a final deformation state characterized by the flow stresses τ_1 and τ_2 respectively. This change in flow stress will be the change in athermal forest resistance from S_{0_1} to S_{0_2} less any change in lattice resistance (Eq. 6.7). Since the

lattice resistance, is controlled by the atomic scale, it will remain independent of the dislocation structure. Then,

$$\tau_2 - \tau_1 = (S_{0_2} - S_{0_1}) \frac{\mu}{\mu_0} . \tag{6.33}$$

Let $\Delta\gamma$ be the inelastic strain increment between the two states and $dS_0/d\gamma = \alpha\,\mu\,/(2\,C)$, the athermal resistance strain hardening rate as defined in Eq. 6.29 with the shear modulus expressed at the test temperature T. Then, the transition shear strain amplitude is

$$\Delta\gamma_{trans} = \Delta\gamma - \frac{S_{0_2} - S_{0_1}}{\alpha\,\mu_0\,/(2\,C)} . \tag{6.34}$$

The final expression for the fraction f of the Orowan stress at which the bowing stress saturates is obtained after equating Eqs. 6.34 and 6.32 and solving for f. This gives f in terms of the initial value of S_0, and the two parameters that need be determined from a monotonic or large strain amplitude test, $\Delta\gamma$ and $\Delta S_0 = S_{0_2} - S_{0_1}$ (or equivalently $\Delta\tau$):

$$f = - \frac{\alpha\,h_b}{ln(1-g_{tr})\,S_{0ini}\,\mu/\mu_0} \left[\Delta\gamma - \frac{2\,C}{\alpha\,\mu_0}\,\Delta S_0\right] + \alpha . \tag{6.35}$$

To maintain $dS_0 = 0$ during the kinematic hardening range for any $|B| < g_{tr}\,|B_{sat}|$, define an integer i in Eq. 6.29,

$$dS_0 = \frac{\alpha\,\mu_0}{2\,C}\; i\;|d\gamma| , \tag{6.36}$$

so that,

$$i = \begin{cases} 0 & if\ \ |\tau_{bow}| = |B| + S_0\,\mu/\mu_0 \ < \ g_{tr}\,f\,S_0\,(\mu/\mu_0)\,/\,\alpha \\ 1 & if\ \ otherwise \end{cases} \tag{6.37}$$

Appendix 6.A shows the complete set of equations associated with a slip system.

6.5 Formulation for Multiple-Slip

The shear strain rate for the six $\{110\}< 110 >$ slip systems in NiAl crystals can be resolved into a particular orientation and added up to obtain the macroscopic inelastic strain rate tensor:

$$\dot{\epsilon}^p_{ij} = \sum_{k=1}^{6} \frac{1}{2} \left(n_i^k \, b_j^k + b_i^k \, n_j^k \right) \dot{\gamma}^k \, . \tag{6.38}$$

n and **b** were already defined in connection with Eq. 6.16.

When loading takes place along one of the cubic axes, only four $\{110\}< 110 >$ systems are active. They are also equally stressed. Then, the relation between the macroscopic inelastic strain rate $\dot{\epsilon}^{in}$ and the resolved shear strain in any of the four active $\{110\}< 110 >$ systems results (see Appendix 5.C):

$$\dot{\epsilon}^{in} = \sum_{k=1}^{4} 0.5 \, \dot{\gamma}^k = 2 \, \Delta\gamma^k \qquad \text{for} \quad k = 1, 2, 3, \; or \; 4 \, . \tag{6.39}$$

6.6 Determination of Material Parameters

Two different types of material parameters or functions need be determined for the present formulation: (*i*) those that can be found from the observed dislocation structure and, (*ii*) those which at present must be found from experimental stress-strain data.

The measured or computed values of the complete set of parameters are given in Appendix 6.A.

Structure material parameters. The lattice friction stress at 0 K, $\hat{\tau}_0$, was deduced from the monotonic yield strength data of $< 100 >$ oriented NiAl crystals, $\sigma_{0.2}$, shown in Fig. 6.2 (Pascoe and Newey, 1968). Despite the differences between the initial homogenized structure from the monotonic tests of Pascoe and Newey, and

the cyclically stabilized structure of interest here, the effect on $\hat{\tau}_0$ will be negligible as the strength at 0 K is mostly due to lattice friction. $\hat{\tau}_0$ was obtained by subtracting the yield strength which becomes independent of temperature, from the extrapolated yield strength to 0 K and resolving it into one of the active slip systems (Schmid factor$_{\{110\}<110>} = 1/2$):

$$\hat{\tau}_0 \equiv \frac{\sigma_{0.2}(0K)}{2} - \frac{\sigma_{0.2}(T \to \infty)}{2} = 982\ MPa\ . \tag{6.40}$$

Due to the uncertainty associated with the data of Fig. 6.2, $\hat{\tau}_0$ should be determined by a Monte-Carlo simulation.

As an approximation, F_0 was obtained from a lattice resistance model based on the nucleation of a double kink of length $\pi\, b \sqrt{\mu/\hat{\tau}_0}$ using a quasi-parabolic Peierls potential (p. 179, Kocks et al., 1975) in terms of already defined quantities and the magnitude of the Burgers vector b:

$$F_0 = \frac{\pi}{4}\, \mu\, b^3 \sqrt{\frac{\hat{\tau}_0}{\mu}}\ . \tag{6.41}$$

With the temperature dependence of the C_{44} shear modulus of NiAl crystals defined in Eq. 4.3, $F_0 = 0.58 \times 10^{-18}$ J at 850°C . This value is consistent with the activation energy of 0.49 $\times 10^{-18}$ J measured in this work. (Note that F_0 turns out to be 36 times larger than the energy per degree of freedom in thermal motion, namely $kT = 0.016 \times 10^{-18}$ J).

The athermal flow stress S_0, calculated from the measured dislocation densities according to Eq. 6.13 for the $\epsilon_m = 0\%$ and the $\epsilon_m = 35\%$ tests, is given in Table 6.1. Here, the ratio between the density of forest dislocation piercing a slip plane that have to be bypassed by gliding dislocations, to the total dislocation density ρ, was taken from Eq. 5.15 as $r = 0.3$.

Material parameters from stress-strain data. The flow stresses measured from the stable hysteresis loops resolved in one of the active $\{110\}< 110 >$ slip

systems (Fig. 6.3) are plotted against the testing temperatures in Fig. 6.4. Here, all elastic interactions were reduced to 0 K. The optimum values of the constants needed to fit the flow stress dependence on strain rate and temperature, namely p, q and $\dot{\gamma}_R$ in Eqs. 6.9 and 6.10, were obtained using a minimization program. Comparison between the model flow stress predictions and the resolved monotonic yield strength data of Fig. 6.2 shows similar tendencies to converge to a lower athermal bound S_0 as temperature is increased. Note that the present model predicts that when the temperature T = T_0, Eq. 6.10, the flow stress $\tau_R \frac{\mu_0}{\mu} = S_0$.

Fig. 6.5 highlights some of the difficulties associated with analytical estimates of the activation energy. Here, the flow stress dependence of the activation energy for the present work is compared to that for which the exponents p and q were analytically derived from a double kink model of the lattice resistance using an quasi-parabolic Peierls potential (Kocks et al., 1975). It can be seen that for the range of flow stresses measured in this work ($\tau_R < 100$ MPa), the activation energy is overestimated by the quasi-parabolic approach.

The mean free path coefficient C in Eq. 6.29 was chosen at 180 to give an isotropic strain hardening rate of $(dS_0/\mu_0)/d\gamma = 0.0023$, which is within the practically observed range of other materials.

A value of $h_b = 650$ MPa ($h_b/\mu = 0.007$) for the initial back stress hardening rate was found to give the optimum fitting to the experimental data.

The fraction of the Orowan stress at saturation, f (Eq. 6.35), was calculated from the increment in flow stress measured between the $\epsilon = 0\,\% \pm 0.5\,\%$ and the $\epsilon = 35\,\% \pm 0.5\,\%$ cyclic tests described in the previous chapter (see Fig. 5.23). In this case, since elastic strains can be neglected, the resolved shear strain amplitude $\Delta\gamma$ in Eq. 6.35 was approximated by half of the total applied strain amplitude $\Delta\epsilon = 35.5\%$, (see Eq. 6.39). Finally, with the resulting values being $\Delta S_0 = 46.5$

MPa and $\Delta\gamma = 0.178\,\%$ and the computational parameter g_{tr} (which defines the fraction of the saturated back stress at which the transition value of B is reached), conveniently set at $g_{tr} = 0.98$, Eq. 6.35 results:

$$f = \frac{\alpha\, h_b}{4\, S_{0ini}\, \mu/\mu_0}\left[0.178 - \frac{2\, C}{\alpha\, \mu_0}\, 46.5\right] + \alpha\,. \tag{6.42}$$

$f = 0.93$ was calculated from the above relation using the athermal forest resistance $S_{0ini} = 40.8$ MPa of the $\epsilon_m = 0\%$ test, $\mu(850°\text{C}) = 91.54$ MPa, $\mu_0 = 121.7$ MPa, $\alpha = 0.6$, and C and h_b as given in this section. With α defining the bowing stress at yielding, f is, as expected, larger due to the increase bowing of gliding dislocations that have developed defects trails as a fraction of the Orowan stress.

6.7 Model Simulations and Predictions

The equations outlined in Appendix 6.A were coded in Fortran F77 (Appendix 6.B), and several predictions and simulations were obtained.

Fig. 6.6 shows the prediction of the structure dependence of the flow stress. An increase in the structure or dislocation density (identified by the mean strain ϵ_m of the cyclic history) at constant strain rate and temperature, basically shifts the flow stress vs. temperature curve upwards by an amount equal to the increase in the athermal forest resistance S_0. The model prediction of the flow stress for the $\epsilon_m = 35\,\%$ test based on the measured dislocation density is within 3 % of the experimentally measured flow stress (data point A in Fig. 6.6), thus showing an excellent agreement.

Model simulation of the temperature and strain rate effects on the stable cyclic responses of $< 100 >$ NiAl crystals is shown in Fig. 6.7. The model not only captures the strain rate sensitivity at both temperatures but also the limited rounding at yield. The small amount of continued plastic flow immediately after reversal (e.g. see Fig.

6.8) is also accounted for. The predictive capabilities of the model are demonstrated in the simulation of arbitrary strain reversals and decreasing strain range tests within the $\pm 0.5\,\%$ range of Fig. 6.8 (a) and (b). In both cases, the rapid attainment of the linear kinematic hardening rate is correctly predicted.

Finally, the model prediction of the stable cyclic response at two different mean strains, as well as the transition between the kinematic and isotropic hardening ranges of the deformation, is shown in Fig. 6.9. Fig. 6.9a reveals the applied strain at which the increase in dislocation density can no longer be balanced by dynamic recovery. The predicted value of the transition shear strain amplitude, (Eq. 6.34), was found to be $\Delta\gamma_{trans} = 1.57\%$. From the analysis of the previous chapter, dislocations will have to glide a distance of approximately 20 forest spacing to accommodate an strain equal to $\Delta\gamma_{trans}$. In addition, the good prediction of the stable shape and kinematic hardening of the hysteresis loop for $\epsilon_m = 35\,\%$ is shown in Fig. 6.9b.

The model does not predict the brief transients, namely overshoots and undershoots in stress lasting $\approx 0.1 - 0.3\,\%$ strain, associated with sudden changes in the imposed deformation rate described in Chapter 5 (see Fig. 5.11).Modeling the transients, which appear to be caused by the sudden release of new dislocations which are eventually stored by the end of the transients, will require incorporating an additional internal variable to account for momentary changes in mobile dislocation density. This is, however, outside the scope of this work.

6.8 Conclusions

A micromechanics approach has been followed to develop a model which accounts, with a maximum error of 5 %, for the flow stress dependence on temperature, strain rate. For stresses above the the flow stress, the kinematic hardening behavior arising from bowing of gliding dislocations that have developed defect trails is properly

represented.

The strain amplitude at which isotropic hardening becomes the dominant mode of deformation was predicted to occur after dislocations glide an average of 20 times the dislocation forest spacing. For monotonic deformations of 35 %, the resulting isotropic hardening associated with dislocation storage inside the crystal, and the subsequent kinematic hardening at $\epsilon = 35\,\% \pm 0.5\,\%$ are correctly predicted. Furthermore, measured dislocation densities at 35 % mean cycle strain were found to be within 3 % of the prediction of the theoretical model. Brief transients caused by strain rate changes cannot be predicted by the present model

Although the physical mechanisms on which the model is based have previously been studied in depth in pure metals, it is the author's understanding that this is the first attempt to quantitatively model the cyclic behavior of a compound based on similar principles. There is no doubt, however, that the present model could benefit from a more rigorous account of the thermal activation of both weak forest obstacles and lattice resistance in the flow rule, and of recovery processes in the evolutionary equations. Extensive additional experimental information would however be needed.

Bibliography

[1] Argon, A.S. and D. Deng (1984),'Mechanisms of Inelastic Deformation of Solids', *Materials Forum*, **11**, 91.

[2] Asaro, R.J., and J.R. Rice (1977),'Strain localization in ductile single crystals',*J. Mech. Phys. Solids*, **25**, 309.

[3] Bishop, J. (1952),'A theoretical examination of the plastic deformation of crystals by glide', *Phil. Mag.*, **44**, 51.

[4] Busso, E.P. (1989), 'Modeling Rate Dependent Single Crystal Cyclic Plasticity for Structural Applications', Proc. of *The Second International Symposium on Plasticity and its Current Applications*, (A.S. Kahn and M. Tokuda eds.), Tsu, Japan, 541.

[5] Cailletaud, G., D. Nouailhas, and P. Poubanne (1988), 'Modeling of viscoplastic behavior of single crystals', Proc. of the *Int. Seminar on the Inelastic Behavior of Solids Models and Utilization* (MECAMAT), Besancon, France, Aug., 257.

[6] Hill, R. (1966),'Generalized constitutive relations for incremental deformation of metal plasticity by multislip', *J. Mech. Phys. Solids,* **14**, 95.

[7] Kocks, U.F. (1966),'A statistical theory of flow stress and work hardening', *Phil. Mag.*, **13**, 541.

[8] Kocks, U.F., A.S. Argon, and M.F. Ashby (1975), *Thermodynamics and Kinetics of Slip*, Progress in Mat. Sci., V. 19, Pergamon Press eds..

[9] Pascoe, R.T. and C.W. Newey (1968), 'The mechanical behavior of the intermediate phase NiAl', *Met. Sci. J.*, **2**, 138.

[10] Paslay, P., C. Wells, and G. Leverant (1970),'An analysis of primary creep of Ni-base superalloys single crystals', *ASME J. App. Mech.*, 759.

[11] Taylor, G. (1938), 'Plastic strains in metals', *J. Inst. Metals*, **62**, 307.

[12] Prinz, F.B., A.S. Argon, and W.C. Moffatt (1982), 'Recovery of dislocation structures in plastically deformed Cooper and Nickel single crystals', *Acta Metall.*, **30**, 821.

[13] Prinz, F.B. and A.S. Argon (1984),'The evolution of plastic resistance in large strain plastic flow of single phase subgrain forming metals', *Acta Metall.*, **32**, 1021.

Table 6.1 Athermal Forest Resistance Calculated from Measured Dislocation Densities (Eq. 6.13)

Mean strain %	ρ $[\mu m^{-2}]$	S_0 [MPa]
0	3.0	40.8
35	13.8	87.3

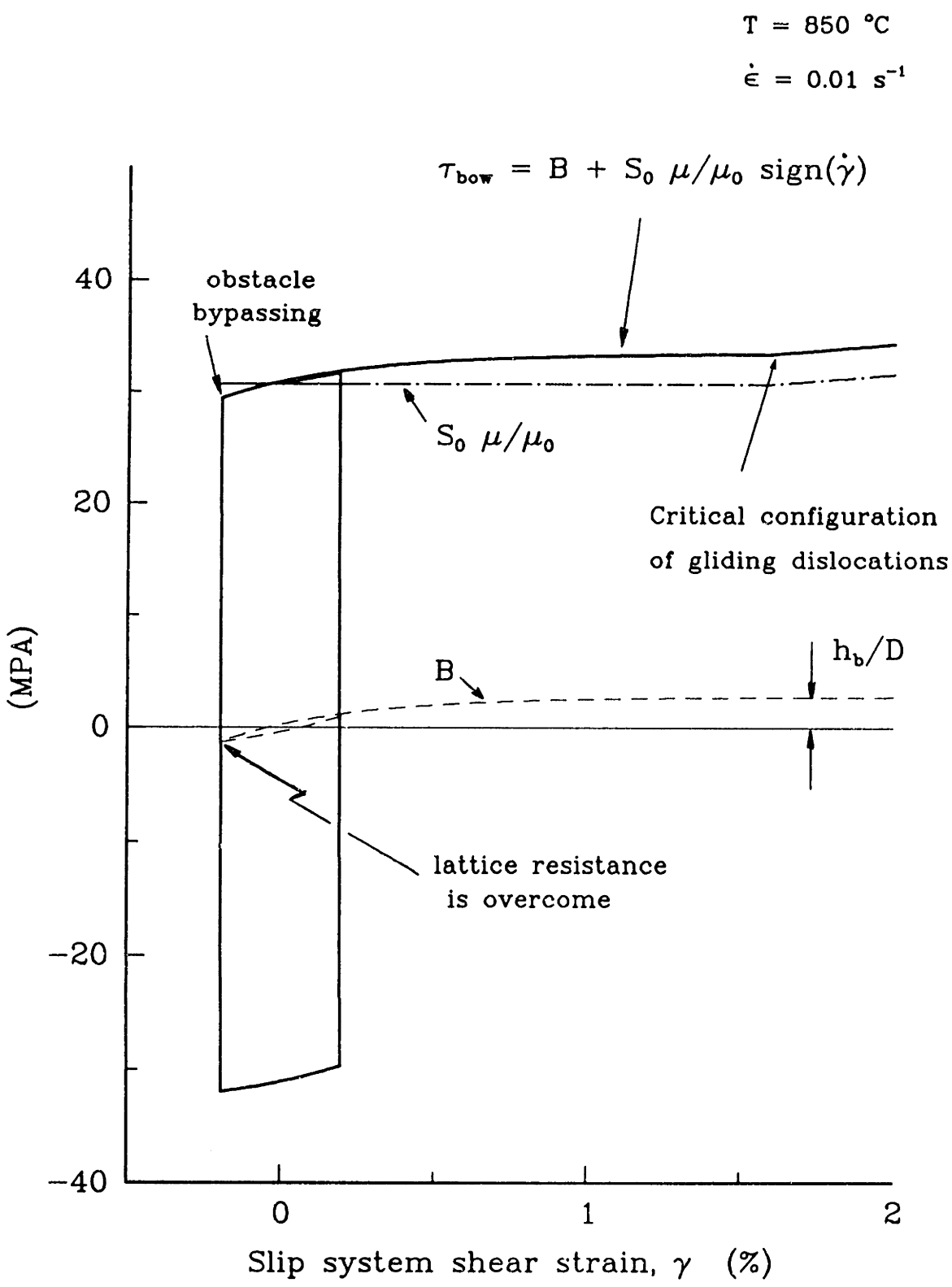

Fig. 6.1 Evolution of the bowing stress, τ_{bow}, and the internal variables S_0 and B

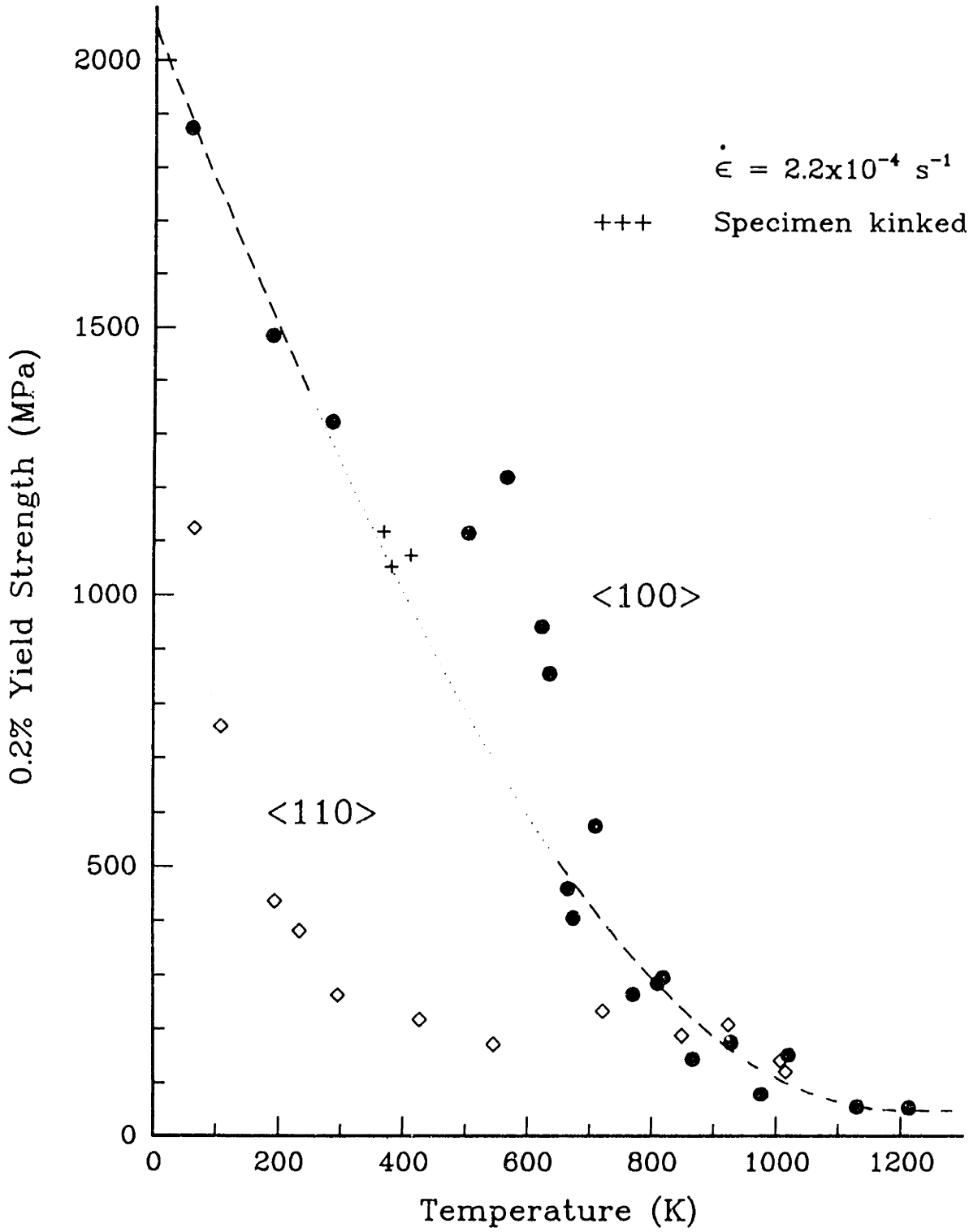

Fig. 6.2 Extrapolation of monotonic 0.2% yield strength for stoichiometric <100> NiAl to 0K (Pascoe et al., 1968)

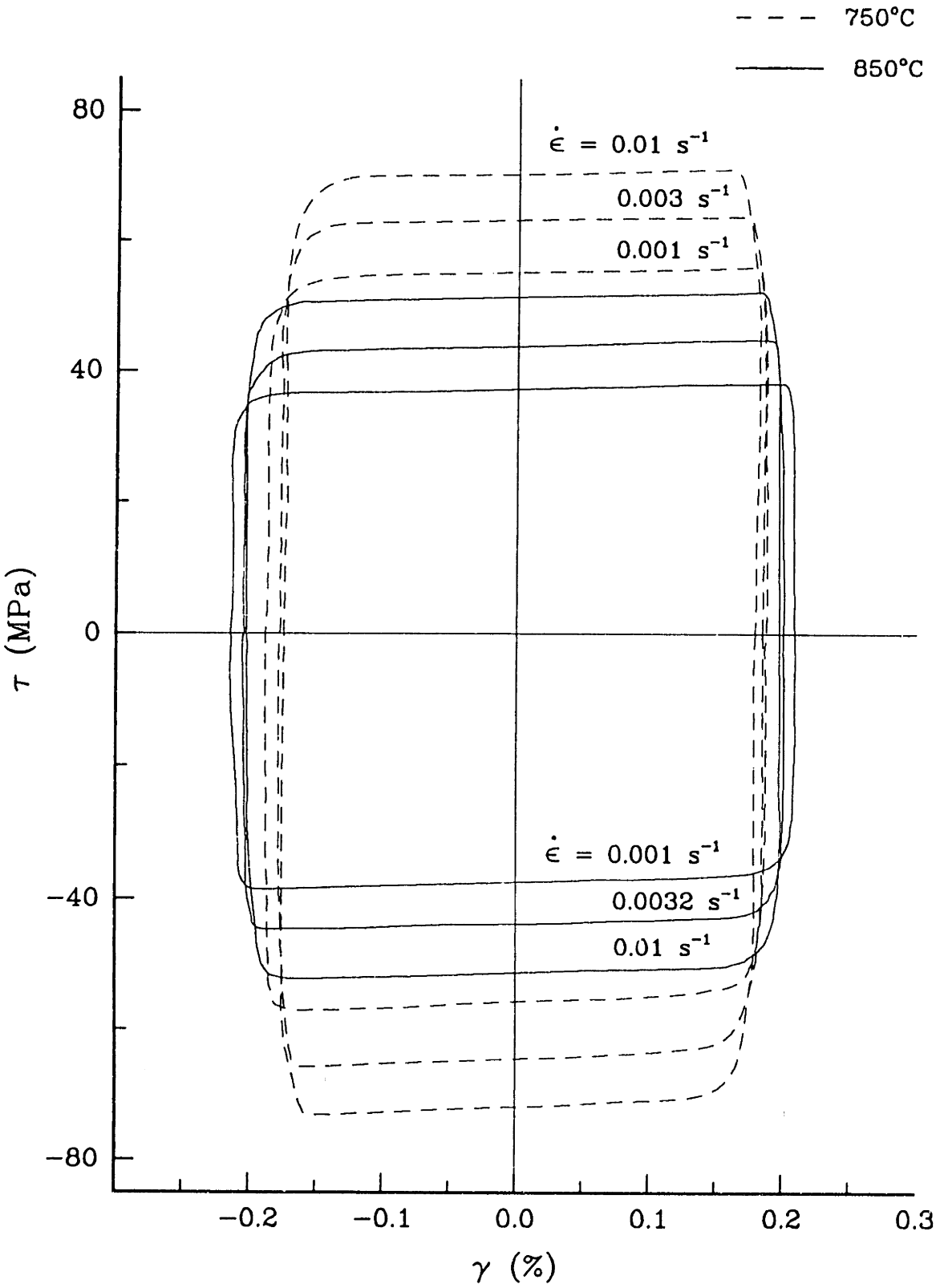

Fig. 6.3 Resolved shear stress vs. inelastic strain in all active {110}<110> slip systems with [001] loading

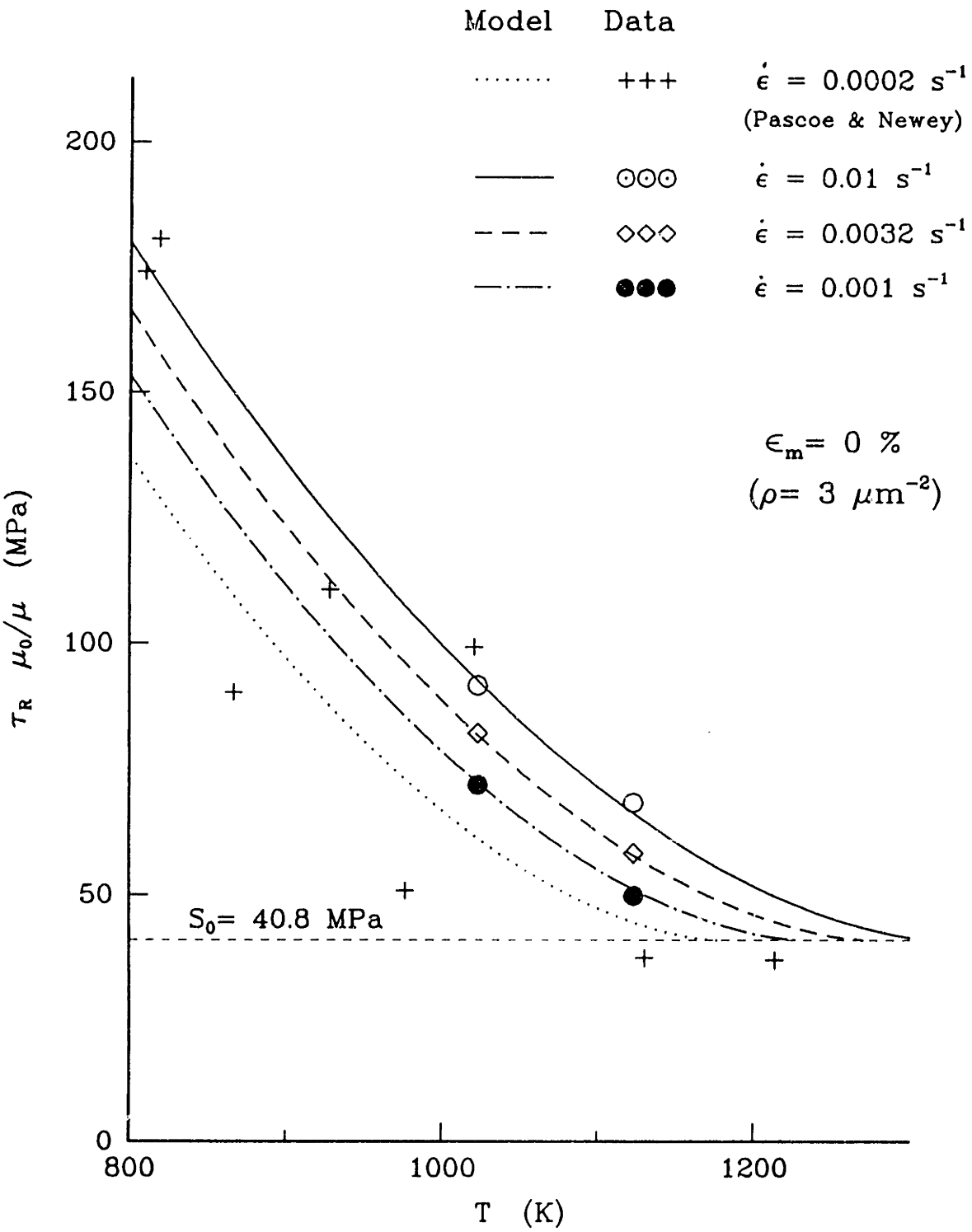

Fig. 6.4 Temperature and strain rate dependence of the flow stress of {110}<110> slip systems at constant structure

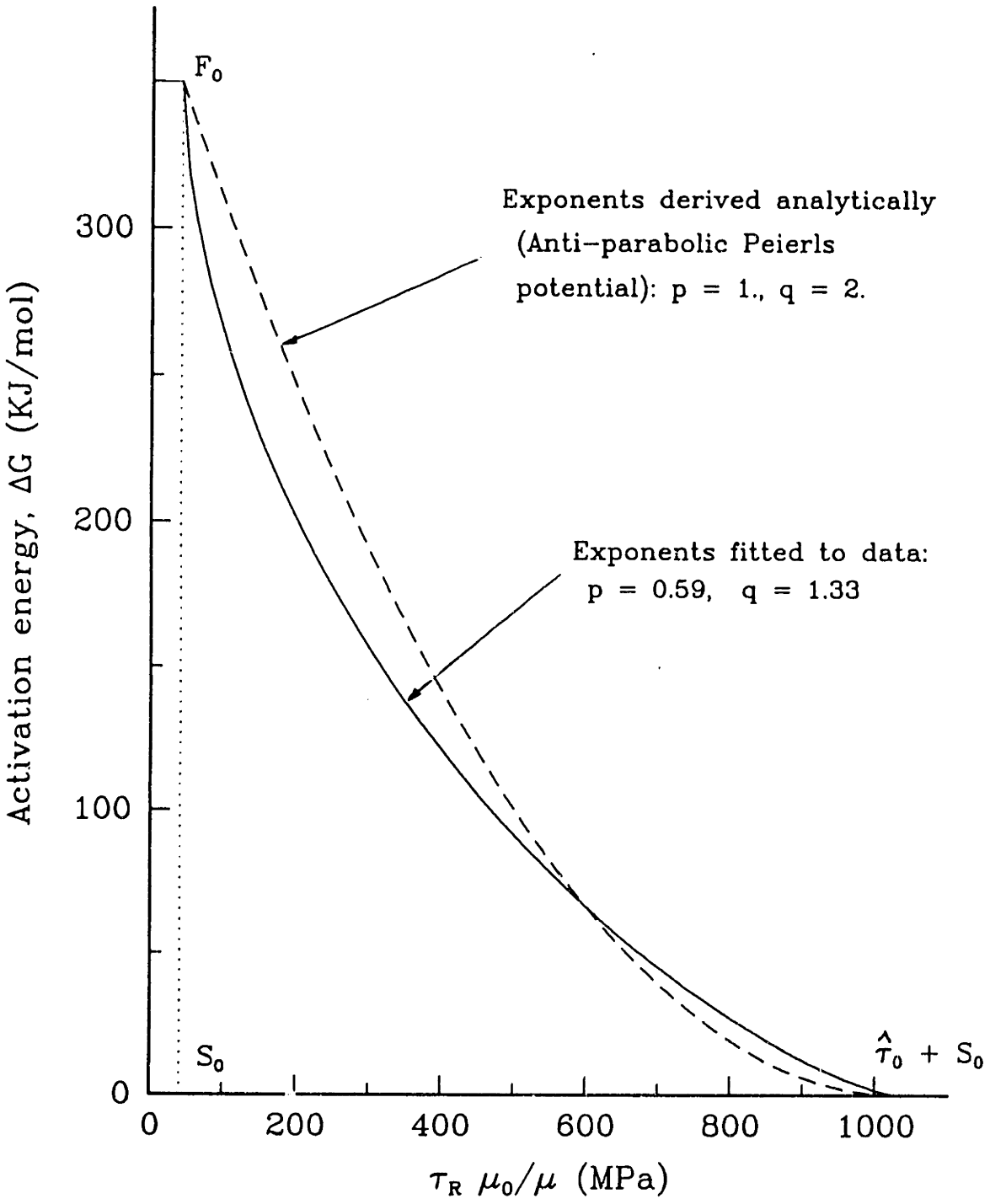

Fig. 6.5 Stress dependence of the activation energy for $\epsilon_m = 0$ ($\rho = 3\ \mu m^{-2}$)

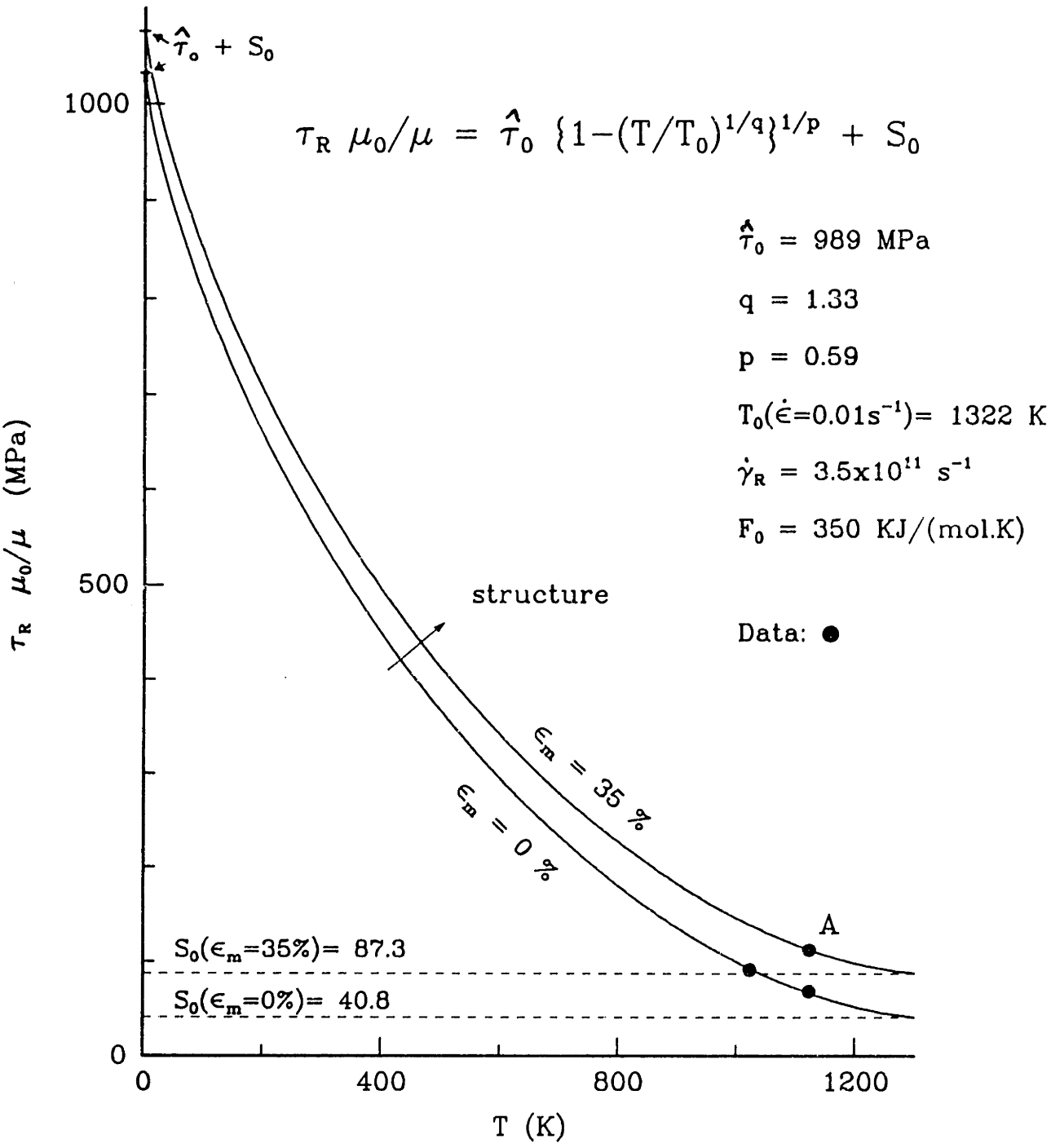

Fig. 6.6 Temperature and structure dependence of the flow stress of {110}<110> slip systems ($\epsilon_{applied} = \epsilon_m \pm 0.5\%$)

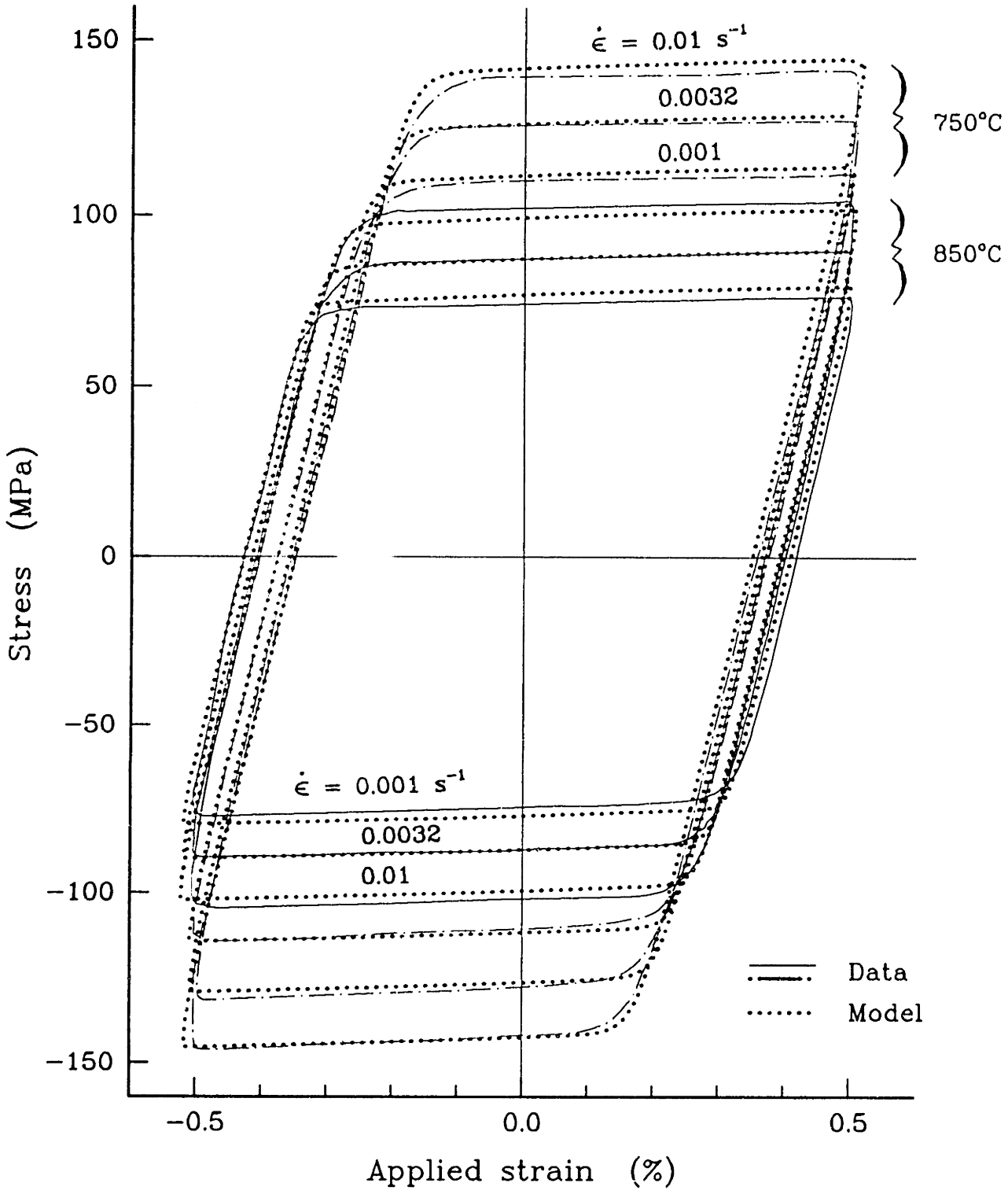

Fig. 6.7 Model simulation of the temperature and strain rate effects of <100> NiAl single crystals cyclic response

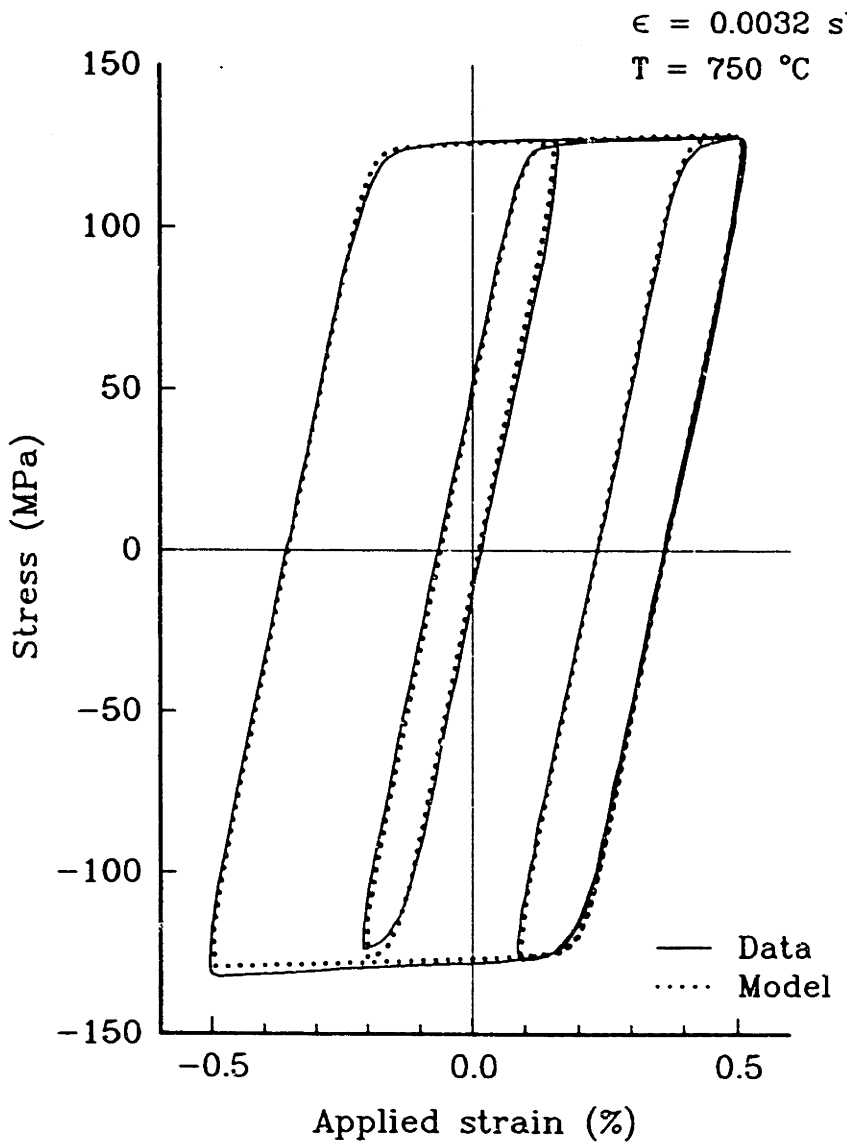

(a) Arbitrary strain reversals

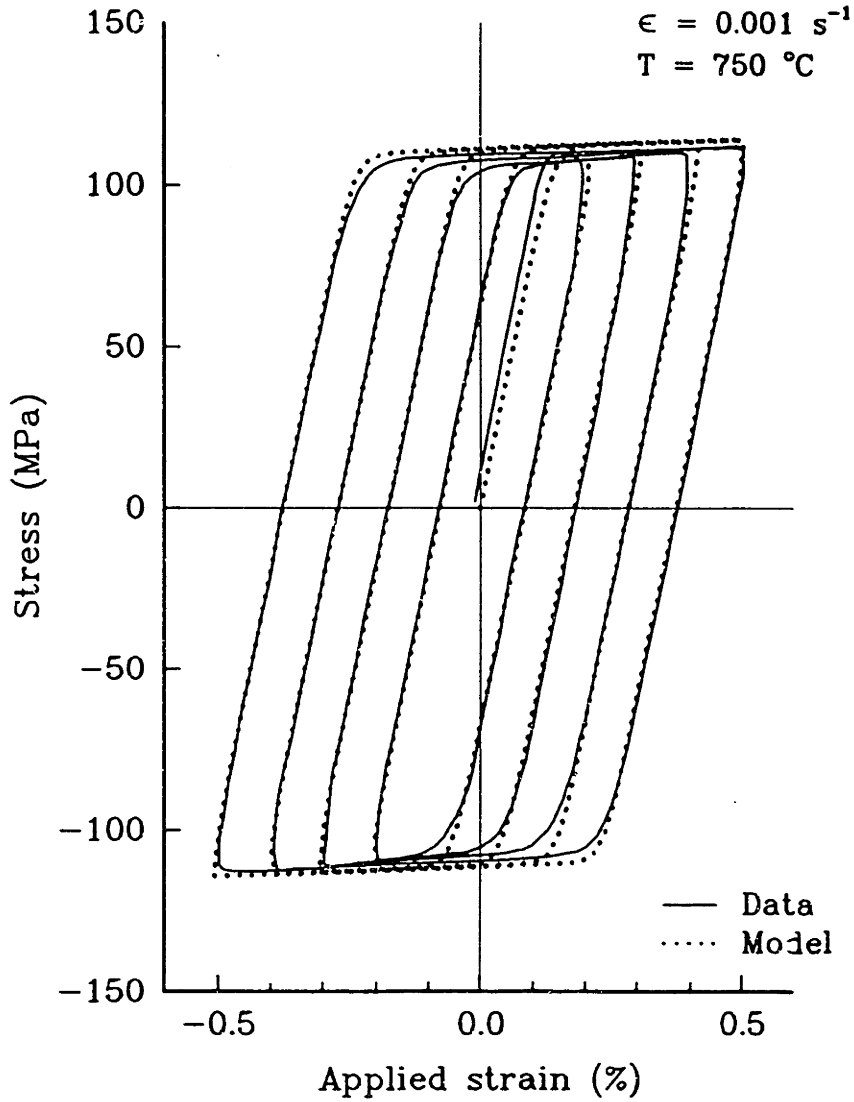

(b) Increasing strain range test

Fig. 6.8 Model prediction of the kinematic cyclic behavior of NiAl

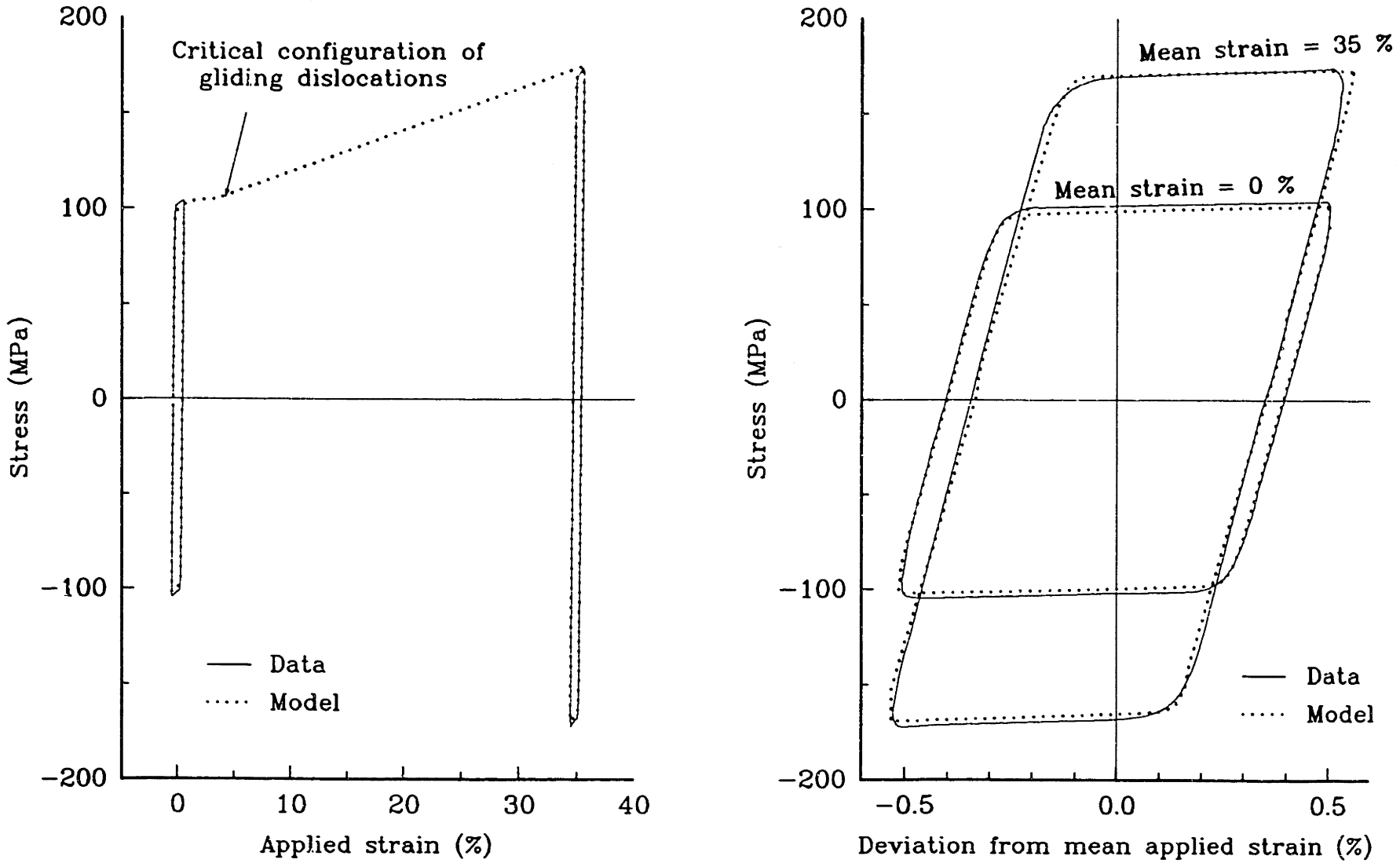

(a) Kinematic and isotropic hardening ranges

(b) Kinematic hardening range

Fig. 6.9 Stabilized cyclic response at two different mean strain levels (T= 850°C, $\dot{\epsilon}$= 0.01 s^{-1})

APPENDIX 6.A Flow and Evolutionary Equations for $\{110\} < 110 >$ Slip Systems

Kinematic hardening ($\Delta\epsilon < 3.1\%$)

Flow rule:

$$\dot{\gamma} = \dot{\gamma}_R \; exp\left\{ -\frac{F_0}{R\,T} \left[1 - \left\langle \frac{|\tau - B| - S_0\,\mu/\mu_0}{\hat{\tau}_o\;\mu\,/\,\mu_0} \right\rangle^p \right]^q \right\} \; sgn(\tau - B) \quad (6.11)$$

Loading variables:

τ : Resolved shear stress in slip system
T : Temperature

Internal variable:

B : Back stress or internal stress ($\equiv \tau_{bow} - S_0\,\mu/\mu_0\,sign(\dot{\gamma})$)

Evolution of B:

$$\dot{B} = \left\{ 1 - \frac{B}{(f/\alpha - 1)\,S_0\,\mu/\mu_0}\,sgn(\dot{\gamma}) \right\} h_b\,\dot{\gamma} \quad (6.27)$$

Material constants chosen to fit the data: $\dot{\gamma}_R,\ p,\ q,\ h_b$

Isotropic hardening

Internal variable:

S_0 : Athermal forest resistance ($\equiv \alpha\,\mu_0\,b\,(r\,\rho)^{1/2}$)

Evolution of S_0:

$$\dot{S}_0 = \frac{\alpha\,\mu_0}{2\,C}\;i\;|\dot{\gamma}| \qquad \text{where} \quad i = \begin{cases} 0 & if \;\; \frac{|B| + S_0\,\mu/\mu_0}{f\;S_0\,\mu/\mu_0\,/\alpha} < g_{tr} \\ 1 & if \;\; otherwise \end{cases} \quad (6.33)$$

New material constant introduced: C

Definition of model parameters:

- μ : C_{44} shear modulus at temperature T
- μ_0 : shear modulus at 0 K
- b : Burgers vector of $\{110\}< 110 >$ systems
- $\hat{\tau}_o$: lattice friction stress at 0 K
- $F_0 \equiv \frac{\pi}{4} \mu_0 b^3 \sqrt{\frac{\hat{\tau}_o}{\mu_0}}$: total free energy necessary to overcome the lattice resistance without the aid of external work (determined from a quasi-parabolic potential)
- ρ : total dislocation density per unit volume
- $r = \rho_I / \rho$: ratio of the density of randomly distributed impenetrable discrete obstacles arising from forest dislocations being cut by either gliding edge or screw dislocations to the total dislocation density
- α : ratio between the flow stress contributions to the total glide resistance from a non-regular and a regular arrangement of obstacles. (Statistical factor associated with gliding dislocations traversing a random field of impenetrable dislocation forests).
- C : mean free path of gliding dislocations between sources and storage points in units of mean forest spacing $l_I = (r\,\rho)^{-1/2}$ (chosen so as to obtain a typical value for $(dS_0/\mu_0)/d\gamma = \alpha\,/\,2/C)$
- g_{tr} : ratio between the bowing stress at which dislocation loops and multiplication sources are activated and the saturated bowing stress $|\tau_{bow}|_{sat}$.
- $f = \frac{\alpha\, h_b}{[-ln(1-g_{tr})]\, S_{0ini}\, \mu/\mu_0}\ [0.178 - 46.5\,(2\,C)/(\alpha\,\mu_0)] + \alpha$: ratio between the saturated bowing stress $|\tau_{bow}|_{sat} \equiv |B_{sat}| + S_0\,\mu/\mu_0)$ and the Orowan stress $\tau_{oro} = \mu\, b\, (r\rho)^{1/2}$.
- h_b : initial hardening rate for the back stress at a reversal point

Values estimated from other than the stress-strain data:

μ	=	$1.144 \times 10^5 - 26.882\,[T(K) - 273]\ MPa$	
b	=	$4.07 \times 10^{-10}\ m$	
$\hat{\tau}_o$	=	$989\ MPa$	Pascoe and Newey's $\sigma_{0.2}$ data
ρ_{ini}	=	$3\ \mu m^{-2}$	Steady state response for $\epsilon_m = 0\,\%$
r	=	0.3	$r_{edge} \simeq r_{screw}$
α	=	0.85	(Kocks, Argon)
g_{tr}	=	0.98	(Computational parameter for isotropic hardening)

Calculated values from above:

f	=	0.93	(Elastic interactions reduced to 850^oC)
S_{0ini}	=	$40.8\ MPa$	
F_0	=	$0.58 \times 10^{-18}\ J$	

Material constants chosen to fit the data:

h_b	=	$650\ MPa$	
C	=	180	Obtained from $(dS_0/\mu_0)/d\gamma = 0.0023$
$\dot{\gamma}_R$	=	$3.5725 \times 10^{11}\ s^{-1}$	
p	=	0.59	
q	=	1.33	

```
C
C                    APPENDIX 6.B
C
C ---------------------------------------------------------------------
      PROGRAM NIAL
C ---------------------------------------------------------------------
C
      IMPLICIT REAL*8 (A-H,O-Z)
      COMMON/ CONST1 /  GDOT0, F0, GC, T, G, G0, TAUhat, p, q
      COMMON/ CONST2 /  E, hb, hs, alpha
      COMMON / FLAG  /  IFLAG, Bsat, f
      COMMON  STRAINR(0:100), irmp
      EXTERNAL FU1, FU2, FU3
C
      OPEN(17, FILE='OUTS',STATUS='FRESH')
      OPEN(18, FILE='OUTB',STATUS='FRESH')
      OPEN(19, FILE='OUTAU',STATUS='FRESH')
      OPEN(20, FILE='OUTSIG',STATUS='FRESH')
      OPEN(21, FILE='OUTDOT',STATUS='FRESH')
      OPEN(22, FILE='OUTBOW',STATUS='FRESH')
C
C Data
C
      DATA       GDOT0,       F0,  GC, TAUhat,   p,     q,       G0
     +   /   3.5725D11, 349911., 8.3,  989.2, 0.59, 1.33,  121731. /
      DATA         S0R,        E,   alpha,        r,    C,   hb
     +   /        40.8,  80000.,   0.85,   0.3125,  180.,  650. /
      DATA      burgers  / 4.07D-10 /
C
C Strain history
C
      EDOT   = 0.01                ! Applied strain rate
      irmpmx = 6                   ! Number of ramps
      DATA STRAINR(1), STRAINR(2),STRAINR(3)/0.0051,-0.0052, 0.0051 /
      DATA STRAINR(4) / 0.3556/
      STRAINR(5) = STRAINR(4) - 0.011
      STRAINR(6) = STRAINR(4)
C
C Temperature in C and shear modulus
C
      TC = 850.
      G  = 1.14392D5 - 26.8818D0 * TC
      T  = TC + 273.D0
C
C Initial value of the athermal resistance at the given temperature
C
      S0         = S0R / G0 * G
C
C Strain hardening rate for the forest resistance
C
      hs = alpha * G / 2.D0 / C
C
C Fraction of the Orowan stress at which the critical
C configuration of gliding dislocation segments are reached
C
      f      =  0.125 * hb / S0 * alpha *
     +          (0.355 - (65.65 - S0)* 2. / hs)
C
C Macroscopic strain amplitude at which the bowing stress saturates
C in the slip system
C
      Esat  = f * S0 / alpha / 0.125 / hb
C
C Computational parameters
```

```
C
      BETA  = 0.01                        ! Time incr. scalar
      PFREQ =  50.                        ! Output printing frequency
C
C Initial conditions
C
      DSTRAIN     = 0.
      STRAIN      = 0.
      STRAINR(0)  = 0.
      GAMMA       = 0.
      B           = 0.
      S           = S0
      SIG         = 1.
      TAU         = SIG / 2.D0
      i           = 0
      j           = i
      IFLAG       = 1
      K           = 0                       ! Counter for WRITE
C
C Write initial conditions to plot files
C
        ZERO = 0.
        WRITE(17,50) GAMMA * 100., S                  ! S
        WRITE(18,50) GAMMA * 100., B                  ! B
        WRITE(19,50) GAMMA * 100., TAU                ! TAU
        WRITE(20,50) STRAINR(0) * 100., ZERO           ! SIG
        WRITE(21,51) TAU, GAMMADOT                ! GAMMADOT
        WRITE(22,50) GAMMA * 100, S               ! BOWING STRESS
   50   FORMAT(E10.4, 5X, F9.2)
   51   FORMAT(F9.2, 5X, E10.4)
C
      DO 200 irmp = 1, irmpmx
        i = (STRAINR(irmp) - STRAINR(irmp-1)) /
     +      DABS(STRAINR(irmp) - STRAINR(irmp-1))
        STRAIN = STRAINR(irmp-1)

C Initial time increment for the ramp
        Dt    = BETA * S0 / E / EDOT

        DO WHILE (DABS(STRAIN + i * 1.D-10 - STRAINR(irmp-1)) .LT.
     +            DABS(STRAINR(irmp) - STRAINR(irmp-1)))

          IF (DABS(STRAIN  - STRAINR(irmp)) .LT. DSTRAIN) THEN
              DSTRAIN = STRAINR(irmp) - STRAIN
              Dt      = DABS(DSTRAIN) / EDOT
          ELSE
              DSTRAIN = EDOT * Dt * i
              STRAIN  = STRAIN  + DSTRAIN
          ENDIF
C
C  If loading rate has not change sign from previous load ramp,
C  then close reversal point flag so that Bsat is not updated in FU3
C
          IF(mm .EQ. i) IFLAG = 0
C
C  Define Gammadot and rate of change of internal variables
C
          F1       = FU1(TAU, B, S)                ! gammadot
          GAMMADOT = F1
          IF(F1 .NE. 0.D0)  j = F1 / DABS(F1)
          F3 = FU3(S, B, GAMMADOT)              ! Sdot
          F2 = FU2(S, B, GAMMADOT)              ! Bdot
C
C Define unknown incremental quantities
```

```
C
            DGAMMA  = F1 * Dt
            DSIG    = E * (DSTRAIN - DGAMMA * 2.D0)
            DTAU    = DSIG / 2.D0
            DB      = F2 * Dt
            DS      = F3 * Dt
C
C Update variables at the end of Dt
C
            GAMMA    = GAMMA + DGAMMA
            TAU      = TAU + DTAU
            SIG      = SIG + DSIG
            B        = B  + DB
            S        = S  + DS
            TAUBOW   = i * S + B
C
C  Close reversal point flag at the first strain increment
C  following a load reversal
C
            IF((STRAIN .EQ. STRAINR(irmp-1)+DSTRAIN).AND.
     +                                              (IFLAG.EQ.1)) THEN
              IFLAG  =   0
            ENDIF
C
C Print updated values
C
            K = K + 1
            IF(irmp .EQ. 4 ) THEN
              pfreq = 100.
            ELSE
              pfreq =   10.
            ENDIF
            IF(INT(K / PFREQ) - K / PFREQ) 160, 150, 160
  150         WRITE(17,50) GAMMA * 100., S
              WRITE(18,50) GAMMA * 100., B
              WRITE(19,50) GAMMA * 100., TAU
              WRITE(20,50) STRAIN * 100., SIG
              WRITE(21,51) TAU, GAMMADOT              ! GAMMADOT
              WRITE(22,50) GAMMA * 100., TAUBOW
  160       CONTINUE
        END DO
        mm      = i
        IFLAG   =  1  ! Open flag to define reversal point
  200 CONTINUE
      CLOSE(17)
      CLOSE(18)
      CLOSE(19)
      CLOSE(20)
      CLOSE(21)
      CLOSE(22)
      END
C
C ---------------------------------------------------------------------
C
      FUNCTION FU1(TAU, B, S)             ! GammaDot
      IMPLICIT REAL*8 (A-H,O-Z)
      COMMON/ CONST1 /  GDOT0, F0, GC, T, G, G0, TAUhat, p, q
C
      FACTOR = DABS(TAU - B) - S
      IF(FACTOR / DABS(FACTOR) .LE. 0.D0) THEN
        FU1 = GDOT0 * (TAU - B) / DABS(TAU - B) * EXP(- F0 / GC / T)
      ELSE
        FU1 = GDOT0 * (TAU - B) / DABS(TAU - B) * EXP(- F0 / GC / T *
     +       (1.D0 - (FACTOR / TAUhat / G * G0)**p)**q)
```

```
      ENDIF
      RETURN
      END
C-----------------------------------------------------------------------
      FUNCTION FU2(S, B, GAMMADOT) !BDot
      IMPLICIT REAL*8 (A-H,O-Z)
      COMMON/ CONST2 /  E, hb, hs, alpha
      COMMON / FLAG  /  IFLAG, Bsat, f

      IF(GAMMADOT .EQ. 0.D0) THEN    !  PP
        FU2 = 0.D0
        GOTO 100
      ENDIF
      Bmax = Bsat / 0.98

      FU2 =  (1.D0 - B / Bmax  * GAMMADOT / DABS(GAMMADOT))
     +        * hb * GAMMADOT
  100 RETURN
      END
C-----------------------------------------------------------------------
      FUNCTION FU3(S, B, GAMMADOT)           ! SDot
      IMPLICIT REAL*8 (A-H,O-Z)
      COMMON/ CONST2 /  E, hb, hs, alpha
      COMMON / FLAG  /  IFLAG, Bsat, f
C
C Activation of multiplication sources when the absolute value of
C the bowing  stress  B  reaches 98 % of its maximum value
C (Define at each  reversal point, e.g. when IFLAG = 1)
C
      IF(IFLAG .EQ. 1)  THEN
        Bsat = 0.98 * f * S / alpha
      ENDIF

      IF(DABS(B) .GE. Bsat) THEN
        i = 1
      ELSE
        i = 0
      ENDIF

      FU3 =  hs * DABS(GAMMADOT) * i
      RETURN
      END
C-----------------------------------------------------------------------
```

Chapter 7

Modeling the Surface Roughening of a High Temperature Protective Coating

Abstract

An exploratory study of the role of surface instabilities in the development of surface roughening in aluminide protective coatings of gas turbine airfoils has been performed. A finite element analysis using an elasto-visco-plastic model is employed to investigate the growth of initial surface undulations under generalized plane strain deformation and typical thermal and mechanical service loads. An initial undulation in a homogeneous coating gave rise to strength inhomogeneities leading to a decrease of the undulation. The study also revealed that thermal loads play a critical role in the development of surface roughening, and that surface roughening in an original flat coating surface can be triggered by the numerical residuals associated with the solution algorithm of the finite element analysis.

7.1 Introduction

In this chapter, the surface waviness which develops in aluminide protective coatings under service conditions typical of gas turbine service will be studied. Holmes and McClintock (1990) found that roughening developed after NiAl-coated Ni-base superalloy single crystal specimens were subjected to 6000 thermal cycles typical of gas turbine service at coating compressive strain amplitudes greater than -0.20% (e.g. Fig. 7.1).

The development of surface undulations or *roughening* of the free surface of homogeneously strained materials has been previously studied theoretically for rate-independent material behavior. For small deformations, surface roughening has been attributed to non-uniform deformation of certain materials, where free surface cyclic deformation was found to be kinematically irreversible and lead to progressive roughening (McClintock, 1962). Large deformations, on the other hand, can lead to surface roughening by bifurcation phenomena (e.g. Hill and Hutchinson, 1975; Hutchinson and Tvergaard, 1980; Yoshikawa et al., 1987). A crucial aspect of the Hutchinson theory is the development of corners on the yield surface allows for ready bifurcation.

Berg and McClintock (1966) studied the motion of the free boundary of a body which undergoes non-linear viscous deformation under plane strain conditions. They found that the free surface returned to its original configuration if the load was exactly reversed.

A detailed analysis of typical temperatures and strain histories acting on protective coatings of single crystals of $\gamma - \gamma'$ alloys was presented in Chapter 1 (see also Busso and McClintock, 1988). These boundary conditions and thermal loads will be used in this study to investigate NiAl coating surface roughening. It is important to point out that similar service conditions on a NiCoCrAlY overlay coating (Chapter 2) did not caused coating roughening. Here, a small deformation finite element anal-

ysis of the NiAl coating under generalized plane strain conditions is performed to study the non-linear growth of surface instabilities starting from either a flat surface or a 10 % surface waviness.

As an approximation, the functional form of the flow and evolutionary equations for NiAl single crystals developed in Chapter 6 will be used here as a guide to describe the uniaxial stress-strain response of a polycrystalline isotropic NiAl coating. The effect of grain boundary sliding in the rate-dependent response of polycrystalline NiAl, not accounted for by the present model, is expected to be negligible due to the bamboo-type structure with a grain size of the order of the coating thickness, $100\,\mu m$ (see Fig. 7.1). In addition, the troughs of some surface undulations appeared to have originated away from grain boundaries.

7.2 Constitutive Model

The micromechanics model introduced in Chapter 6 will next be extended to 3-D and expressed within a continuum mechanics framework. The material behavior is governed by the stress tensor $\mathbf{T}$, and by two internal variables, namely a scalar or athermal forest resistance S_0, and a second order traceless symmetric back stress $\mathbf{B}$ $(tr\,\mathbf{B} = 0)$. The physical interpretation of the two internal state variables is as discussed in Chapters 5 and 6.

The model flow and evolutionary equations, assuming small deformations and rotations, are defined as follows,

Evolution equation for the stress T:

Assuming small deformations and rotations,

$$\dot{\mathbf{T}} = \mathcal{L}\,[\mathbf{D} - \mathbf{D}^p] - \dot{\theta}\,3\,\kappa\,\alpha\,\mathbf{I}\,, \tag{7.1}$$

where,

$\dot{\mathbf{T}}$	time derivative of the stress $\mathbf{T}$,
$\mathbf{D}$	total strain rate tensor,
$\mathbf{D}^p$	inelastic strain rate tensor,
$\dot{\theta}$	rate of change of absolute temperature θ,
$\mathcal{L} = 2\,G\,\mathbf{I} - \left[\kappa - \frac{2}{3}G\right]\,\mathbf{1}\otimes\mathbf{1}$	fourth order isotropic elasticity tensor,
$G = \hat{G}(\theta),\ \kappa = \hat{\kappa}(\theta)$	polycrystalline shear and bulk moduli,
$\alpha = \hat{\alpha}(\theta)$	coefficient of thermal expansion,
$\mathbf{I}$	fourth order identity tensor,
$\mathbf{1}$	second order identity tensor.

The equation for $\mathbf{D}^p$, or flow rule, is given in a standard form in terms of the *direction* of plastic flow $\mathbf{N}$ and equivalent tensile plastic strain rate $\dot{\bar{\epsilon}}^p$:

$$\mathbf{D}^p = \sqrt{\frac{3}{2}}\ \dot{\bar{\epsilon}}^p\ \mathbf{N}\,. \tag{7.2}$$

The direction of $\mathbf{N}$ is given in terms of an effective stress, defined by the difference between the deviator of the stress tensor $\mathbf{T}'$ and $\mathbf{B}$, and the equivalent tensile stress

$$\bar{\sigma} = \sqrt{\frac{3}{2}\,(\mathbf{T}' - \mathbf{B})\cdot(\mathbf{T}' - \mathbf{B})}\,, \tag{7.3}$$

as,

$$\mathbf{N} = \sqrt{\frac{3}{2}}\ \frac{\mathbf{T}' - \mathbf{B}}{\bar{\sigma}}\,. \tag{7.4}$$

Similarly, the equivalent back stress $\bar{B}$ is defined as,

$$\bar{B} = \sqrt{\frac{3}{2}\ \mathbf{B}\cdot\mathbf{B}}\ . \tag{7.5}$$

The equivalent tensile plastic strain rate $\dot{\bar{\epsilon}}^p$ is prescribed by an analogous relation to that given in Eq. 6.11:

$$\dot{\bar{\epsilon}}^p = \dot{\epsilon}_R\ exp\left\{-\frac{F_0}{R\,T}\left[1 - \left\langle\frac{\bar{\sigma}/2 - S_0\,\mu/\mu_0}{\hat{\tau}_0\ \mu\,/\,\mu_0}\right\rangle^p\right]^q\right\}\ . \tag{7.6}$$

Evolution equations for the independent internal variables:

$$\dot{\mathbf{B}} = h\,\mathbf{D}^p - \frac{h}{(f/\alpha - 1)\,S_0\,\mu/\mu_0}\,\mathbf{B}\,\dot{\bar{\epsilon}}^p\,. \tag{7.7}$$

$$\dot{S}_0 = \frac{\alpha\,\mu_0}{4\,C}\,i\,\dot{\bar{\epsilon}}^p \qquad \text{where} \quad i = \begin{cases} 0 & if \ \frac{\bar{B}+S_0\,\mu/\mu_0}{f\,S_0\,\mu/\mu_0/\alpha} < g_{tr} \\ 1 & if \ otherwise \end{cases} \tag{7.8}$$

The slip-system model of the previous chapter has now been fashioned to a polycrystalline material.

The polycrystalline elastic properties of NiAl are those reported in Chapter 4, and the thermal expansion coefficients taken from Kaufman (1982). The remaining material parameters (with $h = h_b/2$ in Eq. 7.7) have already been defined and evaluated in the previous chapter, e.g. see summary given in Appendix 6.A.

A semi-implicit numerical integration scheme to integrate the above equations over a time increment in an incremental finite element analysis is presented in Appendix 7.A.

7.3 Boundary Conditions and Model of the coating

The thermal and mechanical loads acting on the coating were chosen from the service simulations of Chapter 1 which led to the development of coating roughening (Holmes and McClintock, 1990). The selected temperature cycle, shown in Fig. 7.2a, is characterized by heating from 520 to 1090°C in 4.5s, a holding time of 60s at 1090°C , and cooling back to 520°C in 15s.

Since the coating constitutes a thin film lying on a much thicker single crystal substrate, its in-plane components of displacements are determined by those of the substrate. The coating in-plane components of the total substrate strain, ϵ_i, include

its elastic, inelastic and thermal components,

$$\epsilon_i(t) = \epsilon_i^{el}(t) + \epsilon_i^{in}(t) + \epsilon_i^{th}(t) . \tag{7.9}$$

The boundary conditions are set by the tangential $\epsilon_1(t)$ and the through-specimen-thickness $\epsilon_3(t)$ defined in Fig. 7.3. Their evolutions with time are given in Figs. 7.2b and c. The large prestrains at $t = 0$ in Figs. 7.2 b and c are due to the heating from room temperature to 520 °C (initial cycle temperature).

The finite element model of the coating consisted of two generalized plane strain eight-noded elements with an initial surface imperfection defined by (see Fig. 7.4):

$$x_2 = 0.5\,\Delta x_2\ cos\left(\frac{\pi\, x_1}{\ell_1}\right) + \ell_1 . \tag{7.10}$$

Here, Δx_2 is the initial depth and ℓ_1 the half-wave length of the imperfection. $\Delta x_2/\ell_1 = 0.1$ was chosen to represent a moderate coating roughening observed by Holmes and McClintock (1990). The evolution of the nodal displacement of the coating surface along the x_2 direction with cycling, u_2, will be monitored and reported at the end of each cycle.

The loading boundary conditions defined in the coating, Fig. 7.3, are such that the surface of the coating is traction-free, while

$$\begin{aligned} \text{along}\quad x_1 &= 0,\ u_1 = T_{12} = 0; \\ \text{along}\quad x_2 &= 0,\ u_1 = \epsilon_1(t)\, x_1,\ u_2 = 0; \\ \text{along}\quad x_1 &= \ell_1,\ u_1 = \epsilon_1(t)\, \ell_1,\ T_{12} = 0; \\ \text{and laterally,}\quad \epsilon_3 &= \text{given.} \end{aligned} \tag{7.11}$$

7.4 Finite-Element Implementation

The constitutive equations outlined in Section 7.2 and the time integration scheme described in Appendix 7.A have been successfully implemented as a user material

subroutine in the finite element code ABAQUS (1986). The user material subroutine (UMAT), coded in FORTRAN 77, is given in Appendix 7.B, and the main ABAQUS input file in Appendix 7.C.

The subroutine UMAT contains the general equations for integrating the stress components and state variables, and also for calculating the Jacobian matrix, $\partial \Delta \mathbf{T} / \partial \Delta \epsilon$, for use in the overall Newton scheme of ABAQUS.

In order to perform the time integration of the stiff constitutive equations considered here, automatic control of the size of a variable time increment was done by using the *VISCO procedure in ABAQUS. Here, the automatic control of a time increment Δt is based on comparisons of an error measure CEMAX against a user-specified tolerance measure CETOL. The value of CEMAX, which must be updated in the user material subroutine and returned to the main program through an existing ABAQUS common block CERROR, was based on the maximum value determined from two different criteria: maximum inelastic strain-rate increment and maximum inelastic strain increment. (i) The first criterion, designed to control the time increment when the inelastic strain rate is changing rapidly such as at yielding, is given by the difference between the equivalent tensile plastic strain rate $\dot{\bar{\epsilon}}^p$ across an increment multiplied by the time increment Δt. (ii) The second error criterion is necessary to limit the maximum equivalent plastic strain increment, $d\bar{\epsilon}^p$, in a time increment when the stresses and equivalent plastic strain rates are not changing significantly. This is done by prescribing a parameter PROPS(2), or maximum equivalent plastic strain increment allowed in a time step, so that the additional error measure is defined by $d\bar{\epsilon}^p$ / PROP(2) CETOL . Thus, Δt is chosen so that it adopts the larger value of the two measures, viz.

$$CEMAX \equiv max \left[\left| \dot{\bar{\epsilon}}^p_{n+1} - \dot{\bar{\epsilon}}^p_n \right| \Delta t \, , \, \frac{|d\bar{\epsilon}^p|}{\text{PROPS(2)}} \, CETOL \right] \, , \qquad (7.12)$$

at any integration point, and never exceeds the user-specified tolerance CETOL.

PROPS(2) was chosen as 0.1 %, and CETOL as 4 % of a typical elastic strain, namely

$$CETOL \equiv 0.04 \frac{\text{flow stress}}{\text{Young's modulus}} = 0.04 \frac{200\,MPa}{140000 MPa} = 6 \times 10^{-5} (7.13)$$

Further, the nodal force tolerance for the solution of the equilibrium equations at each increment in the finite element analysis was taken as 1 % of a typical boundary nodal force,

$$PTOL = 0.01 \frac{(\text{flow stress})}{2} \ell_1^2 .$$

7.5 Results and Discussion

Fig. 7.5 gives the results for a coating with the initial wave height to half-wave length ratio $\Delta x_2/\ell_1 = 0.01$. Due to being computationally intensive, only six full load cycles were computed. Fig. 7.5a shows the way the displacements of the nodes defining the crest and the trough of the imperfection (Nodes 2 and 10 respectively) along x_2 evolve with cycling. The initial upward displacement of the coating surface arises due to a change in elastic strains as a result of the relaxation of the stresses during the first two cycles. After Cycle 3, however, the displacements of Points 2 and 10 evolve in different directions. The resulting effect on the imperfection is seen in Fig. 7.5b, which shows the growth of the actual depth of the waviness or imperfection $[(u_2)_2 - (u_2)_{10}]$ normalized by ℓ_1 as function of load cycles. The negative growth of the imperfection in Fig. 7.5 implies that cycling does not accentuate the imperfection, but instead seems to be driving the coating towards a flat configuration. Inspection of the distribution of the equivalent stress $\bar{\sigma}$ at the beginning of the first cycle in Fig. 7.6a shows, as expected, higher stresses in the smaller crossection at the trough of the imperfection. Since the deformation will initially be localized in this region, the athermal forest resistance S_0 (proportional to the dislocation density) will evolve faster there with a resulting increase in strength. Subsequently, the trough region

should be relatively harder to deform than the crest region. Fig. 7.6b shows the distribution of the athermal forest resistance at the end of Cycle 5. It clearly reveals a higher strength in the trough region. Thus, the initially inhomogeneous stress distribution led to inhomogeneities in the material strength which, in turn, caused the initial surface waviness to decrease.

Without an initial surface undulation ($\Delta x_2 = 0$), Fig. 7.7 shows the crest and trough nodal displacements of the free coating surface and the growth of the roughening. It can be seen that, since the relative displacement of Nodes 2 and 10 increases with cycling, a surface imperfection appears to begin developing from an originally homogeneous material subjected to a uniform stress distribution. To investigate the role that the numerical residuals associated with the solution algorithm of the nonlinear equilibrium equations at each increment (PTOL) may play in the development of the coating roughening, a run was performed with a nodal force tolerance equal to 0.5 % of a typical nodal force. As shown by the dotted line curve of Fig. 7.7, the same growth trend of the coating surface was obtained, even though the magnitude of the displacements for the two analyses differ by approximately 10 %. It appears that the initial strength inhomogeneities needed to give rise to surface roughening was triggered by the numerical analysis. Fig. 7.8 shows the distribution of the athermal forest resistance in the coating at the end of the 8th cycle. Here, the higher resistance is associated with the smaller vertical displacement (Node 10 in Fig. 7.7a) of the right hand side of the coating.

Although it is difficult to predict how this roughening will continue evolving, it is very unlikely that the present growing trend will be reversed. It should be noted that the similarities between the *triggering* mechanism for the development of surface roughening in the present numerical analysis, and material inhomogeneities, such as inclusions or impurities in the material, which may in a similar manner give rise to the initiation of surface imperfections. As has been experimentally verified (Coffin,

1963; Holmes and McClintock, 1990), this localized cyclic deformation in the coating could accentuate the local oxidation rates and eventually lead to coating cracking.

Finally, an analysis of the coating *without surface imperfections* under *isothermal conditions*, Fig. 7.9a, reveals that pure mechanical loading alone does not trigger the roughening observed under non-isothermal conditions. The drop in displacement in the first cycle is associated with the stress relaxation that took place during the first cycle. An isothermal analysis on a coating with an *initial surface imperfections*, Fig. 7.9b, revealed however a growth of surface roughening. From the contours of the athermal forest resistance S_0 at the end of cycle 8 in Fig. 7.10, the material, despite the initial stress inhomogeneity, appears not to have developed the strength inhomogeneities needed to cause a decrease of the initial surface roughening similar to that observed in the non-isothermal case.

7.6 Conclusions

The role of both initial surface imperfections and thermo-mechanical loads on the formation of surface roughening in aluminide diffusion coatings has been studied numerically.

In a coating with an initial surface undulation under non-isothermal conditions, the initially inhomogeneous stress distribution was found to give rise to material strength inhomogeneities which decrease the initial perturbation. The same coating under isothermal conditions however, shows an increase in the initial perturbation apparently due to the small scale of the strength inhomogeneity.

Surface roughening in an initially flat coating, however, developed only under non-isothermal conditions. The triggering of the strength inhomogeneity seems to arise from the numerical residuals associated with the solution algorithm of the non-linear equilibrium equations.

Bibliography

[1] ABAQUS (1986). A general purpose finite element code with emphasis on nonlinear applications, version 4.6. *Hibbitt, Karlsson, and Sorensen Inc.,* Providence, R.I.

[2] Berg, Charles A., and Frank A. McClintock (1966), 'A note on plane nonlinear creep of free boundaries', *Journal of Applied Mathematics and Physics*, **17**, 453.

[3] Busso, E.P., and F.A. McClintock (1988),'Stress-strain histories in coatings on single crystal specimens of a turbine blade alloy', *Int. J. Solids Structures*, **24**, 1113.

[4] Coffin Jr., L.F. (1963),'Cyclic-strain-induced oxidation of high temperature alloys', *Trans. of A.S.M.,* **56**, 339.

[5] Holmes, J.W., and F.A. McClintock (1990), 'The chemical and mechanical processes of thermal fatigue degradation of an aluminide coating',*Met. Trans.*, **21 A**, 1209.

[6] Hutchinson, J.W., and V. Tvergaard (1980),'Surface instabilities on statically strained plastic solids', *Int. J. Mech. Sci.,* **22**, 339.

[7] Kaufman, M. (1982),'Physical and mechanical properties of an aluminide coating', *TMS-AIME*, Paper No. F82-11.

[8] McClintock, F.A (1963), 'On the plasticity of the growth of fatigue cracks', *Fracture of Solids*, D.C. Drucker, J.J. Gilman eds., Met. Soc. AIME, Conf. Ser. 20, Interscience, 65.

[9] Yoshikawa, T., T. Abe, and S. Nagaki (1987),'Surface bifurcation and surface roughening of inhomogeneous material during plastic deformation', in *Low Cycle Fatigue of Elasto-Plastic Behavior of Materials*, K.T. Rie (ed.), Elsevier Applied Sci. (pub.), 101.

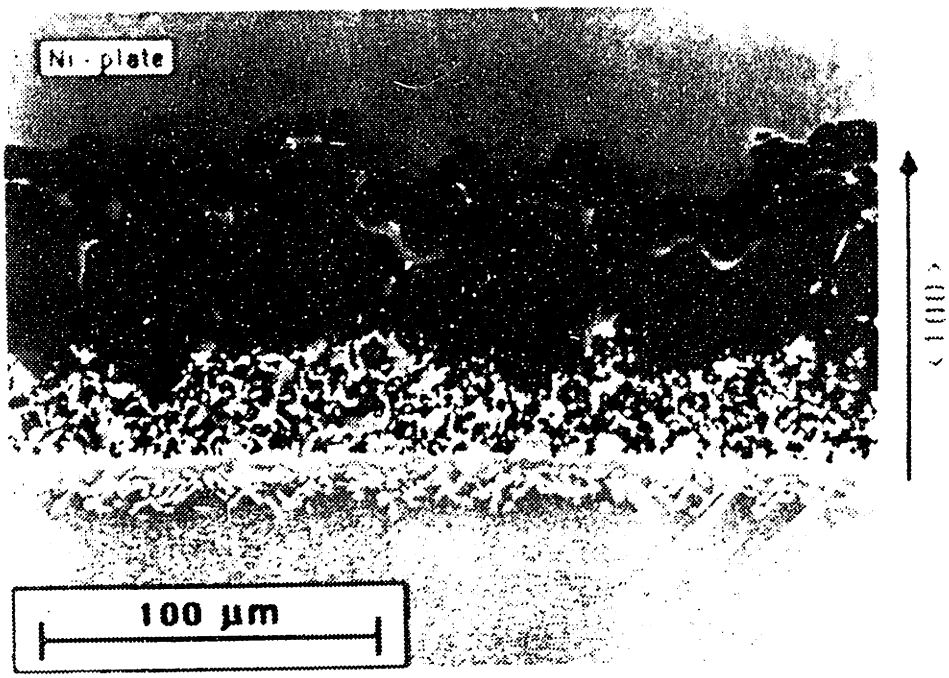

8s heat, 30s cool: $-0.45 < \epsilon^{elast} < 0.01\%$

Fig. 7.1 Micrograph showing surface roughening of an aluminide diffusion coating after 6000 thermal cycles (Holmes and McClintock, 1990)

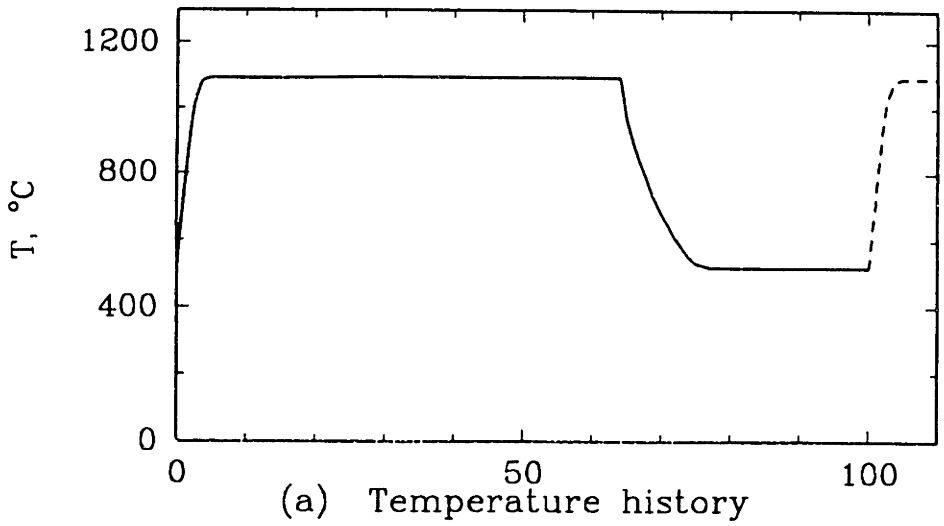

(a) Temperature history

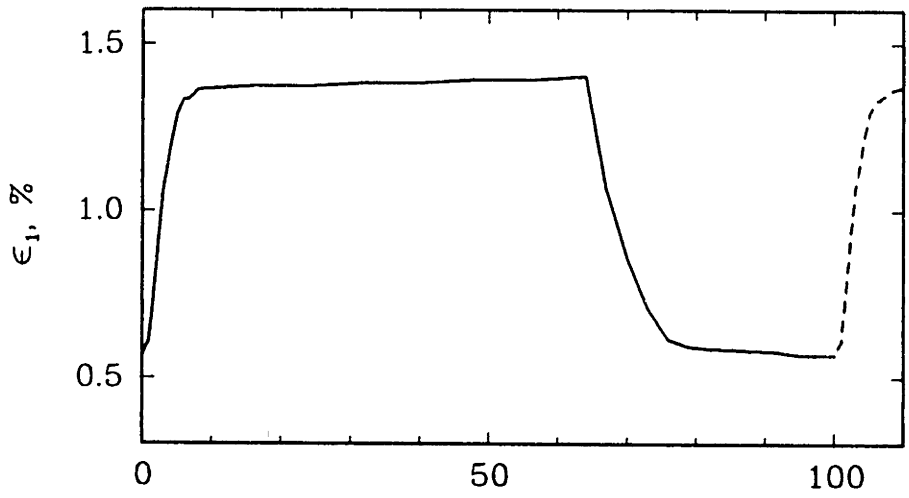

(b) Strain history along x_1 axis (long.)

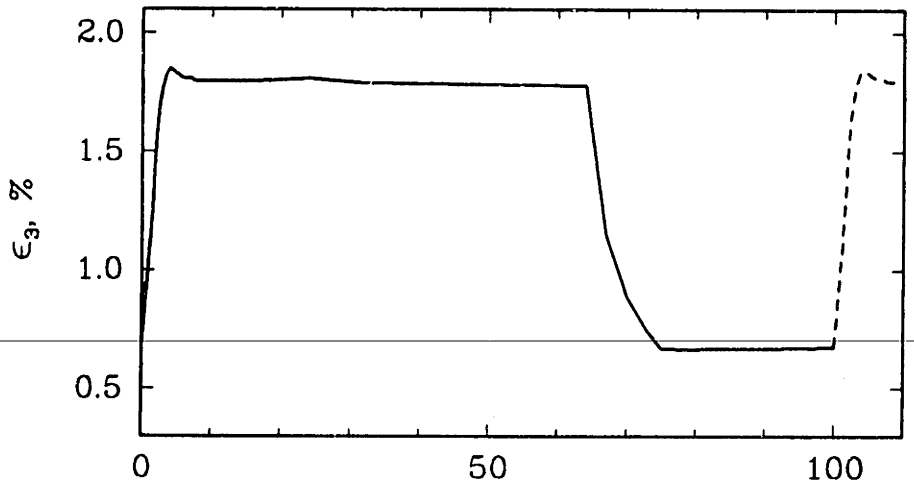

(c) Strain history along x_3 axis (transverse)

Fig. 7.2 Mechanical and thermal loads acting on the coating (Busso and McClintock, 1988)

$$\epsilon_i(t) = \epsilon_i^{el}(t) + \epsilon_i^{in}(t) + \epsilon_i^{th}(t)$$

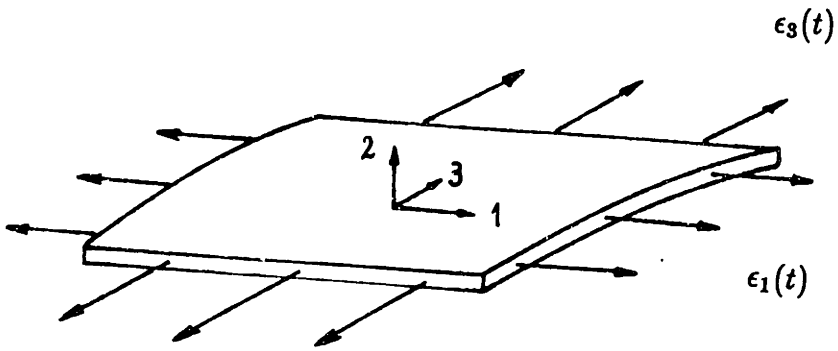

Fig. 7.3 In-plane mechanical loads imposed on the coating by the monocrystalline $(\gamma - \gamma')$ substrate

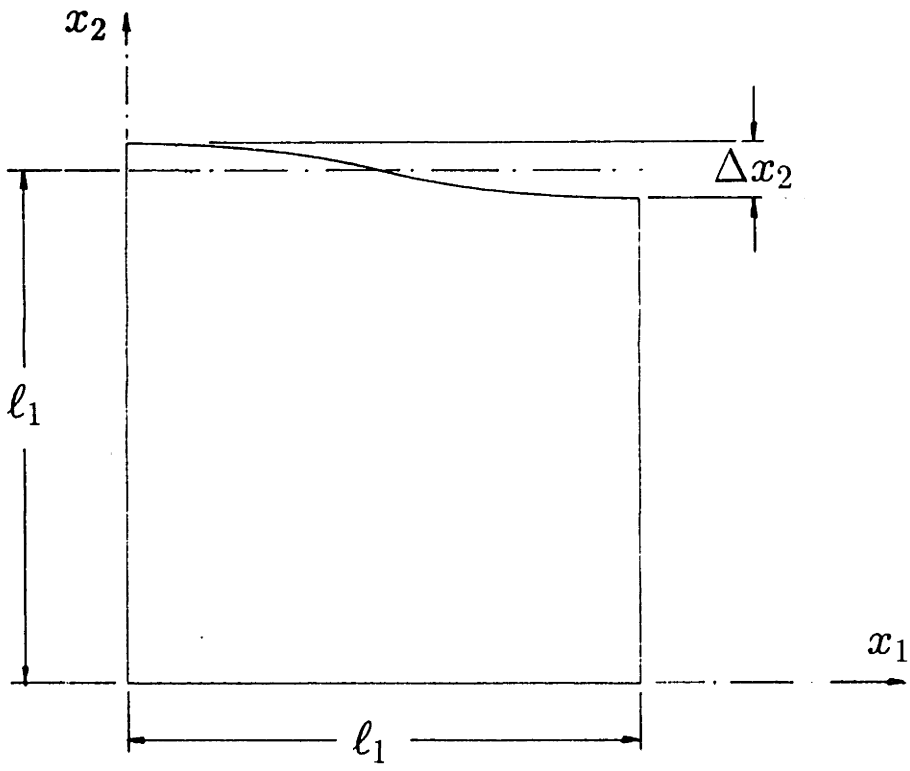

Fig. 7.4 Initial coating undulation

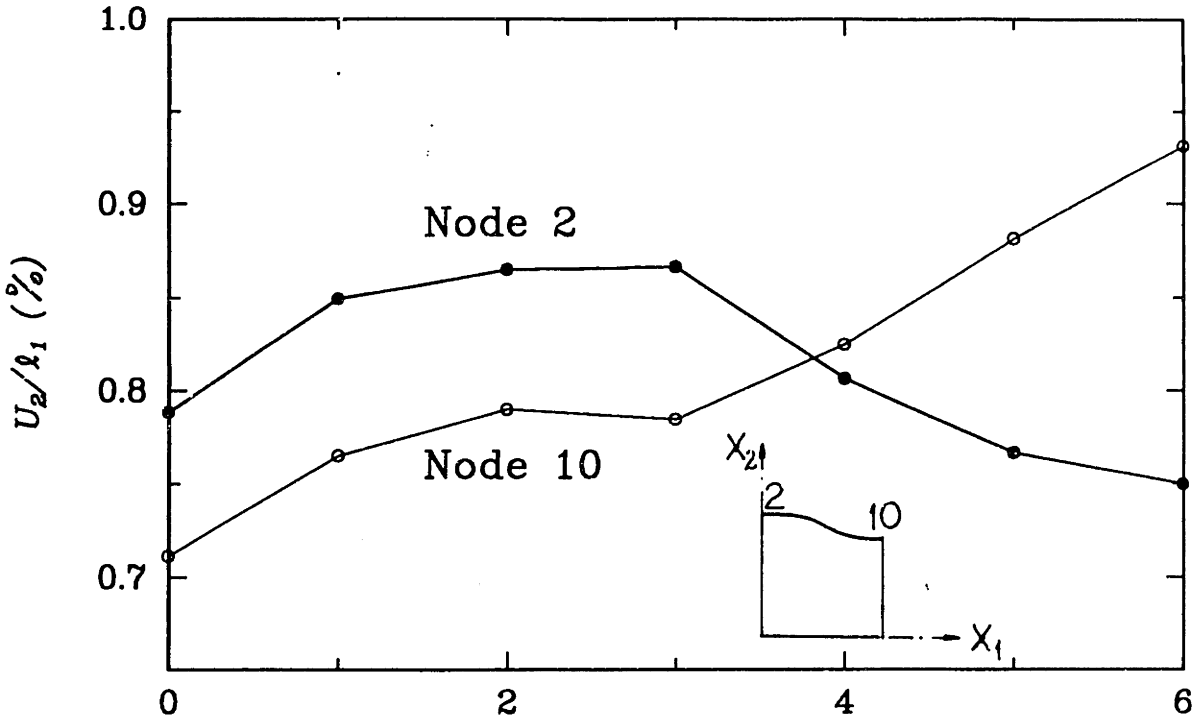

(a) Nodal displacements

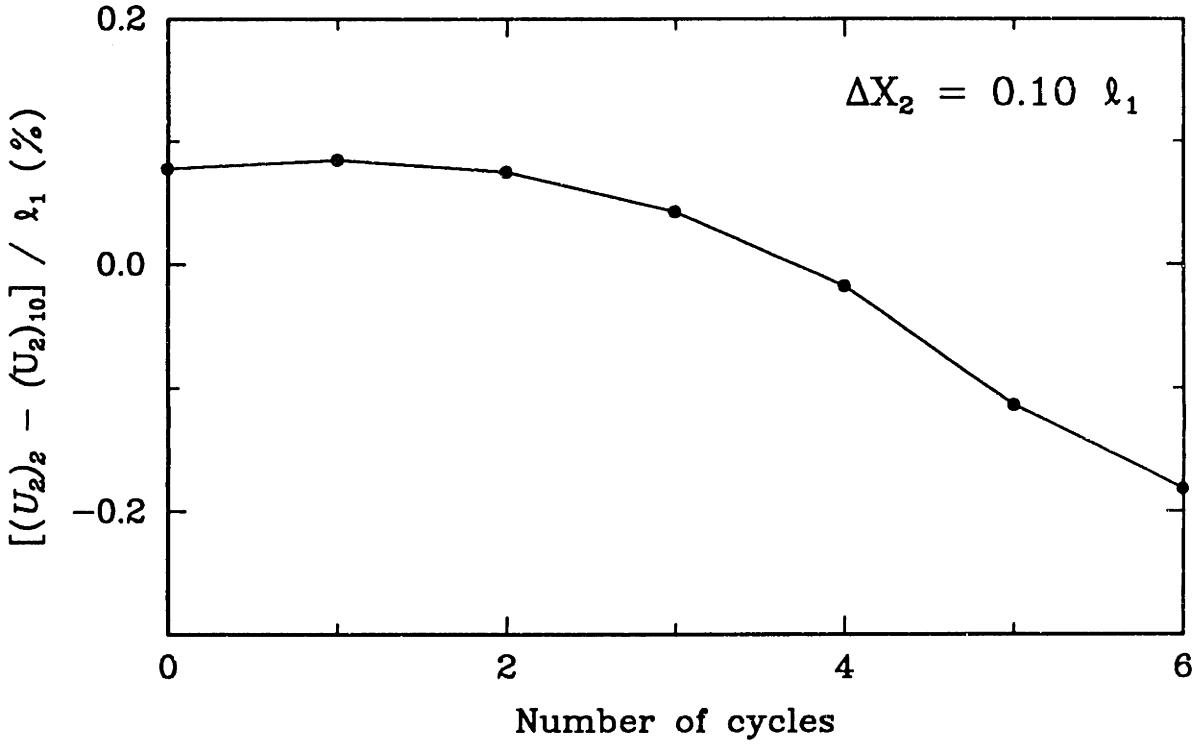

(b) Difference of nodal displacements

Fig. 7.5 Growth of initial waviness as function of load cycles (ΔX_2= 0.10 ℓ_1, PTOL= 1% F_{node})

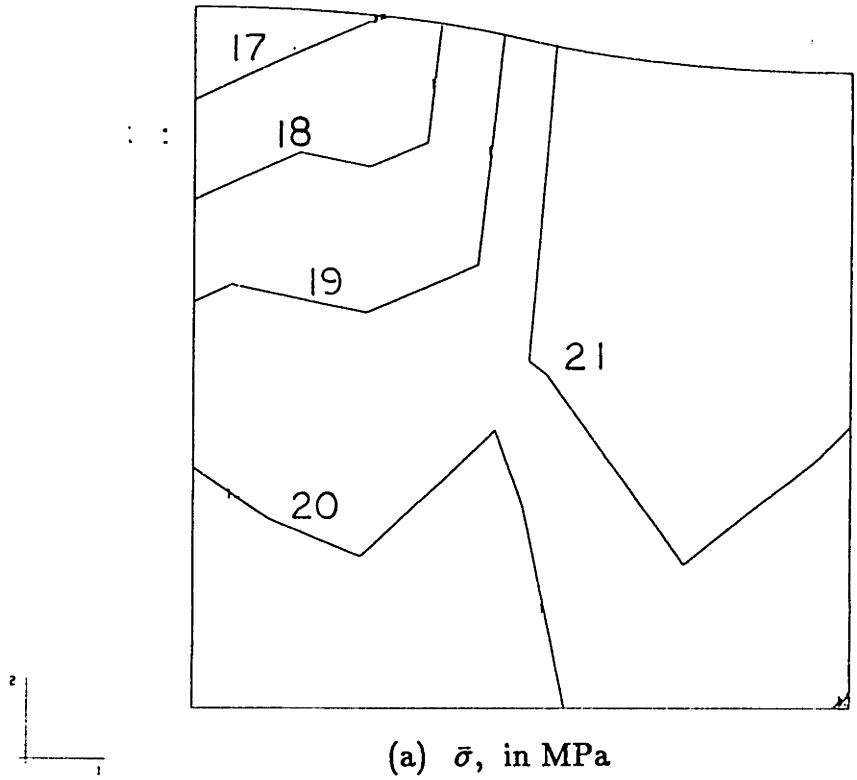

(a) $\bar{\sigma}$, in MPa

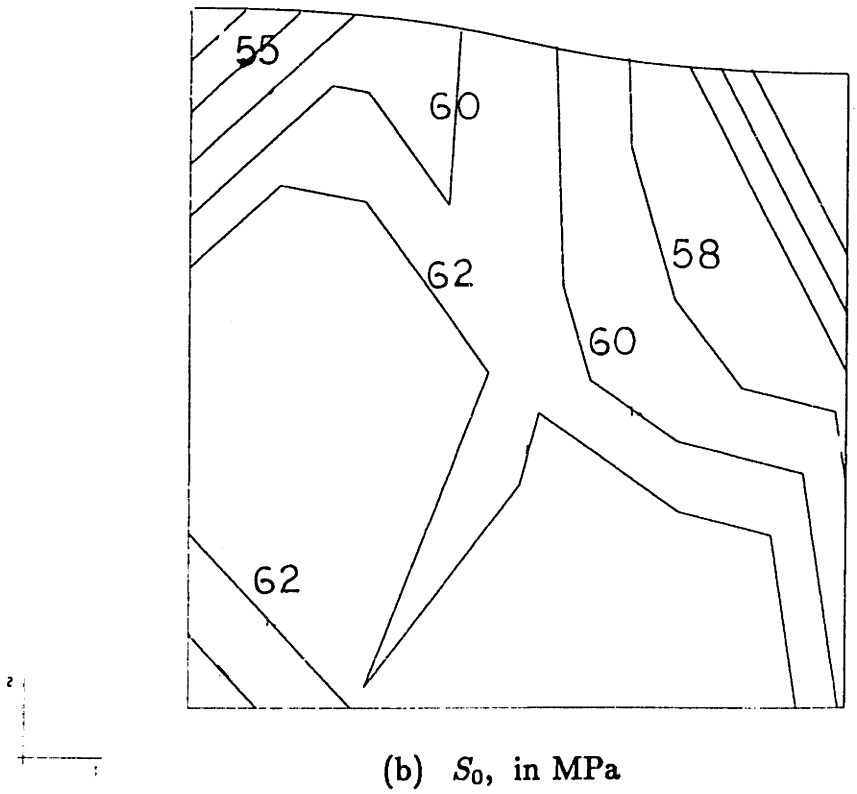

(b) S_0, in MPa

Fig. 7.6 Contour plots of: (a) equivalent effective stress at beginning of cycling and, (b) athermal forest resistance at end of cycle 6

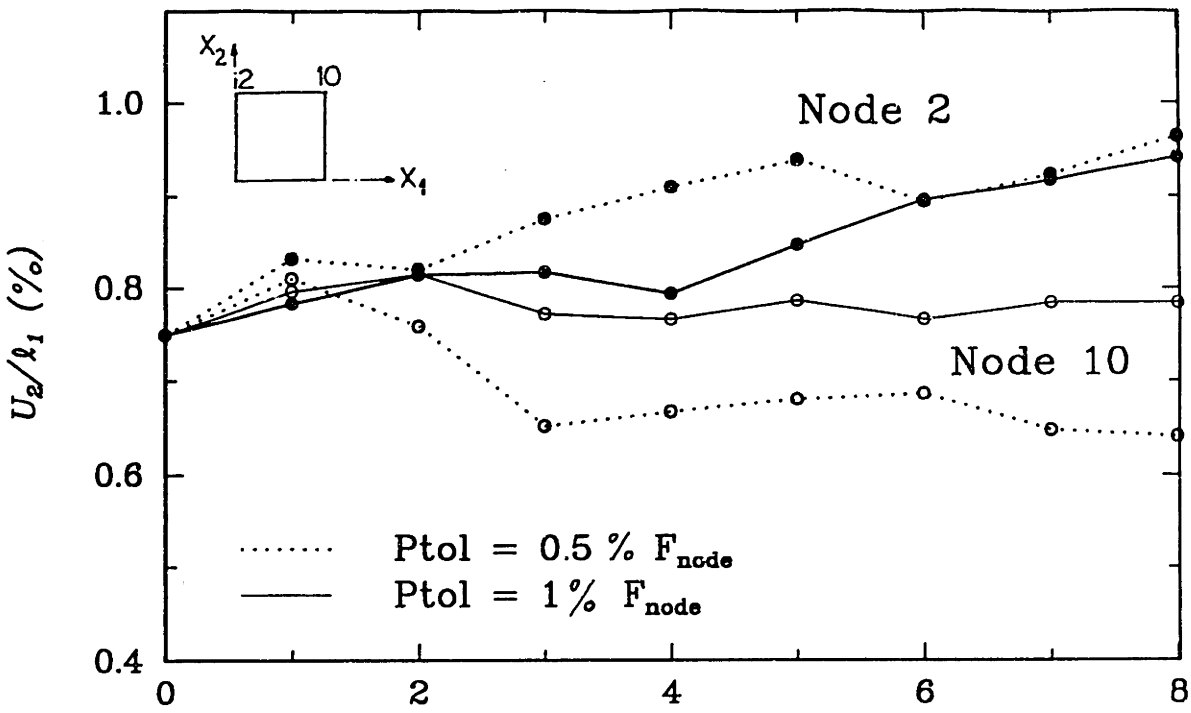

(a) Nodal displacements

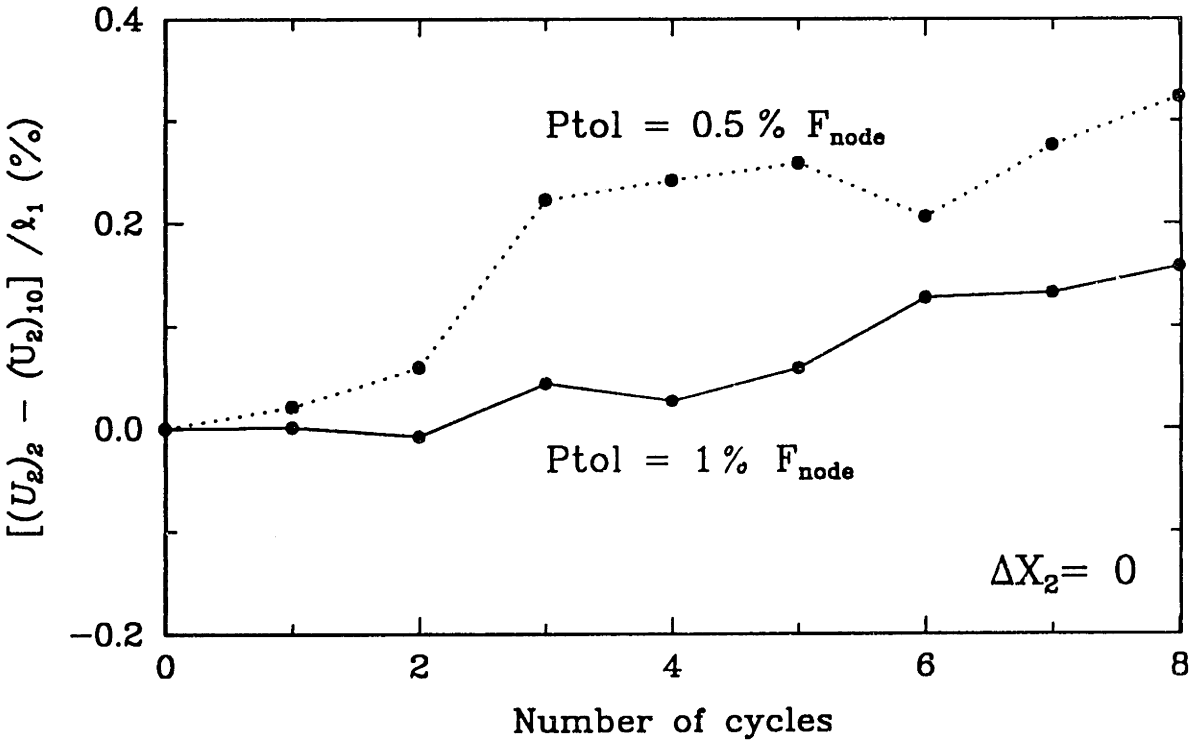

(b) Difference of nodal displacements

Fig. 7.7 Growth of surface inhomogeneity for a coating with no initial waviness ($\Delta X_2 = 0$)

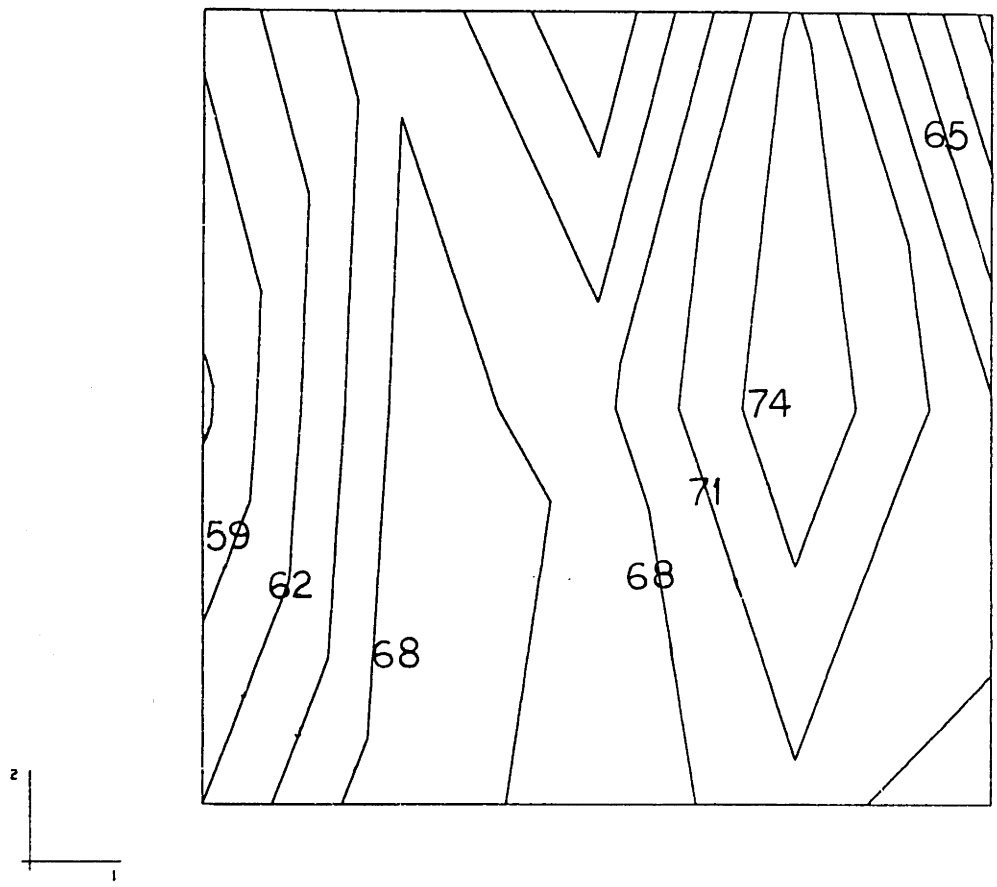

S_0, in MPa

Fig. 7.8 Contours of the athermal forest resistance at end of cycle 8 for a coating with no initial waviness ($\Delta x_2 = 0$)

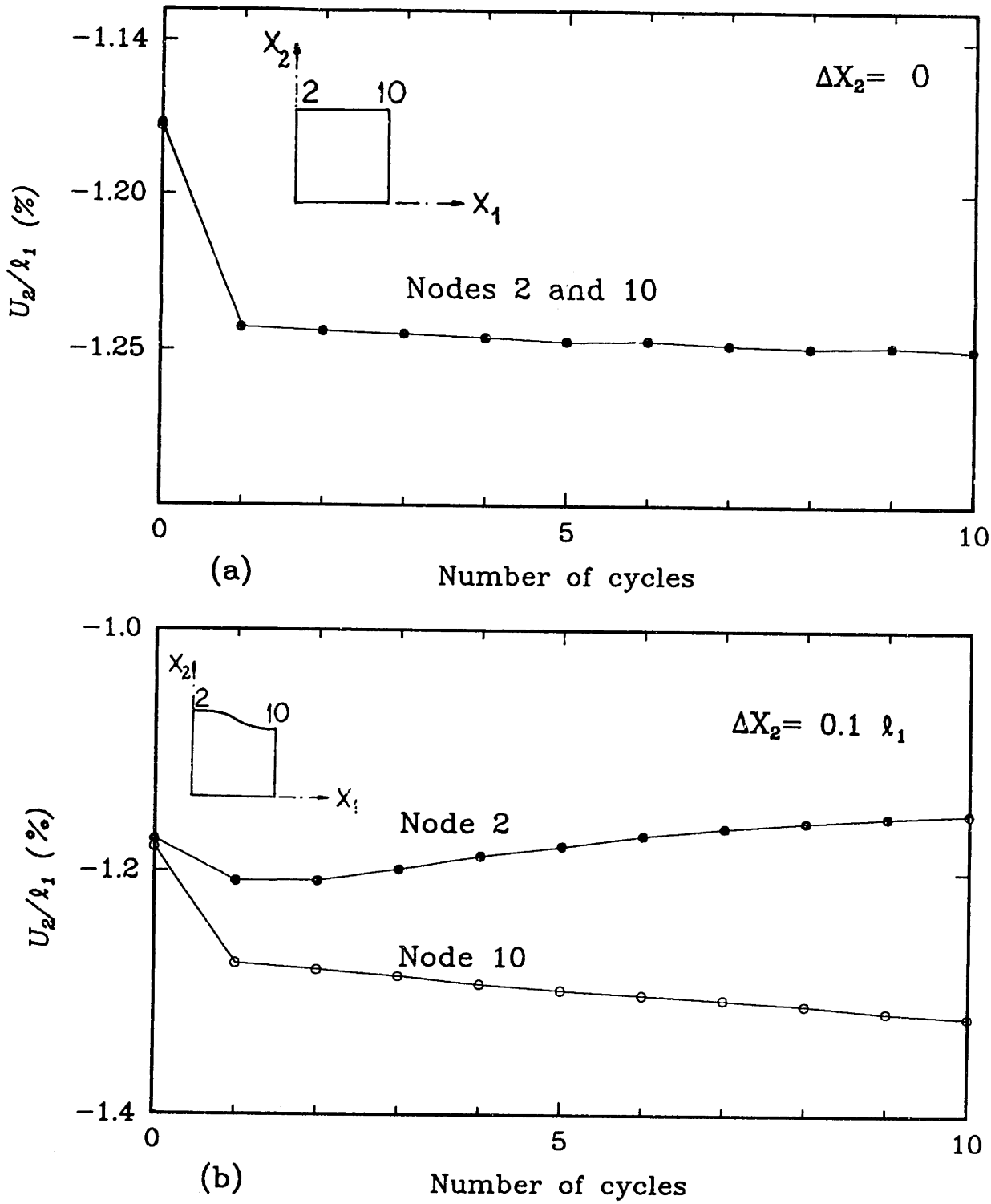

Fig. 7.9 Coating surface displacements for isothermal loading conditions (T= 850 °C)

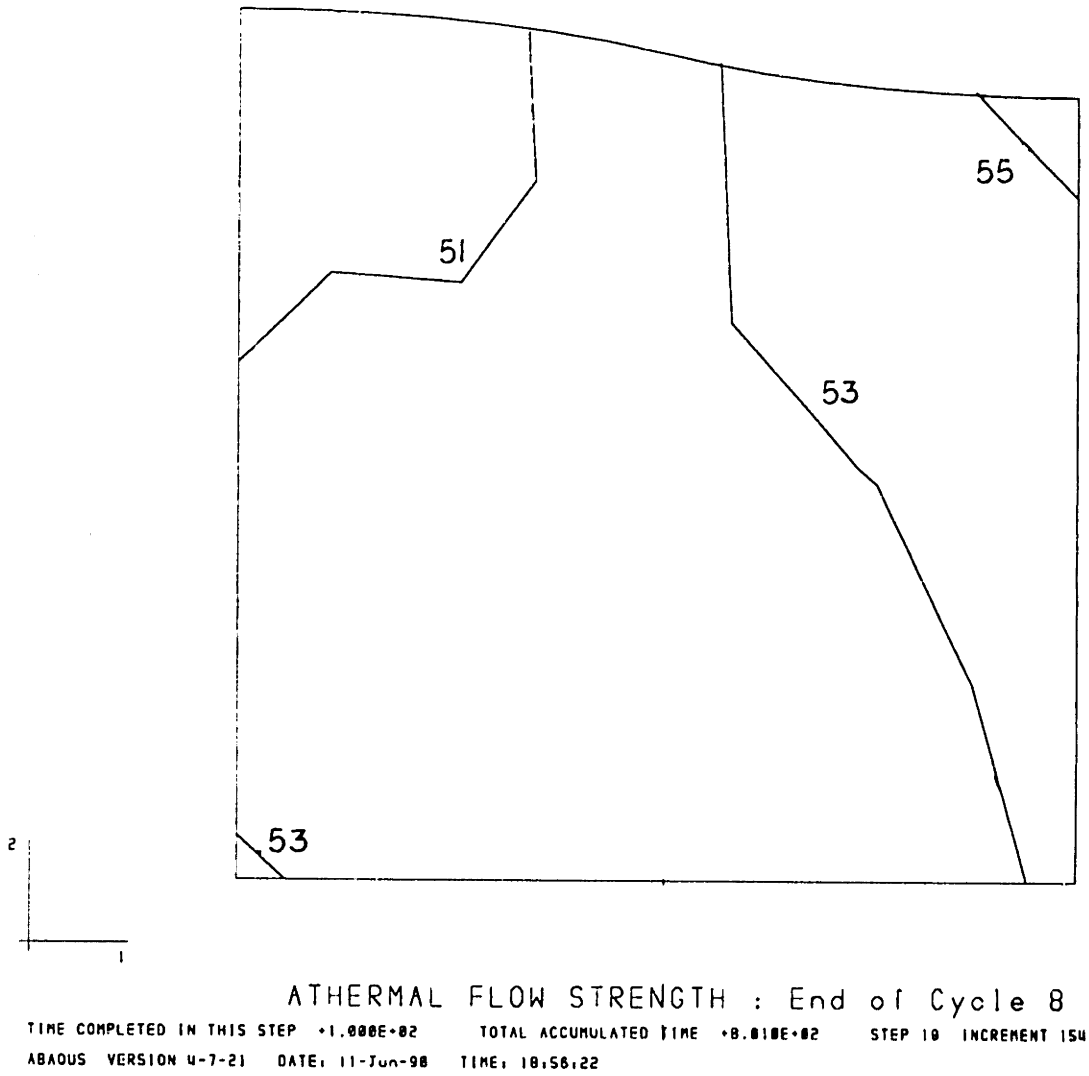

Fig. 7.10 Contours of the athermal forest resistance S_0 at the end of cycle 8 for a coating with $\Delta x_2/\ell_1 = 0.1$ and isothermal loading conditions (850 ^oC)

Appendix 7.A Numerical Integration Scheme

7.A.1 Semi-implicit Integration of Flow and Evolutionary Equations

In this appendix, the flow and evolutionary equations defining the constitutive model presented in Section 7.2 will be integrated numerically to obtain an estimate of the integral of the differential equations during a time increment. Let us assume that the value of the stress and the internal variables at time t_n are,

$$\mathbf{T}_n,\ \mathbf{B}_n,\ S_{0n}\ . \tag{7.A.1}$$

To integrate numerically the flow and evolutionary equations forward in time, the increments $\Delta\mathbf{T}$, ΔS_0, and $\Delta\mathbf{B}$ during each time increment $\Delta t = t_{n+1} - t_n$ must be found.

The relevant equations of Section 7.2 can be expressed in functional form[1] as,

$$\dot{\bar{\epsilon}}^p = \hat{f}(\bar{\sigma},\ S_0,\ \theta)\ , \tag{7.A.2}$$

$$\dot{S}_0 = \hat{g}(\bar{\sigma},\ S_0,\ \theta)\ , \tag{7.A.3}$$

$$\dot{\mathbf{B}} = \mathbf{h}(\mathbf{T}',\ \bar{\sigma},\ S_0,\ \mathbf{B},\ \theta)\ , \tag{7.A.4}$$

where,

$$\bar{\sigma} = \bar{\sigma}(\mathbf{T}',\ \mathbf{B})\ . \tag{7.A.5}$$

An approximation to the above equations at t_{n+1} in terms of the gradient at time t_n can be obtained by using a Taylor-series expansion. Thus, an expansion of the functions $\hat{f}_{n+1}$, $\hat{g}_{n+1}$, and $\mathbf{h}_{n+1}$ around t_n yields[2],

$$\dot{\bar{\epsilon}}^p_{n+1} = \hat{f}_n + \hat{f}_{,S_0}\,\Delta S_0 + \hat{f}_{,\theta}\,\Delta\theta + \hat{f}_{,\bar{\sigma}}\,\Delta\bar{\sigma}\ , \tag{7.A.6}$$

[1] A prime of any tensor denotes its deviatoric part.

[2] The first derivate of any function y with respect to any variable x is expressed as $y_{,x}$.

$$\dot{S}_{0_{n+1}} = \hat{g}_n + \hat{g}_{,S_0}\,\Delta S_0 + \hat{g}_{,\bar{\sigma}}\,\Delta\bar{\sigma} + \hat{g}_{,\theta}\,\Delta\theta\,, \tag{7.A.7}$$

$$\dot{B}_i = \hat{h}_{i_n} + \hat{h}_{i,_{S_0}}\,\Delta S_0 + \hat{h}_{i,_{\bar{\sigma}}}\,\Delta\bar{\sigma} + \hat{h}_{i,_{\theta}}\,\Delta\theta + \hat{h}_{i,_{B_i}}\,\Delta B_i + \sum_{j=1}^{4} \hat{h}_{i,_{T_j'}}\,\Delta T_j'\,. \tag{7.A.8}$$

Here,

$$\hat{h}_i \equiv \frac{h_i}{1 - \Delta t\, h_{i,_{B_i}}}\,. \tag{7.A.9}$$

After some algebraic operations and arrangements, the stress at the end of the increment is given by the following equation:

$$\mathbf{T}_{n+1} = 2\,\bar{\mu}\,\boldsymbol{\Delta\epsilon}' - C_3\,\mathbf{T}_n^{*'}\,(\mathbf{T}_n^{*'}\cdot\boldsymbol{\Delta\epsilon}') + (C_4 - C_5\,\Delta\theta)\,\mathbf{T}_n^{*'} - (p_n - \kappa\, tr\boldsymbol{\Delta\epsilon} + 3\,K\,\alpha\,\Delta\theta)\,\mathbf{1} + \mathbf{B}_n + \frac{\Delta\mathbf{B}}{1+\beta}\left\{\beta\,\mathbf{I} + \frac{\phi_1}{\phi_4}\,(\mathbf{N}_n\otimes\mathbf{N}_n)\right\}\,, \tag{7.A.10}$$

where,

$$\mathbf{T}_n^{*'} = \mathbf{T}_n' - \mathbf{B}_n\,, \tag{7.A.11}$$

$$\Delta\mathbf{B} = \Delta t\left\{\hat{\mathbf{h}}_n + \hat{\mathbf{h}}_{,\theta}\,\Delta\theta + \hat{\mathbf{h}}_{,S_0}\,\Delta t\,\eta_{S_0}\,(\hat{g}_{,S_0} + \hat{g}_{,\theta}\,\Delta\theta) + (\hat{\mathbf{h}}_{,\bar{\sigma}} + \hat{\mathbf{h}}_{,S_0}\,\Delta t\,\eta_{S_0}\,\hat{g}_{,\bar{\sigma}})\,\Delta\bar{\sigma}\right\}\,, \tag{7.A.12}$$

$$\Delta\bar{\sigma} = \frac{(\eta-1)\,\bar{\sigma}_n}{\phi_7} + \frac{3\,\bar{\mu}}{\phi_7\,\bar{\sigma}_n}\left(\mathbf{T}_\mathbf{n}^{*'}\cdot\boldsymbol{\Delta\epsilon}'\right) + \frac{\phi_8}{\phi_7}\,, \tag{7.A.13}$$

$$\eta_{S_0} \equiv \frac{1}{1 - \Delta t\, g_{,S_0}}\,, \tag{7.A.14}$$

$$\beta \equiv \frac{3\,\mu\,\Delta t\,\dot{\bar{\epsilon}}_n^p}{\bar{\sigma}_n}\,, \tag{7.A.15}$$

$$\bar{\mu} \equiv \frac{\mu}{1+\beta}\,, \tag{7.A.16}$$

$$\eta \equiv 1 - \frac{\phi_2}{\phi_4}\,\Delta\theta - \frac{\phi_3}{\phi_4} - C_3\left(\mathbf{T}_n^{*'}\cdot\boldsymbol{\Delta\epsilon}'\right)\,, \tag{7.A.17}$$

and

$$C_1 \equiv \frac{2\,\mu}{1+\beta}\,, \tag{7.A.18}$$

$$C_2 \equiv \kappa - \frac{C_1}{3}, \tag{7.A.19}$$

$$C_3 \equiv C_1 \frac{\phi_1}{\phi_4} \frac{3}{2} \frac{1}{\bar{\sigma}_n^2}, \tag{7.A.20}$$

$$C_4 \equiv 1 - \frac{\phi_3}{\phi_4}, \tag{7.A.21}$$

$$C_5 \equiv \frac{\phi_2}{\phi_4}. \tag{7.A.22}$$

Also,

$$\phi_1 \equiv 3\,\mu\,\Delta t \left\{ \hat{f}_{,\bar{\sigma}} - \frac{\dot{\bar{\epsilon}}^p}{\bar{\sigma}_n} + \hat{f}_{,S0}\,\Delta t \frac{1}{(1 - \Delta t\,\hat{g}_{,S0})}\,\hat{g}_{,\bar{\sigma}} \right\}, \tag{7.A.23}$$

$$\phi_2 \equiv 3\,\mu\,\frac{\Delta t}{\bar{\sigma}_n} \left\{ f_{,\theta} + \hat{f}_{,S0}\,\Delta t\,\hat{g}_{,\theta} \frac{1}{(1 - \Delta t\,\hat{g}_{,S0})} \right\}, \tag{7.A.24}$$

$$\phi_3 \equiv 3\,\mu\,\frac{\Delta t}{\bar{\sigma}_n}\,\hat{f}_{,S_0}\,\Delta t\,\hat{g}_n \frac{1}{1 - \Delta t\,\hat{g}_{,S_0}} + \beta, \tag{7.A.25}$$

$$\phi_4 \equiv 1 + \phi_1 + \beta, \tag{7.A.26}$$

$$\phi_7 \equiv 1 - \frac{3}{2} \frac{1}{\bar{\sigma}_n\,(1+\beta)} \left(\frac{\phi_1}{\phi_4} - 1 \right) \Delta t \left\{ \mathbf{T}_n^{*\prime} \cdot \left[\hat{\mathbf{h}}_{,\bar{\sigma}} + \hat{\mathbf{h}}_{,S_0}\,\Delta t\,\eta_{S_0}\,\hat{g}_{,\bar{\sigma}} \right] \right\}, \tag{7.A.27}$$

$$\phi_8 \equiv \frac{3}{2} \frac{1}{\bar{\sigma}_n\,(1+\beta)} \left(\frac{\phi_1}{\phi_4 - 1} \right) \left\{ \mathbf{T}_n^{*\prime} \cdot \hat{\mathbf{h}}_n + \mathbf{T}_n^{*\prime} \cdot \hat{\mathbf{h}}_{,\theta}\,\Delta\theta + \mathbf{T}_n^{*\prime} \cdot \mathbf{h}_{,S_0}\,\Delta t\,\eta_{S_0}\,(\hat{g}_{,S_0} + \hat{g}_{,\theta}\,\Delta\theta) \right\}. \tag{7.A.28}$$

The increment of the athermal flow resistance S_0 is given by,

$$\Delta S_0 + \Delta t\,\eta_{S_0}\,\{\hat{g}_n + \hat{g}_{,\bar{\sigma}}\,\Delta\bar{\sigma} + \hat{g}_{,\theta}\,\Delta\theta\}. \tag{7.A.29}$$

The Jacobian can be calculated using the following relation:

$$\mathcal{L}^{tan} = C_1\,\mathbf{I} + C_2\,\mathbf{1} \otimes \mathbf{1} - C_3\,\mathbf{T}_n \otimes \mathbf{T}_n. \tag{7.A.30}$$

Appendix 7.B User Material Subroutine

An ABAQUS user material subroutine coding the flow and evolutionary equations of Section 7.2 with the time-integration procedure of Appendix 7A is presented at the end of this appendix. The statements are written in FORTRAN 77. In what follows, some details of the coding are presented.

In ABAQUS, second order tensors (matrices) are stored as vectors. Important vector variables in UMAT, which has been written exclusively for plane strain problems, are:

1. STRESS : This vector contains the stress tensor components at the beginning of the time increment, and is passed from the main program to be updated within UMAT to the values at the end of the time increment.

2. DSTRAN : This vector contains the strain increment tensor components and is passed into the UMAT.

The (I,J) component of the Jacobian matrix DDSDDE represents the derivative of the increment on STRESS(I) with respect to DSTRAN(J). In STRESS and DSTRAN, direct components are stored first, followed by the shear components. There are NDI direct and NSHR shear components. The total number of components are NTENS. Then, DDSDDE is dimensioned accordingly (NTENS, NTENS).

STATEV is the array of 12 independent and dependent state variables:

STATEV(1) : athermal forest resistance ($S0$)

STATEV(2-5) : deviatoric back stress components ($\mathbf{B}$)

STATEV(6) : mechanical strain component in direction 1

STATEV(7) : mechanical strain component in direction 3

STATEV(8) : plastic strain component in direction 1

STATEV(9) : plastic strain component in direction 3

STATEV(10) : equivalent deviatoric back stress ($\bar{B}$)

STATEV(11) : temperature (TEMP)

STATEV(12) : equivalent effective stress

The variables 6-10, and 12 are including for plotting purposes only. The temperature TEMP is prescribed internally in the UMAT through the subroutine SUBTEMP, which has TIME and DTIME as input parameters. The temperature-dependent material constants and the partial derivatives of the flow and evolutionary equations are all evaluated in the subroutine UMEDOT.

For the first increment in the first step of an ABAQUS calculation, the state variables are initialized inside the UMAT with zero values. They are subsequently changed within the UMAT to their initial values.

```
C*****************************************************************
C
C                ABAQUS USER MATERIAL FOR AN ISOTROPIC
C
C                        VISCOPLASTIC MODEL
C
C                           VERSION 4.7
C
C                    --  Written by E.P. Busso --
C
C*****************************************************************
C
C  State Variables:
C    STATEV(1)    -   athermal component of flow stress (S0)
C    STATEV(2-5)  -   deviatoric back stress components (B)
C    STATEV(6)    -   mechanical strain component in direction 1
C    STATEV(7)    -   mechanical strain component in direction 3
C    STATEV(8)    -   plastic strain component in direction 1
C    STATEV(9)    -   plastic strain component in direction 3
C    STATEV(10)   -   equivalent deviatoric back stress (BEQ)
C    STATEV(11)   -   temperature
C    STATEV(12)   -   equivalent effective stress (SIG)
C
C  Material constant used in UMAT:
C    PROPS(1)     - initial value for the athermal flow stress S0
C    PROPS(2)     - limit on equiv. plastic tensile strain increment
C
C  Notes:
C          1.     This UMAT was developed for either a plane strain
C                 or a generalize plane strain model
C          2.     This UMAT can deal with non-isothermal conditions
C          3.     This UMAT interfaces with the *VISCO procedure in
C                 ABAQUS. Automatic time step control is performed
C                 using the CEMAX parameter. The timestep is decreased
C                 if CEMAX exceeds the user's specified CETOL
C
C*****************************************************************
      SUBROUTINE UMAT (STRESS,STATEV,DDSDDE,SSE,SPD,SCD, RPL,DDSDDT,
     1 DRPLDE,DRPLDT, STRAN,DSTRAN,TIME,DTIME,TEMP,DTEMP,PREDEF,DPRED,
     2 CMNAME, NDI,NSHR,NTENS,NSTATV,PROPS,NPROPS,COORDS,DROT)
      IMPLICIT REAL*8 (A-H,O-Z)
      CHARACTER*8 CMNAME
      COMMON / CERROR / RESMAX(30),JNREMX(30),ERRMAX(2),CETOL,CSLIM,
     1 CEMAX,PCTOL,TLIMIT,PSUBIN,RESMIN,DUMAX(30),JNDUMX(30),
     2 ERRPRE,UDELSS,PTOL,AMTOL,DMKET,DMRETL,SIGTOL,DSIGMX,
     3 UTOL,UMAX,U4MAX,VMAX,V4MAX,AMAX,A4MAX,TMAX,EPPMAX,RMAX,R4MAX,
     4 NGOPEN,NGCLOS,ROTTOL,ROTFAC,JRIKND,NINCCS,RIKUB,RIKUMX,RIKMU,
     5 RIKLAM,RIKDLA,RIKRO,RIKOLD,RIKLMX,QMAX,DUMAXP,STRRAT,PCUT,
     6 RIKDLO,TERRPR,JCIT1,JCITER,NELFP,NELFPT,AELFPL,MAXVIO,MAXCHP,
     7 KAXVIO,KAXCHP,PTOLVI(2),PERRMX,UERRMX,STOLFA,NSOLBD,NSHLBD,
     8 COMERR,UERRI,PERRI,JCEREL(4),CERMAX(4)
      DIMENSION    STRESS(NTENS),STATEV(NSTATV),DDSDDE(NTENS,NTENS),
     1 DDSDDT(NTENS), DRPLDE(NTENS), STRAN(NTENS),DSTRAN(NTENS),
     2 PREDEF(1),DPRED(1),PROPS(NPROPS),COORDS(3),DROT(3,3)
      DIMENSION    STREFF(4), B(4), DB(4), FB(4), DBDSIG(4), DBDS(4),
     1 DBDB(4), DBDTEMP(4), ETAB(4), DEPS(4), DEFFS(4)
      REAL*8 MU, KAPPA, MU2, KAPPA2
      DATA ZERO,ONE,TWO,THREE,SMLSIG /0.0D0,1.0D0,2.0D0,3.0D0,1.0D-20/
C-----------------------------------------------------------------
      NDIPL1=NDI+1
C-----------------------------------------------------------------
C  Calculate the temperature at the beginning and end of Dt in SUBTEMP
C-----------------------------------------------------------------
      CALL SUBTEMP(TIME, DTIME, TEMP, DTEMP)
C-----------------------------------------------------------------
C  Calculate material properties at beginning and end of Dt in UMPROP
C-----------------------------------------------------------------
      CALL UMPROP(TEMP,DTEMP,MU,KAPPA,ALPHA1,ALPHA2,MU2,KAPPA2)
C-----------------------------------------------------------------
C  Initialize the state variables and the Cauchy stress components
C-----------------------------------------------------------------
      IF (STATEV(1) .LE. ZERO) THEN
        STATEV(1) = PROPS(1)
        DO 10, I=1,11
  10      STATEV(1+I) = ZERO
        DO 20, I=1,4
  20      STRESS(I)   = 0.01
      ENDIF
C-----------------------------------------------------------------
C  Set the initial values of the independent state variables
C-----------------------------------------------------------------
        S0 = STATEV(1)
        DO 30, I=1,4
  30      B(I) = STATEV(1+I)
C-----------------------------------------------------------------
C  Convert STRESS to its deviatoric part, calculate the pressure P1 at
C  the beginning state, and calculate the effective stress tensor STREFF
C-----------------------------------------------------------------
      CALL UMINV (STRESS,P1,DUMM,NDI,NTENS)
      DO 40 I=1, NTENS
  40    STREFF(I) =  STRESS(I) - B(I)
C-----------------------------------------------------------------
C  Calculate the beginning state SIG1 (equiv. stress)
C-----------------------------------------------------------------
      CALL UMINV (STREFF,DUMM,SIG1,NDI,NTENS)
C-----------------------------------------------------------------
C  Calculate the beginning state BEQ1 (equiv. back stress)
C-----------------------------------------------------------------
      CALL UMINV (B, PB, BEQ1, NDI, NTENS)
C-----------------------------------------------------------------
C  Calculate the trace of the strain increment
C-----------------------------------------------------------------
      TRACE = ZERO
      DO 50 I=1,NDI
   50   TRACE = TRACE + DSTRAN(I)
C-----------------------------------------------------------------
C  Calculate the deviatoric shear strain components
C-----------------------------------------------------------------
      DO 60 I=1,NDI
   60   DSTRAN(I) = DSTRAN(I) - TRACE/THREE
      DO 70 I=NDIPL1,NTENS
   70   DSTRAN(I) = DSTRAN(I) / TWO
C-----------------------------------------------------------------
C  Dot product between the deviatoric strain increments and the
C  effective stress deviators
C-----------------------------------------------------------------
      SDTSI = ZERO
      DO 80 I=1,NTENS
   80   SDTSI = SDTSI + STREFF(I) * DSTRAN(I)
C-----------------------------------------------------------------
C  Calculate the equivalent strain rate, the evolution of the internal
C  variables and their derivatives at the beginning of Dt
C-----------------------------------------------------------------
      CALL UMEDOT    (SIG1,B,BEQ1,S0,TEMP,NTENS,F1,DFDSIG,DFDS,
     1       DFDTEMP,FS,DSDSIG,DSDS,DSDTEMP,FB,DBDSIG,DBDS,DBDB,
     2 DBDTEMP,STREFF)
C-----------------------------------------------------------------
C Calculate the Jacobian terms
```

Appendix.7.B

```
C-----------------------------------------------------------------------
      IF(SIG1 .GT. SMLSIG) THEN
        BETA  =  THREE * MU * DTIME * F1 / SIG1
        ETAS = ONE / (ONE - DTIME * DSDS)
        DO 90 I=1, NTENS
   90     ETAB(I) = ONE / (ONE - DTIME * DBDB(I))
C- - - - - - - - - - - - - - - - - - - - - - - - - - - - - - - - - - - -
        PHI1  = THREE * MU * DTIME * (DFDSIG - F1 / SIG1 + DFDS * DTIME
     +            * ETAS * DSDSIG)
        PHI2  = THREE * MU * DTIME / SIG1 * (DFDTEMP + DFDS * DTIME *
     +            ETAS * DSDTEMP)
        PHI3  = THREE * MU * DTIME**TWO / SIG1 * DFDS * ETAS * FS + BETA
        PHI4  = ONE + BETA + PHI1
        PHI3HAT = ONE - PHI3/PHI4 - PHI2/PHI4 * DTEMP
        C1    = TWO * MU / (ONE + BETA)
        C2    = KAPPA - C1 / THREE
        C3    = THREE / TWO / SIG1**TWO * C1 * PHI1 / PHI4
C- - - - - - - - - - - - - - - - - - - - - - - - - - - - - - - - - - - -
        R1    = ZERO
        R2    = ZERO
        DO 100 I=1, NTENS
          R1 =  R1 + STREFF(I) * ETAB(I) * (DBDSIG(I) + DBDS(I) *
     +            DTIME * ETAS * DSDSIG)
  100     R2 =  R2 + STREFF(I) * ETAB(I) * (DB(I) + DBDTEMP(I) * DTEMP
     +            + DBDS(I) * DTIME * ETAS * (FS + DSDTEMP * DTEMP))
        PHI9  = THREE/TWO / SIG1 /(ONE+BETA) * DTIME * (-ONE+ PHI1/PHI4)
        PHI7  = ONE - PHI9 * R1
        PHI8  = PHI9 * R2
        ETA   = PHI3HAT - C3 * SDTSI
        DSIG  = (ETA - ONE) / PHI7 * SIG1 + THREE * C1/TWO / PHI7 / SIG1
     +           * SDTSI + PHI8 / PHI7
C- - - - - - - - - - - - - - - - - - - - - - - - - - - - - - - - - - - -
      ELSE
        C1    = TWO * MU
        C2    = KAPPA - C1 / THREE
        C3    = ZERO
        ETA   = ONE
        DSIG  = ZERO
      END IF
C-----------------------------------------------------------------------
C Calculate the Jacobian
C-----------------------------------------------------------------------
      DO 120 I=1, NTENS
      DO 120 J=1, NTENS
  120   DDSDDE(I,J) = - C3 * STRESS(I) * STRESS(J)
      DO 130 I=1, NDI
        DDSDDE(I,I) = DDSDDE(I,I) + C1
      DO 130 J=1, NDI
  130   DDSDDE(I,J) = DDSDDE(I,J) + C2
      DO 140 I=NDIPL1, NTENS
  140   DDSDDE(I,I) = DDSDDE(I,I) + C1 / TWO
C-----------------------------------------------------------------------
C Update S0 and the deviatoric back stress components B(I) by
C approximating their evolutionary equations using Taylor's series
C expansions about the beginning state (semi-implicit mehod of integ.)
C-----------------------------------------------------------------------
      DS0   = DTIME * ETAS * (FS + DSDSIG * DSIG + DSDTEMP * DTEMP)
      S0    =   S0 + DS0
C - - - - - - - - - - - - - - - - - - - - - - - - - - - - - - - - - - -
      DO 160 I=1, NTENS
        DB(I) = DTIME * ETAB(I) * (FB(I) + DBDTEMP(I) * DTEMP +
     +            DBDS(I) * DS0 + DBDSIG(I) * DSIG)
  160   B(I)  = B(I) + DB(I)
C-----------------------------------------------------------------------
```

```
C Calculate plastic strain increments and an equivalent plastic shear
C strain increment for post-processing and timestep control purposes
C-----------------------------------------------------------------------
      IF(SIG1 .GT. SMLSIG) THEN
        PHI5 = THREE/TWO * DTIME / SIG1 *(F1 + DFDS * DS0 + DFDTEMP *
     1    DTEMP + (DFDSIG - F1/SIG1) * DSIG)
        PHI6 = THREE/TWO * DTIME/SIG1 * F1
        DTEDB = ZERO
        DO 170 I=1, NTENS
  170     DTEDB = DTEDB + STREFF(I) * DB(I)
        DO 180 I=1, NTENS
          DEFFS(I) = C1 * DSTRAN(I) + (ETA-ONE) * STREFF(I) + ONE
     1    / (ONE+BETA) * (- DB(I) + PHI1/PHI4 * THREE/TWO / SIG1**TWO
     2    * STREFF(I) * DTEDB)
  180     DEPS(I) = PHI5 * STREFF(I) + PHI6 * DEFFS(I)
      ELSE
        DO 190 I=1, NTENS
  190     DEPS(I) = ZERO
      END IF
C-----------------------------------------------------------------------
C  Calculate the equivalent shear strain increment
C-----------------------------------------------------------------------
      EQDEPS = ZERO
      DO 200 I= 1, NDI
  200   EQDEPS = EQDEPS + DEPS(I)**(2.D0) / TWO
      DO 210 I= NDIPL1, NTENS
  210   EQDEPS = EQDEPS + DEPS(I)**(2.D0)
      EQDEPS = DSQRT(THREE * EQDEPS)
C-----------------------------------------------------------------------
C  Update the effective and deviatoric stress components
C-----------------------------------------------------------------------
        DO 220 I=1,NTENS
          STREFF(I) = STREFF(I) + DEFFS(I)
  220     STRESS(I) = STREFF(I) + B(I)
C-----------------------------------------------------------------------
C  Calculate the equivalent stress at the end of Dt
C-----------------------------------------------------------------------
      CALL UMINV (STREFF, DUMM, SIG2, NDI, NTENS)
C-----------------------------------------------------------------------
C  Update the equivalent back stress BEQ
C-----------------------------------------------------------------------
      CALL UMINV (B, PB, BEQ2, NDI, NTENS)
C-----------------------------------------------------------------------
C  Calculate the equivalent strain rate at the end of Dt
C-----------------------------------------------------------------------
      TEMP2 = TEMP + DTEMP
      CALL UMEDOT    (SIG2,B,BEQ2,S0,TEMP2,NTENS,F2,DFDSIG,DFDS,
     1  DFDTEMP,FS,DSDSIG,DSDS,DSDTEMP,FB,DBDSIG,DBDS,DBDB,DBDTEMP,
     2  STREFF)
C-----------------------------------------------------------------------
C  Calculate the pressure at the end of the increment
C-----------------------------------------------------------------------
      P2 = P1 + KAPPA * (THREE * ((TEMP-25.) * (ALPHA2-ALPHA1) +
     +     ALPHA2 * DTEMP) - TRACE)
C-----------------------------------------------------------------------
C  Calculate elastic strain components and convert deviatoric stress
C  to complete stress
C-----------------------------------------------------------------------
      ELAST1   =   STRESS(1) / (TWO * MU) - P2 / (THREE * KAPPA2)
      ELAST3   =   STRESS(3) / (TWO * MU) - P2 / (THREE * KAPPA2)
      DO 230 I=1,NDI
  230   STRESS(I) = STRESS(I) - P2
C-----------------------------------------------------------------------
C  Update the state variables.
```

Appendix.7.B

```
C-----------------------------------------------------------------------
      STATEV(1)     = S0
      DO 240 I=1, NTENS
  240   STATEV(1+I) = B(I)
      STATEV(8)     = STATEV(8) + DEPS(1)
      STATEV(9)     = STATEV(9) + DEPS(3)
      STATEV(6)     = ELAST1 + STATEV(8)
      STATEV(7)     = ELAST3 + STATEV(9)
      STATEV(10)    = BEQ2
      STATEV(11)    = TEMP2
      STATEV(12)    = SIG2
C-----------------------------------------------------------------------
C  Calculate the difference between the equivalent tensile plastic
C  strain rates across an increment times the size of the time
C  increment. To be used by the automatic integration scheme of ABAQUS.
C  (DSQRT(3) converts shear strains to tensile strains)
C-----------------------------------------------------------------------
      DIFF  = DTIME * DABS(F1 - F2) / DSQRT(THREE)
      CEMAX = DMAX1(CEMAX, DIFF)
C-----------------------------------------------------------------------
C  Extra automatic timestep control measure: limit the size of the
C  plastic strain increment in a time increment, and provide ABAQUS
C  with the larger of the two CEMAX to compare against CETOL
C-----------------------------------------------------------------------
      IF(PROPS(2) .GT. ZERO) THEN
        DEPCHK = EQDEPS / DSQRT(THREE) / PROPS(2) * CETOL
        CEMAX  = DMAX1(CEMAX, DEPCHK)
      END IF
C-----------------------------------------------------------------------
      RETURN
      END
C***********************************************************************
C                          SUBROUTINE UMINV                             C
C***********************************************************************
C  This subroutine calculates:                                          C
C       XINV1 = - (1/3) * trace(X),                                     C
C  converts X to its deviatoric part X', and calculates                 C
C       XINV2 = DSQRT(1.5 * X' * X')                                    C
C***********************************************************************
      SUBROUTINE UMINV (X,XINV1,XINV2,NDI,NTENS)
      IMPLICIT REAL*8 (A-H,O-Z)
      DIMENSION X(NTENS)
      DATA ZERO,ONE,TWO,THREE /0.0D0,1.0D0,2.0D0,3.0D0/
C
      NDIPL1 = NDI + 1
      XINV1  = ZERO
      XINV2  = ZERO
      DO 10 I=1,NDI
   10   XINV1 = XINV1 - X(I)
      XINV1 = XINV1 / THREE
      DO 20 I=1,NDI
   20   X(I) = X(I) + XINV1
      DO 30 I=1,NDI
   30   XINV2 = XINV2 + (X(I)**2) / TWO
      DO 40 I=NDIPL1,NTENS
   40   XINV2 = XINV2 + X(I)**2
      XINV2 = DSQRT(THREE * XINV2)
      RETURN
      END
C***********************************************************************
C                         SUBROUTINE UMEDOT                             C
C***********************************************************************
C
C    This subroutine calculates the equivalent inelastic strain rate,
C    the rate of change of the internal variables B and S0, and their
C    derivatives
C
C***********************************************************************
      SUBROUTINE UMEDOT(SIG,B,BEQ,S0,TEMP,NTENS,F,DFDSIG,DFDS,
     1        DFDTEMP,FS,DSDSIG,DSDS,DSDTEMP,FB,DBDSIG,DBDS,DBDB,
     2 DBDTEMP,STREFF)
      IMPLICIT REAL*8 (A-H,O-Z)
      DIMENSION  FB(NTENS),DBDSIG(NTENS),DBDS(NTENS),DBDB(NTENS),
     1        DBDTEMP(NTENS),B(NTENS),STREFF(NTENS)
      DATA ZERO,ONE,TWO,THREE,SMLSIG /0.0D0,1.0D0,2.0D0,3.0D0,1.0D-20/
C-----------------------------------------------------------------------
C Material constants used
C-----------------------------------------------------------------------
      DATA       GDOT0,       F0,  GC, TAUhat,   p,     q,      G0
     +   /   7.146D11,  349911., 8.3,  989.2, 0.59, 1.33,  121731. /
      DATA          E,   alpha,       r,    C,   hb,   xsat
     +   /     80000.,    0.85,  0.3125, 100.,  325.,   4.0 /
C-----------------------------------------------------------------------
      IF(SIG .LE. SMLSIG) SIG = SMLSIG
C-----------------------------------------------------------------------
C Shear modulus of single crystal, G = C44, and temperature in Kelvin
C-----------------------------------------------------------------------
      G  = 1.14392D5 - 26.8818D0 * TEMP
      TK = TEMP + 273.D0
C-----------------------------------------------------------------------
C Fraction of the Orowan stress at which the critical
C configuration of gliding dislocation segments are reached
C-----------------------------------------------------------------------
      frac = alpha * G0 * 325. / (40.8D0 * G * xsat) * (0.355 -
     +       69.9D0 / (alpha * r**0.5 * G / 2.D0 / C)) + alpha
      fracal = frac / alpha - 1.D0
C-----------------------------------------------------------------------
C Reduce equivalent stresses for flow rule and correct S0 for temp.
C-----------------------------------------------------------------------
      SIGF = SIG / 2.D0
      S    = S0 / G0 * G
C-----------------------------------------------------------------------
C  Calculate the equivalent inelastic strain rate
C-----------------------------------------------------------------------
      X    = SIGF - S
      IF(TK .GT. 1273.) TK = 1243.
      IF(X .LE.0.D0) THEN
        F = GDOT0 * EXP(-F0 / GC / TK)
      ELSE
        F  = GDOT0 * EXP(- F0 / GC / TK *
     +       (1.D0 - ( X / TAUhat / G * G0)**p)**q)
      ENDIF
C-----------------------------------------------------------------------
C Calculate the rate of change of the deviatoric back stress B
C-----------------------------------------------------------------------
      DO 10 I= 1, NTENS
   10   FB(I) =  hb * F * (1.5D0 * STREFF(I)/SIG - B(I) / fracal / S)
C-----------------------------------------------------------------------
C Non-zero evolution of S0 when multiplication sources are activated
C (when the equivalent bowing stress reaches a fraction ysat of its
C saturated value (ysat = 1-exp(-xsat), where xsat = strain amplitude
C to saturation in terms of the time constant tau = 2 xsat / epsilonsat)
C-----------------------------------------------------------------------
      ysat   = 1.D0 - DEXP(- xsat)
      Bsat = ysat * S * fracal
      IF(BEQ .GE. Bsat) THEN
        i = 1
      ELSE
```

Appendix.7.B

```
        i = 0
      ENDIF
      hs0 = alpha * r**0.5D0 * G0 / (4*C)
      FS =  hs0 * F * i
C-----------------------------------------------------------------------
C Calculate the material derivatives
C-----------------------------------------------------------------------
      X    = SIGF - S
      IF( X / DABS(X) .LE. 0.D0) THEN
        DFDSIG = 0.D0
        DFDS   = 0.D0
        DFDTEMP= GDOT0 * F0 / GC / TK**2.D0 * DEXP(-F0/GC/TK)
      ELSE
        X1 = X / TAUhat / G * G0
        DFDSIG = GDOT0 * F0 * p * q / (2.D0 * GC * TK * TAUhat * G/G0)*
     +         DEXP(- F0/GC/TK * (1.D0 - X1**p)**q) * (1.D0 -
     +         X1**p)**(q-1.D0) * X1**(p-1.D0)
        DFDS   = - 2.D0 * G / G0 * DFDSIG
        DFDTEMP = GDOT0*F0 / GC * DEXP(-F0/GC/TK * (1.D0 - X1**p)**q) *
     +          ( (1.D0 - X1**p)**q / TK**2.D0 + q * p * G0 * 26.8818D0/
     +          (TK * TAUhat * G**2.D0)   *  (1.D0-X1**p)**(q-1.D0) *
     +          X1**(p-1.D0) * SIGF)
      ENDIF
C . . . . . . . . . . . . . . . . . . . . . . . . . . . . . . . . . . .
      DO 20 K=1, NTENS
        DBDB(K)  = hb * 1.5D0 / SIG * (1.5D0**0.5D0 * STREFF(K) *
     1       (F/SIG - DFDSIG) - F) - hb * G0 / fracal / S0 / G * (F -
     2       1.5D0**0.5D0 * B(K) * DFDSIG)
        DBDTEMP(K) = 1.5D0*hb * STREFF(K)/SIG * DFDTEMP - hb * B(K)
     1    * G0 / (S0 * fracal) * ( 26.88 * F / G**2 + DFDTEMP / G)
        DBDSIG(K)  = hb * (1.5D0 * STREFF(K) * (- F / SIG**2.D0 +
     1     DFDSIG / SIG) - B(K) / fracal / S * DFDSIG)
        DBDS(K)  = 1.5D0 * hb * STREFF(K) / SIG * DFDS + hb / fracal
     +             * G0/G * B(K) * (F / S0**2.D0 - DFDS / S0)
  20  CONTINUE
C . . . . . . . . . . . . . . . . . . . . . . . . . . . . . . . . . . .
      DSDS    =   hs0 * i * DFDS
      DSDSIG  =   hs0 * i * DFDSIG
      DSDTEMP =   hs0 * i * DFDTEMP
      RETURN
      END
C***********************************************************************
C                        SUBROUTINE SUBTEMP
C***********************************************************************
C
C    This subroutine calculates the temperature at the beginning of Dt
C    and the temperature rise during the time increment
C
C***********************************************************************
      SUBROUTINE SUBTEMP(TIME, DTIME, TEMP, DTEMP)
      IMPLICIT REAL*8 (A-H,O-Z)
      DIMENSION  TITEM(25), TEM(25)
C
      DATA TITEM/0.,1.,2.,3.,3.5,4.,4.5,5.,6.,7.,8.,65.,66.,67.,68.,69.,
     +         70.,71.,72.,73.,74.,75.,76.,78., 101./
      DATA TEM /25.,520.,716.,943.,1014.,1050.,1075.,1087.,1090.,1090.,
     +  1090.,1090.,968.,889.,832.,774.,721.,678.,645.,609.,579.,551.,
     +  532.,520.,520./
C-----------------------------------------------------------------------
      TIMEF = TIME + DTIME
      TIME1 = TIME
      TIME2 = TIMEF
C                              CYCLE 2
      IF(TIME .GT. 101.) THEN
        TIME1 = TIME - 100.
      ENDIF
      IF(TIMEF .GT. 101.) THEN
        TIME2 = TIMEF - 100.
      ENDIF
C                              CYCLE 3
      IF(TIME .GT. 201.) THEN
        TIME1 = TIME - 200.
      ENDIF
      IF(TIMEF .GT. 201.) THEN
        TIME2 = TIMEF - 200.
      ENDIF
C                              CYCLE 4
      IF(TIME .GT. 301.) THEN
        TIME1 = TIME - 300.
      ENDIF
      IF(TIMEF .GT. 301.) THEN
        TIME2 = TIMEF - 300.
      ENDIF
C                              CYCLE 5
      IF(TIME .GT. 401.) THEN
        TIME1 = TIME - 400.
      ENDIF
      IF(TIMEF .GT. 401.) THEN
        TIME2 = TIMEF - 400.
      ENDIF
C                              CYCLE 6
      IF(TIME .GT. 501.) THEN
        TIME1 = TIME - 500.
      ENDIF
      IF(TIMEF .GT. 501.) THEN
        TIME2 = TIMEF - 500.
      ENDIF
C                              CYCLE 7
      IF(TIME .GT. 601.) THEN
        TIME1 = TIME - 600.
      ENDIF
      IF(TIMEF .GT. 601.) THEN
        TIME2 = TIMEF - 600.
      ENDIF
C                              CYCLE 8
      IF(TIME .GT. 701.) THEN
        TIME1 = TIME - 700.
      ENDIF
      IF(TIMEF .GT. 701.) THEN
        TIME2 = TIMEF - 700.
      ENDIF
C                              CYCLE 9
      IF(TIME .GT. 801.) THEN
        TIME1 = TIME - 800.
      ENDIF
      IF(TIMEF .GT. 801.) THEN
        TIME2 = TIMEF - 800.
      ENDIF
C                              CYCLE 10
      IF(TIME .GT. 901.) THEN
        TIME1 = TIME - 900.
      ENDIF
      IF(TIMEF .GT. 901.) THEN
        TIME2 = TIMEF - 900.
      ENDIF
C-----------------------------------------------------------------------
C  Calculate the temperature at the beginning and end of Dt
C-----------------------------------------------------------------------
```

```
*BOUNDARY,AMP=DIX5
9,1,,1.
*BOUNDARY,AMP=DIZ5
100,1,,1.
*NODE PRINT,NSET=OUT,FREQ=10000

*PLOT, FREQ=1000
                              CYCLE 5 - HOLD
*DISPLACED
U,1.
*END STEP
** -    -    -    -    -    -    -    -    -    -    -    -
**                            STEP # 16, CYCLE 5 - COOLING
**
*STEP, INC=20000, NLGEOM, CYCLE = 15
*VISCO,PTOL=0.1,CETOL=6.00E-5
0.01,36.,0.01E-10
*BOUNDARY,AMP=DIX5
9,1,,1.
*BOUNDARY,AMP=DIZ5
100,1,,1.
*NODE PRINT,NSET=OUT,FREQ=10000
U, COORD
*PLOT, FREQ=300
                              CYCLE 5 - COOLING
*DISPLACED
U,1.
*END STEP
** -    -    -    -    -    -    -    -    -    -    -    -
**                            STEP # 17, CYCLE 6
**
*STEP, INC=20000, NLGEOM, CYCLE = 15
*VISCO,PTOL=0.1,CETOL=6.00E-5
0.01,100.,0.01E-10
*BOUNDARY,AMP=DIX6
9,1,,1.
*BOUNDARY,AMP=DIZ6
100,1,,1.
*NODE PRINT,NSET=OUT,FREQ=10000
U, COORD
*PLOT, FREQ=300
                              CYCLE 6 - COOLING
*DISPLACED
U,1.
*END STEP
** -    -    -    -    -    -    -    -    -    -    -    -
**                            STEP # 18, CYCLE 7
**
*STEP, INC=20000, NLGEOM, CYCLE = 15
*VISCO,PTOL=0.1,CETOL=6.00E-5
0.01,100.,0.01E-10
*BOUNDARY,AMP=DIX7
9,1,,1.
*BOUNDARY,AMP=DIZ7
100,1,,1.
*NODE PRINT,NSET=OUT,FREQ=10000
U, COORD
*PLOT, FREQ=300
                              CYCLE 7 - COOLING
*DISPLACED
U,1.
*END STEP
** -    -    -    -    -    -    -    -    -    -    -    -
**                            STEP # 19, CYCLE 8
**
*STEP, INC=20000, NLGEOM, CYCLE = 15
*VISCO,PTOL=0.1,CETOL=6.00E-5
0.01,100.,0.01E-10
*BOUNDARY,AMP=DIX8
9,1,,1.
*BOUNDARY,AMP=DIZ8
100,1,,1.
*NODE PRINT,NSET=OUT,FREQ=10000
U, COORD
*PLOT, FREQ=300
                              CYCLE 8 - COOLING
*DISPLACED
U,1.
*END STEP
** -    -    -    -    -    -    -    -    -    -    -    -
**                            STEP # 20, CYCLE 9
**
*STEP, INC=20000, NLGEOM, CYCLE = 15
*VISCO,PTOL=0.1,CETOL=6.00E-5
0.01,100.,0.01E-10
*BOUNDARY,AMP=DIX9
9,1,,1.
*BOUNDARY,AMP=DIZ9
100,1,,1.
*NODE PRINT,NSET=OUT,FREQ=10000
U, COORD
*PLOT, FREQ=300
                              CYCLE 9 - COOLING
*DISPLACED
U,1.
*END STEP
** -    -    -    -    -    -    -    -    -    -    -    -
**                            STEP # 21, CYCLE 10
**
*STEP, INC=20000, NLGEOM, CYCLE = 15
*VISCO,PTOL=0.1,CETOL=6.00E-5
0.01,100.,0.01E-10
*BOUNDARY,AMP=DIX10
9,1,,1.
*BOUNDARY,AMP=DIZ10
100,1,,1.
*NODE PRINT,NSET=OUT,FREQ=10000
U, COORD
*PLOT, FREQ=300
                              CYCLE 10 - COOLING
*DISPLACED
U,1.
*END STEP
```

Chapter 8

A Different Micromechanics Approach to Model Visco-Plasticity in Materials with a Well Developed Subgrain Structure

Abstract

Flow and evolutionary equations are proposed to describe the cyclic behavior of single phase single crystals exhibiting a well developed subgrain structure. The model focusses on small strain histories and follows a micromechanics approach. The resulting equations involve three internal state variables per slip system: the isotropic deformation resistance, and a net and a long range back stress arising from the polarization of mobile dislocations against weak and strong obstacles and the polarization of these strong obstacles respectively.

8.1 Introduction

Detailed dislocation models aimed at describing the structure evolution of materials with well developed subgrain boundaries have shown to be very complex (e.g. see Printz and Argon, 1984). The intricate coupling between strain hardening and recovery processes as well as the difficulties associated with experimental studies often make a precise mechanistic description of the physical processes an out-of-reach goal. One of the important features associated with the evolution of this type of dislocation structure under small cyclic deformation histories is that, for comparable elastic and inelastic strains after a load reversal, there is a tendency to move only progressively increasing parts of the dislocation structure, in contrast to "steady state" creep when most of the dislocation structure evolves. Thus, the initial slope of the stress-strain curve is more associated with polarization than hardening. However, the term "hardening" rather than "polarization" will still be used here for familiarity.

An increased degree of complexity is present when, as it is relevant in the general context of the present work, a model is required to provide acceptable fatigue life predictions for small inelastic strains. This translates into the following severe modelling requirements:

1. Smooth elastic-plastic transition on reversed yielding.

2. Evolution of the hysteresis loops towards a stabilized state under symmetric strain cycles (e.g. cyclic hardening or softening).

3. Relaxation of the mean stress under unsymmetric strain cycling.

4. Cyclic creep (ratcheting) in the direction of the mean stress under unsymmetric stress cycles.

The classical continuum mechanics approach to model cyclic deformation (e.g.

see recent reviews by Lindholm, 1987; Krempl, 1987) typically does not properly describe the smooth elastic-plastic transition on load reversal, or cyclic creep under a mean stress.

In this chapter, an idealized dislocation network model will first be discussed to identify the internal variables needed to model the desired features of the material's stress-strain macroscopic response. Second, a possible model to deal with these features will be outlined (see also Busso, 1989). An approach contained within a unified micromechanics framework will be pursued to describe small deformations of monocrystalline alloys, where the difficulties associated with the actual dislocation structure require a more phenomenological approach in the selection of the internal state variables. Here, Taylor's isotropic hardening will be assumed, with all systems hardening at the same rate.

8.2 Idealized Network Model

A typical dislocation structure (e.g. in NiAl crystals in Fig. 8.1) can be idealized as a network of dislocation cells with free-moving dislocations in between. When a shear stress is applied, the motion of these mobile dislocations will be impeded by a number of low-resistance obstacles such as intersecting dislocations, and by strong obstacles such as dislocation cell walls or dislocation tangles. Figs. 8.2a and b show such an idealization, with just a few dislocations for simplicity, in the unstressed and stressed conditions. A possible way of modeling the resulting inelastic strain seems to require two separate components, one arising from the mobile dislocations and one from the motion of the cell walls under the combined action of the applied stress and the forces from the mobile dislocations.

Further insight into the physics of the problem can be achieved by considering the rate-independent network model of Fig. 8.3. Denote the mobile and wall strain

sources described above by γ_m and γ_w, and the resultant inelastic strain by γ. Represent the mobile dislocations and the dislocation cell wall structure by linear spring - perfectly plastic friction elements characterized by K_m, f_m, and K_w, f_w, respectively. Let their interaction be modelled by a linear spring K_{mw}, and the evolution of the dislocation structure under "isotropic" hardening conditions or steady state deformation, by a friction element with current strength f_s.

The resultant stress-inelastic strain response of the network model can be conceived of as being composed of various portions successively taking part during the deformation history, Fig. 8.4. Once the strength for mobile plastic flow f_m is overcome, internal stresses B_m (or equivalently volume averaged forces) begin to arise due to local forces trying to elastically unload dislocations which have already overcome weak obstacles, pushing them back against these obstacles, and are modelled by the stress in spring K_m. Mobile dislocation motion also polarizes the mobile dislocations against the cell walls and builds up a stress B_{mw} in the spring K_{mw}. When the combined action of B_{mw} and the applied stress τ (or equivalently the force F in Fig. 8.3) on the cell walls is large enough to overcome their strength f_w, there is a break in the slope of the stress-inelastic strain curve and an internal stress B_w $(= K_w\ \gamma_w)$ develops. Further straining eventually drives the structure to isotropic hardening conditions, the friction element f_s is activated at $\gamma = \gamma_s$, and its *isotropic* hardening prevails. If the load is reversed at Point A, the elastic energy stored in the spring elements, or equivalently their internal stresses, will aid the reverse motion of dislocations. Thus, the doubling of the original stress-inelastic strain curve occurs until the isotropic strength $-f_{sr} = -f_s(\gamma_r - \gamma_s)$ is reached. The amount of reverse inelastic strain up to this point, $(\gamma_r - \gamma)$, is a measure of the Bauschinger effect commonly observed in metals. As shown in Fig. 8.4, a new load reversal at Point B before reaching $-f_{sr}$ closes the cycle at Point A, whereas a reversal after isotropic hardening, Point C,

would show strain hardening. When f_s is regarded as non-hardening, the resultant stress-strain curve, shown in dotted lines in Fig. 8.4, models the important feature of path-dependent hardening at the yield strength, Point D. Note that this model could easily be extended to rate dependent deformation and recovery effects.

To successfully model material behavior such as that described here will require a large number of internal parameters, and to model the further desired features described in Section 8.1 would involve an even greater number. In view of the inherent difficulty of this type of model, an approximate one containing a limited number of internal variables and a single inelastic strain source will be developed to model these types of stress-strain behavior.

8.3 Crystallographic Model

For rate-independent plasticity, the above behavior associated with small strain reversals can be approximated by models employing the concept of a two-surface theory, introduced under different forms by Iwan (1967), Mroz (1969), and Dafalias and Popov (1976), among others. Exploration of possible modeling approaches led to proposing an extension of Dafalias and Popov's model to increase strain reversal hardening effects, include dynamic recovery, and introduce rate-dependent effects. (Dafalias and Popov's two-surface model was chosen as a starting point for its extremely good fit of stress during strain reversals of $\Delta\epsilon_{total} = 2Y/E$ to 4 %). Note that with rate-dependence, the concept of a bounding surface becomes a bounding potential. Note also that on one slip system, the deformation is uni-dimensional, but circular surfaces will be used here as convenient descriptors.

8.3.1 Physical basis for the internal variables.

Consider the behavior of each slip system (i) in terms of two potential surfaces in stress space, Fig. 8.5, with their radii defined by S_1 and S_2, and their centers by B_1 and B_2 respectively.

Assume that initially mobile dislocations move only after overcoming the yield strength S_1 (the macroscopic result of f_m in the network model of Fig. 8.3). Define the internal or back stress B_1 as the center of the elastic region. It can be thought of as an internal stress arising from the current combined behavior of the internal stress sources described by the network of Fig. 8.3. Thus, since B_1 reflects the polarization arising from mobile dislocation motion against both low-resistance and strong obstacles, as well as the polarization of the strong obstacles, B_1 will be referred to as the net back stress.

Further assume that during both transient and steady state deformation, the isotropic part of the strength associated mainly with the overall motion of the dislocation cells is characterized by the isotropic deformation resistance or strength variable S_2. It represents a simplification of the behavior of the friction elements f_w and f_s of Fig. 8.3.

Finally, characterize the evolution of B_1 in terms of the isotropic strength S_2 and of a "long range" back stress B_2, which represents the polarization of the cell structure associated with, for example, bowing of dislocation cell walls and segments (analogous to B_w in the network model). Here, the bounding potential surface, given by $\tau_b = B_2 \pm S_2$[1], helps set the transient hardening rate for B_1^i and defines its bound as steady state is approached. Directional hardening mechanisms responsible for the Bauschinger behavior discussed above are characterized by evolutionary equations

[1]In what follows, the upper and lower signs will correspond to forward and reverse slip respectively.

for both B_1 and B_2.

8.3.2 Evolutionary relations for a slip system interacting with others

The evolution equation for the net back stress on the slip system i, B_1^i , is taken first of all as proportional to the hardening function for the bounding potential, h_b^i:

$$h_b^i = \frac{\partial B_2^i}{\partial \gamma^i} \pm \frac{\partial S_2^i}{\partial \gamma^i} \tag{8.1}$$

Here, $\dot{B}_1^i$ will be modified by a transient factor involving two parameters a^i and a_r^i. As Fig. 8.6 shows, a^i is the distance between the current value of $B_1^i + S_1^i$ and the bound τ_b^i (Point D). a_r^i, defined as a constant for each strain reversal by Dafalias and Popov, is defined here as a variable to account for its changes due to the changes in h_b^i during the transient or polarizing stage of the deformation. Thus, it is defined as the distance at the last reversal point between $B_{1r}^i + S_1^i$ (Point C in Fig. 8.6) and the intersection of the tangent to the current value of the bound τ_b^i (Point D) with the strain at the reversal point γ_r^i (Point F). It depends on τ_b^i, h_b^i, the values of the inelastic strain reversal $(\gamma^i - \gamma_r^i)$ and the net back stress at the last reversal point B_{1r}^i. In terms of the internal variables:

$$a^i = (S_2^i \pm B_2^i) - (S_1^i \pm B_1^i)$$

$$a_r^i = (S_2^i \pm B_2^i) - (S_1^i \pm B_{1r}^i) \mp h_b^i (\gamma^i - \gamma_r^i) \tag{8.2}$$

In this proposed model, the transient factor is tentatively further modified by a term which depends on the rate of hardening of B_1^i at the last load reversal, $h_{B_{1r}}^i$, see Fig. 8.6. Dafalias and Popov's model has a similar term which depends instead on a constant value of a_r^i taken at the last load reversal. The purpose of this term is to provide a measure of the amount of inelastic strain generated during the last

load reversal, e.g., it provides more hardening for small strain reversals. It should be pointed out that although the modification of the transient factor by either $h^i_{B_{1r}}$ or a^i_r fails to satisfy short mid-range strain reversals, at least $h^i_{B_{1r}}$ is a constant value for each load excursion in contrast to the variable a^i_r.

Then the evolution for B^i_1 , expressed in terms of the material constants $f, c, E,$ and m, is:

$$\dot{\mathrm{B}}^i_1 = h^i_b \left[1 + \frac{f}{1 + c(E/h^i_{B1r})^m} \; \frac{1}{a^i_r/a^i - 1}\right] \dot{\gamma}^i \ . \tag{8.3}$$

The limiting cases for Eq. 8.3 are:

(i) on reversal of $\dot{\gamma}^i$: $\quad a^i \to a^i_r \quad$ so that $\quad \dot{\mathrm{B}}^i_1 \to \infty, \quad$ and

(ii) towards steady state $\quad a^i \to 0 \quad$ so that $\quad \dot{\mathrm{B}}^i_1 \to \dot{\tau}^i_b = h^i_b \, \dot{\gamma}^i$.

Thus, Eq. 8.3 allows modeling the smooth elastic-plastic transition after a load reversal.

The isotropic strength S^i_2 is assumed to evolve following the work hardening form proposed by Hill (1966) modified by a dynamic recovery term, which drives S^i_2 towards a saturation value, and by an exponential term which allows maintaining $\dot{S}^i_2 \approx 0$ during the transient or polarizing (Bauschinger) stage of deformation:

$$\dot{S}^i_2 = \left\{\sum_{j=1}^{N} h_{ij} \, |\dot{\gamma}^j| - r_2 \, (S^i_2 - S^i_{20}) \, \left|\dot{\gamma}^i\right|\right\} \; exp\left(-\frac{a^i}{0.1 \, S^i_2}\right) . \tag{8.4}$$

Here, r_2 and S^i_{20} are constants, N is the number of slip systems, and h_{ij} the hardening modulus which accounts for the latent hardening behavior of single crystals. With Taylor's isotropic hardening, $h_{ij} = h_1 =$ constant.

The evolution rate of B^i_2 also follows a hardening-recovery form, simplified to depend only on two constants h_2 and r_3 :

$$\dot{\mathrm{B}}^i_2 = h_2 \frac{S^i_2}{S^i_{20}} \, \dot{\gamma}^i - r_3 \left|\dot{\gamma}^i\right| \; \mathrm{B}^i_2 \ . \tag{8.5}$$

Coupling between S_2^i and B_2^i is necessary to account for the dependence of B_2^i on the current value of the isotropic strength S_2^i outside the Bauschinger regime. Note that the model in its present form cannot account for cyclic strain softening, and only stable cyclic responses can be modeled.

8.3.3 Flow rule

The resolved shear stress for the slip system can be found from the applied stress tensor $\underline{\sigma}$. Let $\mathbf{n}^i$ and $\mathbf{b}^i$ denote, respectively, the vector normal to a particular slip plane and a permissible slip direction. Then,

$$\tau^i = \mathbf{n}^i \cdot \underline{\sigma} \cdot \mathbf{b}^i \ . \tag{8.6}$$

Rate and thermal effects appear in the flow rule (the effect of temperature on recovery should be incorporated by making r_2, and r_3 in Eq. 8.4 and 8.5 temperature dependent), where the inelastic shear strain rate in the system, $\dot{\gamma}^i$, is given by a power function (although hyperbolic or exponential functions could be used) of its resolved shear stress τ^i, and the internal variables B_1^i , B_2^i , and S_2^i . The temperature T is included through a constant thermal activation energy Q_0:

$$\dot{\gamma}^i = \dot{\gamma}_0 \ \ exp\left(-\frac{Q_0}{R\,T}\right) \ \ \left\langle \frac{|\tau^i - B_1^i| - S_1^i}{S_2^i} \right\rangle^n \ sgn(S_0\,\mu/\mu_0 \cdot B_1^i) \ , \tag{8.7}$$

where R is the gas constant, and $\dot{\gamma}_0$, n, and S_1^i are material constants. The braquets $< >$ imply that with $x = |\tau^i - B_1^i| - S_1^i$, $< x >= x$ for $x > 0$, and $< x >= 0$ for $x \leq 0$. The $sgn(\tau^i - B_1^i)$ allows modeling both the negative and positive slip on the system. Further contribution to the inelastic strain rate from the excess of stress over the potential bound will be considered.

Appendix 8.A shows the complete set of equations associated with a slip system.

8.3.4 Formulation for multi-slip

In principle, the shear strain rate for m slip systems can now be resolved into a particular orientation and added up to obtain the macroscopic inelastic strain rate tensor. Then,

$$\dot{\epsilon}^p_{ij} = \sum_{k=1}^{m} \frac{1}{2} \left(\mathbf{n}^k_i \, \mathbf{b}^k_j + \mathbf{b}^k_i \, \mathbf{n}^k_j \right) \dot{\gamma}^k \, . \tag{8.8}$$

The stress rate tensor expressed in the cubic symmetry axes is then given in terms of the anisotropic elastic stiffness tensor $\underline{\mathbf{D}}$, the total strain rate tensor $\underline{\dot{\epsilon}}$, the thermal strain rate tensor $\underline{\dot{\epsilon}}^{th}$, and $\underline{\dot{\epsilon}}^p$:

$$\dot{\tau}_{pq} = D_{pqij} \left(\dot{\epsilon}_{ij} - \dot{\epsilon}^p_{ij} - \dot{\epsilon}^{th}_{ij} \right) . \tag{8.9}$$

8.4 Model Simulations

The stress-inelastic strain curves of Fig. 8.7 show reversed (A to B) and forward (B to C) single slip as simulated by the proposed model in its rate-independent form with no recovery. Note the bounding of the strength ($= B^i_1 \pm S^i_1$) by τ^i_b. Another important feature in modeling cyclic plasticity is satisfied by the simulation of Fig. 8.8, which shows how the model correctly describes two different hardening rates obtained at Point 7 as the result of two different loading paths with different prior hardening rates (3-7-8 and 6-7-9).

When small deformation histories do not lead to an increase in disloaction density (as it was seen in Chapters 5 and 6 for NiAl), the isotropic resistance S_2 will remain unchanged. Fig. 8.9 shows how the internal variables will evolve in a particular slip system under this condition for a material with similar properties as the NiAl crystals previously studied. Fig. 8.10 shows how a more rounded shape than those hysteresis loops introduced in Chapter 5 could properly be dealt with this proposed model. Similarly, the model prediction of the dependency of the kinematic hardening

rate on strain range can be seen in the amount of strain hardening exhibited by the different cycles shown in the decreasing strain range test of Fig. 8.11.

8.5 Summary

The proposed form for the rate-dependent hardening behavior of the slip systems properly describes the smooth elastic-plastic transition after a load reversal which, for materials with well developed subgrain structures subjected to small deformation histories, is critical to describe accurately the material response. To achieve this, the evolution equation for the net back stress has been formulated in terms of the isotropic deformation resistance and a long and short range back stresses. It consists of an extension of a two-surface rate-independent model in that an evolving bounding value for the net back stress with recovery is presented.

Bibliography

[1] Printz, F.B., and A.S. Argon (1984),"The evolution of plastic resistance in large strain plastic flow of single phase subgrain-forming metals', *Acta Metall.*, **32**, 1021.

[2] Busso, E.P. (1989), 'Modeling Rate Dependent Single Crystal Cyclic Plasticity for Structural Applications', Proc. of *The Second International Symposium on Plasticity and its Current Applications*, (A.S. Kahn and M. Tokuda eds.), Tsu, Japan, 541.

[3] Dafalias, Y.F. and E.P. Popov (1976), 'Plastic internal variables formalism of cyclic plasticity', *J. Appl. Mech.*, **98**, 645.

[4] Hill, R. (1966), 'Generalized constitutive relations for incremental deformation of metal plasticity by multislip', *J. Mech. Phys. Solids*, **14**, pp. 95.

[5] Iwan, W.D. (1967),'On a class of models for the yielding behavior of continuous and composite systems', *J. Appl. Mech.*, **34**, 662.

[6] Krempl, E. (1987),'Models of viscoplasticity. Some concepts on equilibrium (back) stress and drag stress', *Acta Mec.*, **69**, 25.

[7] Lindholm, U.S. (1987), 'Unified viscoplastic constitutive equations and their applications', *ASME Winter Annual Meeting,* **V. 1**, Boston, MA, 77.

[8] Mroz, Z. (1969),'An attempt to describe the behavior of metals under cyclic loads using a more general workhardening model', *Acta Mech.*, **7**, 199.

Fig. 8.1 Dislocation network in NiAl after 35% strain at 850°C

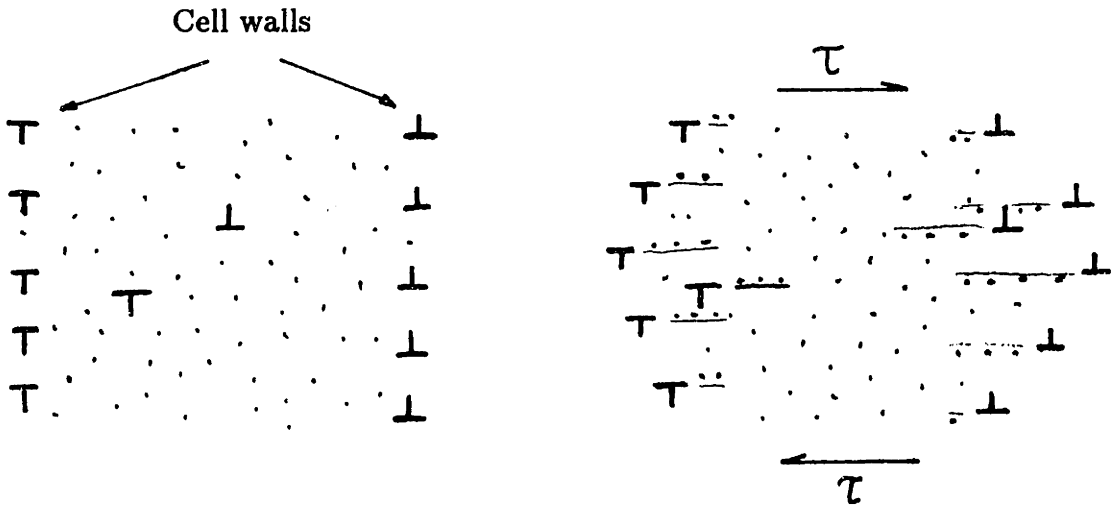

(a) Unstressed (b) Stressed

Fig. 8.2 Idealized dislocation network with weak obstacles shown by (...)

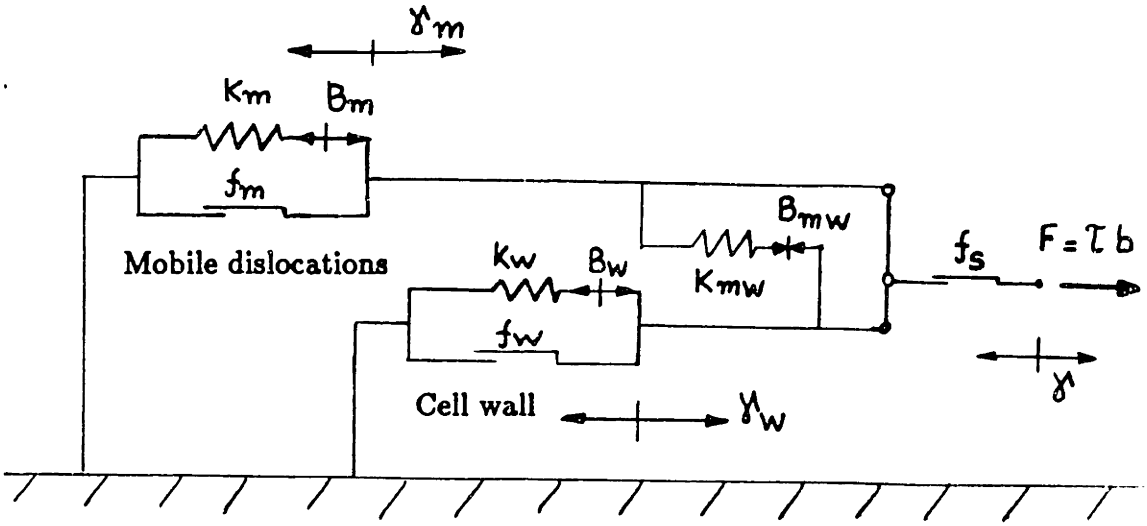

Fig. 8.3 Idealized network model

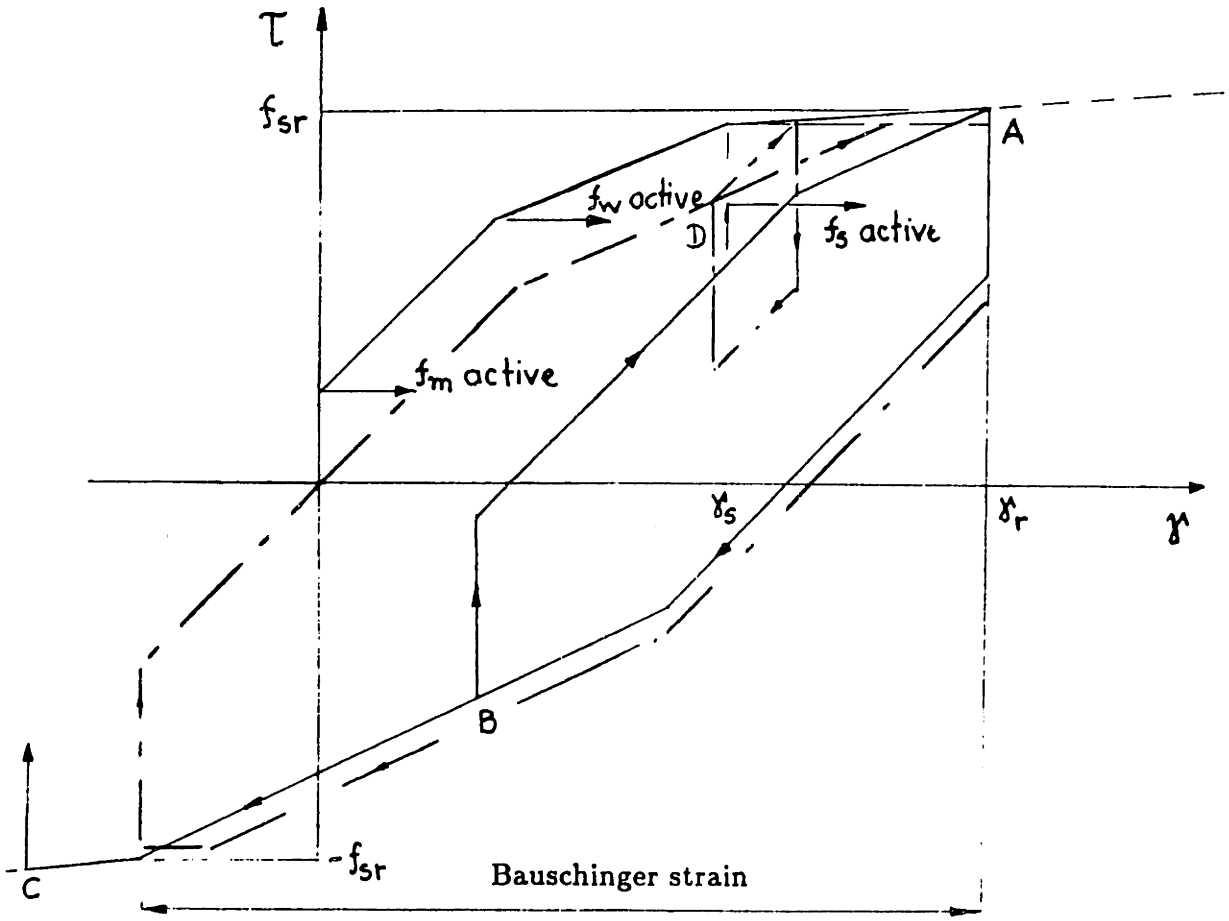

Fig. 8.4 Stress-inelastic strain response of network model

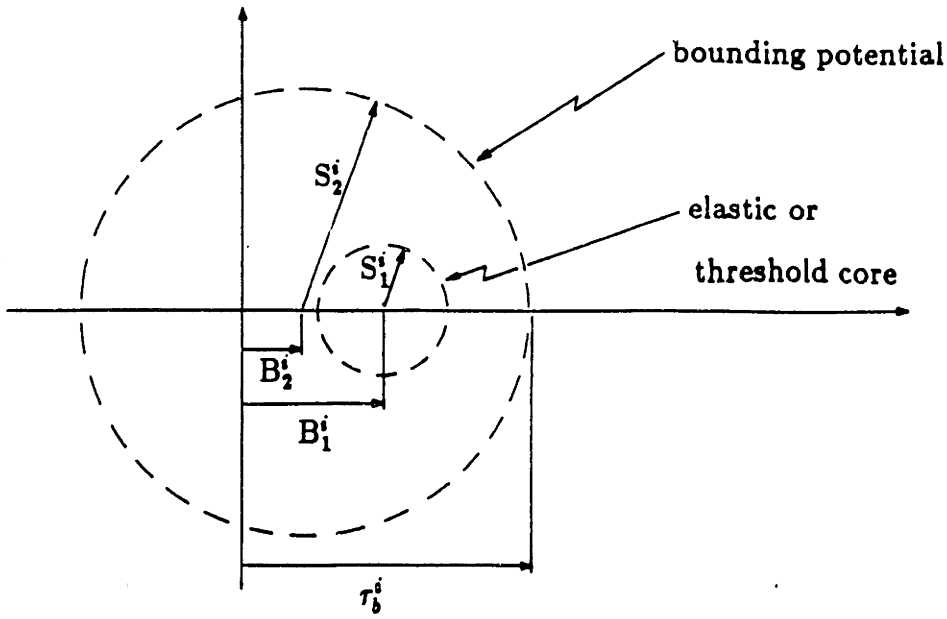

Fig. 8.5 Internal state variables associated with a slip system (i)

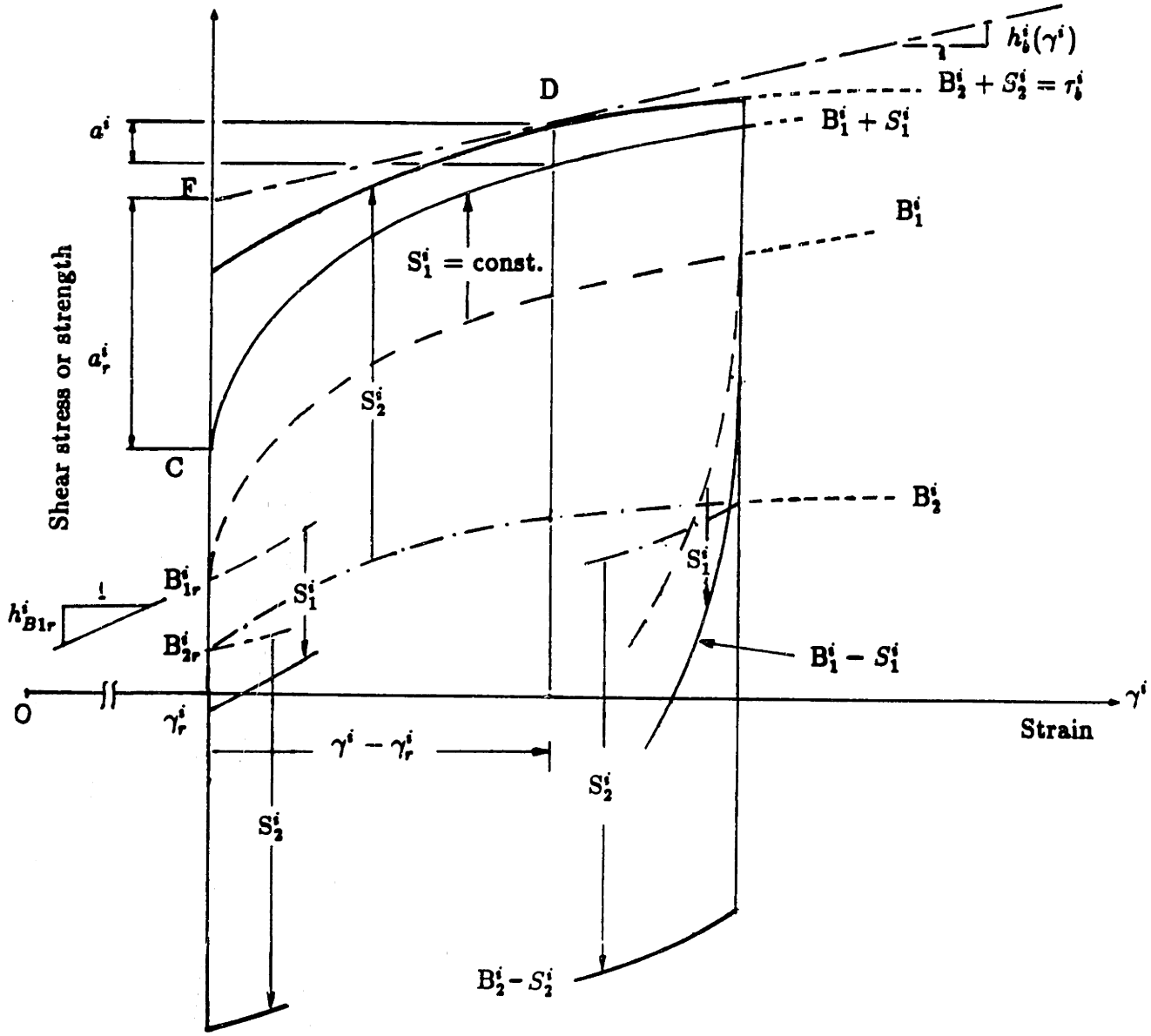

Fig. 8.6 **Bounding potential model for the evolution of the net** back stress, B_1, of **a slip system (i)**

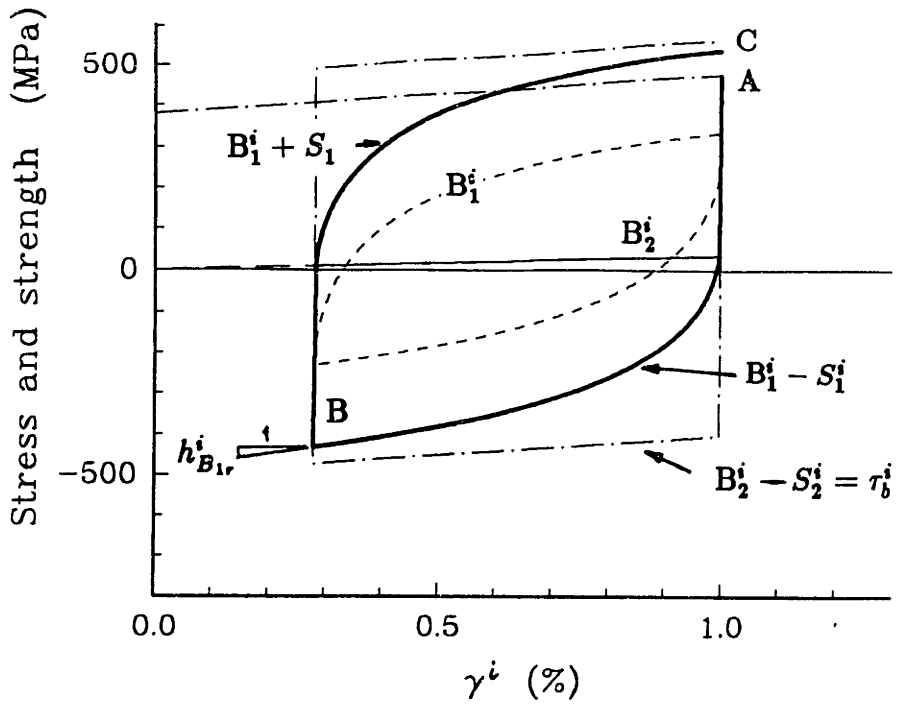

Fig. 8.7 **Rate independent simulation with a two–surface model with no recovery**

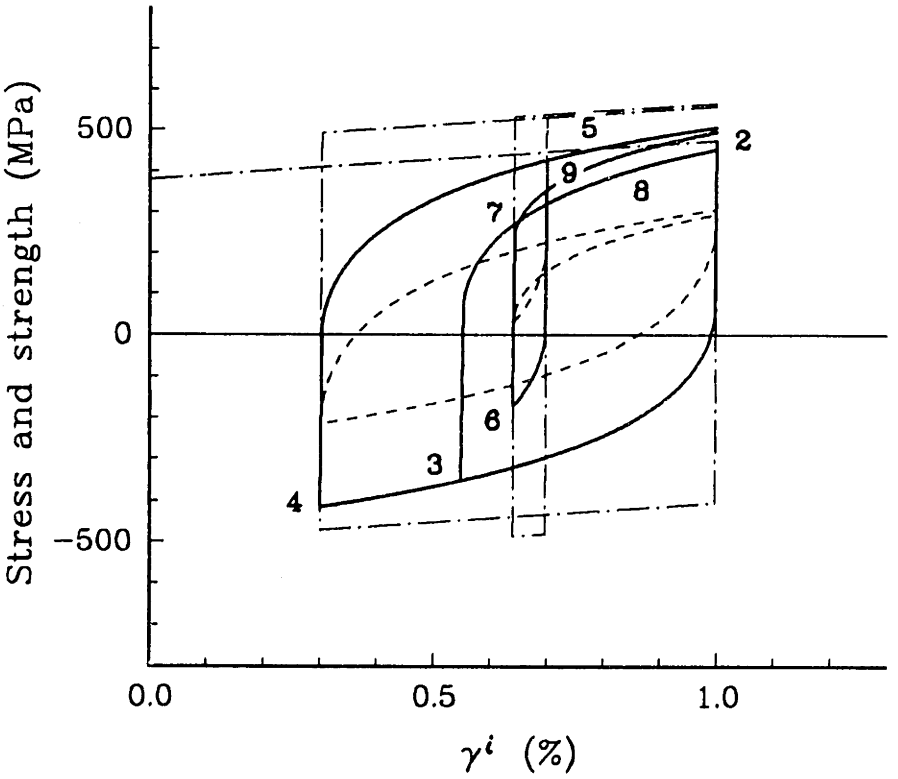

Fig. 8.8 **Path–dependent hardening at Point 7**

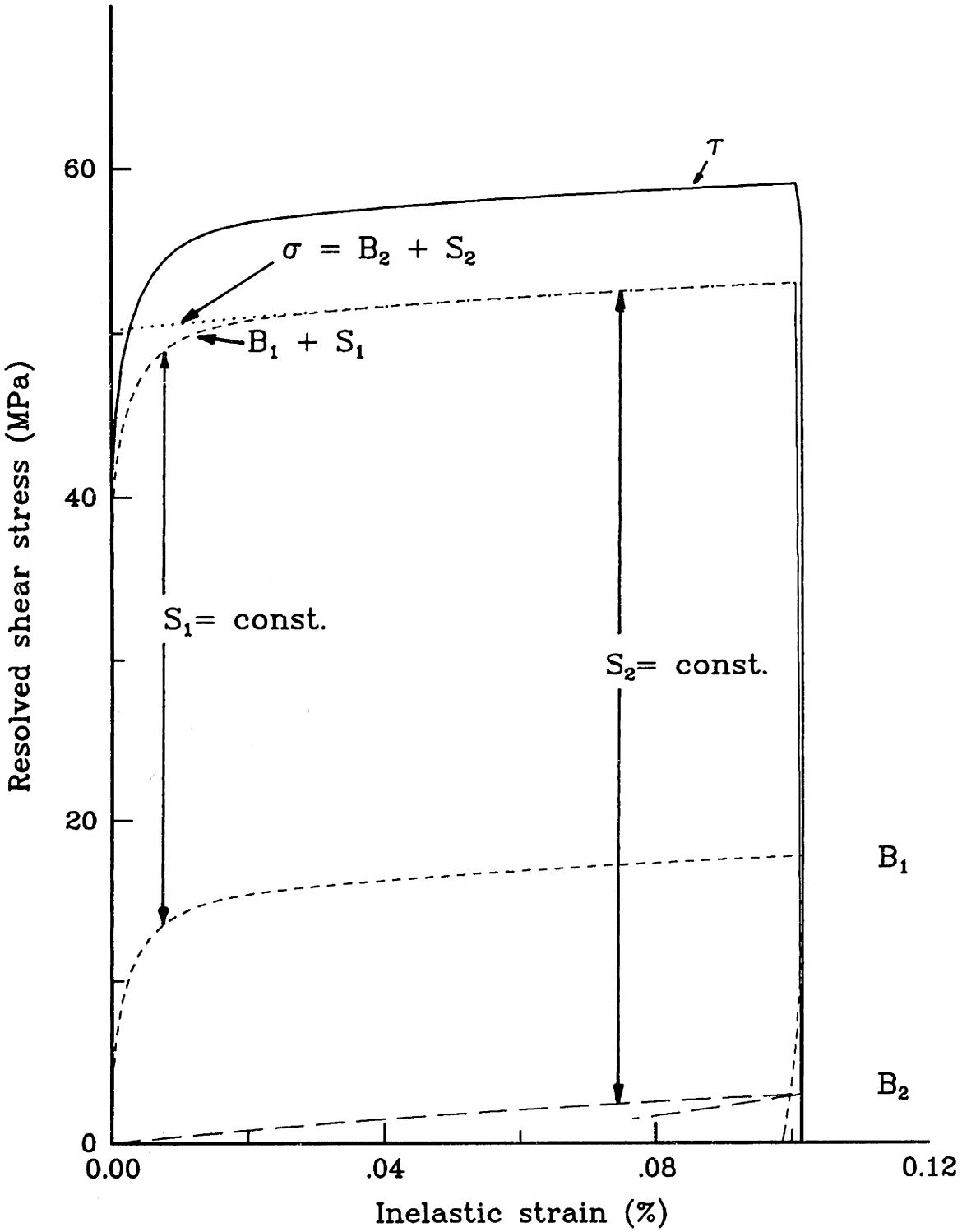

Fig. 8.9 Model prediction of the evolution of the back stresses in an active slip system when the isotropic deformation resistance remains constant

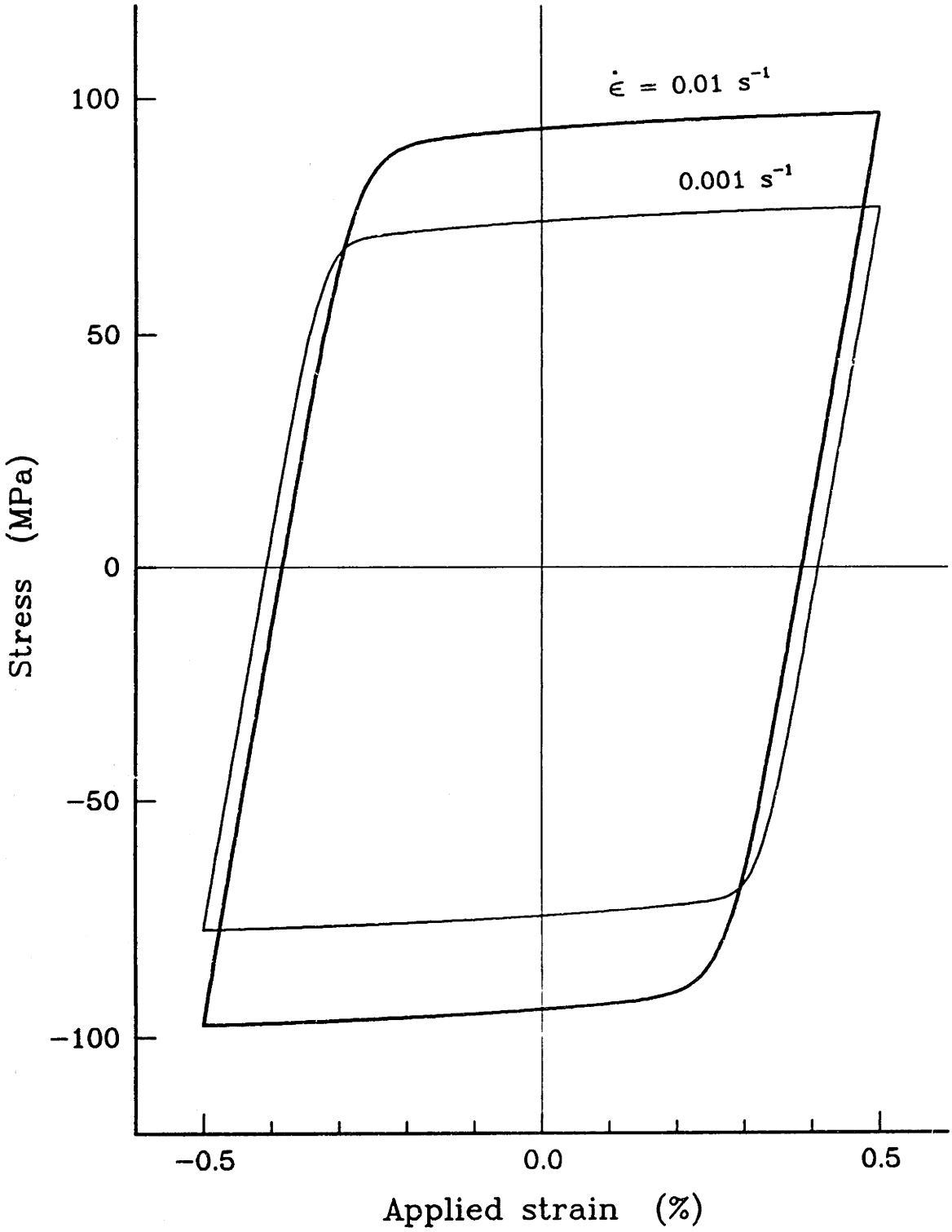

Fig. 8.10 Model simulation of the strain rate effects of stable hysteresis loops

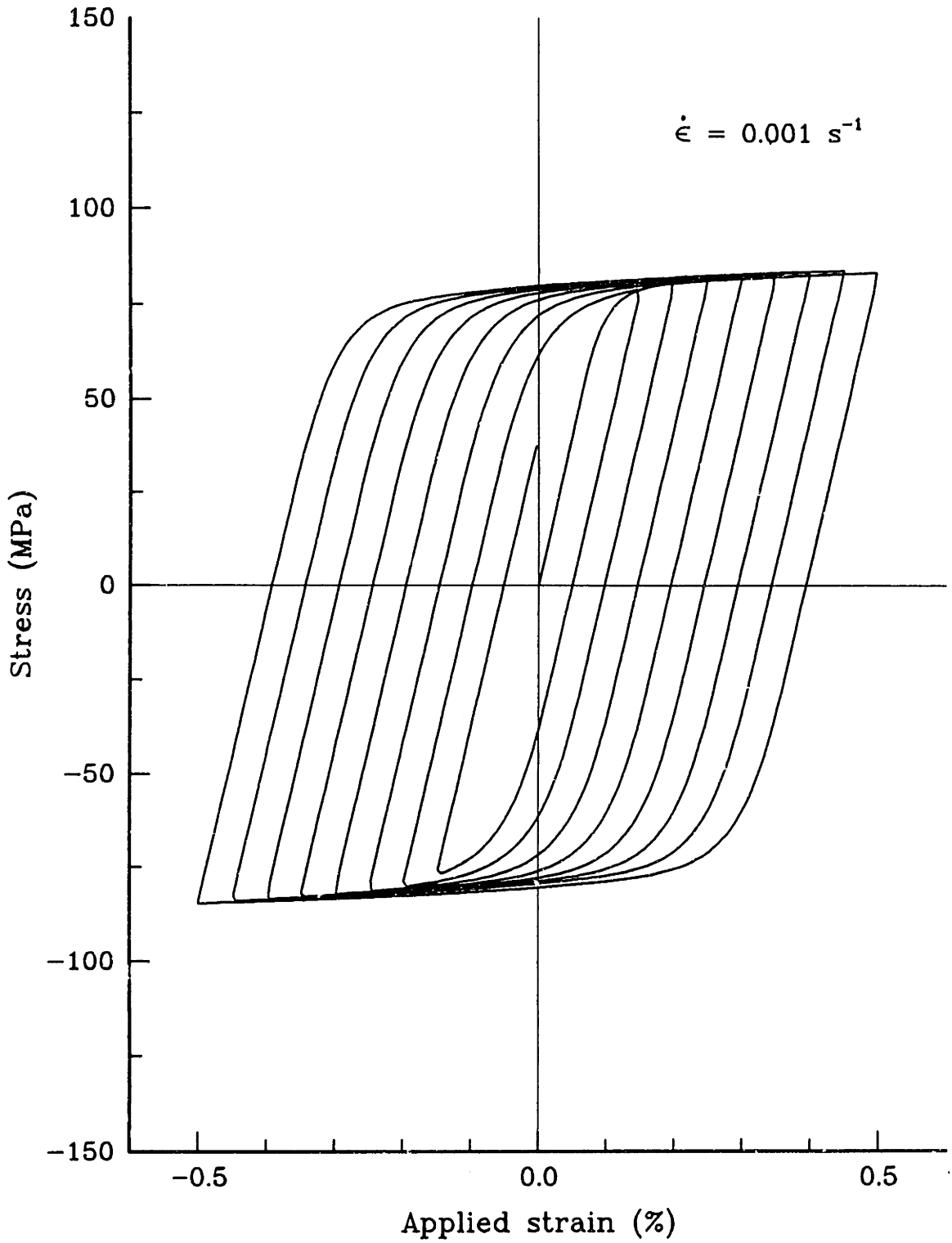

Fig. 8.11 Model simulation of a decreasing strain range test

Appendix 8.A

Flow and Evolutionary Equations for the Slip System i

Flow rule

$$\dot{\gamma}^i = \dot{\bar{\gamma}}_0 \left\langle \frac{|\tau^i - \mathrm{B}_1^i| - S_1^i}{S_2^i} \right\rangle^n sgn(\tau^i - \mathrm{B}_1^i) \tag{1}$$

Evolutionary equations

$$\dot{\mathrm{B}}_1^i = h_b^i \left[1 + C \frac{1}{(a_r^i / a^i - 1)}\right] \dot{\gamma}^i \tag{2}$$

$$\dot{S}_2^i = \left\{ \sum_{j=1}^{N} h_{ij} |\dot{\gamma}^j| - r_2 (S_2^i - S_{20}^i) |\dot{\gamma}^i| \right\} exp\left(-\frac{a^i}{0.1 S_2^i}\right) \tag{3}$$

$$\dot{\mathrm{B}}_2^i = h_2 \frac{S_2^i}{S_{20}^i} \dot{\gamma}^i - r_3 |\dot{\gamma}^i| \mathrm{B}_2^i \tag{4}$$

where,

$$a^i = \left(S_2^i \pm \mathrm{B}_2^i\right) - \left(S_1^i \pm \mathrm{B}_1^i\right), \text{ and } \quad a_r^i = \left(S_2^i \pm \mathrm{B}_2^i\right) - \left(S_1^i \pm \mathrm{B}_{1r}^i\right) \mp h_b^i \left(\gamma^i - \gamma_r^i\right)$$

$$C = \frac{f}{1 + c\,(E/h_{B1r}^i)^m}$$

and for single slip,

$$h_b^i = h_2 \frac{S_2^i}{S_{20}^i} \mp r_3 \mathrm{B}_2^i + \left\{h_1 - r_2 (S_2^i - S_{20}^i)\right\} exp\left(-\frac{a^i}{0.1 S_2^i}\right)$$

Internal state variables:

B_1^i	Net back stress or center of the elastic region
B_2^i	Long range back stress for the bounding potential
S_2^i	Isotropic strength

History dependent parameters:

$h_{B_{1r}}^i$	Rate of hardening of B_1^i at the last load reversal
γ_r^i	Inelastic strain at the last load reversal
B_{1r}^i	Net back stress at the last load reversal

Loading variable:

τ^i	Resolved shear stress

Material constants:

S_1^i, $\dot{\bar{\gamma}}_0$, n, $h_1 (= h_{ij})$, h_2, r_2, r_3, S_{20}^i, f, c, E, m